UNIVERSIDAD AUTONOMA DE MADRID

DOCTORAL THESIS

Imaging ultrafast electron and nuclear dynamics in hydrogenic molecules

Author:

Roger Yulier Bello Romero

Supervisors:

Prof. Dr. Fernando Martín García

Dr. Alicia Palacios Cañas

September 11, 2017

Abstract

Light-induced ultrafast molecular dynamics occur on temporal scales ranging from tens of femtoseconds, involving nuclear rearrangements, to few tens of attoseconds, when dealing with electrons. The interplay between nuclear and electron dynamics plays a crucial role in bond breaking and formation and intramolecular processes, thus being the ultimate responsible for chemical reactivity in molecules. The investigation of molecular excitation and ionization processes at their natural time scales has become an active field of research thanks to the impressive progresses in laser technology and the current capabilities of large-scale computing sources. In this thesis, we report a complete theoretical study on unexplored photoionization phenomena of hydrogenic molecules by one and multi-photon absorption. We perform nearly exact ab-initio calculations and develop simplified models to gain further physical insight on the observed phenomena. The main goal is to elucidate the effects of electron correlation and the coupled electron-nuclear motion in ultrafast molecular photoionization processes, in a joint theoretical and experimental work. The wide range of processes here investigated by means of different radiation sources are expected to shed some light on the underlying physical phenomena governing ultrafast molecular dynamics of simple and complex targets.

We first study the one-photon single ionization of H_2 in two different energy regions. At high energies ($\hbar\omega$=400 eV), we propose an imaging scheme, which uses the photo fragments spectra to visualize electron correlation terms, as well as the dependencies of the H_2 two-electron wave function on the internuclear distance. At low energies, where the doubly excited states are accessible, we report vibrationally resolved photoelectron spectra exhibiting the signature of autoionizing states. By using the nuclear motion as an internal clock we have reconstructed the time evolution of the autoionization process.

Secondly, we present our recent results on the use of XUV pump-IR probe schemes to induce and control an asymmetric photoelectron ejection phenomena upon H_2 photoionization. In the one hand, pumping with an isolated attosecond XUV pulse, we found the electron ejection asymmetries to be the consequence of

the interference between different quantum paths leading to energy-degenerate states with different spacial symmetry. On the other hand, pumping with a train of attosecond pulses, we employ the reconstruction of attosecond beating by interference of two-photon transitions (RABBITT) technique in order to access the phase of the electron scattering states in both dissociative and non-dissociative channels. This is the first application of the RABBITT technique in a light molecule, where the coupling of electronic and nuclear motion leaves a distinct trace in the phase of the entangled molecular wave packet.

We have also investigated the use of a "more standard" XUV pump-IR probe approach to gain access to the electron-electron correlation terms in D_2 photoionization. In this scenario, synchrotron and time-resolved experiments with attosecond resolution are combined to map the ultrafast dissociation of a highly excited D_2^+ molecule. Correlations between the two electrons lead to a superposition of excited ionic states, which dictates the pathways along which the highly-excited molecule dissociates. By using Coulomb explosion imaging, we can assess the relative contribution of competing parent ion states to the dissociation process for different orientations of the molecule with respect to the laser polarization.

Finally, we have explored two-photon (one-color) single ionization of the H_2 molecule via resonantly excited molecular states of the neutral species. State-of-the-art experiments performed in the free-electron laser (FEL) facility at FERMI have shown that selective excitation into specific vibrational states allows one to disentangle the influence of the nuclear degrees of freedom in the photoionization channel. In particular, the ratio between dissociative and non-dissociative ionization yields can be controlled by varying the laser parameters in the FEL.

Resumen

La dinámica molecular inducida por pulsos láser tiene lugar en escalas de tiempo que van desde unas decenas de femtosegundos, inherente al movimiento de los núcleos, hasta unas decenas de attosegundos, inherente al movimiento electrónico. El acoplamiento de los grados de libertad electrónicos y nucleares juega un papel crucial en la ruptura y formación de enlaces químicos, así como en procesos intramoleculares inducidos por pulsos láser, y por tanto, es responsable de la reactividad química observada en moléculas. El vertiginoso desarrollo de la tecnología láser en las últimas décadas, en conjunción con la extraordinaria potencia de cálculo que ofrecen los superordenadores actuales, han permitido el estudio de procesos de ionización y excitación en moléculas en sus escalas de tiempo características, haciendo de la denominada "attociencia" uno de los campos de investigación más prometedores. Esta tesis presenta un estudio teórico de la ionización de moléculas de H_2/D_2 por absorción de uno o varios fotones. Para ello, empleamos métodos ab-initio que permiten resolver numéricamente la ecuación de Schrödinger dependiente del tiempo, en combinación con modelos analíticos que permiten simplificar y tener una una visión más general de los procesos estudiados, al tiempo que pueden aplicarse a sistemas más complejos. El principal objetivo de esta tesis es investigar el efecto de la correlación electrónica y el acoplamiento entre los grados de libertad electrónicos y nucleares en procesos ultrarrápidos observados en fotoionización de moleculas. Este estudio se ha realizado, en su mayor parte, en estrecha colaboración con diferentes grupos experimentales trabajando con diversas fuentes de radiación láser.

En primer lugar, estudiamos la ionización inducida por la absorción de un solo fotón en diferentes regiones energéticas del espectro. En el caso de fotones de altas energías ($\hbar\omega$=400 eV), hemos demostrado cómo distinguir los distintos términos responsables de la correlación electrónica en la función de onda (bi-electrónica) del H_2, y al mismo tiempo discernir cómo varían los mismos en función de la distancia entre los núcleos. A bajas energías, donde los estados doblemente excitados de la molécula son accesibles, reportamos los espectros foto-electrónicos resueltos vibracionalmente, donde se observa la huella del proceso de autoionización. El movimiento nuclear actúa como reloj interno del sistema permitiendo reconstruir

la evolución temporal del proceso de autoionización.

En un segundo bloque, investigamos el uso de técnicas de *pump-probe* combinando pulsos de attosegundos en la región del ultravioleta extremo (XUV) con campos de infrarrojo (IR). Para ello, hemos abordado tres escenarios distintos. Primero, hemos empleado un pulso aislado XUV junto con un campo IR, lo que permite inducir y controlar la emisión asimétrica del fotoelectrón. Dicha asimetría proviene de la interferencia resultante entre diferentes trayectorias cuánticas que permiten acceder a estados energéticamente degenerados pero con una simetría espacial distinta. En segundo lugar, hemos empleado un esquema análogo pero empleando trenes de pulsos XUV, lo que nos permite aplicar la técnica de RABBITT (reconstrucción de la oscilación de attosegundos por medio de la interferencia de transiciones a dos fotones), técnica empleada para extraer las fases de los estados electrónicos del continuo. Este trabajo ha permitido demostrar la relevancia de los estados doblemente excitados y el movimiento nuclear en dichas fases. Este es el primer estudio en el que se emplea la técnica RABBITT en moléculas ligeras, y por tanto, la primera demostración del efecto del movimiento nuclear en la definición y extracción de estas fases. Por último, en un esquema *pump-probe* más "estándar", investigamos la disociación ultrarrápida de estados catiónicos excitados tras ionizar la molécula de D_2 usando un pulso XUV. La excitación-ionización a estos estados mediante la absorción de un sólo fotón es exclusivamente debida a los términos de correlación electrónica. En el caso de pulsos ultracortos, la interacción con el láser da lugar a una superposición de estados del ión. La imágen temporal de la dinámica ultrarrápida asociada a este proceso se captura en la explosión Coulombiana de la molécula.

Por último, hemos investigado la ionización inducida por la absorción de dos fotones a través de estados intermedios resonantes con la energía del fotón. Este estudio está motivado por mediciones recientes llevadas a cabo utilizando laseres de electrones libre (FEL, por sus siglas en inglés). Seleccionando los estados vibracionales (intermedios) que son excitados, lo que es posible gracias a la flexibilidad y resolución de los FEL en la emisión de frequencias, podemos investigar la influencia del movimiento nuclear en la fotoionización. De hecho, demostramos experimental y teóricamente, que es posible controlar el peso relativo entre la ionización disociativa y no disociativa variando los parámetros del FEL.

Contents

Chapter 1

Introduction

Capturing the ultrafast electron dynamics on their natural time scale has been the main driving force that has brought attosecond science to be one of the most active research fields nowadays. The development of the new ultrashort radiation sources in conjunction with the improvement of advanced photo-fragment detection techniques such as velocity map imaging (VMI) [1–3] and cold target recoil-ion momentum spectroscopy (COLTRIMS) [4, 5] has enabled unprecedented experimental capabilities for triggering, manipulating and eventually controlling electron dynamics in atoms and molecules on femtosecond (fs) and even attosecond (as) time scales. Particular interest is focused on molecular targets that involve processes ranging from the attosecond time scale, associated with electron dynamics, to the femtosecond timescales, distinctive of nuclear vibrations and molecular dissociation processes. The shortest pulses are currently produced by means of high-order harmonic generation (HHG) [6] from atoms and molecules. The production of high-order harmonics has been observed to occur after the interaction of an atom or molecule with strong infrared (IR) pulses (I=10^{13}-10^{16} Wcm^{-2}). This process generates a series of short and energetic electromagnetic pulses, i.e. an attosecond pulse train (APT). High harmonic generation (HHG) [7], can be explained with the widely known three-step model, based on the strong-field approximation. In brief, in the HHG process the attosecond pulses are produced every half a period of the IR seeding electromagnetic field, with a total duration that is a fraction of the IR period. This technique has been successfully used to create pulses with typical wavelengths in the vacuum ultraviolet (VUV) and soft X-ray (XUV) energy regions, with pulse durations down to 67 as [8, 9]. The first experimental generation of a train of attosecond pulses (APT) [10] was demonstrated at the very beginning of our century, closely followed by the first demonstration of an isolated attosecond pulses (SAP) [11]. These experimental achievements gave birth to a fervent scientific activity pursuing the manipulation of electron dynamics in atoms and molecules with an unprecedented spatial and time resolution [12]. Molecular targets raise more attention, because of the possibility of manipulating chemical reactions acting at the natural time scale at

which the electrons move, being ultimately responsible for the breaking and formation of chemical bonds [13]. Attosecond pulses (SAP or APT) have been applied in combination with IR laser fields to investigate a large variety of phenomena manipulating electron dynamics in molecules, such as tomographic imaging of molecular orbitals [14], control of electron localization during molecular dissociation [15–17] or exploring ultrafast charge migration processes in biomolecules [18]. An alternative approach to produce highly-intense XUV pulses is to use the free electron laser (FEL) [19–22], where a beam of electrons at relativistic velocities traverses an undulator. Through the process of self-amplified spontaneous emission (SASE), the electrons produce a coherent laser pulse with photon energies up to 700 eV and intensities up to 10^{16} Wcm^{-2}. These relatively long and strongly intense fields are suitable to explore nonlinear response in molecules [23–25]. Nevertheless, for many years, molecular photoionization has been explored using synchrotron radiation. The high intensities, monochromaticity and high tunability of synchrotron radiation sources are suitable to explore a wide range of processes in molecular targets providing substantial information on their structure and chemical properties. For instance, anisotropies in the angular distributions of emitted electrons [26], the complete photo-fragmentation of hydrogenic molecules [27, 28] and Young's double-slit interferences [29, 30] have been observed in photoionization of diatomic molecules by synchrotron radiation.

The analysis and interpretation of the complex processes induced in molecules by the different radiation sources require the support of nearly exact theoretical methods. Moreover, very often the successful experimental applications have been led and anticipated by theoretical predictions. For instance, ultrafast charge migration was theoretically predicted to occur in large molecules [31] and has only been recently demonstrated in an experiment combining an attosecond pulse and IR fields [18]. In the same way, using a more modest molecular target, the first experimental attempt to explore the coupled electron-nuclear dynamics in the H_2 molecule, by using an XUV pump-XUV probe scheme [32], followed the scheme proposed in a preceding theoretical work [33]. Despite the developments in supercomputing capabilities, in most of the molecules, the presence of electron-electron correlation and the nuclear degrees of freedom in combination with the size of the problem has made the implementation of such theoretical methods a formidable task, therefore, making the simplest H_2/D_2 molecules the ideal targets of study. As the simplest molecule presenting electron-electron correlation and an effective coupling between the electron and nuclear degrees of freedom, the H_2/D_2 molecules represent an important test-bed for developing a complete understanding of molecular physics on the smallest spatial and fastest vibrational temporal scales. For example, experiments prompting and controlling electron localization have been performed [15, 16, 34, 35], fast nuclear motions have been observed [36, 37], and tests of quantum electrodynamics concepts have been implemented in chemical systems [38].

This thesis is intended to theoretically describe the imprint of electron correlation and the coupled electron-nuclear degrees of freedom in hydrogenic molecules, under the influence of different radiation sources. In particular the physical processes induced in the H_2/D_2 molecules when illuminated with synchrotron radiation, pump-probe schemes combining UV (SAP or APT) with IR pulses, and the long UV pulses coming from the FEL facilities. We are specifically interested in those processes where electron correlation plays a fundamental role and those leading to control of autoionization and of multi-photon single ionization. It should be highlighted that most of the theoretical work has been performed in close collaboration with experimental groups, therefore reproducing realistic radiation source interactions and observable phenomena. The interpretation and understanding of the photo-induced phenomena is achieved by means of ab-initio calculations in combination with simplified models that can be later used for other molecular targets. To our knowledge, our ab initio method is the only available procedure to describe single photoionization problems in H_2/D_2, including all electronic and nuclear degrees of freedom within the Born-Oppenheimer (BO) approximation (full-dimensional) and, at the same time, accurately describing autoionization (process solely governed by electron correlation). Our methodology is implemented in three distinct blocks. Firstly, we compute bound and scattering molecular states using a Feshbach-like formalism that allows for an accurate description of the doubly excited states (highly correlated electronic states lying above the ionization threshold). Secondly, we obtain the dipole couplings between the molecular states to describe the light-molecule interaction. Finally, these ingredients can be used to follow the evolution of the system under the influence of different radiation sources by solving the time-dependent Schrödinger equation (TDSE) or using the time-dependent perturbation theory (TDPT) depending on the process under investigation. The main advantage of this spectral method lies in the simplicity that it provides to extract different physical observables resolved in ejection angles and energies of the molecular fragments. Thus, allowing to understand the physics behind each process in a simple way and making the transition to larger molecules less abrupt. The flexibility and accuracy of the method has been stablished in numerous successful comparisons with experiments, in a single or multi-photon regimes where different physical processes are induced [16, 26, 39–42]. The major restraint of this method is the impossibility to correctly describe double ionization processes, because of the difficulty to retrieve the scattering states associated to a four-body Coulomb breakup problem, nonetheless, in some specific situations this deficiency can be bypassed with help of sophisticated models.

This manuscript is structured in four main parts. Part I is devoted to the description of the theoretical approach. The method has been developed over years in our group, although for the work presented here, new software development has been required as discussed in the theory section. Parts II and III present the

theoretical results employing synchrotron radiation and pump-probe schemes, respectively. While, in Part IV we present the theoretical results for two-photon (one-color) single ionization using the relatively long pulses generated in FEL facilities. Although, as we have mentioned, most of the work has been performed in collaboration with recognized experimental groups (as properly indicated in each section), in this manuscript we mostly focus on our theoretical contribution. We start the theoretical methods in Chapter 2, where we provide the reader with specific information about the methods used to obtain both electronic and nuclear states within the BO approximation. How to describe the electronic scattering states with the correct boundary conditions and how to deal with the doubly excited states embedded in the electronic continuum. A detailed explanation of the spectral method employed to solve the TDSE and the new implementation of the 2^{nd} order TDPT are presented in Chapter 3. This chapter also describes how to extract the different physical observables from the TDSE and TDPT solutions. The result section is opened in Chapter 4, where we have used the high-energy photo fragmentation of the molecule to image the correlated molecular wave function. A high-energy photon ionize the molecule leaving the ion in an excited state. Then, by mapping the kinetic energy release with an specific internuclear distance we were able to visualize the square of H_2 correlated wave function. Chapter 5 shows vibrationally resolved photoelectron spectra exhibiting the signature of autoionizing states. Using the fast nuclear motion in the ion as an internal clock of the autoionization event, we were able to retrieve the build-up in time of those signatures. In Chapter 6 we studied the relevance of electron-electron correlation in the dissociative photoionization of D_2 through a highly excited of D_2^+ molecule. An XUV pulse ionize the D_2 molecule leaving the ion in an excited dissociative state, then with a delayed IR we mapped the wave-packet moving through the D_2^+ state into the Coulomb explosion channel. Chapter 7 is devoted to the study of the asymmetries in the electron ejection. By using an XUV pump-IR probe scheme, and the interference between different quantum paths leading to the same state we were able to create and control asymmetries in the electron ejection direction. In Chapter 8 we use the RABBITT technique to retrieve the phase of the scattering states, with particular emphasis in the effect of the nuclear motion and autoionization on these phases. The main characteristics of the two-photon (one-color) single ionization of the H_2 is presented in Chapter 9. In particular the possibility of controlling the relative weight between the dissociative and non-dissociative channels is studied. Finally, some additional background information can be found in the Appendices.

Part I

Theoretical Methods

Chapter 2

Ab-initio Spectral Methods

2.1 Diatomic molecules: Born-Oppenheimer approximation

Our theoretical description of diatomic molecules subject to radiation sources uses a spectral method. In this chapter, we describe the methodology employed to obtain the stationary wave functions that describe a diatomic molecule with one and two electrons, within the Born-Oppenheimer (BO) approximation. The BO approximation allows one to separately obtain the electronic and nuclear structure, therefore greatly reducing the computational effort, while keeping coupled the nuclear and electronic degrees of freedom through the solution of the Schrödinger equation. In this way, we first evaluate the electronic wave functions for each internuclear distance, and the resulting eigenvalues are later employed to obtain the vibrational wave function by solving the time-independent Schrödinger equation for the nuclei. We will neglect mass polarization terms and relativistic effects, and we also assume that there is no interaction between the vibrational and rotational motion. Since we are interested in molecular processes induced by ultrashort radiation sources, rotational effects occur at much longer time scales and can thus be ignored in the present description. In our description, the origin of the electronic coordinates is placed in the nuclear center of mass. Atomic units (m_e=e=$\hbar$=1) will be used throughout this thesis unless stated otherwise. The Hamiltonian of a diatomic molecule in the body-fixed frame and in the absence of an external field can be dissected according to:

$$\hat{\mathcal{H}}(\mathbf{r}, R) = -\frac{1}{2m_\mu}\nabla_R^2 + \hat{\mathcal{H}}_{el}(\mathbf{r}, R) \tag{2.1}$$

Where $-\nabla_R^2/2m_\mu$ is the relative kinetic energy of the nuclei, m_μ is the reduced mass and $\hat{\mathcal{H}}_{el}(\mathbf{r}, R)$ is the electronic Hamiltonian, which depends parametrically

on R and contains all the potential energy terms (including nucleus-nucleus interaction). The vector $\mathbf{r}$ stands for all the electronic coordinates and R is the internuclear distance. Within the BO framework the total wave function can be written as the product:

$$\Psi_{n\nu}(\mathbf{r}, R) = \frac{\chi_{n\nu}(R)}{R}\psi_n(\mathbf{r}, R) \tag{2.2}$$

The electronic wave function ψ_n complies with:

$$[\hat{\mathcal{H}}_{el}(\mathbf{r}, R) - E_n(R)]\psi_n(\mathbf{r}, R) = 0 \tag{2.3}$$

and the corresponding nuclear wave function $\chi_{n\nu}$:

$$[\hat{T}(R) + E_n(R) - W_{n\nu}]\chi_{n\nu}(R) = 0 \tag{2.4}$$

Where $W_{n\nu}$ is the total energy of the molecule in the ν-th vibrational state associated to the n-th electronic state, $E_n(R)$ is the BO potential energy curve of the n-th electronic state of the molecule and the nuclear kinetic operator $\hat{T}(R)$ is given by:

$$\hat{T}(R) = -\frac{1}{2m_\mu}\frac{d^2}{dR^2} + \frac{J(J+1)}{2m_\mu R^2} \tag{2.5}$$

With J the total angular momentum of the molecule.

2.2 The one-electron diatomic molecule

In our method, the electronic structure of the H_2 molecule is represented using as an underlying basis set the electronic wave functions of the one-electron diatomic molecule, which improves the numerical convergence and decreases the size of the problem. Therefore, this section is focused on the extraction of the electronic structure for the H_2^+ molecule. For the one-electron diatomic system we can write equation 2.3 as:

$$\hat{\mathcal{H}}_{el}\psi_n = \left\{-\frac{1}{2}\nabla^2 - \frac{Z_a}{|\mathbf{r} - \mathbf{R}_a|} - \frac{Z_b}{|\mathbf{r} - \mathbf{R}_b|} + \frac{Z_a Z_b}{R}\right\}\psi_n = E_n(R)\psi_n \tag{2.6}$$

Where $\mathbf{R}_a$ and $\mathbf{R}_b$ are the position vectors of each nucleus and $R = |\mathbf{R}_b - \mathbf{R}_a|$. In many existing works on H_2^+, equation 2.6 is solved using prolate spherical coordinates and both wave functions and energies can be obtained with the desired numerical precision [43–45]. Alternatively it can be solved by expressing the electronic wave function ψ_n in terms of one-center spherical expansion, which allows for an easier implementation, in particular regarding the further inclusion of the nuclear degrees of freedom [46]. For a well defined value of m (m defines the values of the projection of the angular momentum onto the molecular axis), the expansion reads:

$$\psi_n^m(\mathbf{r}, R) = \sum_{l=0}^{l_{max}} \frac{\mathcal{U}_{nl}(\mathbf{r}, R)}{r} \mathcal{Y}_l^m(\hat{\mathbf{r}}) \tag{2.7}$$

Where $\mathcal{Y}_l^m$ holds the angular components expressed is spherical harmonics. And the radial wave function $\mathcal{U}_{nl}$ can be further expanded in a B-spline basis functions [47, 48], for each internuclear distance:

$$\mathcal{U}_{nl}(\mathbf{r}, R) = \sum_{i=1}^{N_B} c_{il}^n \mathcal{B}_i^k(r) \tag{2.8}$$

Where N_B is the number of B-spline functions in the expansion. B-splines are piecewise polynomials of order k defined inside a radial box of size r_{max} . The set of N_B B-splines at each position r are built up by defining a knot sequence $\{t_i\}_i^{N_B+k}$ within the electronic radial box using a recursion formula:

$$\mathcal{B}_i^k(r) = \frac{r - t_i}{t_{i+k-1} - t_i} \mathcal{B}_i^{k-1}(r) + \frac{t_{i+k} - r}{t_{i+k} - t_{i+1}} \mathcal{B}_{i+1}^{k-1}(r) \tag{2.9}$$

And setting the B-splines of order $k = 1$ as $\mathcal{B}_i^1(r) = 1$ for $t_i \leq r < t_{i+1}$ and $\mathcal{B}_i^1(r) = 0$ otherwise [47, 48]. The primary reason for using B-splines basis sets is the flexibility to choose the radial grid points in which the B-splines are defined, this property is paramount to properly describe the asymptotic behaviour of the continuum states because we can place the grid points at very large distance from the nuclei. Another advantage is the banded structure of the matrices in one-electron problems, this allows the use of large basis set without facing complications coming from linear dependences.

To establish the continuity of the ψ_n in $r = 0$ and $r = r_{max}$ it is necessary to exclude from the expansion 2.8 the first and the last B-splines, by doing so we are enforcing the boundary conditions $\mathcal{U}_{nl}(0) = \mathcal{U}_{nl}(r_{max}) = 0$ for all values of

the angular momentum l. Substitution in equation 2.6 and projecting onto $\mathcal{B}_j^k \mathcal{Y}_{l'}^m$ results in a generalized eigenvalue problem for each internuclear distance:

$$\mathbf{H}c = E\mathbf{S}c \tag{2.10}$$

Where:

$$H_{il,jl'} = \int_0^{r_{max}} \int_0^{4\pi} \mathcal{B}_i^k(r)\mathcal{Y}_l^{m*}(\Omega)\hat{\mathcal{H}}_{el}\mathcal{B}_j^k(r)\mathcal{Y}_{l'}^m(\Omega)drd\Omega \tag{2.11}$$

$$S_{il,jl'} = \delta_{ll'} \int_0^{r_{max}} \mathcal{B}_i^k(r)\mathcal{B}_j^k(r)dr \tag{2.12}$$

The overlap matrix S arises from the fact that the B-splines do not constitute an orthonormal basis set of functions. Note that the terms with different values of l are coupled through the electron-nucleus interaction terms (*interchannel coupling*), due to the lack of spherical symmetry, this represent the major difference with respect to the atomic case. Since we are using a one-center expansion it is easier to deal with the coupling term if we expand it in spherical coordinates, the resulting effective Hamiltonian in equation 2.6 is:

$$\begin{aligned}\hat{\mathcal{H}}_{el} = &-\frac{1}{2}\frac{d^2}{dr^2} + \frac{l(l+1)}{2r^2} - \sum_{q=a}^{b} Z_q \sum_{l_q=0}^{\infty} \frac{4\pi}{2l_q+1} \\ &\times \frac{r_<^{l_q}}{r_>^{l_q+1}} \sum_{m_q=-l_q}^{m_q=l_q} \mathcal{Y}_{l_q}^{m_q*}(\theta_q,\phi_q)\mathcal{Y}_{l_q}^{m_q}(\Omega)\end{aligned} \tag{2.13}$$

where we have dropped the additive constant $Z_a Z_b/R$ (added later to the eigenvalues $E_n(R)$), $r_< = min(r, R_q)$, $r_> = max(r, R_q)$ and (θ_q, ϕ_q) are the spherical angles of the nucleus $q = \{a, b\}$. Accordingly, the corresponding matrix elements in equation 2.11 have the following expression:

$$H_{il,jl'} = T_{il,jl'} + \sum_{q=a}^{b} V_{il,jl'}^q \tag{2.14}$$

Where the kinetic energy matrix elements:

$$T_{il,jl'} = \left\{ -\frac{1}{2}\int_0^{r_{max}} \mathcal{B}_i^k(r)\frac{d^2}{dr^2}\mathcal{B}_j^k(r)dr + \frac{l(l+1)}{2}\int_0^{r_{max}} \frac{\mathcal{B}_i^k(r)\mathcal{B}_j^k(r)}{r^2}dr \right\}\delta_{ll'} \quad (2.15)$$

are block diagonal in ls and the matrix elements for the *interchannel coupling* become:

$$\begin{aligned} V^q_{il,jl'} = -Z_q \sum_{l_q=0}^{\infty} \frac{4\pi}{2l_q+1}\int_0^{r_{max}} \mathcal{B}_i^k(r)\frac{r_<^{l_q}}{r_>^{l_q+1}}\mathcal{B}_j^k(r)dr \\ \times \sum_{m_q=-l_q}^{m_q=l_q} \mathcal{Y}_{l_q}^{m_q*}(\theta_q,\phi_q)\int_0^{4\pi} \mathcal{Y}_l^{m*}(\Omega)\mathcal{Y}_{l_q}^{m_q}(\Omega)\mathcal{Y}_{l'}^{m}(\Omega)d\Omega \end{aligned} \quad (2.16)$$

We have placed the diatomic molecule oriented along the z-axis and the origin is placed at the nuclear geometrical center, which coincides with the center of mass for the homonuclear targets we are considering. Thus, the spherical coordinates for the nucleus $\mathcal{Y}_{l_q}^{m_q*}(\theta_q,\phi_q)$ are simple constant values particularly for $(\theta_a,\phi_a) = (0,0)$ and $(\theta_a,\phi_a) = (\pi,0)$ namely $\mathcal{Y}_{l_q}^{m_q*}(\theta_a = 0,\phi_a = 0) = (-1)^{l_q}\mathcal{Y}_{l_q}^{m_q*}(\theta_b = \pi,\phi_b = 0) = \sqrt{(2l_q+1)/4\pi}$ if $m_q = 0$ and are exactly zero if $m_q \neq 0$, given that the pair $\{l_q, m_q\}$ fulfills $|l-l'| \leq l_q \leq l+l'$ and $m+m'+m_q = 0$. In all the previous expressions, since the B-splines are polynomials in each segment [47, 48], the radials integrals can be performed to machine accuracy using Gauss-Legendre quadrature and the angular ones are analytical (Clebsch-Gordan coefficients) [49], thus all matrix elements are implicitly computed exactly. Note that this method can provide an accurate description of the bound electronic states, while the continuum states requires to include the proper boundary conditions as later explained in the present manuscript.

In the case of homonuclear molecules $Z_a = Z_b$, therefore the electronic wave function has a specific inversion symmetry, *gerade* if it remains constant under the inversion of the electronic coordinates or *ungerade* when it changes its sign under the same inversion procedure, since the inversion operation for a spherical harmonic are given by $\mathcal{Y}_l^m(-\hat{\mathbf{r}}) = (-1)^l\mathcal{Y}_l^m(\hat{\mathbf{r}})$ only even values the angular momentum are allowed for the *gerade* symmetry while only odd for *ungerade*. The quality in the representation of the *interchannel coupling* term strongly depends on the number of angular momenta l_{max} included in the expansion, as the internuclear distance increases this number should increase since the difference from the atom-like spherical symmetry become more evident.

Commonly for the one-electron wave function calculations we use a set of 450 B-splines of order $k = 8$ in a linear sequence of knots points enclosed in a $r_{max} =$

300 a.u. electronic box, with an expansion in angular momentum going from $l = 0$ up to $l = 16$. It should be noted that this is a rather large basis set, both in the radial and angular components, in contrast with most existing works [16, 17, 50]. We aim to describe new processes such as attosecond electron streaking in molecules induced by the combined action of XUV and intense IR fields which may drive the electrons at large distances, thus requiring these large basis sets.

2.3 Two-electron diatomic molecule

Having established the methodology employed to obtain the eigenvalues and wave functions in the mono-electronic molecular system, we now explain the procedure to describe the molecular structure of the two-electron molecular target. The Hamiltonian of an isolated two-electron diatomic molecule reads:

$$\hat{\mathcal{H}}_{el} = -\frac{1}{2}\sum_i \nabla_i^2 - \sum_i \frac{Z_a}{|\mathbf{r}_i - \mathbf{R}_a|} - \sum_i \frac{Z_b}{|\mathbf{r}_i - \mathbf{R}_b|} + \sum_{i>j} \frac{1}{|\mathbf{r}_j - \mathbf{r}_i|} + \frac{Z_a Z_b}{R} \tag{2.17}$$

There are several ways to obtain the eigenvalues and eigenfunctions of the previous Hamiltonian. One can expand the wave function directly in a basis of B-splines or use a *Configuration Interaction* (CI) procedure, that is obtain a set of one-electron wave functions in a basis of B-splines (as we did in the previous section) and then use those to build up the CI matrix. We have used the former approach, which significantly reduces the computational effort and consists in directly use antisymmetrized products of one-electron wave functions, i.e. eigenstates of the one-electron molecule H_2^+ (ψ_n^m).

$$\begin{aligned}\Psi^\Lambda =& \sum_{m_1,m_2}\sum_{n_1,n_2} C_{n_1,n_2}^{m_1,m_2}\Phi_{n_1,n_2}^{m_1,m_2} \\ =& \frac{1}{2}\left\{\psi_{n_1}^{m_1}(\mathbf{r}_1)\psi_{n_2}^{m_2}(\mathbf{r}_2) \pm \psi_{n_2}^{m_2}(\mathbf{r}_1)\psi_{n_1}^{m_1}(\mathbf{r}_2)\right\}\left\{s_\alpha(1)s_\beta(2) \mp s_\alpha(2)s_\beta(1)\right\}\end{aligned} \tag{2.18}$$

Where $\Lambda = |m_1 + m_2|$ corresponds to the absolute value of the z-component of the total electronic angular momentum (corresponding to a given symmetry of the system labeled as $\Sigma(\Lambda = 0)$, $\Pi(\Lambda = 1)$, $\Delta(\Lambda = 2)$,...), $\psi_n^m(\mathbf{r})$ are the one-electron wave functions and s_x are the spin components of the wave function. The possible combinations between the spin components provides the correct multiplicity of the state: in a triplet state ($s_\alpha(1)s_\beta(2) + s_\alpha(2)s_\beta(1)$) or in a singlet ($s_\alpha(1)s_\beta(2) - s_\alpha(2)s_\beta(1)$). Since the ψ_n^m are eigenfunctions of the H_2^+ Hamiltonian, building up the matrix of the total Hamiltonian (equation 2.17) would only require the calculation of the electron-electron interaction term, which is one of the main advantages of using one electron wave functions as basis set. Since we

are using a mono-centric expansion the calculation of the electron-electron interaction term $\langle\psi_{n_1}^{m_1}\psi_{n_2}^{m_2}|1/r_{12}|\psi_{n_3}^{m_3}\psi_{n_4}^{m_4}\rangle$ is similar to that in the atomic case, by using the same expansion we used for the *interchannel coupling* in the last section

$$\frac{1}{r_{12}} = \sum_k \frac{r_<^k}{r_>^{k+1}} P_k(\cos\theta_{12}) \tag{2.19}$$

The radial components of this integral are calculated by using the method of the auxiliary Z^k function which is the standard procedure in atomic systems [51, 52]. To improve the convergence speed of the bound states the CI is complemented with additional Slater-type-orbitals STO, functions of the type $r^n \exp(-\gamma_{nl} r)\mathcal{Y}_l^m(\hat{\mathbf{r}})$ (normally n runs from $n = 1$ to $n = 10$, $l = 0 - 11$ and γ_{nl}=8). For convenience the STO are expanded in the same B-splines basis.

2.4 Electronic continuum states

In this section we address the problem of the evaluation of electronic continuum states in molecules (scattering states). Unlike the atomic systems, for which evaluation of the electronic continuum lying just above the first ionization threshold is a single-channel scattering problem, in molecules it is always a multichannel scattering problem as a consequence of the non-central character of the molecular potential. Therefore we will begin the discussion by presenting the approach employed to solve the multichannel scattering problem, and then we will present the formalism for the description of Feshbach resonances in the continuum, i.e. doubly excited states of the neutral molecule, whose energies lie above the ionization threshold.

2.4.1 Non-resonant continuum states

We first consider the mono-electronic molecule (generalization to multi electronic molecules should not present any difficulty [53]). If the system has N_c open channels there will be N_c independent boundary conditions corresponding to N_c independent continuum states with the same energy. We can think of the electronic continuum as having an infinite number of channels, one for each value of the angular momentum of the scattered electron.

In contrast with the single channel case, the continuum states resulting from the diagonalization of the Hamiltonian do not reproduce the correct asymptotic behaviour, because there is no asymptotic proportionality between the correct continuum wave functions and those resulting from diagonalization. Moreover, only a single independent solution is obtained at each energy. An elegant solution to this problem is to employ the Garlekin or least-square approach [54–57], which

can be applied to the multichannel case, giving the full set of N_c independent solutions at each specific energy E. The essence of the method is to minimize the residual vector $\mathcal{R}_E = (\hat{\mathcal{H}}_{el} - E)F$ for a fixed value of the electron energy E by defining:

$$b_i = \langle \mathcal{B}_i | \hat{\mathcal{H}}_{el} - E | F \rangle = \sum_j \mathcal{A}_{ij}(E) c_j \tag{2.20}$$

Where $\hat{\mathcal{H}}_{el}$ is the Hamiltonian 2.6 and:

$$\mathcal{A}_{ij}(E) = H_{ij} - E S_{ij} \quad F = \sum_i c_i \mathcal{B}_i \tag{2.21}$$

where S_{ij} and H_{ij} are the overlap and the Hamiltonian matrix elements (i.e. equations 2.11 and 2.12) respectively, minimizing $\sum_i b_i^* b_i$ and imposing in the process the condition $\sum_i c_i^* c_i = 1$ to avoid trivial solutions, leads to the eigenvalue equation:

$$\mathcal{A}^\dagger \mathcal{A} c = \lambda c \tag{2.22}$$

The minimum will match the eigenvalue with the value closest to zero. In the case of N_c coupled partial waves, there always will be N_c eigenvalues with absolute value considerably smaller than the others which correspond to the N_c independent solutions needed. Using a flexible basis as B-splines the N_c eigenvalues are always very close to zero (as we have checked) and separated from the others by orders of magnitude. Under these circumstances the wave function can formally be written as:

$$\Psi_{\mu E}(\mathbf{r}) = \sum_{\mu'=1}^{N_c} c_{\mu\mu'} F_{\mu\mu'}(\mathbf{r}) \tag{2.23}$$

The $F_{\mu\mu'}$ solutions found will be normalized by simply applying the asymptotic conditions which should be satisfied by an outgoing channel wave. In the asymptotic region any solution $F_{\mu\mu'}$ should be written as linear combination of the asymptotic solutions of the Schrödinger equation, namely regular $\mathcal{F}_\mu$ and irregular $\mathcal{G}_\mu$ Coulomb functions [49]:

$$F_{\mu\mu'}(r) = \sqrt{\frac{2}{\pi k_\mu}} \{ A_{\mu\mu'} \mathcal{F}_\mu(r) + B_{\mu\mu'} \mathcal{G}_\mu(r) \} \tag{2.24}$$

Fitting the solutions $F_{\mu\mu'}$ when $k_\mu r \gg 1$ will produce a $N_c \times N_c$ matrices $\mathbf{A}$ and $\mathbf{B}$ with elements $A_{\mu\mu'}$ and $B_{\mu\mu'}$. On the other hand, the scattering asymptotic conditions of the final state demand an outgoing wave in the μ channel and incoming wave in the rest:

$$F^{-}_{\mu\mu'}(r) = \frac{1}{r}\sqrt{\frac{1}{2\pi k_{\mu'}}}\left(\delta_{\mu\mu'}e^{i\theta_{\mu'}} - \mathcal{S}^{\dagger}_{\mu\mu'}e^{-i\theta_{\mu'}}\right) \tag{2.25}$$

where $\mathcal{S}^{\dagger}_{\mu\mu'}$ are the adjoint matrix elements of the S-matrix between the channels μ and μ', $k_\mu = \sqrt{2E}$ is the electron momentum and $\theta_{\mu'}$ is the total phase of the one-electron wave function in a Coulomb potential:

$$\theta_\mu = k_\mu r - \frac{1}{2}l_\mu\pi + \frac{Z-1}{k_\mu}\ln(2k_\mu r) + \arg\Gamma(l_\mu + 1 - i(Z-1)/k_\mu) \tag{2.26}$$

Thus, the solution $\mathbf{F}^{-}$ with the correct boundary conditions can be related to linear combinations of those with the arbitrary ones through the linear transformation:

$$\mathbf{F}^{-} = \mathbf{F}\cdot\mathbf{N} \tag{2.27}$$

where the transformation matrix $\mathbf{N}$ and the $\mathbf{K}$ matrix in terms of $\mathbf{A}$ and $\mathbf{B}$ are given by:

$$\mathbf{N} = (\mathbf{A} + i\mathbf{B})^{-1} \quad \pi\mathbf{K} = -\mathbf{A}^{-1}\mathbf{B} \tag{2.28}$$

The resulting wave functions have the proper K-matrix normalization. A necessary condition for the method to work is that the basis set must reproduce the asymptotic region. This condition can be easily satisfied with B-splines by choosing a box size large enough to contain a significant part of the asymptotic region. An easy way to check the quality of the fitting and the basis set is to look at the asymmetry of the $\mathbf{K}$ matrix, which for the exact solution must be symmetric. An appreciable asymmetry may evidence a poor solution.

There are a few points worth noticing: i) the solution for a specific energy will not be zero at r_{max}, so it necessary to keep the last B-spline in the expansion which is different from zero at r_{max}, having only one boundary condition, at the origin, and a free boundary condition at the other end will allow a solution for any energy, at a difference with the two-point boundary condition, which gives only the eigenvalues corresponding to the diagonalization process. ii) Although the method has proven to be very accurate it has the disadvantage that one has to diagonalize the $\mathcal{A}^{\dagger}\mathcal{A}$ matrix for each continuum wave function or electronic

energy. This requirement can become very expensive in the case of bigger systems where a bigger basis set is needed to get accurate results. iii) Finally, the fitting in equation 2.24 is performed using a least square approach. In order to impose the condition $k_\mu r \gg 1$ the fitting is done only in the region $[r_{max} - \lambda, r_{max}]$ where λ is the wavelength of the scattering state.

2.4.2 Resonances in the continuum: Feshbach formalism

As in atoms, the electronic continuum may include Feshbach resonances associated with multiply excited states of the molecule. The corresponding energies are located above the ionization threshold. Therefore they belong to the continuum spectrum, the properties of such states are fully dictated by electron-electron correlation. The conventional picture is that of a bound state embedded in and coupled to a non-resonant continuum [58, 59]. As a consequence of the coupling, due to the non-stationary terms of the Hamiltonian, ejection of one the electrons to the continuum can happen in the absence of any external perturbation i.e. laser field. For this reason the states are also called autoionizing states. To deal with the doubly excited states we are going to follow the Feshbach procedure [58], the procedure allows us to deal with the resonant and non-resonant contributions to the wave function in the continuum independently. Therefore we can use different methods suited to treat each component. Moreover, it also allows one to accurately obtain the physical resonance parameters (energy position, autoionization width, Fano profiles, etc) [60, 61] without fitting the cross section.

In the Feshbach procedure the non-resonant and resonant components of the wave function are assigned to two orthogonal complementary subspaces $\mathcal{P}$ and $\mathcal{Q}$. The Feshbach projection operators are defined such that the wave function:

$$\psi = \hat{\mathcal{P}}\psi + \hat{\mathcal{Q}}\psi \tag{2.29}$$

where $\hat{\mathcal{P}}\psi$ and $\hat{\mathcal{Q}}\psi$ correspond to the scattering-like component and the resonant component of the total electronic wave function respectively, and satisfy the following properties:

$$\lim_{r_i \to \infty} \hat{\mathcal{P}}\psi = \psi \quad \lim_{r_i \to \infty} \hat{\mathcal{Q}}\psi = 0 \tag{2.30}$$

completeness

$$\hat{\mathcal{P}} + \hat{\mathcal{Q}} = 1 \tag{2.31}$$

idempotency

$$\hat{\mathcal{P}}^2 = \hat{\mathcal{P}} \quad \hat{\mathcal{Q}}^2 = \hat{\mathcal{Q}} \tag{2.32}$$

orthogonality

$$\hat{\mathcal{P}}\hat{\mathcal{Q}} = \hat{\mathcal{Q}}\hat{\mathcal{P}} = 0 \tag{2.33}$$

To calculate the doubly excited states we follow a similar CI procedure as the one employed for the bound states, but the $\mathcal{Q}$ projection is performed by excluding all configurations containing the orbitals of the ion that can result after the decay of the resonance state. The doubly excited states, $\psi_r(\mathbf{r}, R) \equiv \hat{\mathcal{Q}}\psi_r(\mathbf{r}, R)$ are the eigenvalues of the Feshbach $\mathcal{Q}$-projected electronic Hamiltonian.

$$(\hat{\mathcal{Q}}\hat{\mathcal{H}}_{el}\hat{\mathcal{Q}} - E_r(R))\psi_r(\mathbf{r}, R) = 0 \tag{2.34}$$

To built a single $\mathcal{Q}$-subspace can be inconvenient, instead it is better to split $\mathcal{Q}$ and calculate each series of resonant states $\{\psi_r\}_{\mathcal{Q}_\alpha}$ seated energetically above the ionization threshold $E_\alpha(R)$ and below the next one $E_{\alpha+1}(R)$. The Feshbach projector $\hat{\mathcal{P}}$ corresponding to the threshold α in a two electron system, can be written in terms of one-electron operators

$$\hat{\mathcal{P}}_\alpha(1,2) = 1 - \hat{\mathcal{Q}}_\alpha(1,2) = \hat{\mathcal{P}}_\alpha(1) + \hat{\mathcal{P}}_\alpha(2) - \hat{\mathcal{P}}_\alpha(1)\hat{\mathcal{P}}_\alpha(2) \tag{2.35}$$

where

$$\hat{\mathcal{P}}_\alpha(i) = |\psi_\alpha(i)\rangle\langle\psi_\alpha(i)| \tag{2.36}$$

and $\psi_\alpha(i)$ is the one-electron orbital corresponding to the threshold α . Then the resonances are constructed in series of resonance sub-space for instance the $\mathcal{Q}_{\alpha=1}$ series arises using the operator $\hat{\mathcal{P}}_{\alpha=1}(i) = |1s\sigma_g(i)\rangle\langle 1s\sigma_g(i)|$, then for $\mathcal{Q}_{\alpha=2}$ series using the operator $\hat{\mathcal{P}}_{\alpha=1}(i)+\hat{\mathcal{P}}_{\alpha=2}(i) = |1s\sigma_g(i)\rangle\langle 2p\sigma_u(i)|+|2p\sigma_u(i)\rangle\langle 2p\sigma_u(i)|$, and in general $\mathcal{Q}_{\alpha=n}$ series using the operator $\sum_n \hat{\mathcal{P}}_{\alpha=n}(i)$. As an illustration, we show the configurations normally used in the construction of the first two series of doubly excited states.

- $\mathcal{Q}_1\,{}^1\Sigma_g^+$: $1\sigma_u n\sigma_u(n = 1, 70)$, $1\pi_u n\pi_u(n = 1, 70)$, $2\sigma_g n\sigma_g(n = 2, 35)$, $2\sigma_u n\sigma_u(n = 2, 18)$, $3\sigma_g n\sigma_g(n = 3, 18)$, $1\pi_g n\pi_g(n = 1, 10)$, $1\delta_g n\delta_g(n = 1, 10)$ and $2\pi_u n\pi_u(n = 2, 10)$.
- $\mathcal{Q}_1\,{}^1\Sigma_u^+$: $1\sigma_u n\sigma_g(n = 2, 70)$, $1\pi_u n\pi_g(n = 1, 70)$, $2\sigma_g n\sigma_u(n = 2, 35)$, $2\sigma_u n\sigma_g(n = 2, 18)$, $3\sigma_g n\sigma_u(n = 1, 18)$, $1\pi_g n\pi_u(n = 1, 10)$, $1\delta_g n\delta_u(n = 1, 10)$ and $2\pi_u n\pi_g(n = 2, 10)$.
- $\mathcal{Q}_2\,{}^1\Sigma_g^+$: $1\pi_u n\pi_u(n = 1, 70)$, $2\sigma_g n\sigma_g(n = 2, 70)$, $2\sigma_u n\sigma_u(n = 3, 18)$, $3\sigma_g n\sigma_g(n = 3, 18)$, $1\pi_g n\pi_g(n = 1, 10)$, $1\delta_g n\delta_g(n = 1, 10)$ and $2\pi_u n\pi_u(n = 2, 70)$.

– $\mathcal{Q}_2\,{}^1\Sigma_u^+$: $1\pi_u n\pi_g(n=1,70)$, $2\sigma_g n\sigma_u(n=2,70)$, $2\sigma_u n\sigma_g(n=3,18)$, $3\sigma_g n\sigma_u(n=3,18)$, $1\pi_g n\pi_u(n=2,10)$, $1\delta_g n\delta_u(n=1,10)$ and $2\pi_u n\pi_g(n=2,10)$.

To evaluate the non-resonant component of the continuum states we use an $\mathcal{L}^2$ close coupling approach. The method has been described in detail elsewhere [50, 62–65], therefore here we only provide a summary of the main steps in the method. For each partial wave μ and energy E the projected wave function $\Psi^{\Omega-}_{\mu E}$ will be eigenfunctions of the set of operators $\hat{\Omega} = \left\{\hat{S}^2, \hat{S}_z, \hat{L}_z, \hat{\sigma}, \hat{\pi}\right\}$ with their corresponding eigenvalues $\Omega \equiv \{S(S+1), M_s, \Lambda, \sigma, \pi\}$, S is the total electronic spin, M_s its z-component, Λ the absolute value of the z-component of the total electronic angular momentum (Σ, Π,...), σ is the reflexion symmetry with respect to the XZ plane (± 1) and π is the symmetry with respect to the inversion center (*gerade* or *ungerade*). For an specific channel μ and total electronic energy E one can use the following expansion:

$$\hat{\mathcal{P}}\Psi^{\Omega-}_{\mu E}(\mathbf{r}_1,\mathbf{r}_2) = \hat{\Theta}\left(\sum_{\mu'=1}^{N_c}\psi^{\Omega}_{\mu'}(\mathbf{r}_1,\hat{r}_2)F^{\Omega}_{\mu\mu'}(r_2)\right) \tag{2.37}$$

where $\hat{\Theta}$ is the symmetrization operator, $\psi^{\Omega}_{\mu'}$ are combinations of the target states (H_2^+ states) with the angular functions of the scattered electron to form eigenfunctions of $\hat{\Omega}$, and N_c is the number of channels (open and closed). The channel index is defined as $\mu = (\alpha, l)$ where α stands for the set of quantum numbers describing the state of the target and l is the angular momentum of the scattered electron. For open channels $F^{\Omega}_{\mu\mu'}$ follows equation 2.25.

Our $\mathcal{L}^2$ close coupling method makes use of the fact that the discretization of a single channel can be performed easily, so in the first step it neglects the *inter-channel coupling*, therefore the multichannel problem is converted in a collection of single channel problems that can be solved independently. In a second step, the coupling between channels is introduced using a Lippman-Schwinger formalism which explicitly impose the correct boundary conditions. More exactly for each channel μ we define a set of orthogonal uncoupled continuum states (USC):

$$\chi^0_{\mu E} = \hat{\Theta}(\psi^{\Omega}_{\mu}(\mathbf{r}_1,\hat{r}_2)\xi_{\mu E}(r_2)) \tag{2.38}$$

Each UCS can be associated with the projection operator $\hat{P}_\mu$ satisfying:

$$\hat{P}_\mu\chi^0_{\mu E} = \chi^0_{\mu E} \quad \hat{P}_\mu\hat{P}_{\mu'} = \delta_{\mu\mu'}\hat{P}_\mu \tag{2.39}$$

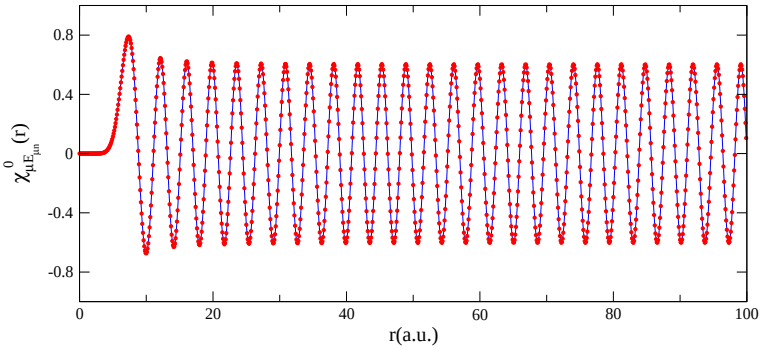

FIGURE 2.1: Scattering wave function of the H atom for $\mu = 11$ and $E_{\mu n} = 1.53$ a.u., normalized to the Dirac delta by two different methods. Red circles: fitting to a linear combination of regular and irregular Coulomb function. Blue full line: using equation 2.44.

So that the UCS are eigenfunctions of the zero-order uncoupled Hamiltonian:

$$\left(\sum_{\mu'} \hat{P}_{\mu'} \hat{\mathcal{H}}_{el} \hat{P}_{\mu'} - E \right) \chi^0_{\mu E} = 0 \tag{2.40}$$

To represent the radial continuum functions $\xi_{\mu E}$, we use a finite basis set of one-electron orbitals. This leads to a discrete spectrum $\{E_{\mu n}\}$ and to discretized UCS wave functions $\tilde{\chi}^0_{\mu n}$. As it is well known discrete states coming from a diagonalization are normalized to a Kronecker delta:

$$\langle \tilde{\chi}^0_{\mu n} | \tilde{\chi}^0_{\mu n'} \rangle = \delta_{nn'} \tag{2.41}$$

when in fact continuum states are normalized to a Dirac delta function:

$$\langle \chi^0_{\mu E_{\mu n}} | \chi^0_{\mu E_{\mu n'}} \rangle = \delta(E_{\mu n} - E_{\mu n'}) \tag{2.42}$$

However in the single channel case, discretized $\tilde{\chi}^0_{\mu n}$ and the continuum wave functions $\chi^0_{\mu E_{\mu n}}$ are identical up to a normalization factor often called *density of states*:

$$\chi^0_{\mu E_{\mu n}} = \rho^{1/2}_{\mu}(E_{\mu n}) \tilde{\chi}^0_{\mu n} \tag{2.43}$$

The *density of states* $\rho_{\mu}(E_{\mu n})$ can be found in two different ways, the first one

is to compare with the exact solution (linear combination of regular and irregular Coulomb function 2.24) in the asymptotic region. The second method, and the one we have used for the UCS consist in extracting the *density of states* from the discretized spectrum itself [66], in this scenario the *density of states* can be evaluated with a simple two-point interpolation formula:

$$\rho_\mu(E_{\mu n}) = |\partial E_{\mu n'}/\partial n'|^{-1}_{n'=n} = 2/(E_{\mu(n+1)} - E_{\mu(n-1)}) \tag{2.44}$$

Both methods will provide the same result as shown in figure 2.1, where we illustrate the accuracy of the method by comparing the scattering wave function for the hydrogen atom at a given energy employing both methods. In summary, for each channel μ the UCS are built using our calculated target states and the radial component of the wave function which is constructed in two steps. First we evaluate the one-electron orbitals 2.7 but now restraining the angular momentum l to that of the ejected electron in the channel μ. Then the UCS are obtained by diagonalization of the H_2 Hamiltonian in the basis of configurations built from orbitals and target states.

The scattering states with correct boundary conditions are related to the UCS through the Lippmann-Schwinger equation :

$$\hat{\mathcal{P}}\Psi^{\Omega-}_{\mu E} = \chi^0_{\mu E} + \hat{G}^-_p(E)\hat{V}\chi^0_{\mu E} \tag{2.45}$$

where

$$\hat{V} = \sum_{\substack{\mu\mu' \\ \mu\neq\mu'}} \hat{P}_\mu \hat{\mathcal{H}}_{el} \hat{P}_{\mu'} \tag{2.46}$$

and the Green function:

$$\hat{G}^-_p(E) = \lim_{\eta\to 0} \frac{1}{E - \hat{\mathcal{H}}_{el} + i\eta} \tag{2.47}$$

The $\hat{G}^-_p(E)$ operator matrix elements can be can be easily obtained following the procedures described in [62–65]. One starts by defining the Green's operator associated with the uncoupled Hamiltonian:

$$\hat{G}^-_0(E) = \lim_{\eta\to 0} \frac{1}{E - \sum_\mu \hat{P}_\mu \hat{\mathcal{H}}_{el} \hat{P}_\mu + i\eta} \tag{2.48}$$

In the UCS basis the operator $\hat{G}_0^-(E)$ takes the form:

$$\hat{G}_0^-(E) = \sum_{\mu'} \sum_{\substack{n' \\ E_{\mu' n'} \neq E_{\mu n}}} \frac{|\tilde{\chi}^0_{\mu' n'}\rangle\langle\tilde{\chi}^0_{\mu' n'}|}{(E_{\mu n} - E_{\mu' n'})} + i\pi \sum_{\mu} \rho_\mu(E_{\mu n}) |\tilde{\chi}^0_{\mu n}\rangle\langle\tilde{\chi}^0_{\mu n}| \tag{2.49}$$

Where we have assumed that the discretized UCS fulfil the closure relation in the $\mathcal{P}$ sub-space:

$$\hat{\mathcal{P}} = \sum_{\mu} \hat{P}_\mu = \sum_{\mu n} |\tilde{\chi}^0_{\mu n}\rangle\langle\tilde{\chi}^0_{\mu n}| \tag{2.50}$$

The Greens functions $\hat{G}_0^-(E)$ and $\hat{G}_p^-(E)$ can be related using standard scattering theory:

$$\hat{G}_p^-(E) = \hat{G}_0^-(E) + \hat{G}_0^-(E)\hat{V}\hat{G}_p^-(E) \tag{2.51}$$

Using equation 2.49 the closure relation in equation 2.51, and projecting from the left and from right onto $\tilde{\chi}^0_{\mu n}$ we obtain:

$$\sum_{\mu'' n''} \mathcal{C}_{\mu' n' \mu'' n''} \langle\tilde{\chi}^0_{\mu'' n''}|\hat{G}_p^-(E)|\tilde{\chi}^0_{\mu n}\rangle = \mathcal{D}_{\mu' n'} \tag{2.52}$$

Where

$$\mathcal{C}_{\mu' n' \mu'' n''} = \delta_{\mu'' \mu'}\delta_{n'' n'} - \Xi_{\mu'}(E_{\mu' n'})\langle\tilde{\chi}^0_{\mu' n'}|\hat{V}|\tilde{\chi}^0_{\mu'' n''}\rangle \tag{2.53}$$

$$\mathcal{D}_{\mu' n'} = \delta_{\mu' \mu}\delta_{n' n}\Xi_{\mu'}(E_{\mu' n'}) \tag{2.54}$$

and

$$\Xi_{\mu'}(E_{\mu' n'}) = \begin{cases} i\pi\rho_{\mu'}(E_{\mu' n'})\delta_{n n'} & \text{for } E = E_{\mu' n'} \\ 1/(E - E_{\mu' n'}) & \text{for } E \neq E_{\mu' n'} \end{cases} \tag{2.55}$$

Therefore, the $\hat{G}_p^-(E)$ matrix elements are the solutions of the system of linear equations given in equation 2.52, which can be solved using standard numerical procedures. The coefficient matrix $\mathcal{C}$ multiplying the unknowns $\hat{G}_p^-(E)$ matrix elements is the same for all μ, so that each system of equations differs only in the right-hand side column vector $\mathcal{D}$. Thus the same matrix inversion is needed to solve equation 2.52 for different open channels. Finally the $\hat{\mathcal{P}}\Psi^{\Omega-}_{\mu E}$ for each open

channel can be written as:

$$\hat{\mathcal{P}}\Psi^{\Omega-}_{\mu E_{\mu n}} = \rho_{\mu}^{1/2}(E_{\mu n}) \times \left(\tilde{\chi}^{0}_{\mu n} + \sum_{\mu' n'} \sum_{\mu'' n''} \langle \tilde{\chi}^{0}_{\mu' n'} | \hat{G}^{-}_{p}(E_{\mu n}) | \tilde{\chi}^{0}_{\mu'' n''} \rangle \langle \tilde{\chi}^{0}_{\mu'' n''} | \hat{V} | \tilde{\chi}^{0}_{\mu n} \rangle \tilde{\chi}^{0}_{\mu' n'} \right) \tag{2.56}$$

There are a few points noteworthy here, i) the diagonalization of equation 2.40 must produce a UCS with the energy $E_{\mu n} = E$. In general this requirement is not naturally fulfilled (different UCS have different eigenvalues due to the centrifugal potential and we need to be the same to properly apply the Lippmann-Schwinger formalism), but can be imposed by adding a potential well i.e, $V(r) = 0$ for $r < r_0$ and $V(r) \to \infty$ if $r \geq r_0$ and then shift the position of r_0 until one of the eigenvalues satisfies the desired condition. ii) Typically we choose a grid of energies matching the eigenvalues of a particle in box of the same size of the electronic box and then calculate $\hat{\mathcal{P}}\Psi^{\Omega-}_{\mu E}$ in it. This procedure prevents large displacements of the r_0 value from the box edge r_{max}, with the subsequent loss of orthogonality among the continuum states. iii) Diagonalization of equation 2.40 may produce some bound eigenstate satisfying the condition $E_{\mu n} = E$ by chance, thus the existence of bound uncoupled states should be explicitly checked in the UCS used in the close coupling calculation. In order to be able to use these states later in the TDSE (and to be consistent in the propagation), one must choose the box size r_{max} large enough to ensure that the scattered electron does not reach the edge of the box during the time propagation. With r_{max} known one chooses the electronic grid and calculates the $\hat{\mathcal{P}}\Psi^{\Omega-}_{\mu E}$ states in it. The need for the closure relation means that a complete basis is required.

Finally we show as an example the configurations normally used in the construction of the UCS required to built the continua associated with the two lowest ionization thresholds:

- $^1\Sigma_u^+$ $[H_2^+(1s\sigma_g), \epsilon l]$ $1\sigma_g n\sigma_u$ $(n = 1, 450)$ up to six partial waves $l = 1, 3, 5, 7, 9$ and 11
- $^1\Sigma_g^+$ $[H_2^+(1s\sigma_g), \epsilon l]$ $1\sigma_g n\sigma_g$ $(n = 1, 450)$ up to six partial waves $l = 0, 2, 4, 6, 8$ and 10
- $^1\Sigma_u^+$ $[H_2^+(2p\sigma_u), \epsilon l]$ $1\sigma_u n\sigma_g$ $(n = 1, 450)$ up to six partial waves $l = 0, 2, 4, 6, 8$ and 10
- $^1\Sigma_g^+$ $[H_2^+(2p\sigma_u), \epsilon l]$ $1\sigma_u n\sigma_u$ $(n = 1, 450)$ up to six partial waves $l = 1, 3, 5, 7, 9$ and 11

2.5 Nuclear motion and vibrational states.

In the BO approximation the vibrational wave functions are solution of Schrödinger equation 2.4 and 2.5

$$\left\{-\frac{1}{2m_\mu}\frac{d^2}{dR^2}+\frac{J(J+1)}{2m_\mu R^2}+E_n(R)\right\}\chi_{n\nu}(R)=W_{n\nu}\chi_{n\nu}(R) \tag{2.57}$$

Where m_μ is the reduced mass of the nuclei, J is rotational quantum number, $E_n(R)$ is the n-th potential electronic curve and $W_{n\nu}$ is the total vibronic energy. This a one-dimensional equation that can be solved using conventional numerical techniques, nonetheless here we are going to expand $\chi_{n\nu}(R)$ in a B-splines basis $\mathcal{B}_i^k$, defined in a vibrational box of size R_{max}.

$$\chi_{n\nu}(R)=\sum_i^{N_B} d_{i\nu}^m \mathcal{B}_i^k(R) \tag{2.58}$$

Substitution equation 2.58 into equation 2.57 leads to an eigenvalue problem similar to 2.10 that can be easily solved using conventional diagonalization methods. All the results were obtained using $N_B = 240$ B-splines of order $k = 8$ defined in a box $R_{max} = 12$ a.u. In order to get accurate vibrational wave functions and energies, the potential energy curves corresponding to the different electronic states of H_2^+ were obtained using the code OEDM [43] and for the case of H_2 potential energy curves of reference [67] were used. Vibrational states above the dissociation limit correspond to nuclear continuum states normalized to the Kronecker delta, in order to impose the correct Dirac delta normalization we renormalized the states using the *density of states* [66], as we did in the single-channel continuum state case equation 2.43.

$$\chi_{n\nu}(R)=\rho_{n\nu}^{1/2}\widetilde{\chi}_{n\nu}(R)\quad \rho_{n\nu}=2/(W_{n(\nu+1)}-W_{n(\nu-1)}) \tag{2.59}$$

Besides the correct normalization the vibrational continuum states must satisfy the adequate asymptotic incoming boundary condition that is:

$$\lim_{R\to\infty}\chi_{n\nu}(R)=\frac{1}{R}\sqrt{\frac{m_\mu}{2\pi k_{n\nu}}}\left(e^{i\theta_{n\nu}}-\mathcal{S}_{n\nu}^{\dagger}e^{-i\theta_{n\nu}}\right)\quad \theta_{n\nu}=k_{n\nu}R-J\pi/2 \tag{2.60}$$

The $k_{n\nu}$ is the nuclear momentum and $\mathcal{S}$-matrix contains the short range nuclear phase shift $\delta_{n\nu}$, $\mathcal{S}_{n\nu}=\exp(-2i\delta_{n\nu}(k_{n\nu}))$, that can be extracted from the calculation by fitting the real nuclear wave function obtained from the diagonalization procedure to the known asymptotic analytic form

$$\lim_{R\to\infty} \chi_{n\nu}(R) = \frac{1}{R}\sqrt{\frac{2m_\mu}{\pi k_{n\nu}}} \sin\left(\theta_{n\nu}(k_{n\nu}) + \delta_{n\nu}(k_{n\nu})\right) \tag{2.61}$$

at the end of the nuclear box. Our real vibrational state has to be multiplied by the factor $\exp(-i\delta_{n\nu}(k_{n\nu}))$ in order to satisfy the incoming boundary condition in equation 2.60. This extra phase added to the nuclear wave functions is going to be paramount in the description of interferences of nuclear wave-packets dissociating through different potential energy curves.

Chapter 3

Radiation-matter interaction

3.1 Interaction with electromagnetic radiation

The classical interaction between a single free electron with an electromagnetic field is given by the *minimal-coupling* Hamiltonian:

$$\hat{\mathcal{H}}_{mc} = \frac{1}{2}[\hat{\mathbf{p}} + \mathbf{A}(\mathbf{r}, t)]^2 - \Phi(\mathbf{r}, t) \tag{3.1}$$

The quantized character of the electromagnetic field can be ignored for fields containing many photons, as the one produced by lasers. In classical electrodynamics the external electric $\boldsymbol{\mathcal{E}}$ and magnetic fields $\boldsymbol{\mathcal{B}}$ can be written in terms of the external vector potential $\mathbf{A}$ and scalar potential Φ.

$$\boldsymbol{\mathcal{E}} = -\nabla\Phi - \frac{\partial \mathbf{A}}{\partial t} \qquad \boldsymbol{\mathcal{B}} = \nabla \times \mathbf{A} \tag{3.2}$$

The Hamiltonian in equation 3.1 will be then defined as a *semi-classical* interaction of an electron with an electromagnetic field, i.e. we use a classical representation of the electromagnetic field while the molecular target is described fully quantum-mechanically.

The potentials $\mathbf{A}$ and Φ are not entirely defined, since the electric $\boldsymbol{\mathcal{E}}$ and magnetic fields $\boldsymbol{\mathcal{B}}$ remain constant under the gauge transformations:

$$\begin{aligned} \mathbf{A} \rightarrow \mathbf{A}' &= \mathbf{A} + \nabla g \\ \Phi \rightarrow \Phi' &= \Phi - \frac{\partial g}{\partial t} \end{aligned} \tag{3.3}$$

In the following we are going to capitalize on this circumstance by adopting the Coulomb gauge (also known as transverse gauge) which is defined by the

condition:

$$\nabla \cdot \mathbf{A} = 0 \qquad \Phi(\mathbf{r}, t) = 0 \tag{3.4}$$

by imposing this conditions the Hamiltonian 3.1 becomes:

$$\hat{\mathcal{H}}_{mc} = \frac{1}{2}\hat{\mathbf{p}}^2 + \hat{\mathbf{p}}\mathbf{A}(\mathbf{r}, t) + \frac{1}{2}\mathbf{A}^2(\mathbf{r}, t) \tag{3.5}$$

Then the Hamiltonian can be split in two components, the field free (molecular 2.17) and the interaction terms

$$\hat{\mathcal{H}}_{mc} = \hat{\mathcal{H}}_0 + \hat{\mathcal{V}}_{int} \tag{3.6}$$

where the interaction with the electromagnetic field is described by the term

$$\hat{\mathcal{V}}_{int} = \hat{\mathbf{p}}\mathbf{A}(\mathbf{r}, t) + \frac{1}{2}\mathbf{A}^2(\mathbf{r}, t) \tag{3.7}$$

The state of the molecule in this case is dictated by the TDSE:

$$i\frac{\partial}{\partial t}\Psi(t) = (\hat{\mathcal{H}}_0 + \hat{\mathcal{V}}_{int})\Psi(t) \tag{3.8}$$

On the other hand for a monochromatic plane-wave the vector potential can be written as:

$$\mathbf{A}(\mathbf{r}, t) = \mathbf{A}(t)e^{i\mathbf{kr}} + c.c \tag{3.9}$$

When the wavelength of the radiation is much larger than the distance over which the interaction with the molecules takes place, it is common to use the *dipole approximation*, in which the spatial dependence of the vector potential is ignored, and the vector potential is assumed to be uniform in space:

$$\mathbf{A}(\mathbf{r}, t) = \mathbf{A}(t)(1 + i\mathbf{kr} + \dots) + c.c \simeq \mathbf{A}(t) \tag{3.10}$$

This is a valid approximation since the wavelengths considered in this work are typically of several hundreds of atomic units, which is much larger than the size of a atom or a molecule. Moreover, within the *dipole approximation* the term $\mathbf{A}^2$ in equation 3.7 only has a dependence on the time parameter, we can remove it from the equation by simply including a global factor in the wave function:

$$\Psi^v(t) = \exp\left\{\frac{i}{2}\int_{-\infty}^{t}\mathbf{A}^2(t')dt'\right\}\Psi(t) \tag{3.11}$$

the latter transforms the interaction potential in the Hamiltonian into the so called *velocity* gauge

$$\hat{\mathcal{V}}^{v}_{int} = \hat{\mathbf{p}}\mathbf{A}(t) \tag{3.12}$$

Equivalently, the Göpert-Mayer unitary transformation

$$\Psi^{l}(t) = \exp\left\{i\mathbf{A}(t)\mathbf{r}\right\}\Psi(t) \tag{3.13}$$

leads to the interaction Hamiltonian in the *length* gauge

$$\hat{\mathcal{V}}^{l}_{int} = \hat{\mathbf{r}}\boldsymbol{\mathcal{E}}(t) \tag{3.14}$$

In principle both gauges are formally equivalent and should yield the same result for all physical observables, however this is only true in an exact calculation. In practice, one must truncate the basis sets, which may lead to different behavior of the physical observables and numerical convergence for the *length* and *velocity* gauges. In fact, comparing the results obtained with different gauges usually becomes a useful tool to evaluate the "completeness" of the basis set employed. The gauge selection should be done taking into account several factors i.e. the convergence speed, the observables involved etc.. In the present work, we did check the suitability of both *length* and *velocity* gauges, although most of the presented results have been obtained using the *velocity* gauge, since the convergence with angular momentum is faster. Therefore, improving considerably the computing efficiency for the computation of the dipole matrix elements (in particular, those involving electronic continuum states).

3.2 Time-dependent Feshbach close-coupling method

The wave function describing the state of the molecule under the influence of a laser field is given by the solution of the time dependent Schrödinger equation (TDSE). As stated in the previous section the full Hamiltonian of the system can be partitioned into $\hat{\mathcal{H}} = \hat{\mathcal{H}}_0 + \hat{\mathcal{V}}_{int}$ where $\hat{\mathcal{H}}_0$ is the unperturbed Hamiltonian (i.e. equation 2.1) and $\hat{\mathcal{V}}_{int}$ contains the interaction with the field (equations 3.14 or 3.12), under these circumstances the use of the interaction picture is very convenient and helpful. In the interaction picture the TDSE reads:

$$i\frac{\partial}{\partial t}\Psi_I(t) = \hat{V}_I(t)\Psi_I(t) \tag{3.15}$$

Where the connection to Schrödinger picture is given by:

$$\Psi_I(t) = e^{i\hat{\mathcal{H}}_0 t}\Psi(t) \qquad \hat{V}_I(t) = e^{i\hat{\mathcal{H}}_0 t}\hat{\mathcal{V}}_{int}(t)e^{-i\hat{\mathcal{H}}_0 t} \tag{3.16}$$

Now using the eigenstates of the unperturbed Hamiltonian:

$$\hat{\mathcal{H}}_0\psi_n = E_n^0\psi_n \tag{3.17}$$

we can expand the interaction picture wave function in the basis of eigenstates of the unperturbed Hamiltonian:

$$\Psi_I(t) = \sum_n a_n(t)\psi_n \tag{3.18}$$

Substituting this *ansatz* into equation 3.15, and projecting from the right onto the eigenfunctions of the isolated Hamiltonian ψ_m^*, one obtains a system of coupled linear differential equations for the time evolution of the expansion coefficients:

$$i\dot{a}_m(t) = \sum_n \langle\psi_m^*|\hat{\mathcal{V}}_{int}|\psi_n\rangle e^{-i\omega_{mn}t}a_n(t) \tag{3.19}$$

where $\omega_{nm} = E_n - E_m$, this can be solved using any integration method i.e. Runge-Kutta, Bulirsch-Stoer or Crank-Nicolson.

In order to have a real description of the molecular autoionization and photoionization in time we need to modify the original Feshbach stationary formalism for the solution of TDSE. Recalling the Feshbach partition 2.29:

$$\Psi(t) = \hat{\mathcal{P}}\Psi(t) + \hat{\mathcal{Q}}\Psi(t) \tag{3.20}$$

Inserting this *ansatz* into the TDSE and projecting individually onto each subspace, we obtain two time dependent coupled equations:

$$i\frac{\partial}{\partial t}\begin{bmatrix}\hat{\mathcal{Q}}\Psi(t)\\ \hat{\mathcal{P}}\Psi(t)\end{bmatrix} = \begin{pmatrix}\hat{\mathcal{Q}}\hat{\mathcal{H}}_{el}\hat{\mathcal{Q}} & \hat{\mathcal{Q}}\hat{\mathcal{H}}_{el}\hat{\mathcal{P}}\\ \hat{\mathcal{P}}\hat{\mathcal{H}}_{el}\hat{\mathcal{Q}} & \hat{\mathcal{P}}\hat{\mathcal{H}}_{el}\hat{\mathcal{P}}\end{pmatrix}\begin{bmatrix}\hat{\mathcal{Q}}\Psi(t)\\ \hat{\mathcal{P}}\Psi(t)\end{bmatrix} \tag{3.21}$$

Neglecting non-adiabatic couplings, the projectors and the nuclear kinetic energy operator commute such that $[\hat{T}(R), \hat{\mathcal{Q}}] = [\hat{T}(R), \hat{\mathcal{P}}] = 0$ and $\hat{\mathcal{P}}\hat{T}(R)\hat{\mathcal{Q}} = \hat{\mathcal{Q}}\hat{T}(R)\hat{\mathcal{P}} = 0$. Under these circumstances the resonance-continuum couplings originate completely from electron-electron interaction, namely $\hat{\mathcal{P}}\hat{\mathcal{H}}_{el}\hat{\mathcal{Q}}$ or its Hermitian conjugate. In our case this approximation is very reasonable since the lifetime of the autoionizing states are controlled almost entirely by electron-electron interaction. Taking into account the latter commutation rules the unperturbed

Hamiltonian and interaction potentials will be transformed into:

$$\hat{\mathcal{H}}_0 \rightarrow \hat{\mathcal{H}}^0_{fesh} = \hat{\mathcal{Q}}\hat{\mathcal{H}}_{el}\hat{\mathcal{Q}} \oplus \hat{\mathcal{P}}\hat{\mathcal{H}}_{el}\hat{\mathcal{P}} \quad \hat{\mathcal{V}}_{int}(t) \rightarrow \hat{\mathcal{V}}_{int}(t) + \hat{\mathcal{Q}}\hat{\mathcal{H}}_{el}\hat{\mathcal{P}} + \hat{\mathcal{P}}\hat{\mathcal{H}}_{el}\hat{\mathcal{Q}} \quad (3.22)$$

The interaction potential now involves two components; one time-dependent describing the interaction with the laser field and another time-independent accounting for autoionization. Therefore now we are able to use in our spectral expansion 3.18 the eigenstates of the new unperturbed Hamiltonian 3.22 from which we can get a complete set of vibronic states.

Accordingly our spectral expansion includes:

1. The BO wave functions $\{\psi^{\varepsilon_\alpha}_{\alpha l_\alpha}\chi_{v_\alpha}\}$ with a total energies $\{W_{\alpha v_\alpha} = \varepsilon_\alpha + E_{v_\alpha}\}$, that includes the scattering state (solution of the $\hat{\mathcal{P}}\hat{\mathcal{H}}_{el}\hat{\mathcal{P}}$ eigensystem) 2.56 and vibrational state v_α in the potential energy curve of the electronic state α. Where α is the ionization threshold, ε_α the electron kinetic energy, l_α is its angular momentum and E_{v_α} the vibrational energy.

2. The BO wave functions $\{\psi_r\chi_{v_r}\}$ with a total energies $\{W_{rv_r}\}$, that includes the r-th resonant state (solution of the $\hat{\mathcal{Q}}\hat{\mathcal{H}}_{el}\hat{\mathcal{Q}}$ eigensystem) 2.34 and vibrational state v_r in the potential energy curve of the resonant state r.

3. The BO wave functions $\{\psi_b\chi_{v_b}\}$ with a total energies $\{W_{bv_b}\}$, that includes the b-th bound state (eigenvalues of 2.17) and vibrational state v_b in the potential energy curve of the bound state b.

The methodology employed to compute the vibronic (vibrational and electronic) eigenstates of the molecule has been explained in detail in Chapter 2. Using these vibronic states, the expansion in equation 3.18 can be formally written in the Schrödinger picture as:

$$\begin{aligned}\Psi(\mathbf{r}, R, t) = &\sum_b \sum_{v_b} C_{bv_b}(t)\psi_b(\mathbf{r}, R)\chi_{v_b}(R)e^{-iW_{bv_b}t} \\ &+ \sum_r \sum_{v_r} C_{rv_r}(t)\psi_r(\mathbf{r}, R)\chi_{v_r}(R)e^{-iW_{rv_r}t} \\ &+ \sum_{\alpha l_\alpha} \int d\varepsilon_\alpha \sum_{v_\alpha} C^{l_\alpha \varepsilon_\alpha}_{\alpha v_\alpha}(t)\psi^{\varepsilon_\alpha}_{\alpha l_\alpha}(\mathbf{r}, R)\chi_{v_\alpha}(R)e^{-iW_{\alpha v_\alpha}t}\end{aligned} \quad (3.23)$$

and the system of coupled linear differential equations 3.19 then can written as:

$$i\frac{\partial}{\partial t}\begin{pmatrix}\mathbf{C}_b \\ \mathbf{C}_r \\ \mathbf{C}_c\end{pmatrix} = \begin{pmatrix}\mathbf{V}(t)^{b'}_b & \mathbf{V}(t)^r_b & \mathbf{V}(t)^c_b \\ \mathbf{V}(t)^b_r & \mathbf{V}(t)^{r'}_r & [\boldsymbol{\mathcal{Q}}\boldsymbol{\mathcal{H}}_{el}\boldsymbol{\mathcal{P}} + \mathbf{V}(t)]^c_r \\ \mathbf{V}(t)^b_c & [\boldsymbol{\mathcal{P}}\boldsymbol{\mathcal{H}}_{el}\boldsymbol{\mathcal{Q}} + \mathbf{V}(t)]^r_c & \mathbf{V}(t)^{c'}_c\end{pmatrix}\begin{pmatrix}\mathbf{C}_b \\ \mathbf{C}_r \\ \mathbf{C}_c\end{pmatrix} \quad (3.24)$$

where, for the sake of clarity, we have shortened the notation such that the indexes stands for: $b = \{bv_b\}$, $r = \{rv_r\}$ and $c = \{\alpha v_\alpha l_\alpha \varepsilon_\alpha\}$. The evaluation of the matrix elements first requires the evaluation of the electronic and vibrational wave functions and all possible dipole couplings among them, thus including all degrees of freedom of the system. For instance, the matrix elements in the last column display the couplings between the continuum vibronic states $\{\psi^{\varepsilon_\alpha}_{\alpha l_\alpha}\chi_{v_\alpha}\}$ and the bound vibronic states $\{\psi_b\chi_{v_b}\}$ (upper block), resonant states $\{\psi_r\chi_{v_r}\}$ (middle block) and the continuum vibronic states $\{\psi^{\varepsilon'_{\alpha'}}_{\alpha' l'_{\alpha'}}\chi_{v'_{\alpha'}}\}$ (lower block). In general these couplings can be calculated in the velocity gauge as:

$$\mathbf{V}(t)^c_n = A(t)\int_0^R \chi_{v_n}(R)\langle\psi_n(\mathbf{r},R)|\mathbf{e}_\mu\hat{\mathbf{p}}|\psi^{\varepsilon_\alpha}_{\alpha l_\alpha}(\mathbf{r},R)\rangle\chi_{v_\alpha}(R)dR \tag{3.25}$$

where $\mathbf{e}_\mu$ is the polarization vector of the laser field. In our approach, we initially compute the electronic couplings in a very dense grid of internuclear distances, and then we perform the above-indicated integral using a Gauss-Legendre quadrature.

The present method presents a variety of advantages: i) it allows to have an unambiguous interpretation of the autoionization process in time, unlike the stationary Feshbach approach, since the total scattering wave function is assembled in time allowing the simultaneous population and the population transfer between the resonant and non-resonant components through the $\boldsymbol{\mathcal{Q}\mathcal{H}}_{el}\boldsymbol{\mathcal{P}}$ couplings and dipole couplings induced by the laser field. ii) Due to the properties expressed in equation 2.30 the $\hat{\mathcal{Q}}\hat{\mathcal{H}}_{el}\hat{\mathcal{P}}$ and $\hat{\mathcal{P}}\hat{\mathcal{H}}_{el}\hat{\mathcal{Q}}$ terms will vanish when $t \to \infty$, meaning that in the asymptotic limit the eigenfunctions of the $\hat{\mathcal{Q}}\hat{\mathcal{H}}_{el}\hat{\mathcal{Q}}$ and $\hat{\mathcal{P}}\hat{\mathcal{H}}_{el}\hat{\mathcal{P}}$ are also eigenfunctions of the total Hamiltonian. Therefore, the expansion coefficients $\mathbf{C}_c$ of the subspace $\mathcal{P}$ truly represent physical ionization amplitudes once stationary asymptotic limit is reached. Consequently the coefficients $\mathbf{C}_b$, $\mathbf{C}_r$ and $\mathbf{C}_c$ provide direct access to the probability of the system being in one of the BO vibronic states when the field is off, making the task of extracting information a lot easier, the task of extracting observables will be addressed in the following sections.

In practice one needs to calculate the matrix elements in equation 3.24 only once, because the laser fields characteristics appear merely as a factor. Therefore we can capitalize on that, calculating the matrix elements appearing in equation 3.24 and then solving the system of coupled linear differential equations for each specific laser field. This is very convenient, because the calculation of the coupling matrix elements requires a gargantuan computational effort. On the other hand, the calculation of the matrix elements should be in compliance with the laser field used. For instance, the size of the electronic and nuclear box in space has to be chosen such that one obtains a large enough density of discretized states for a

given pulse width $\Delta\omega$. In other words, the conditions $\Delta\varepsilon_n \ll \Delta\omega$, $\Delta W_{v_\alpha} \ll \Delta\omega$ are fulfilled (energy spacing of discretized electronic and vibrational states should be appreciably smaller than the pulse width in order to properly represent a "continuum" of energies). Furthermore, the box size must be large enough to be able to describe photoelectrons at large distances and avoid unphysical reflexions, which depends on the maximum total energy absorbed by the system (equivalently, the largest frequencies within the pulse). In addition, in order to properly describe autoionization, the interval between consecutive points in the electronic grid must be smaller than the resonance width $\Delta\varepsilon_n \ll \Gamma_r$. Therefore once the matrix elements have been calculated, there is only a certain number of problems that we can study. This implies that the parameters (basis set, box size, angular momenta, etc..) employed for the basis sets used in the calculation of the matrix elements strongly determine the type of problems that can be addressed.

Notice that the electronic couplings $\boldsymbol{\mathcal{Q}}\boldsymbol{\mathcal{H}}_{el}\boldsymbol{\mathcal{P}}$ and $\boldsymbol{\mathcal{P}}\boldsymbol{\mathcal{H}}_{el}\boldsymbol{\mathcal{Q}}$ are effective during and after the pulse (until the resonances are fully depleted or the dissociative limit is reached) making the integration time a little bit longer than the duration of the pulse t_{int}~T+1/Γ_r. Moreover, we have used $C_{b=0v_b=0}(t=0)=1$ as the initial condition in equation 3.24 which means that we are putting all the population in the ground state of the system.

3.2.1 Observables

After solving the TDSE, the probability of the system being in a given BO vibronic state can be obtained by a direct projection of the time-dependent wave function onto that state. Because we expanded our wave function as a linear combination of the vibronic eigenstates, the probabilities are simply given by the square of the expansion coefficients in equation 3.23. In current photoionization experiments, there are a variety of detection techniques that measure ionization probabilities resolved in different parameters. A given observable such as dissociative excitation or ionization probabilities, can be experimentally resolved in the energy of all the resulting fragments (electrons or ions), or simply measured as a function of the energy of one of the fragments or as a total yield. As explained in the introduction, in the last years, there has been significant progresses on detection devices that can retrieve all charged fragments in coincidence allowing for the reconstruction of the photoionization event from a fully-energy (and even ejection-angle) differential quantity. Our theoretical approach provides a direct extraction of the excitation and ionization observables as a function of energy and angle of ejection of the photo-fragments, of both ions and electrons. It can be easily shown that the probability differential (resolved) in both electronic and vibrational energies can be written for each partial wave of the scattered electron as:

$$\frac{d^2P_{l_\alpha}}{dE_{v_\alpha}d\varepsilon_\alpha} = \left|C^{l_\alpha\varepsilon_\alpha}_{\alpha v_\alpha}(t_{int})\right|^2 \tag{3.26}$$

Where α is the ionization threshold and t_{int} is the integration time. Given the conditions imposed in equation 2.30, this quantity has a physical meaning once the field is off (since we project onto the eigenstates of the field-free Hamiltonian the projection is only valid at the end of the pulse or at the zero values of the field) and once the non-stationary terms of the Hamiltonian ($\hat{\mathcal{Q}}\hat{\mathcal{H}}_{el}\hat{\mathcal{P}}$ and $\hat{\mathcal{P}}\hat{\mathcal{H}}_{el}\hat{\mathcal{Q}}$) have vanished. We can easily extract the single differential probabilities (electron/proton kinetic energy distributions) from equation 3.26 by just carrying out the integral over the vibrational/electron energies, which in each case result in:

$$\frac{dP}{d\varepsilon_\alpha} = \sum_{l_\alpha}\sum\!\!\!\!\!\!\int_{v_\alpha} dE_{v_\alpha}\left|C^{l_\alpha\varepsilon_\alpha}_{\alpha v_\alpha}(t_{int})\right|^2 \tag{3.27}$$

$$\frac{dP}{dE_{v_\alpha}} = \sum_{l_\alpha}\int d\varepsilon_\alpha\left|C^{l_\alpha\varepsilon_\alpha}_{\alpha v_\alpha}(t_{int})\right|^2 \tag{3.28}$$

the sum-integral symbol in equation 3.27 implies a sum over bound vibrational states of the ion and an integral over the continuum (dissociative) vibrational states.

To gain further insight in the photoionization process we can examine the molecular frame photoelectron angular distributions (MFPADs). The MFPAD provides detailed information about the dynamics of the system and, as we will see in the following chapters in different joint experimental-theoretical applications, can be used as a probe of the molecular geometry or the vibronic state. The asymptotic wave function describing a scattered electron, with energy ε_α in channel α and emitted in the Ω_e direction, satisfying incoming boundary conditions can be written in a partial wave expansion [68]:

$$\Psi^-_\alpha(\mathbf{r},R,t) = \sum_{l_\alpha m_\alpha} i^{l_\alpha}e^{-i\sigma_{l_\alpha}(\varepsilon_\alpha)}\psi^{\varepsilon_\alpha}_{\alpha l_\alpha m_\alpha}(\mathbf{r},R)\chi_{v_\alpha}(R)\mathcal{Y}^{m_\alpha *}_{l_\alpha}(\Omega_e)e^{-iW_{\alpha v_\alpha}t} \tag{3.29}$$

where $\sigma_{l_\alpha}(\varepsilon_\alpha) = \arg\Gamma(l+1-Z/k)$ is the long range Coulomb phase. Projecting the total wave function onto this asymptotic expression one can obtain the fully differential cross section (differential in ejection angle, electron and vibrational energies). The reproduction of the experimental conditions (molecular orientation, energy and angle-resolved quantities, etc..) is highly dependent on the radiation source employed, as well as on the detection techniques. For instance, from the experimental point of view, the most complete measurement, differential in all photo-fragments energies and angles, implies the detection of the

momentum of all the fragments in coincidence. Multicoincidence reactions microscope like COLTRIMS [4, 5] are adapted to measure the full fragmentation of a few body system. From the measured time-of-flight of the particles and the position of impact on the detector the three dimensional momentum of the particles is measured, as a consequence the direction along the internuclear axis the proton escape is also determined. Therefore this type of measurements imposes asymptotic conditions that should be reproduced in order to properly compare with the experiment. To satisfy the boundary conditions in which electron ejection angles are measured with respect to the ejection of the ion fragment, the total molecular wave function should be projected onto a combination of *gerade* and *ungerade* channels that localizes one of the protons in a given center. When only the α=$1s\sigma_g$ and α=$2p\sigma_u$ channels are being considered the proper combination is:

$$\Psi^{-}_{u,d} = \frac{1}{\sqrt{2}}(\Psi^{-}_{1s\sigma_g} \pm \Psi^{-}_{2p\sigma_u}) \tag{3.30}$$

where u (Upward) and d (Downward) indicate the center in which the proton is being projected. Performing the projection one can obtain the expression for the fully differential probability (proton and electron kinetic energy and solid angle of the emitted electron).

$$\frac{d^3P_{u,d}}{dE_v d\varepsilon d\Omega_e} = \frac{1}{2}\left|\sum_{lm} i^{-l} e^{i\sigma_l(\varepsilon)} Y_l^m(\Omega_e)\left(C^{lm\varepsilon}_{1s\sigma_g v_g} \pm C^{lm\varepsilon}_{2p\sigma_u v_u}\right)\right|^2 \tag{3.31}$$

where the sum over l and m should be consistent with the total symmetry *gerade* or *ungerade* and with channel α explicitly indicated in the expression.

On the other hand, if one is not able to distinguish fragments coming from the same event, the projection onto one center or the other is unnecessary. In this case the probability fully differential would be:

$$\frac{d^3P}{dE_{v_\alpha} d\varepsilon_\alpha d\Omega_e} = \left|\sum_{l_\alpha m_\alpha} i^{-l_\alpha} e^{i\sigma_{l_\alpha}(\varepsilon_\alpha)} C^{l_\alpha \varepsilon_\alpha}_{\alpha v_\alpha}(t_{int}) \mathcal{Y}^{m_\alpha}_{l_\alpha}(\Omega_e)\right|^2 \tag{3.32}$$

In some experimental applications, the definition of the so-called electron *asymmetry parameter* can be very useful. The electron *asymmetry parameter* is defined as the difference in the electron yield between the left and right halves of the plane perpendicular to the molecular axis and containing the inversion center.

$$A^e = \frac{P_l - P_r}{P_l + P_r} \tag{3.33}$$

it can be easily calculated by integrating in the left or right halves individually:

$$\begin{aligned} P_l &= \int_0^{\frac{\pi}{2}} \int_0^{2\pi} \frac{d^3P}{dE_v d\varepsilon d\Omega_e} \sin(\theta_e) d\theta_e d\phi_e \\ P_r &= \int_{\frac{\pi}{2}}^{\pi} \int_0^{2\pi} \frac{d^3P}{dE_v d\varepsilon d\Omega_e} \sin(\theta_e) d\theta_e d\phi_e \end{aligned} \tag{3.34}$$

The *asymmetry parameter* thus provides a measure of the degree of asymmetry in the electron (proton) ejection upon the photoionization event. As we discuss in each section of the results, this parameter can further be defined as differential in both electron and nuclear kinetic energy release, or integrated in one or both magnitudes. Moreover, depending on the detection capabilities in a given experiment the *asymmetry parameter* should be calculated using different expressions. For instance, in the case of the asymmetry induced by electron localization [15, 16, 35, 69], the ionization observables are given by equation 3.31 where the electron ejection is captured as a function of the proton ejection. Conversely, in some experiments using VMI techniques [1–3] that only detect electron or ions without coincidences, the ionization observables are directly given by equation 3.32. Specific details on the relevant observables for different experimental set ups are respectively provided in the different sections of the results.

The spectral method used to solve the TDSE is general, in the sense that it can be applied to a variety of systems and light-induced processes. One only needs to expand the total wave function as linear combination of the eigenstates of the field free Hamiltonian, calculate the dipole couplings among those states and plug those couplings into the TDSE method. Multiphoton ionization is a particularly demanding problem, more specifically, in the above threshold ionization (ATI) limit that involves continuum-continuum dipole matrix elements. The description of the later couplings are the most expensive (given the large number of discretized states required for most applications) and the hardest to converge due to the highly oscillatory behaviour of the continuum states. Moreover, the larger the number of absorbed photons, the larger is the total angular momenta of the molecular system required, which makes the problem more expensive. In order to illustrate the validity of our spectral method to describe the ATI processes, and consequently the accuracy of the dipole coupling among discretized continuum states, we show a test-bed example performed in the hydrogen atom. Figure 3.1, compares the ATI photoelectron spectra obtained with our method and the corresponding quantity reported in [70] obtained with a split-operator method. The hydrogenic states are expanded in terms of N=2400 B-splines of order k=8 distributed inside a box of r_{max}=1200 a.u. The use of such a large box guarantees that all the necessary conditions explained in the last section are fulfilled. The results in both cases have been obtained using a 30-cycle $\cos^2$ laser pulse with ω=0.35

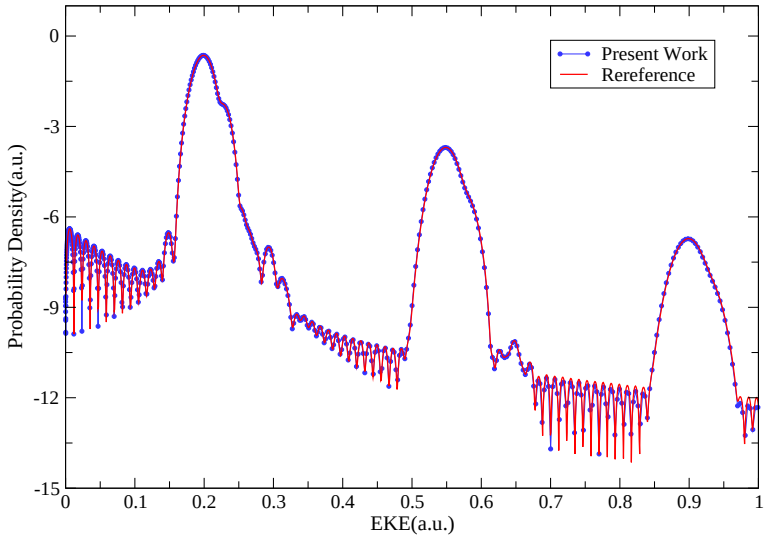

FIGURE 3.1: ATI photoelectron spectrum from hydrogen ground state using a 30-cycle $\cos^2$ laser pulse with ω=0.35 a.u. and I=1.4 10^{13} W/cm^2. The comparison between the result obtained with the present spectral method and the one (using split-operator method) in reference [70] is shown.

a.u. and I=1.4$\times 10^{13}$ W/cm^2. The spectra obtained with the two different methods are in excellent agreement. Notice that the photoelectron spectrum shown in the figure corresponds to processes involving the absorption of several photons, thus indicating the high accuracy of our spectral method down to slightly details.

3.3 Second-order time-dependent perturbation theory

The numerical integration of the TDSE in equation 3.24 becomes an impractical problem when the interaction times with the radiation source reach a few hundreds of atomic units (i.e. for tens of femtoseconds). However, the interaction with radiation sources with relatively low intensities, where non-linear processes do not play any role, allows the use of the time-dependent perturbation theory, which may reduce the computational cost. This is a newly developed implementation with respect to the existing codes that allows to explore two-photon transition processes in the perturbative regime at a much lower cost, opening the door to the investigation of processes with larger pulse durations as it will be shown in Chapter 9. In this context, equation 3.15 written in its integral form reads:

$$\Psi_I(t) = \Psi_I(t_0) - i\int_{t_0}^{t} dt_1 \hat{V}_I(t_1)\Psi_I(t_1) \tag{3.35}$$

where $\Psi_I(t_0)$ is the initial state of the system at t_0, usually the ground state of the system. However, the formalism will remain valid for any initial wavefunction of the system $\Psi_I(t_0)$. Usually it is more convenient to write equation 3.35 using the Dyson series:

$$\begin{aligned}\Psi_I(t) &= \hat{\mathcal{U}}(t,t_0)\Psi_I(t_0) = \sum_n \hat{\mathcal{U}}^{(n)}(t,t_0)\Psi_I(t_0)\\ \hat{\mathcal{U}}^{(n)}(t,t_0) &= (-1)^n \int_{t_0}^{t} dt_1 \int_{t_0}^{t_1} dt_2 \cdots \int_{t_0}^{t_{n-1}} dt_n \hat{V}_I(t_1)\hat{V}_I(t_2)\cdots\hat{V}_I(t_n)\end{aligned} \tag{3.36}$$

The radiative transition amplitude between two eigenstates of the unperturbed Hamiltonian $\hat{\mathcal{H}}_0$, the initial state ψ_i and the final state ψ_f (note that both functions depend on both coordinates, electronic and nuclear) within the perturbative expansion in equation 3.36, can be written as a sum of terms:

$$c_{if} = c_{if}^{(0)} + c_{if}^{(1)} + c_{if}^{(2)} + \cdots \quad \text{where} \quad c_{if}^{(n)} = \langle\psi_f|\hat{\mathcal{U}}^{(n)}(t,t_0)|\psi_i\rangle \tag{3.37}$$

Since we are interested in two-photon absorption processes, we can drop the zero-order and first-order terms in equation 3.36. Using the fact that the eigenstates of the unperturbed Hamiltonian constitute a complete basis set and transforming from the interaction picture to the Schrödinger one. The expression for the second-order radiative transition amplitude after the end of the laser pulse reads:

$$c_{if}^{(2)} = -\sum\!\!\!\!\!\!\int_n \int_{t_0}^{t} dt_1 \int_{t_0}^{t_1} dt_2 e^{E_{fn}t_1} e^{E_{ni}t_2} \langle\psi_f|\hat{\mathcal{V}}_{int}(t_1)|\psi_n\rangle\langle\psi_n|\hat{\mathcal{V}}_{int}(t_2)|\psi_i\rangle \tag{3.38}$$

where $E_{fn} = E_f - E_n$ and $E_{ni} = E_n - E_i$. Using the specific form of the interaction operator in *velocity* gauge (equation 3.12) yields:

$$\begin{aligned}c_{if}^{(2)} &= -\sum\!\!\!\!\!\!\int_n \langle\psi_f|\hat{\mathbf{e}}_\mu\hat{\mathbf{p}}|\psi_n\rangle\langle\psi_n|\hat{\mathbf{e}}_\mu\hat{\mathbf{p}}|\psi_i\rangle\mathcal{G}(E_i,E_n,E_f,A(t))\\ \mathcal{G}(E_i,E_n,E_f,A(t)) &= \int_{t_0}^{t} dt_1 \int_{t_0}^{t_1} dt_2 e^{E_{fn}t_1} e^{E_{ni}t_2} A(t_1)A(t_2)\end{aligned} \tag{3.39}$$

As an example we use a pulse at mean frequency ω with a Gaussian envelope and peak vector potential A_0. Gaussian envelopes are usually employed

because they lead to manageable analytical expressions, although other mathematical functions (as sine-squared envelopes) essentially provide similar analytical expressions and the same numerical outcome. The potential vector can be then defined as:

$$A(t) = \frac{A_0}{2}\exp(i\omega t - zt^2) + c.c \qquad z = \ln 16/T^2 + ic_0 \tag{3.40}$$

where T is the temporal full width at half maximum (FWHM) of the pulse, and c_0 represents a possible linear temporal chirp on the frequency. Using the rotating wave approximation and taking $t_0 \to -\infty$ and $t \to \infty$ this would produce:

$$\mathcal{G} = \frac{A_0^2}{4}\int_{-\infty}^{\infty} dt_1 \int_{-\infty}^{t_1} dt_2 e^{iE_{fn\omega}t_1 - zt_1^2} e^{iE_{ni\omega}t_2 - zt_2^2} \tag{3.41}$$

where $E_{fn\omega} = E_{fn} - \omega$, $E_{ni\omega} = E_{ni} - \omega$. The integrals in equation 3.41 can be simplified by way of a simple variable transformation $\tau = (t_1 + t_2)/2$, $\xi = (t_1 - t_2)/2$, $E_t = E_{fn\omega} + E_{ni\omega}$ and $\Delta = E_{fn\omega} - E_{ni\omega}$. The two-photon shape function for Gaussian pulses then reads:

$$\mathcal{G} = \frac{A_0^2}{2}\int_{-\infty}^{\infty} e^{iE_t\tau - 2z\tau^2} d\tau \int_0^{\infty} e^{i\Delta\xi - 2z\xi^2} d\xi = \frac{\pi A_0^2}{8z} e^{-E_t^2/8z} w\Big(\frac{\Delta}{\sqrt{8z}}\Big) \tag{3.42}$$

where $w(x)$ is the complex *error* function [49]. In this approach the observables can be calculated in the same way we have explained in the previous section.

In the perturbative regime, the outcome of the TDPT and the result of the TDSE should be identical. The time-independent lowest-order perturbation theory (LOPT), on the other hand, provides the long-time limit of the pulse duration. This is illustrated in figure 3.2 that displays the comparison between our calculated cross section (using the method previously explained) and calculations using the LOPT for the two photon ionization of the H atom (left panel) [72, 73] and H_2^+ molecule (within the fixed nuclei approximation (*FNA*) R=2.0 a.u.) (right panel) [71]. As long as the duration of the pulse increases the TDPT results nicely converges to the LOPT result as expected. The convergence is faster in the H atom than in the H_2^+ molecule. When the photon energy exceeds the ionization threshold the continuum-continuum transitions are involved. In the LOPT framework one has to calculate the contributions to the continuum states from outside the electronic box [74] in order to properly describe these transitions. However, in the TDPT framework as for the TDSE case this step is unnecessary, as shown in the H atom case (ω>0.5 a.u.), saving a lot of work and time. In the H atom, the singularities appearing at a given photon energies are due to the intermediate states, in

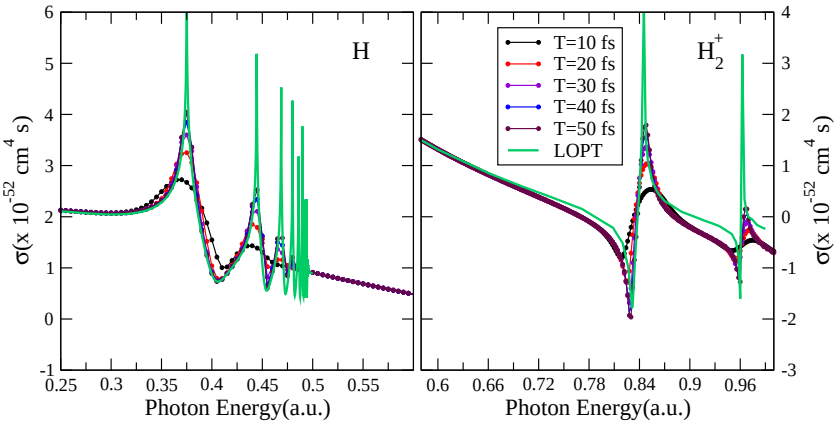

FIGURE 3.2: Two photon cross section of H (left panel) and H_2^+ (*FNA* R=2.0 a.u.) (right panel) as a function of the photon energy. Comparison between LOPT (green solid line) extracted from references [71–73] and time dependent perturbation theory for different pulse durations is displayed.

resonance with the one-photon absorption. While, for H_2^+ we observe similar profiles as long as we stay within the *FNA*, i.e., we observe an atomic-like behaviour. However, as it has been shown in previous works within our group [23, 24] the inclusion of the nuclear degrees of freedom smooths out the singularities. Regardless of the fact that this example (H_2^+) was done within the *FNA*, we pursued to show the dependence of the obtained outcome with the pulse duration, which follows the same behaviour in the full-dimensional problem. Note that having calculated the dipole couplings between the states (initial-intermediates-final) only evaluation of the error function in equation 3.42 is required.

Summarizing, figure 3.2 validates the fact that we can use our spectral method in combination with the TDSE or TDPT frameworks obtaining equal accuracy in the results. When to employ each or both approaches directly depends on the experimental conditions that we aim to reproduce. One should carefully take into account that the solution of the TDSE enables the description of non-linear processes and interaction with intense fields (i.e. reproducing Stark shift effects or Rabi oscillations) as long as the relevant couplings are introduced, while the n-th order TDPT is limited by the n-th order employed and assumes an unperturbed initial state. On the other hand, the latter approach allows the description of larger interaction times with the light at a lower computational cost. In the following

sections we illustrate their appropriateness depending on the experimental conditions. Note that most of the present theoretical work has been developed in close collaboration with experimental groups, which implies a remarkable challenge in order to provide a solid interpretation and, furthermore, to elucidate the mechanisms underlying the observed phenomena.

Part II

Electron Correlation in molecular photoionization

Chapter 4

Imaging electron correlation

The tool box for imaging molecules is well equipped today. Some of the techniques visualize the mean geometrical structure, others image the single electron density or single electron orbitals. Molecules, however, are many-body systems for which the correlation between the constituents is often decisive and the spatial and momentum distribution of one electron depends on the positions and momenta of the other electrons and the nuclei. Such correlations have escaped direct observation by imaging techniques so far. Here we investigate an imaging scheme which visualizes correlations between electrons by coincident detection of the electronic and nuclear fragments after high-energy photo fragmentation. This work has been performed in collaboration with the experimental group led by Prof. R. Dörner at Institut für Kernphysik in Frankfurt. The experimental set up combines a synchrotron radiation source with the most advanced detection techniques using COLTRIMS, which nowadays allows for a high-resolution in the angle and energy emission of photo-fragments. This work uses this technique to examine parts of the H_2 two-electron wave function in which electron-electron correlation beyond the mean-field level is prominent and we visualize the dependence of the correlated two electron wave function on the internuclear distance. Electron correlation is at the heart of several well-known quantum effects as superconductivity or giant magnetoresistance. In molecules the fundamental importance of electron correlation can already be perceived when, e.g., comparing values of molecular binding energies obtained within the commonly used Hartree-Fock approximation to those actually occurring in nature. Mean field approaches, as the Hartree-Fock one, intrinsically neglect electron-electron correlation, as it considers only an overall mean electric field generated by the electron ensemble. Already for the simple H_2 molecule, this approach yields, for example, dissociation energies which are off by 0.6 eV (on a total energy of approximately 4.5 eV). As correlation has already a large impact on a global property such as the dissociation energy, it can be anticipated that it has an even stronger effect on local details of the atomic or molecular wave functions.

To fully characterize electron correlation, however, the many-electron wave

function of an atom or a molecule has to be directly examined. For the case of the H_2 molecule, it turns out that this is experimentally achievable: here we present a novel theoretical (experimental) approach that allows us to visualize the square of its correlated two-electron wave function. There are two key elements to our approach: the first one is photoelectron emission to image one of the electrons and the second one is coincident detection of the quantum state of the remaining electron. Photoionization itself is a well-studied process, which in solid state physics is routinely used as a powerful tool for band structure imaging [75]. Although photoionization has also been proposed to image molecular orbitals [76], only the reverse process, high-harmonic generation, has succeeded in acomplishing this goal [14]. Other techniques for imaging molecular orbitals are electron momentum spectroscopy [77] or strong field tunnel ionization [78]. Here we use photoionization to image the correlated molecular wave function.

4.1 Double slit, confinement and non-Franck-Condon effects

In this section we present a study of one-photon single ionization of H_2 at a photon energy of $\hbar\omega$=400 eV. We have chosen this specific energy due to the possibility of comparison with experimental data, although all the conclusions reached in this chapter remain valid for photons of a few hundred eV. At these high photon energies the photoelectron acquires a very large energy independent of the kinetic energy of the residual ion or the nuclei. It is well known that a continuum wave function of a fast electron exhibits an strong oscillatory behaviour, so one needs to reproduce this oscillatory behaviour with enough accuracy in order to extract reliable information from the continuum wave function. As we stated earlier B-splines basis sets are well suited for this kind of problems. In this case, for the construction of the final electronic continuum wave function in equation 2.56 the close coupling expansion includes all partial waves with $l \leq$11 associated with the six lowest ionization thresholds of H_2 $^2\Sigma_g^+(1s\sigma_g)$, $^2\Sigma_u^+(2p\sigma_u)$, $^2\Pi_u(2p\pi_u)$, $^2\Sigma_g^+(2s\sigma_g)$, $^2\Sigma_u^+(3p\sigma_u)$ and $^2\Sigma_g^+(3d\sigma_g)$. The mono-electronic orbitals used to construct the UCS and the bound states are expanded in a basis of 410 B-splines per angular momentum in a r_{max}=60 a.u. electronic box, which represents a huge increment if compared with basis set used in other calculations. The corresponding angular components include spherical harmonics up to l=16. The vibrationally (bound and dissociative) wave functions have been expanded in a 240 B-splines in a R_{max}=12 a.u. vibrational box. Therefore, the final wave function accounts for the interferences among the ionization thresholds and angular momenta of the ejected electron. In addition all the calculated wave functions include electron-correlation and the two-center character of the molecular potential. To further check the convergence of the close coupling expansion, we performed additional

calculations in which higher ionization thresholds were included but no important modifications were observed in any of the observables.

Single photon absorption (at high photon energies) in the case of H_2 molecule can be expressed by the following reactions:

$$H_2 + \hbar\omega \Rightarrow H_2^+(v)\text{+e}^-$$

$$H_2 + \hbar\omega \Rightarrow H^+\text{+H(n)+e}^-$$

Where v is the vibrational number of the ground state of the ion ($1s\sigma_g$) and n is the dissociation limit (meaning the state of the residual H atom). In previous works [79, 80] non-dissociative ionization was studied in detail, while here we are committing to study both non-dissociative and dissociative ionization, paying special attention to the ionization process through higher ionization thresholds and the effect of electron correlation in this process. Note that autoionization is not included, since at this photon energies the doubly excited states (DES) are hardly populated. Dissociation going to different states of the atom produces products (electrons and protons) with different energies, therefore from the experimental point of view if one measures in coincidence protons and electrons the dissociative limit can be unambiguously determined. Moreover, by momentum reconstruction one can determine the orientation of the molecule with respect to the light polarization direction. In the following, we obtain the one-photon ionization cross section for molecules placed parallel and perpendicular with respect to the light polarization vector.

In figure 4.1 we present the contribution of each ionization threshold α to the total cross section for each molecular orientation, i.e. for both symmetries $^1\Sigma_u^+$ and $^1\Pi_u$. For both symmetries we can split the ionizations thresholds in three different groups regarding their relative importance at a given photon energy. First $1s\sigma_g$ is largely dominant for all photon energies, then we have the cross section of the $2s\sigma_g$ and the $2p\sigma_u$ thresholds very close in value but almost two order of magnitude smaller that one of the $1s\sigma_g$, followed by all the remaining thresholds going mostly to the n=2 dissociation limit way to far from the previous ones. The $1s\sigma_g$ cross section has contributions from the non-dissociative and the dissociative channels, being the non-dissociative the most important, all the other thresholds are purely dissociative. We know from simple inspection to the Franck-Condon (FC) factors that those ionization thresholds appear at different regions in the cross section differential in proton energy, therefore we can expect only these three thresholds to have a non-negligible cross section at this photon energy.

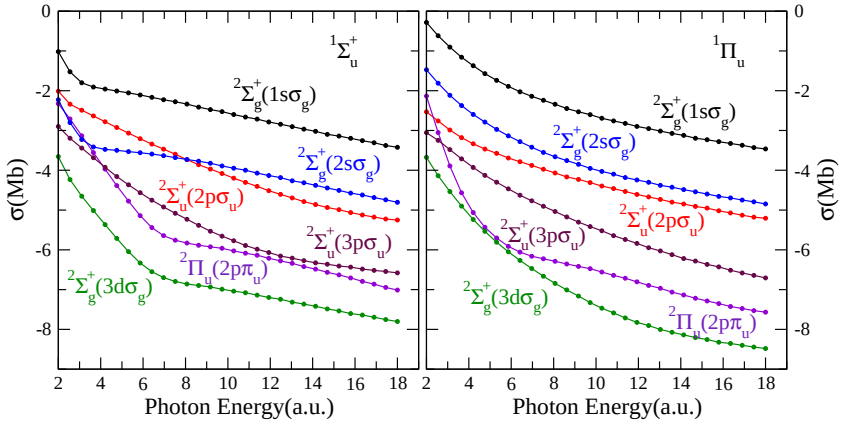

FIGURE 4.1: $^1\Sigma_u^+$(left panel) and $^1\Pi_u$(right panel) photoionization cross sections of H_2 as a function of the photon energy. Contributions from the first six ionization thresholds are shown.

To get further insight one can dissect the cross-section by contributions from each partial wave. In figure 4.2 we present the contribution of the different partial waves associated with each ionization threshold and for each symmetry $^1\Sigma_u^+$ and $^1\Pi_u$. In the case of the $^1\Sigma_u^+$ symmetry the different partial waves of all three relevant thresholds exhibit a minimum at very specific photon energies (blurred in the total due to the sum over partial waves), leading to shallow dips in the total photionization cross section. Such minima are expected to appear when the momentum of the ejected electron satisfies the condition $k_e R \sim l\pi$ [81] and are associated with electron confinement at a given internuclear distance. Figures 4.1 and 4.2 also show that the inclusion of higher partials waves and ionization thresholds in the calculations is totally unnecessary.

In the non-dissociative ionization the residual H_2^+ ion remains in the $1s\sigma_g$ and can be left in any of the vibrational states, so the higher the electron energy the lower the vibrational states. The non-dissociative process is the most important contribution to the total cross section presented in the figure 4.1. The non-dissociative cross section is about two orders of magnitude bigger than the non-dissociative one. In previous works vibrational ratios have been used to observe the Young's double slit interferences in diatomic molecules [30]. Thus, although it is not the main topic of this chapter, we should describe the main features at this photon energy. In figure 4.3 we show the cross sections differential in vibrational energy of the residual H_2^+ ion for each symmetry $^1\Sigma_u^+$ and $^1\Pi_u$. The FC distributions predict the v=2,3 vibrational states to present the largest population. In

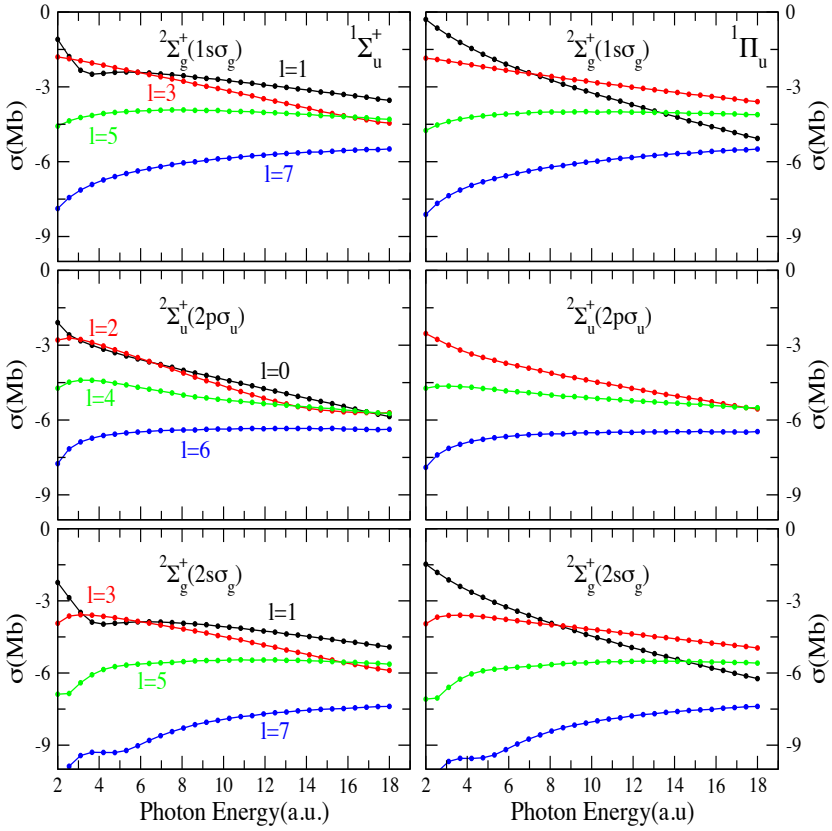

FIGURE 4.2: Partial wave contributions to the photoionization cross sections of H_2 associated with the ionization thresholds $1s\sigma_g$, $2p\sigma_u$ and $2s\sigma_g$. Results for $^1\Sigma_u^+$(left panel) and $^1\Pi_u$(right panel) are shown.

both symmetries the population of the final vibrational states follow a FC distributions, nonetheless the relative contributions of the partial waves do not follow such a simple behaviour. In the perpendicular case the l=3 partial wave dominates for all v, the l=5 is important at low v while the other partial waves are barely populated. In the parallel case the dominant partial wave is l=1, while l=5 and l=3 are important for low and high v respectively. Therefore in both symmetries the relative contributions of each partial wave depend on the energy of the ejected electron. This implies very different angular distributions for different energy sharing. Is worth noting that the relative importance of each partial wave is

in perfect agreement with what has been shown in figure 4.2.

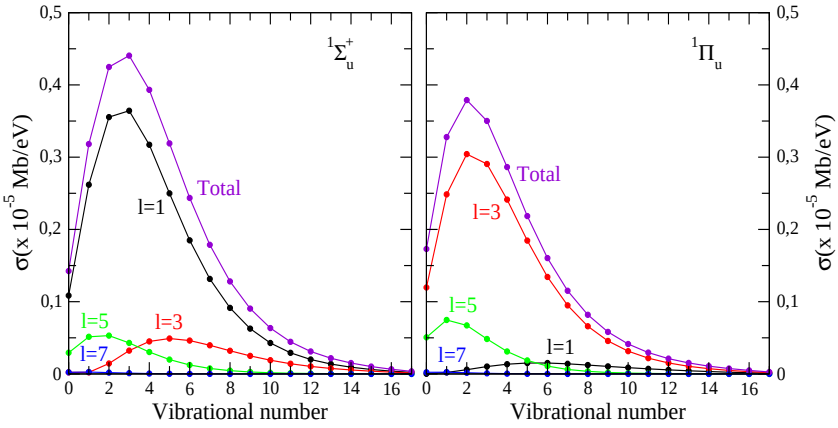

FIGURE 4.3: $^1\Sigma_u^+$(left panel) and $^1\Pi_u$(right panel) non-dissociative photoionization cross section of H_2 as a function of the vibrational number of the residual H_2^+ ion. Partial wave contributions in each symmetry are shown.

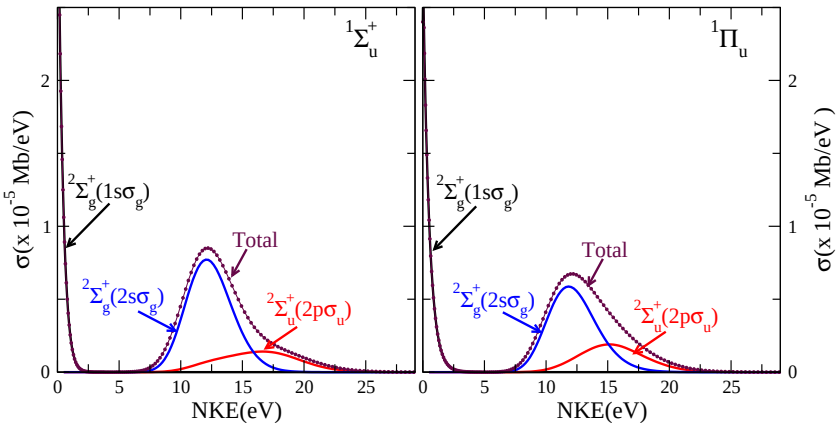

FIGURE 4.4: Nuclear kinetic energy spectra for both $^1\Sigma_u^+$ and $^1\Pi_u$ final symmetries. Contributions from the more relevant ionization thresholds to the total spectra are shown.

In figure 4.4 we show the cross sections differential in the kinetic energy of

nuclei for each symmetry, the contribution of each relevant ionization threshold is also shown. As stated earlier, the $2p\sigma_u$ and the $2s\sigma_g$ provide the predominant contributions to the dissociative process at high NKE. For low NKE it is well known that for one photon absorption the $1s\sigma_g$ is the only populated. The population of states beside the $1s\sigma_g$ is possible only due to electron correlation, since the photon is promoting one electron into the continuum and the second electron is left in an excited state of the ion. Thus, creating a perfect alternative to the Coulomb explosion channel (hard to obtain from the theoretical point of view) to investigate electron correlation at high photon energy. Fortunately those states dissociate to a different limit of the Hydrogen atom, H(n=1) and H(n=2) respectively, allowing to experimentally discriminate the electrons associated with a specific threshold (if other state dissociating to H(n=2) were added, this task would be impossible). Here it is worth mentioning that the Coulomb explosion channel was not included in the calculations (the way the scattering states are defined allows only treatment of single ionization problems). The Coulomb explosion signal is expected to be peaked at NKE=19.43 eV overlapping with the $2p\sigma_u$ state, however it can be discriminated as the others thresholds. The $2p\sigma_u$ and $2s\sigma_g$ are peaked at different NKE energies when comparing both symmetries, this is related to the difference in the dipole couplings.

We can get a more complete picture by looking at the molecular frame photoelectron angular distributions (MFPAD). In previous works [29, 81–83] it was shown that the condition to observe confinement effects in the parallel geometry ($^1\Sigma_u^+$ symmetry), in terms of the electron energy, is approximately given by the formula:

$$\varepsilon = \frac{l^2\pi^2}{2R^2} \tag{4.1}$$

while in the perpendicular case ($^1\Pi_u$ symmetry), constructive interferences are expected at emission angles given by Young's formula:

$$R\sin\theta_e = n\lambda_e \tag{4.2}$$

where now R is the internuclear distance at which the electron emission occurs, θ_e is the emission angle of the electron with respect to the polarization direction. In order to define the value of R to be used in the previous equation we need to establish a correspondence between R and the kinetic (vibrational if non-dissociative) energy of the residual ion. The mapping between the kinetic energy of the ion and the internuclear distance R can be easily done. As shown in previous works [79, 80, 84, 85], we only have to pick the inner classical turning point associated with each final kinetic energy of the ion or the vibrational energy of the bound state of the ion (the same is true in both situations). Figure 4.5 depicts the mapping procedure. Following the energy conservation:

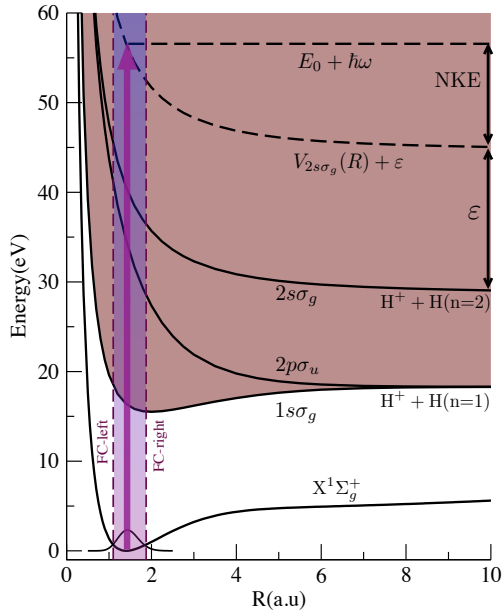

FIGURE 4.5: Relevant potential energy curves of H_2. The figure displays the ground state of the molecule and the potential energy curves of the relevant ionization thresholds. The Franck-Condon region is enclosed within the two vertical lines. The total energy $E_0 + \hbar\omega$ of the system after ionization from the ground state is shared between the electron(energy ε) and the nuclei(NKE) such that $\hbar\omega + E_0 = \varepsilon + NKE + W_\infty = V_\alpha(R) + \varepsilon$.

$$\hbar\omega + E_0 = \varepsilon + NKE + W_\infty = V_\alpha(R) + \varepsilon \quad V_\alpha(R) = NKE + W_\infty \tag{4.3}$$

Where V_α is the potential energy curve of the ionization threshold α we are looking at, ε is the photoelectron energy, W_∞ is the energy in the dissociative limit, NKE is the nuclei kinetic energy, $\hbar\omega$ and E_0 are the photon energy and the ground state energy respectively. By solving equation 4.3 we can map each NKE (or vibrational energy) with a specific internuclear distance R. In the H_2^+ molecule and H_2 double ionization where the molecule undergoes Coulomb explosion upon photoionization we end up with a perfect one-to-one mapping, the well known *reflection approximation* NKE=$1/R$ [27, 28, 86]. Thus the analysis of the MFPADs for different kinetic energies of the ejected electron (or different energies of the residuals protons or ion) at a fixed photon energy allows one to observe the

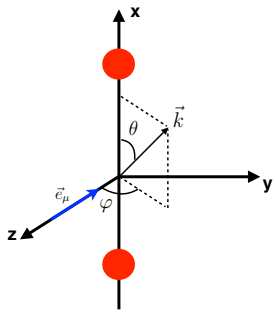

FIGURE 4.6: Polar angles θ and φ defining the direction of the electron momentum $\vec{k}$ with respect to the plane defined by the internuclear axis (x) and the polarization direction $\vec{e}_\mu$.

variation of the double slit patterns and the confinement effects as the molecule vibrates. Moreover, we are going to use this idea to visualize the square of its correlated two-electron wave function in the next section.

For the MFPADs presented below we are considering right handed polarized light (μ=1) with incidence direction perpendicular to the molecular axis. This arrangement leads to a coherent mix of the $^1\Sigma_u^+$ and $^1\Pi_u$ amplitudes. We are going to show the angular distributions in the plane containing the polarization vector and the molecular axis, i.e. $\varphi = 90°$ and $\varphi = 270°$ (see figure 4.6 for notation). Notice, that although we have represented the molecule in figure 4.6 in a vertical position, for a better representation in the following MFPADs the molecule is placed horizontally (equivalent to rotating figure 4.6 by 90°). In order to understand the main features in the MFPADs we are going to compare the results for circularly polarized light with those obtained using linearly polarized light parallel ($^1\Sigma_u^+$ symmetry) and perpendicular ($^1\Pi_u$ symmetry) to the molecular axis. The MFPADs have been calculated using Dill's formalism [68], specific details on the formulation have been explained in appendix A.

In figure 4.7, the comparisons between the MFPADs obtained for the case where the ion is left in the v=0, 4, 12 (R=1.71, 1.34, 1.15 a.u.) vibrational levels ($1s\sigma_g$) and the ones obtained in the *FNA* case at the corresponding internuclear distance are shown. The results have been normalized to the total cross section for a better comparison. The first two values of v are within the FC region while the third is outside that region. The first conclusion one can arrive at is that the mapping works remarkably well, especially for the perpendicular orientation. For the perpendicular orientation, one can see that the electron is ejected mainly in the direction of the polarization vector of the light as expected, however the MFPADs display smaller lobes. Those are consequence of the diffraction produced by the

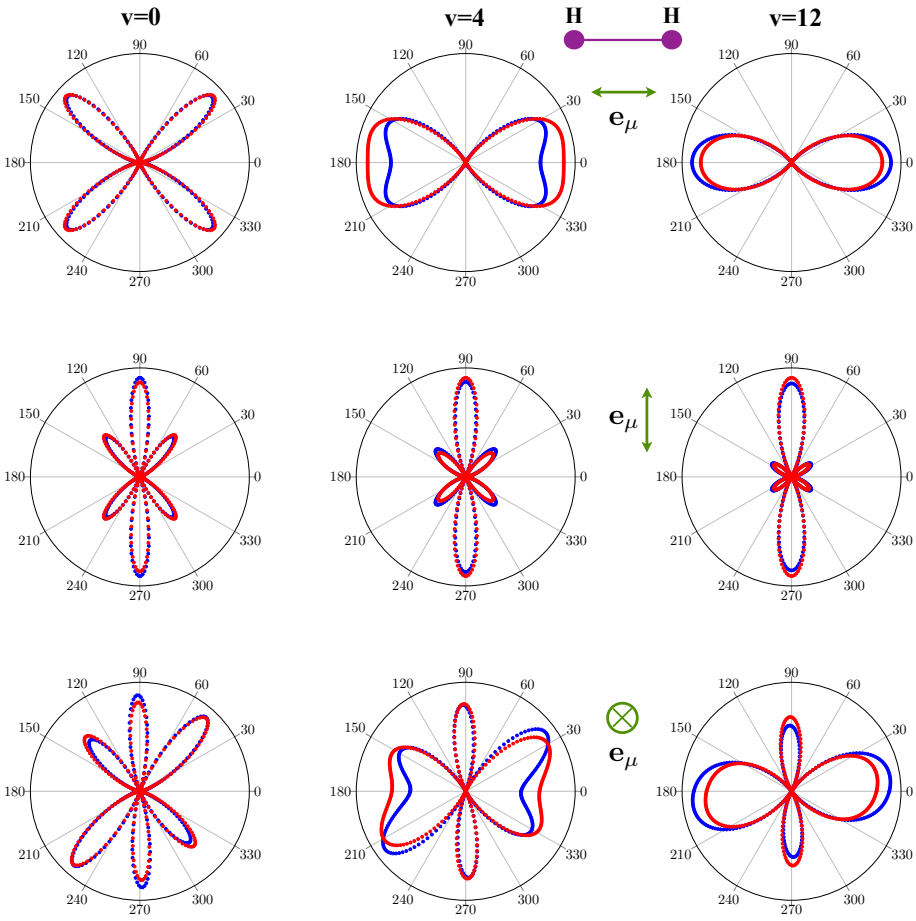

FIGURE 4.7: Electron angular distribution. Upper panel: results obtained with linearly polarized light parallel to the molecular axis ($^1\Sigma_u^+$ symmetry). Middle panels: idem with the light perpendicular to the molecular axis ($^1\Pi_u$ symmetry). Lower panel: results obtained with circularly polarized light with the incidence perpendicular to the molecular axis. Comparison between the angular distributions corresponding to the electrons ejected and leaving the ion in the bound states v=0,4,12 each column respectively (blue points) and the fix nuclei approximation (red points) at the internuclear distance corresponding to the inner turning point of each vibrational number. The MFPADs have been normalized to the total cross section.

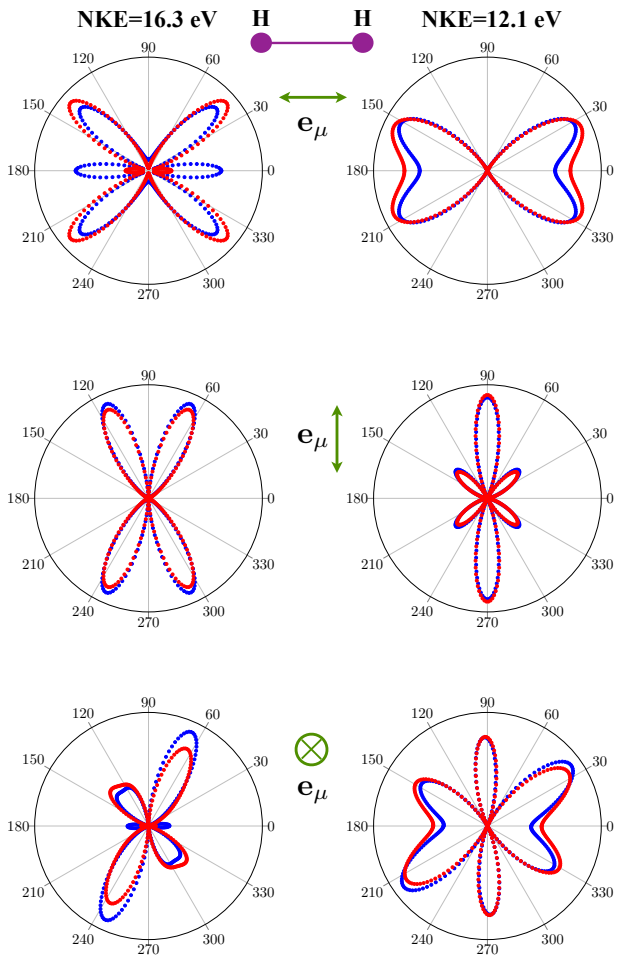

FIGURE 4.8: Electron angular distribution. Upper panel: results obtained with linearly polarized light parallel to the molecular axis ($^1\Sigma_u^+$ symmetry). Middle panels: idem with the light perpendicular to the molecular axis ($^1\Pi_u$ symmetry). Lower panel: results obtained with circularly polarized light with the incidence perpendicular to the molecular axis. Comparison between the angular distributions corresponding to the electrons ejected and the ion dissociating through the $2p\sigma_u$ (NKE=16.3 eV) and the $2s\sigma_g$ (NKE=12.1 eV) each column respectively (blue points) and the fix nuclei approximation (red points) at the internuclear distance corresponding to each NKE. The MFPADs have been normalized to the total cross section.

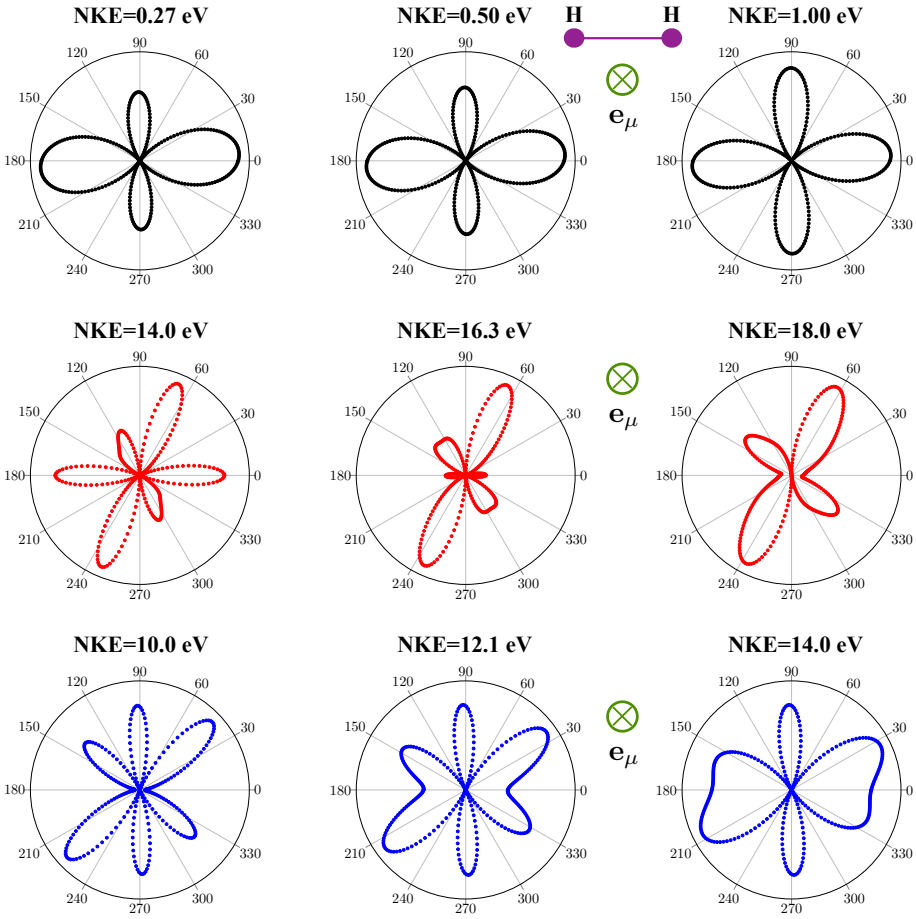

FIGURE 4.9: Electron angular distribution for circularly polarized light. Upper panel: results obtained in the $1s\sigma_g$ channel for NKE=0.27, 0.5 and 1.0 eV from left to right. Middle panels: results obtained in the $2p\sigma_u$ channel for NKE=14.0, 16.3 and 18.0 eV. Lower panel: results obtained in the $2s\sigma_g$ channels for NKE=10.0, 12.1 and 14.0 eV.

double slit. As a matter of fact for a $\hbar\omega$=400 eV photon the wavelength of the ejected electron λ_e ∼1.18 a.u. is comparable to or smaller than the extracted internuclear distances, thus fulfilling the condition 4.2. One also can see that the relative intensity of the lobes decreases as v increases (electronic energy decreases). In fact for a lower electronic energies (higher wavelengths) the double slit condition drops. In the parallel orientation the MFPADs present different characteristics, for v=0 there is almost no emission in the direction of the polarization vector of the light, while for v=12 it has a p-like shape meaning that the electron was ejected following the polarization vector, this abrupt change with the value of v is related to partial wave confinement. For the circularly polarized light, the angular distributions present a superposition of the main characteristics of parallel and perpendicular orientations. However, the combination of such effects can be deceiving, because it may suggest the existence of double slit or confinement effects when there are none, or the opposite obscured them when they are not pronounced. The slight rotation in the MFPADs is due to the rotation of the polarization vector in the same direction, while the differences with respect to the arithmetic average are due to the coherence between perpendicular and parallel symmetries. So far the MFPADs have proven to be key in unraveling features obscured by the integration over emission angles.

In figure 4.8, the equivalent comparison for the dissociative channel is shown. In this case for the $2p\sigma_u$ we pick NKE=16.3 eV and for the $2s\sigma_g$ NKE=12.1 eV and their corresponding internuclear distances (R=1.4 a.u. in both cases). Since in these states electron correlation plays a big role we can not invoke simple models to explain the main features as we did for the $1s\sigma_g$ bound states. However the main conclusions are still valid. Again one can see that the mapping of the internuclear distance works quite well. In the case of the $2s\sigma_g$ channel the MFPADs closely resemble those obtained for the $1s\sigma_g$ bound states. As a matter of fact, on closer inspection of figure 4.2 one can see that the weight of each the partial wave is quite similar for $1s\sigma_g$ and the $2s\sigma_g$, the same is true for both symmetries, so it should be expected the similarities. Other interesting feature is the strong coherence between symmetries in the $2p\sigma_u$ channel, probably due to electron correlation.

Finally in figure 4.9 we present the MFPADs for circularly polarized light, for different NKE of three relevant ionization thresholds. As in the non-dissociative channel there is strong variation in the MFPADs over small NKE changes (especially in the $2p\sigma_u$, $2s\sigma_g$ channel). At these electron energies the first order Born-approximation holds, thus over so small changes in the electron energy no big changes are expected in the scattering wave function. Therefore one may think that the changes in the MFPADs are only due to the variations in the ground state of the molecule as the internuclear distance changes. Although the wave function is not an observable, all of this suggests the idea of using the MFPADs to somehow image a magnitude close related to the wave function. In the following we are going to explore this idea further.

4.2 H_2 wave function imaging

In a very simplified picture, the properties of a photoionization event, given by the ionization amplitude D, are determined by only three ingredients: the ground state of the system ϕ_0, which we want to image, the properties of the dipole operator $\hat{\boldsymbol{\mathcal{O}}}$ and the final state representing the remaining cation and a photoelectron with momentum $\mathbf{k}$, $\chi_{\mathbf{k}}$. The ionization amplitude within the *FNA* framework reads:

$$D(R) = \langle \phi_0(\mathbf{r}, R) | \mathbf{e}_\mu \hat{\boldsymbol{\mathcal{O}}}(\mathbf{r}) | \chi_{\mathbf{k}}(\mathbf{r}, R) \rangle \tag{4.4}$$

where $\mathbf{e}_\mu$ is the light polarization vector, $\mathbf{r}$ represents the electrons coordinates and R the internuclear distance. The ground state wave function is directly accessible provided that the other two constituents do not introduce significant distortions. As an illustration, let us consider the one-electron H_2^+ molecule. At high photoelectron energies, one can approximate the final state by a plane wave, $\chi_{\mathbf{k}}(\mathbf{r}) = e^{i\mathbf{kr}}$. Thus, if we consider circularly polarized light propagating along the z-axis and a molecule fixed along the x-axis (see figure 4.6 for notations), the transition amplitude can be written, in the velocity gauge:

$$D \propto \langle \phi_n(\mathbf{r}) | \frac{\partial}{\partial x} + i \frac{\partial}{\partial y} | e^{i\mathbf{kr}} \rangle = (-k_y + i k_x) \langle \phi_n(\mathbf{r}) | e^{i\mathbf{kr}} \rangle \tag{4.5}$$

Where the R dependence (now a parameter) is now implicit in all the equations. The corresponding photoionization cross section, differential in the electron emission angles and momentum (or MFPAD), is proportional to the square of the transition amplitude:

$$\frac{dP}{d(\cos\theta) d\varphi dk} \quad \propto \quad (k_x^2 + k_y^2) \left| \langle \phi_n(\mathbf{r}, R) | e^{i\mathbf{kr}} \rangle \right|^2 . \tag{4.6}$$

Here θ denotes the polar angle with respect to the molecular axis and φ the corresponding azimuthal angle. Restricting detection of the electrons to the plane containing the molecule and perpendicular to the light propagation direction ($\varphi = 90°$ and $270°$), the above expression reduces to:

$$\frac{dP}{d(\cos\theta) dk} = k^2 \left| \langle \phi_n(\mathbf{r}) | e^{i\mathbf{kr}} \rangle \right|^2 . \tag{4.7}$$

This expression is only applicable to differential probabilities in the (x, y) plane. It can be seen that the integral over $\mathbf{r}$ is proportional to the Fourier transform $\phi_n(\mathbf{k})$

of the $\phi_n(\mathbf{r})$:

$$\frac{dP}{d(\cos\theta)dk} = k^2(2\pi)^{3/2}\left|\frac{1}{(2\pi)^{3/2}}\int d\mathbf{r}\,\phi_n(\mathbf{r})e^{i\mathbf{kr}}\right|^2 \tag{4.8}$$

where we have introduced a $(2\pi)^{3/2}$ factor to make clearer this relationship, i.e.:

$$\frac{dP}{d(\cos\theta)dk} = k^2(2\pi)^{3/2}\left|\phi_n(\mathbf{k})\right|^2. \tag{4.9}$$

Thus, by choosing high photon energies and restricting measurement of the MFPAD to the polarization plane of the circularly polarized light, the ground electronic wave function is directly mapped onto the emitted photoelectron. Figure 4.10 illustrates this mapping procedure for the ground state of H_2^+. As can be seen from panel D, the measured MFPAD for an electron of 380 eV is very similar to $|\phi_0(\mathbf{k})|^2$ for the chosen momentum k (the square of the FT along the circumference shown in panel C). Note that, due to the smallness of the cross section at such high electron momentum, the main features of the FT are only apparent in the logarithmic plot shown in panel C.

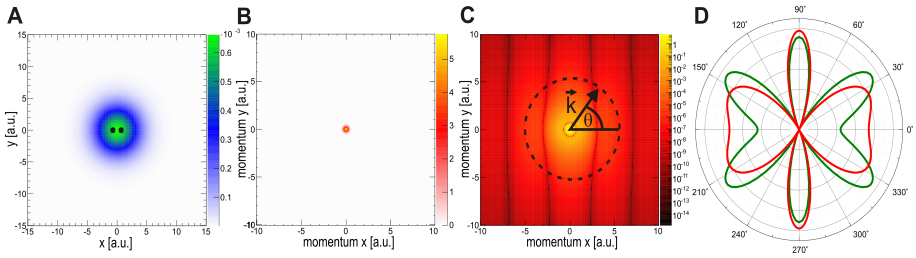

FIGURE 4.10: Imaging of the H_2^+ one-electron wave function. A) The electronic wave function of H_2^+ in the (x, y) plane for an internuclear distance $R = 1.4$ a.u. The position of the two nuclei are indicated by black dots. B) The square of the Fourier transform of A in the (k_x, k_y) plane. C) The same as B, but in logarithmic color scale. Notice the appearance of nearly vertical fringes when $|\vec{k}|$ is significantly different from zero. The approximate periodicity of these fringes is $\Delta k_x \sim 2\pi/R$. The circumference is the region of momentum space associated with an electron kinetic energy of 380 eV (i.e., a radius of $|\vec{k}| = 5.3$ a.u.) and θ is the angle with respect to the molecular axis. D) Polar plot of the intensity distribution along the circumference shown in panel C (red line) and the corresponding MFPAD in the plane of polarization of the ionizing radiation (olive line).

Let us now generalize this concept to the case of a correlated initial state as that of the H_2 molecule. The amplitude describing photoionization from the ground state, $\Psi_0(\mathbf{r}_1, \mathbf{r}_2)$, can now be written:

$$D = \langle \Psi_0(\mathbf{r}_1, \mathbf{r}_2) | \mathbf{e}_\mu \hat{\boldsymbol{\mathcal{O}}}(\mathbf{r}_1, \mathbf{r}_2) | \Phi_f(\mathbf{r}_1, \mathbf{r}_2) \rangle \tag{4.10}$$

where $\Phi_f(\mathbf{r}_1, \mathbf{r}_2)$ is the final continuum state. At high photoelectron energies, the latter can be approximately written as a product of an H_2^+ continuum wave function $\chi_{\mathbf{k}}(\mathbf{r}_2)$ that describes a photoelectron with linear momentum $\mathbf{k}$ and an H_2^+ bound wave function $\phi_n(\mathbf{r}_1)$ that describes the electron remaining in the ion:

$$D = \langle \Psi_0(\mathbf{r}_1, \mathbf{r}_2) | \mathbf{e}_\mu \hat{\boldsymbol{\mathcal{O}}}(\mathbf{r}_1, \mathbf{r}_2) | \phi_n(\mathbf{r}_1) \chi_{\mathbf{k}}(\mathbf{r}_2) \rangle. \tag{4.11}$$

We now write the fully correlated ground state wave function of H_2 as a linear combination of two-electron configurations expressed as antisymmetrized products of Hartree-Fock (HF) orbitals

$$\begin{aligned} \Psi_0 &= 1s\sigma_g^{HF}(\mathbf{r}_1) 1s\sigma_g^{HF}(\mathbf{r}_2) + c_1 2s\sigma_g^{HF}(\mathbf{r}_1) 2s\sigma_g^{HF}(\mathbf{r}_2) \\ &+ c_2 2p\sigma_u^{HF}(\mathbf{r}_1) 2p\sigma_u^{HF}(\mathbf{r}_2) + ... \end{aligned} \tag{4.12}$$

where we have factored out the antisymmetric spin wave function corresponding to a singlet multiplicity and $c_1, c_2 << 1$. The first term in this expansion represents the ground state of H_2 in the HF approximation,

$$\Psi_0^{HF} = 1s\sigma_g^{HF}(\mathbf{r}_1) 1s\sigma_g^{HF}(\mathbf{r}_2) \tag{4.13}$$

which includes screening and exchange but neglects electron correlation. Substituting equation 4.12 in 4.11, retaining the lowest-order non zero terms, and using equation 4.9, the MFPADs associated with the $1s\sigma_g$, $2s\sigma_g$ and $2p\sigma_u$, channels can be written (up to a trivial $k^2(2\pi)^{3/2}$ factor):

$$|\langle \Psi_0 | \mathbf{e}_\mu \hat{\boldsymbol{\mathcal{O}}} | 1s\sigma_g \, \chi_{\mathbf{k}} \rangle|^2 \simeq |\langle 1s\sigma_g^{HF} | 1s\sigma_g \rangle|^2 |\phi_{1s\sigma_g^{HF}}(\mathbf{k})|^2 \tag{4.14}$$

$$|\langle \Psi_0 | \mathbf{e}_\mu \hat{\boldsymbol{\mathcal{O}}} | 2s\sigma_g \, \chi_{\mathbf{k}} \rangle|^2 \simeq |\langle 1s\sigma_g^{HF} | 2s\sigma_g \rangle|^2 |\phi_{1s\sigma_g^{HF}}(\mathbf{k})|^2 \tag{4.15}$$

$$|\langle \Psi_0 | \mathbf{e}_\mu \hat{\boldsymbol{\mathcal{O}}} | 2p\sigma_u \, \chi_{\mathbf{k}} \rangle|^2 \simeq c_2 \langle 2p\sigma_u^{HF} | 2p\sigma_u \rangle|^2 |\phi_{2p\sigma_u^{HF}}(\mathbf{k})|^2 \tag{4.16}$$

where the dependence on $\mathbf{r}_1$ and $\mathbf{r}_2$ is now implicit in all equations. Hence, the partial differential cross sections are proportional to the representation of the ground-state HF orbitals in momentum space and to the overlap between these HF orbitals and the H_2^+ orbitals that define the different ionization thresholds. As can be seen, in the absence of electron correlation, i.e., when the initial state is simply described by Ψ_0^{HF} and therefore the c_i coefficients are zero, ionization can only

be direct (i.e., an electron is ejected into the continuum and the other remains in the $1s\sigma_g$ orbital, equation 4.14) or can be accompanied by excitation of the remaining electron into the $2s\sigma_g$ state (shake-up mechanism, equation 4.15). Ionization and excitation into the $2p\sigma_u$ state is only possible when c_2 is different from zero (equation 4.16), i.e., when electron correlation is not negligible.

To get additional information about the relative magnitude of the partial cross sections, we write the HF orbitals as linear combinations of H_2^+ orbitals. To first order of perturbation theory,

$$1s\sigma_g^{HF} = 1s\sigma_g + \lambda_1 2s\sigma_g + ... \tag{4.17}$$

$$2p\sigma_u^{HF} = 2p\sigma_u + \lambda_2 3p\sigma_u + ... \tag{4.18}$$

and so on, where $\lambda_i << 1$.

Substituting equations 4.17 and 4.18 in 4.14, 4.15 and 4.16, and retaining the lowest-order non zero terms in λ_i, one obtains the following simplified expressions for the above three ionization channels:

$$|\langle\Psi_0|\mathbf{e}_\mu\hat{\boldsymbol{\mathcal{O}}}|1s\sigma_g\,\chi_{\mathbf{k}}\rangle|^2 \simeq |\phi_{1s\sigma_g}(\mathbf{k})|^2 \tag{4.19}$$

$$|\langle\Psi_0|\mathbf{e}_\mu\hat{\boldsymbol{\mathcal{O}}}|2s\sigma_g\,\chi_{\mathbf{k}}\rangle|^2 \simeq \lambda_1|\phi_{1s\sigma_g}(\mathbf{k})|^2 \tag{4.20}$$

$$|\langle\Psi_0|\mathbf{e}_\mu\hat{\boldsymbol{\mathcal{O}}}|2p\sigma_u\,\chi_{\mathbf{k}}\rangle|^2 \simeq c_2|\phi_{2p\sigma_u}(\mathbf{k})|^2 \tag{4.21}$$

where we have used the fact that the H_2^+ orbitals form an orthonormal basis. As can be seen, the dominant mechanism is direct ionization from the $1s\sigma_g$ orbital (equation 4.19). Ionization with simultaneous excitation of the remaining electron (equations 4.20 and 4.21) is much less likely, since both λ_1 and c_2 are small. Ionization through other channels only contributes to second or higher order, thus explaining why they barely contribute to the ionization cross section (see figure 4.1). According to this simple formalism the MFPADs map the different orbitals in momentum space.

Summarizing, in order to map the wave function in momentum space the procedure is the following: Measure (or calculate) the fully differential photoionization cross section using circularly polarized light. For a specific NKE (or ε) select the electrons in the plane containing the molecular axis and polarization vector (equivalently obtain the MFPADs in this plane). A totally equivalent procedure would be: Obtaining the internuclear distance R corresponding to the same NKE, as we did in the previous section. Project the total wave function onto one of the ion orbitals, eliminating the coordinates of all of the electrons but one. Perform the Fourier transform, on the remaining coordinates, to momentum space. Select the distribution with the momentum such that $|\vec{k}| = \sqrt{2\varepsilon}$. The angular dependence of the selected momentum distribution must be in perfect agreement with

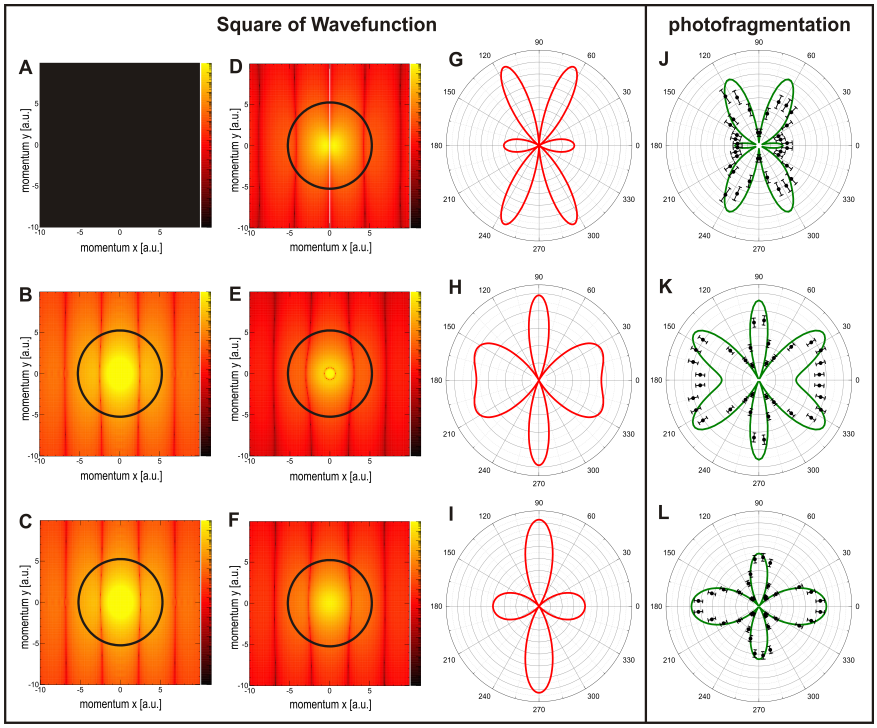

FIGURE 4.11: Correlation imaging of the H_2 two-electron wave function. A - F: momentum distributions of electron A resulting from the projection of the two electron wave function of H_2 onto different H_2^+ states of electron B; A - C: uncorrelated Hartree Fock wave function; D - F: fully correlated wave function. The different quantum states of electron B are $2p\sigma_u$ (A, D), $2s\sigma_g$ (B, E) , and $1s\sigma_g$ (C, F). Circumferences show $|\vec{k}| = 5.3$ a.u. (A, C) and $|\vec{k}| = 5.2$ a.u. (B), which correspond to ionization by a photon of $\hbar\omega$=400 eV energy. G - I: Intensity distributions along the circumferences shown in panels D - F. J - L: Experimental and theoretical MFPADs obtained after photoionization with circularly polarized photons of an energy of $\hbar\omega$=400 eV for the same final states of electron B measured in coincidence. Panels A - I have been calculated using the internuclear distances R mapping the NKE at which panels J - L correspond (see figure 4.12) for details.

the obtained MFPADs.

This tool of high energy photoelectron imaging can now be combined with

coincident detection of the quantum state of a second electron to visualize electron correlation in momentum space. We dissect the entangled two-electron wave function by analyzing a set of *conditional* angularly resolved cross sections corresponding to a high energy continuum electron (A) and a bound electron (B) detected in a different region of the two-electron phase space. Quantum mechanically, this is equivalent to projecting the initial two-electron wave function onto products of different H_2^+ (bound) molecular orbitals and a plane wave (as stated earlier). In doing so, one can thus determine if and how the density distribution of one electron changes upon changing the region of phase space in which one detects the other, correlated, electron.

Figure 4.11 illustrates the whole concept and highlights the differences between the uncorrelated Hartree-Fock wave function and the highly correlated wave function. The corresponding one-electron momentum distributions resulting from the projection of the corresponding ground state wave functions onto different states of the bound electron B, are depicted in figure 4.11 A - C (Hartree Fock) and figure 4.11 D - F (exact) as functions of the momentum components parallel ($k_{x,A}$) and perpendicular ($k_{y,A}$) to the molecular axis. The different rows correspond to the different states in which the second electron B is left after photoionization, i.e. they correspond, from bottom to top, to projections of the ground state wave function onto the n=1$s\sigma_g$, 2$s\sigma_g$, and 2$p\sigma_u$ states of H_2^+. Thus, as in our one-electron example shown in figure 4.10, the different panels in figure 4.11 contain direct images of different pieces of the ground state of H_2 through the square of the corresponding FTs. We note that imaging of electron A without determining the final state of electron B would correspond to a summation over all panels in a column. The role of electron correlation is quite apparent in this presentation: panel A is empty for the uncorrelated Hartree-Fock wave function, since projection of the latter wave function onto the $2p\sigma_u$ orbital is exactly zero, while this is not the case for the fully correlated wave function (panel D); also, panels B and C for the uncorrelated description are identical, while panels E and F for the correlated case are significantly different. As the photoionization process generates electrons of a certain energy (defined by the photon energy), it is not the complete conditional wave function of electron A which is mapped in the experiment. As in the example of figure 4.10 C, a fixed energy corresponds to points around the circumference of a circle. The density distributions pertaining to points around the circles of figure 4.11 A - F are shown in panels 4.11 G - I.

Experimentally, these conditional probabilities are obtained by measuring in coincidence the momentum of the ejected electron and the proton. Which, as explained below, allows to determine the final ionic state characterized by the quantum number n. Panels J to L in figure 4.11 depict the experimental results of the measured angular distributions of electron A and the corresponding ones resulting from our theoretical calculation of the photoionization process. As can be seen, the measured and calculated MFPADs shown in J - L are very similar to the calculated projections in momentum space of the ground state wave function

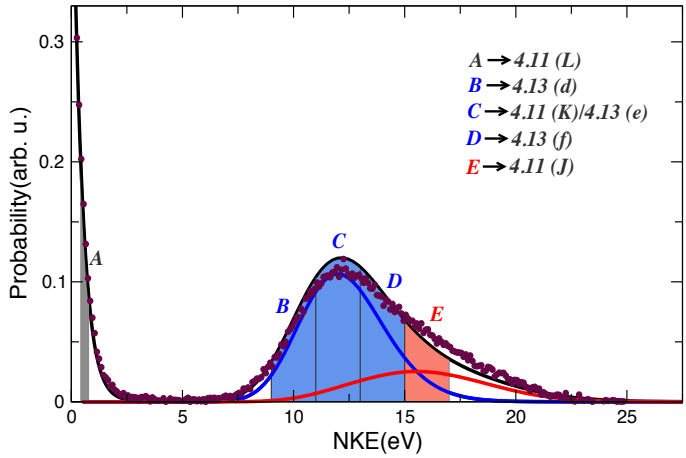

FIGURE 4.12: NKE distribution obtained using circularly polarized light. Maroon circles: experiment, Full lines: theory (Black: Total distributions, Red: $2p\sigma_u$ contribution. Blue: $2s\sigma_g$ contribution). The shaded areas indicate the regions of NKE selected in Figs. 4.11 and 4.13, *A*=(NKE=0.4-0.8 eV, *R*=1.05 a.u.), *B*=(NKE=9-11 eV, *R*=1.6 a.u.), *C*=(NKE=11-13 eV, *R*=1.4 a.u.), *D*=(NKE=13-15 eV, *R*=1.2 a.u.), *E*=(NKE=15-17 eV, *R*=1.4 a.u.).

shown in G - I. In other words, the momentum of the ejected photoelectron faithfully reflects and maps the momentum of a bound state electron in the molecular ground state when the momentum of the second bound electron is constrained by projection of the H_2 wavefunction onto different molecular-ion states. Note in particular panel G is not empty and panels H and I are not identical, as it would be for an uncorrelated H_2 ground state (compare with Panels A - C).

In more detail, the angular emission distributions and the final quantum state of electron B are obtained in the experiment by using the COLTRIMS technique [4, 5] in which the momenta of the charged particles generated by the photoionization process is measured in coincidence. As the singly charged molecule dissociates in the cases presented here into a neutral H atom and a proton, we can obtain the spatial orientation of the molecular axis by measuring the vector momentum of the proton (i.e. its emission direction after the dissociation). The electron emission direction in the molecular frame is then deduced from the relative emission direction of the proton and the vector momentum of the electron. Additionally, the magnitude of the measured ion momentum provides the nuclei kinetic energy (NKE) of the reaction. The latter enables an identification of the quantum state of electron B (i.e. the H_2^+ electronic state), which is demonstrated in figure 4.12.

Figure 4.12 shows the comparison between the measured and theoretically (figure 4.4 properly mixed and renormalized) NKE spectra. From the measured sum of the kinetic energies of the electron and the proton, the asymptotic electronic state of the neutral H fragment can be identified. Taking intervals of NKE instead of single points on the curve comes from the necessity of having enough counts to perform the experimental analysis.

The experimentally and theoretically obtained images show directly the imprint of correlation on the electronic wave function. It is solely due to electron correlation that the momentum distribution of electron A depends strongly on the properties of electron B. The most dramatic example can be seen by comparing the upper and middle rows in figure 4.11, which show electron A under the condition that electron B is detected in the $2p\sigma_u$ and $2s\sigma_g$ states of H_2^+, respectively. Upon this change in the selection of electron B, the maxima in the momentum distribution of electron A become minima and vice versa. This can be intuitively understood in coordinate space. The maxima in the k-space distribution correspond to the constructive interference of the part of the electron density close to one or the other nucleus spaced by R. Thus, inverting maxima to minima in k-space corresponds to a phase shift of π between the wave function at one or the other nucleus in coordinate space. For H_2, the two-electron wave function is gerade, i.e. it has the same sign of the overall phase at both centers. For the large part of the two-electron wave function, this symmetry consideration is also valid for each individual electron (it reflects the fact that both electrons occupy the $1s\sigma_g$ orbital most of the time). Therefore, both electrons have the same phase at both nuclei, which, in turn, is directly reflected in the maximum at $k_x = 0$ and the corresponding maximum in the direction perpendicular to the molecular axis in figure 4.10 E and F. Due to electron correlation, however, this is not strictly true for all parts of the wave function: Projecting electron B onto the $2p\sigma_u$ state highlights this small fraction of the wave function where electron A has the opposite phase at the two nuclei. As explained before, this part of the wave function does not exist for a Hartree Fock wave function and panel A in figure 4.10 is therefore empty. This phase change of the wave function between the nuclei leads to the nodal line through the center in figure 4.10 D and the nodes in panels G and J in the direction perpendicular to the molecular axis.

By plotting the momentum distributions in an narrower region of NKE we can investigate in more details of the two-electron wave function. The distributions in panels D - F of figure 4.11 show nodal lines that lead to corresponding nodes in the angular distributions in panels G - I. As mentioned above. these nodes in k-space are separated by $\Delta k_x = 2\pi/R$. Within the range of R covered by the Franck Condon region, the nodal structure of the electronic wave function changes significantly and figure 4.13 demonstrates how the k-space distribution of the two-electron wave function changes accordingly as a function of R. The

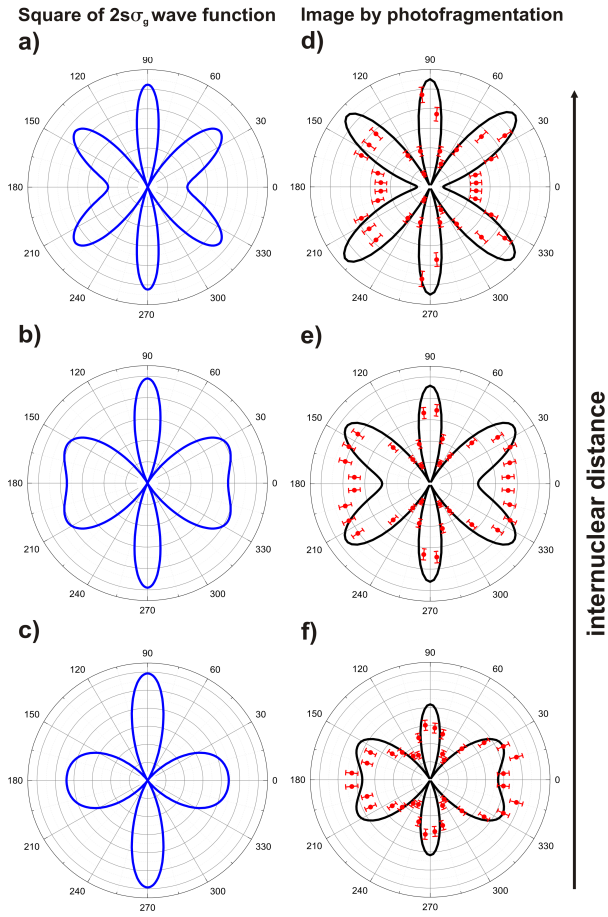

FIGURE 4.13: Dependence of the momentum distribution on the internuclear distance R of the molecule at the instant of photoionization. A to C: Square of the correlated wave function, as shown in figure 4.11 H, but for the NKE (internuclear distance) indicated in figure 4.12. Electron B is projected onto the $2s\sigma_g$ state while electron A is depicted. D to F: Images corresponding to A-C obtained by high energy photoionization, as in figure 4.10.

corresponding experimental and theoretical MFPADs resulting from high energy photoionization follow a similar pattern. Figures 4.11 and 4.13 support our previous claiming of figure 4.9 in the previous section. Thus by measuring the MFPADs at different NKE, we actually probe the momentum distributions of the ground

state wave function.

In a broader context, high energy angular resolved photoionization is a promising route to access molecular wave functions in momentum space. Combined with coincidence detection, it opens the door to image correlations in electronic wave functions. Similar approaches have also been proposed for imaging correlations in superconductors [87]. With the advent of X-Ray free electron lasers and the extension of higher harmonic sources to high photon energies, such correlation imaging bares the promise to make movies of the time evolution of electron correlations in molecules and solid materials.

Chapter 5

Molecular Clock

Photoionization of hydrogenic molecules (H_2, D_2) upon one XUV-photon absorption between $\hbar\omega$=25-44 eV, can also lead to a significant population of doubly excited states. The decay of quasi-bound (resonant) states immersed in the continuum of many-particle systems is one of the most common manifestations of intrinsic two-way interferences in Physics [88–90]. In atoms, resonant states generally show up as asymmetric peaks in the photo-absorption spectra [59, 91], in contrast with bound states, which always manifest as symmetric lorentzian peaks. The origin of the peak asymmetry is the interference between two processes that lead to the same photoelectron energy: direct ionization, which is a fast, almost instantaneous process, and autoionization, which is comparatively much slower, as it typically occurs in the few-femtosecond time scale. As shown by Fano in the early 60s [59], the shape of the resonant peaks, $\sigma(E)$, is completely determined by the resonance position, E_r, the autoionization width, Γ (i.e., the inverse of the resonance lifetime), and the so-called resonant profile (or Fano) parameter, q, through the well-known formula $\sigma(E)$=$\sigma_0(q+\varepsilon)^2/(1+\varepsilon^2)$, where $\varepsilon = 2(E-E_r)/\Gamma$ and σ_0 is a nonresonant background. Although first observed in the photoionization of rare gases [91], Fano profiles are not exclusive of atomic systems. They have also been seen in photoionization spectra of simple molecules (N_2, CO, etc) [92, 93], in scanning tunneling spectra of magnetic impurities lying on metal surfaces [94, 95], in plasmonic systems [96] and optical metamaterials [97, 98], and in matter-wave scattering occurring in Bose-Einstein [99, 100], to name a few examples. In all cases, the origin of the asymmetry is the same as in atoms: the interference between time-delayed processes leading to the same final state.

As a consequence of the delay between the *direct* and the *resonant* processes, the interference takes some time to fully set up. With the advent of attosecond techniques, it has recently been possible to monitor the birth and subsequent evolution of the electronic wave packets generated by atomic resonances, namely He [101], and hence to visualize the build-up of Fano asymmetric profiles with sub-femtosecond time resolution [102]. This has opened the door to the control of electron dynamics in atoms by acting on the time scale inherent to electronic motion.

However, when it comes to H_2, the prototype molecular system, the situation is much more complicated. First, because both the slow electron dynamics associated with autoionization and the fast nuclear dynamics associated with the proton motion occur in the same time scale, a few femtoseconds, so that the usual Fano picture is no longer applicable [103]. Second, because as a consequence of this, photoelectron spectra do not show any trace of resonant peaks [104, 105], and experiments can only uncover them by looking at the dissociative ionization channel ($H_2 \Rightarrow H+H^+ + e^-$) [106, 107], which however accounts for less than a few percent of the total photoionization cross section. And this by resolving the energy of the dissociating fragments, ideally in coincidence to fully access correlations between electronic and nuclear motions, which wears even smaller cross sections.

The combination of these two facts has prevented experimentalists from performing time resolved studies of H_2 autoionization, since the current attosecond pulses, which are required to provide the necessary time resolution, are too weak (much weaker than standard synchrotron radiation sources) to obtain dissociative ionization spectra in coincidence. A similar challenging scenario is expected for any molecule containing a significant proportion of hydrogen atoms.

The situation would be very much alleviated if one could extract time resolved information from the dominant non-dissociative channel. Although no resonance peaks are visible in the total non-dissociative photoionization spectra of H_2, theory has long ago predicted [108] that photoelectron spectra in which the vibrational state of the remaining H_2^+ ion is resolved (hereafter called v-spectra) do show resonance peaks associated with the H_2 doubly excited states (although they vanish when summing over all H_2^+ vibrational states). Furthermore, it has been recently demonstrated [109] that such v-spectra provide a time-energy mapping of autoionization, which can be efficiently used to time resolve the autoionization decay by looking at the population of the bound vibrational states of H_2^+. Hence, nuclear motion can directly provide the time reference and resolution that is required to image the H_2 autoionization dynamics without the need for ultrashort probe pulses as those used in current attosecond pump-probe experiments. In other words, nuclear motion can act as an internal probe of the ultrafast electron dynamics generated by the ionizing field.

Although v-spectra have been measured for many molecules in a wide range of photoelectron energies [30, 110–113], in the case of H_2 they have only been recorded at high photoelectron energies [30]. Therefore, there is no experimental evidence so far that H_2 resonance structures can indeed be resolved in the dominant non-dissociative channel, thus remaining as one of the fundamental unsolved problems in molecular photoionization.

In this work, we report vibrationally resolved photoelectron spectra of H_2 that clearly exhibit the signature of autoionizing states and fully resolve the shape of their corresponding resonant peaks. The fast nuclear motion in the ion internally tracks the autoionization event, and consequently, by using accurate vibrationally-resolved calculations in combination with synchrotron radiation measurements,

one can retrieve the time evolution of the decay process. This work also counts with an experimental counterpart, performed by Prof. S. E. Canton at ELI-ALPS, in Hungary.

5.1 Effects of autoionization on the non-dissociative ionization of H_2

Ionization of the H_2 molecule after absorption of a photon with an energy of $\hbar\omega\sim$30 eV proceeds via two paths (see figure 5.1). The first *direct* channel corresponds to leaving a vibrationally excited H_2^+ ion in the ground electronic $1s\sigma_g$ state. The second *resonant* channel corresponds to populating the $\mathcal{Q}$ series of doubly-excited states accesible by one-photon absorption. These states spontaneously decay into the electronic continuum associated to the ground electronic state of H_2^+ by emitting a photoelectron, through the process of autoionization (AI). The interference of the *direct* and the *resonant* ionization channels records their relative phases by mapping them into amplitude modulations of the population of vibrational state in the H_2^+ electronic ground state as a function of the absorbed energy.

In the particular case of weak fields, we can use first order time dependent perturbation theory, therefore we can retrieve the dipole transition elements (from the ground state to the continuum states) using the one-photon ionization amplitudes resulting from the solution of TDSE, through the following expression [114–116]:

$$C_{\alpha v_\alpha}^{\varepsilon_\alpha l_\alpha m_\alpha}(t=\infty) = -\frac{i}{\hbar}\langle \Psi_{\alpha v_\alpha}^{\varepsilon_\alpha l_\alpha m_\alpha}(\mathbf{r},R)|\mathbf{e}_\mu \hat{\boldsymbol{\mathcal{O}}}|\Psi_0(\mathbf{r},R)\rangle \mathcal{F}(\omega_{ik},\omega,\tau) \tag{5.1}$$

$$\hbar\omega_{ik} + E_0 = E_{v_\alpha} + \varepsilon_\alpha \tag{5.2}$$

$$\mathcal{F}(\omega_{ik},\omega,\tau) = \int_0^\tau A(t) e^{-i\omega_{ik}t} dt \tag{5.3}$$

$$\mathcal{F}(\omega_{ik},\omega,\tau) = \frac{-2i\pi^2 A_0}{(\omega_{ik}-\omega)[4\pi^2 - (\omega_{ik}-\omega)^2\tau^2]} \sin\left[\frac{(\omega_{ik}-\omega)\tau}{2}\right] \tag{5.4}$$

Where $\mathcal{F}(\omega_{ik}, \omega, \tau)$, ω and τ stands for for the Fourier transform, the central frequency and the duration of the laser pulse respectively, $\mathbf{e}_\mu$ is the light polarization vector and $\hat{\mathcal{O}}$ is the dipole operator. From the dipole couplings is straightforward to get the vibrationally resolved photoionization cross section, for randomly oriented molecules:

$$\sigma_{v_\alpha}(\varepsilon_\alpha) = \frac{4\pi^2\omega_{ik}}{3c} \sum_{\mu m_\alpha l_\alpha} |\langle \Psi^{\varepsilon_\alpha l_\alpha m_\alpha}_{\alpha v_\alpha}(\mathbf{r}, R)|\mathbf{e}_\mu \hat{\mathcal{O}}|\Psi_0(\mathbf{r}, R)\rangle|^2 \tag{5.5}$$

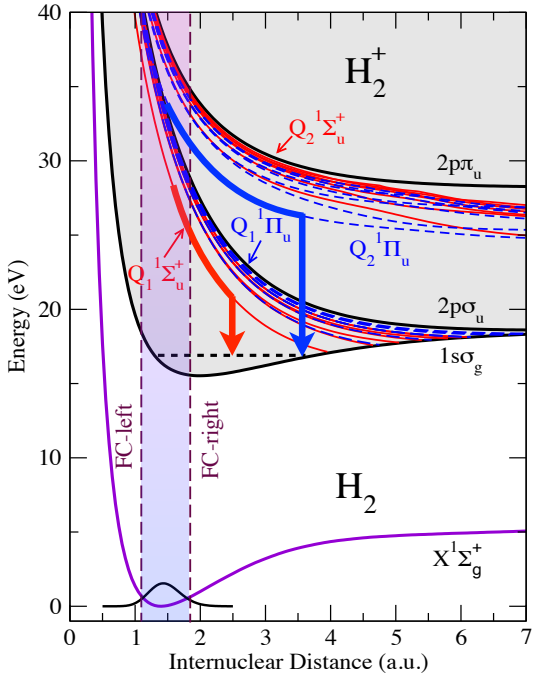

FIGURE 5.1: Potential energy curves of H_2. The figure display the ground state of the molecule. Above the first ionization threshold ($1s\sigma_g$) and below the second ($2p\sigma_u$), within the grey area, the $\mathcal{Q}_1{}^1\Sigma_u^+$ (full red line) and the $\mathcal{Q}_1{}^1\Pi_u$ (dashed blue line) series of doubly excited states are shown. Lying between the second ionization threshold and the third ($2p\pi_u$) the series $\mathcal{Q}_2{}^1\Sigma_u^+$(full red line) and the $\mathcal{Q}_2{}^1\Pi_u$ (dashed blue line) are also shown. The FC region is enclosed within the two vertical lines.

The coefficients $C^{\varepsilon_\alpha l_\alpha m_\alpha}_{\alpha v_\alpha}$ results from the solution TDSE for a T=200 as duration XUV pulse with an intensity of I=10^{12} W/cm^2. The multichannel expansion includes the two lowest ionic states ($1s\sigma_g$, $2p\sigma_u$) and partial waves for the emitted electron up to a maximum angular momentum l=7 enclosed in a box of r_{max}=60 a.u.. The one-electron orbitals for the bound electron are consistently computed in the same radial box using single-center expansions with corresponding angular momenta up to l=16. The first two series of resonances $\mathcal{Q}_1$ and $\mathcal{Q}_2$ have been included. Figure 5.2 show the contributions of $^1\Sigma_u^+$ and $^1\Pi_u$ symmetries to the vibrationally resolved cross section. In particular, the cross section values in the parallel symmetry are in very good agreement with those presented in [108, 117] obtained by a time-independent method. The effect of the doubly excited states is obvious for all v and for both symmetries. In this regard the are few points worth noticing here. The widths of the resonant peaks in the spectra are much broader than those obtained in the *FNA* framework at the equilibrium distance [60, 61]. The increase in the cross section due to the interference with the *resonant* channel is invalidated by the much quicker decrease of the *direct* channel, thus the peaks are less evident than in the atomic photoionization. The position of the peaks shift towards higher photon energies as v increases (the larger the v the larger the photon energy necessary to populate the doubly excited states), due to the systematic change no resonances evidence would be observed for the vibrationally unresolved spectra. It is clear that all the mentioned features are consequence of adding the nuclear degrees of freedom, in fact changing the value R guarantees that the resonance conditions can be achieved by photons of different energies. Therefore, the width of the resonance peaks is given by combination of the width of the resonance and FC factor, this effect can not be reproduced in the *FNA* since it neglects the nuclear degree of freedom leading to unphysical structures in the cross section.

The resonance effects in the $^1\Pi_u$ symmetry appear at much higher photon energies. This would indicate that although we are including in the calculations all the $\mathcal{Q}_1$ and $\mathcal{Q}_2$ series of resonances in both symmetries, the source of the interference is the $\mathcal{Q}_2\,^1\Pi_u$, in contrast with the $^1\Sigma_u^+$ symmetry where the source is the $\mathcal{Q}_1\,^1\Sigma_u^+$ [108, 117]. In fact by simple inspection of the partial width of each resonance [60, 61] the $\mathcal{Q}_1\,^1\Pi_u$ width is much smaller than the width of the $\mathcal{Q}_1\,^1\Sigma_u^+$ and the latter is only comparable in magnitud to those of the $\mathcal{Q}_2\,^1\Pi_u$ decaying to the $1s\sigma_g$ ionization threshold. So we can conclude that the observed structures are consequence of the autoionization of the lowest $\mathcal{Q}_1\,^1\Sigma_u^+$ and $\mathcal{Q}_2\,^1\Pi_u$ doubly excited states of H_2. The corresponding potential energy curves are shown in figure 5.1. These series of states respectively converge to the second and third ionization thresholds of H_2, and can therefore decay by directly emitting an electron and leaving H_2^+ in the ground electronic state $1s\sigma_g$. Decay of $\mathcal{Q}_2$ states can also be accompanied by excitation of the remaining electron to the $2p\sigma_u$ excited state of H_2^+, which is entirely repulsive and therefore does not contribute to the non-dissociative ionization channel.

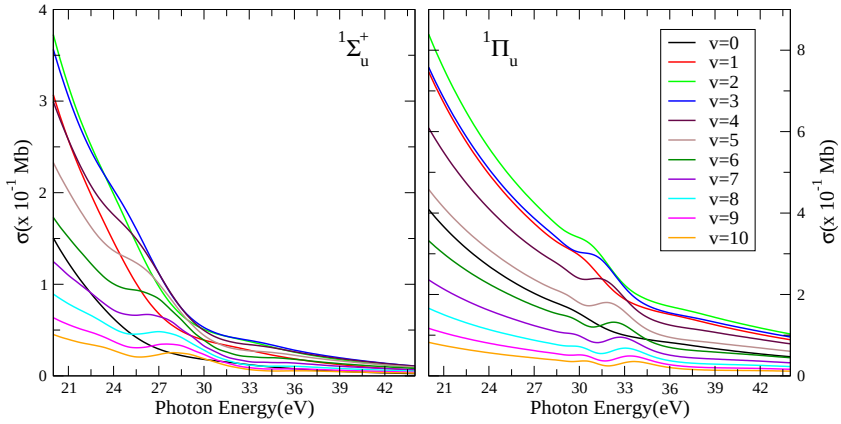

FIGURE 5.2: Vibrationally resolved photoionization spectra of H_2. Results for both $^1\Sigma_u^+$(left panel) and $^1\Pi_u$(right panel) final symmetries are shown.

Although the effects of doubly excited states is clearly visible in the cross section, from the experimental point of view is easier to look at other magnitudes since the cross section decrease quickly with the photon energy, by using the v-ratios you remove the quick decreasing background. In previous works the v-ratios have been used to observe the Young's double slit interferences in diatomic molecules [30]. Figure 5.3 shows the measured and calculated vibrationally resolved photoelectron spectra referred to the spectrum for the dominant ionization channel $H_2+\hbar\omega \Rightarrow H_2+(v{=}2)+e^-$, for randomly oriented molecules. Very prominent features with clearly distinct profiles are observed for photon energies between 24 and 37 eV, in clear contrast with the featureless vibrationally unresolved photoelectron spectrum available in the literature (and in clear agreement with those in figure 5.2). The agreement between the experiment and theory is very good, and the latter is in good agreement with the results presented in [117, 118]. As we said the observed structures are assigned to autoionization from the lowest $\mathcal{Q}_1\,^1\Sigma_u^+$ and $\mathcal{Q}_2\,^1\Pi_u$ doubly excited states, thus confirming the effects of the doubly excited states in the non-dissociative ionization channel. As the molecules are randomly oriented with respect to vector polarization of the light a combination of the effects coming from both resonant states are present in the same spectrum, to highlight this point figure 5.4 depicts a comparison between the v-ratios for randomly oriented molecules and those for each individual symmetry. It can be seen that structures between 32-36 eV are strictly coming from the AI of $\mathcal{Q}_2\,^1\Pi_u$ while those appearing in 25-35 eV region correspond to the AI of $\mathcal{Q}_1\,^1\Sigma_u^+$. As we

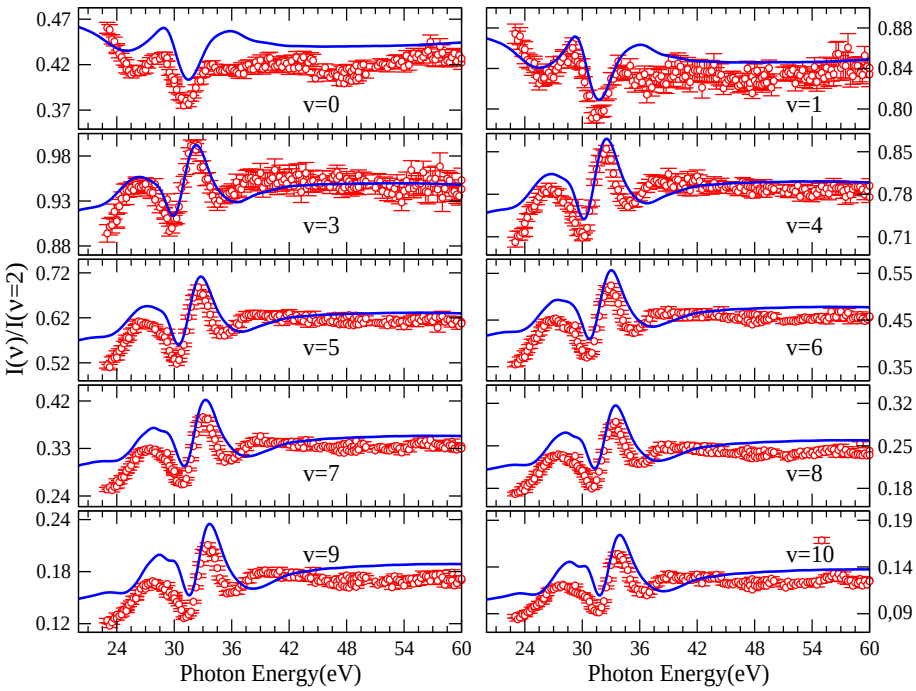

FIGURE 5.3: Ratios of the vibrationally photoionization spectra to the v=2 cross section as a function of the photon energy. Red circles with error bars: experimental results. Full blue curve: theoretical results.

stated earlier, the doubly excited states in each symmetry appear at different photon energies. Therefore, for each symmetry the *resonant* channel interfere with the *direct* channel in different regions of the spectra, allowing to assign the features to one or the other series of doubly excited states.

5.2 Analytical-Model

The time evolution of the coherent superposition of *resonant* and *direct* channel can be retrieved by using an extension of the Fano formalism that incorporates the effect of nuclear motion in a semiclassical way and on an equal footing with electronic motion. For this end we use our previously developed model (see [109] for details). In brief, we start from the *local-approximation* [119–121] and use the semi-classical approach for the wave-packet moving along the potential energy

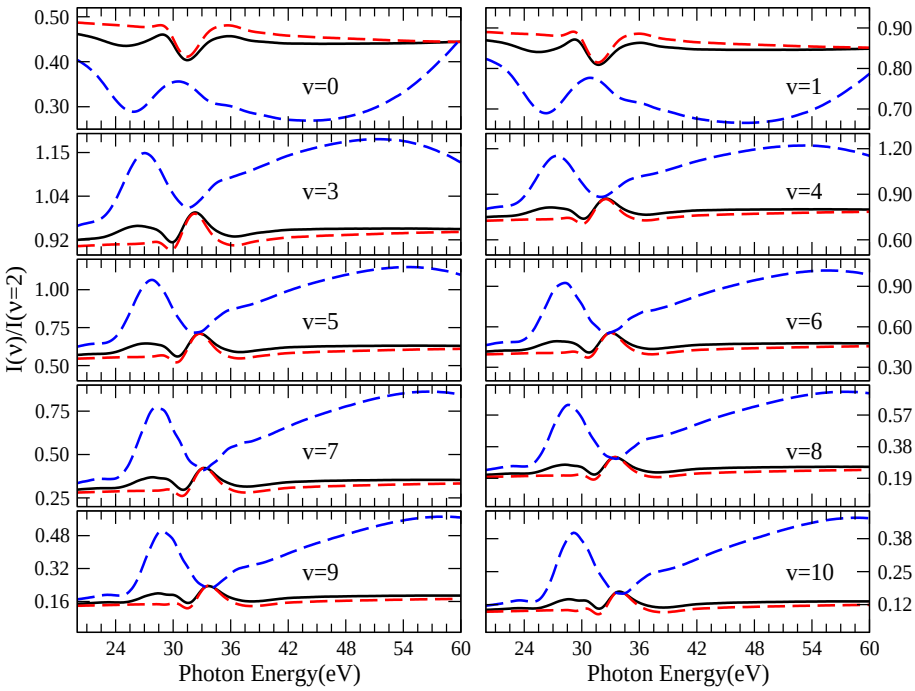

FIGURE 5.4: Same as figure 5.3 but this time we show the contributions of each symmetry. Dashed red curve: ${}^1\Sigma_u^+$ contribution. Dashed blue curve: ${}^1\Pi_u$ contribution and Full black curve: total ratio.

curve of the doubly excited. Under this circumstances the wave-packet can be written as:

$$\chi_Q(R,t) = B(t)e^{iS(R,t)} \qquad \int |\chi_Q(R,t)|^2 dR = 1 \tag{5.6}$$

Where $B(t)$ normalizes the wave-packet to the unity, plugging this anzats into the TDSE for the vibrational motion along the potential energy curve of the doubly excited leads to a Hamilton-Jacobi equation for the phase $S(R,t)$.

$$-\frac{\partial S}{\partial t} = \frac{1}{2m_\mu}\left(\frac{\partial S}{\partial R}\right)^2 + V_r(R) \tag{5.7}$$

where m_μ is the reduced mass. Expanding the potential energy curve $V_r(R)$ and the $S(R,t)$ phase in a Taylor series around the classical trajectory, and keeping up to the second order (only to have a gaussian wave-packet which is good approximation for the ground vibrational state):

$$V_r(R) = V_r(R_{cl}) + \left.\frac{dV_r(R)}{dR}\right|_{R_{cl}} (R - R_{cl}) + \frac{1}{2}\left.\frac{d^2V_r(R)}{dR^2}\right|_{R_{cl}} (R - R_{cl})^2 \tag{5.8}$$

$$S(R,t) = S_{cl}(t) + P_{cl}(t)(R - R_{cl}) - \frac{1}{2}\sigma(t)(R - R_{cl})^2 \tag{5.9}$$

Here $P_{cl}(t)$ and its canonical conjugated $R_{cl}(t)$ dictate the classical trajectory along the potential energy curve (Newton's equation solution), $S_{cl}(t)$ is classical action and $\sigma(t)$ is the time dependent width of the wave-packet. Using equations 5.7, 5.8 and 5.9 we get the following expression for the wave-packet:

$$\chi_Q(R,t) = \left(\frac{\Re(\sigma(t))}{\pi}\right)^{1/4} \exp\left\{iS_{cl} + i(R - R_{cl})P_{cl} - \frac{1}{2}(R - R_{cl})^2\sigma(t)\right\} \tag{5.10}$$

Where $\sigma(t)$ is:

$$\sigma(t) = \sqrt{\mu\alpha(t)}\frac{1 + C\exp(-i\sqrt{4\alpha(t)t/\mu})}{1 - C\exp(-i\sqrt{4\alpha(t)t/\mu})} \qquad C = \frac{1 - \sqrt{\mu\alpha(t)}X_0^2}{1 + \sqrt{\mu\alpha(t)}X_0^2} \tag{5.11}$$

Where X_0 is a parameter related with the width of the wave-packet a time zero and $\alpha(t)$ is the curvature of the potential evaluated at each time step.

$$\sigma(t=0) = \frac{1}{X_0^2} \qquad \alpha(t) = \frac{d^2V_r(R_{cl}(t))}{dR^2} \tag{5.12}$$

Taking into account the width of the doubly excited state, the wave-packet acquire a complex component:

$$\chi_{\Gamma Q}(R,t) = \chi_Q(R,t)\exp\left\{-\frac{1}{2}\int_0^t \Gamma_r(R_{cl}(t'))dt'\right\} \tag{5.13}$$

$$\Gamma_r(R) = 2\pi\sum_{\alpha l_\alpha} |\langle\hat{\mathcal{P}}\psi_{\alpha l_\alpha}^{\varepsilon_\alpha=\varepsilon_r}(\mathbf{r},R)|\hat{\mathcal{P}}\hat{\mathcal{H}}_{el}\hat{\mathcal{Q}}|\psi_r(\mathbf{r},R)\rangle|^2 \tag{5.14}$$

Where $\Gamma_r(R)$ is the width of the doubly excited state [60, 61] in which the wave-packet is moving through. In figure 5.5 the wave-packet $\chi_{\Gamma Q}(R,t)$ in each symmetry is depicted. It can be seen a decrease in the population, due to the AI, the rate of decrease is obviously conditioned by the value of the width (and the value of the integral in exponent of 5.13). After t=2 fs there is not any significant changes in the wave-packets (in the parallel case it is almost depleted), therefore we should expect that all the interferences between the *direct* and *resonant* channels to set up in less than this time. The population of a given vibrational state after the ionization can be found as a coherent superposition of the contributions of the *direct* channel and the *resonant* channel:

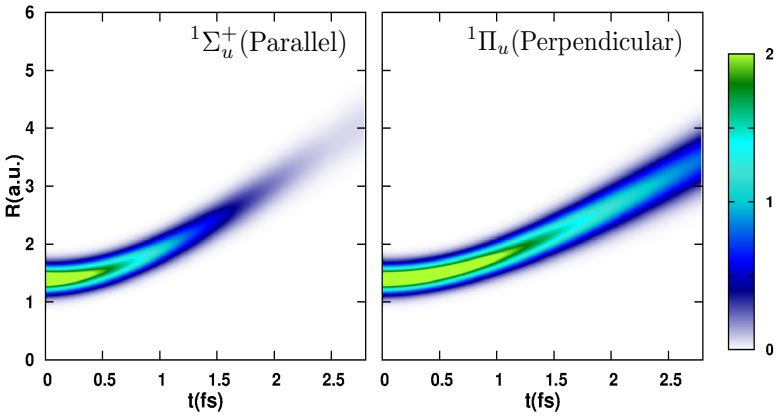

FIGURE 5.5: Nuclear wave-packet 5.13 moving through the potential energy curves of the doubly excited states.

$$a(v,\varepsilon) = |a_v^d(\varepsilon, t=\infty) + a_v^\Gamma(\varepsilon, t=\infty)|^2 \tag{5.15}$$

Where the *direct* a_v^d and the contribution coming from the *resonant* a_v^Γ are calculated as:

$$a_v^d(\varepsilon, t=\infty) = \int \chi_v(R)\langle\psi_{\alpha l_\alpha}^{\varepsilon_\alpha}(\mathbf{r},R)|\mathbf{e}_\mu\hat{\boldsymbol{\mathcal{O}}}|\psi_b(\mathbf{r},R)\rangle\chi_b(R)dR \tag{5.16}$$

$$a_v^\Gamma(\varepsilon,t) = \langle\psi_r(\mathbf{r},R_0)|\mathbf{e}_\mu\hat{\boldsymbol{\mathcal{O}}}|\psi_b(\mathbf{r},R_0)\rangle\int_{t_0}^{t} e^{i(E_v+\varepsilon)t'}\mathcal{I}_v^\Gamma(t')dt' \tag{5.17}$$

$$\mathcal{I}_v^{\Gamma}(t) = \int \chi_v(R)\sqrt{\frac{\Gamma_r(R)}{2\pi}}\chi_{\Gamma Q}(R,t)dR \tag{5.18}$$

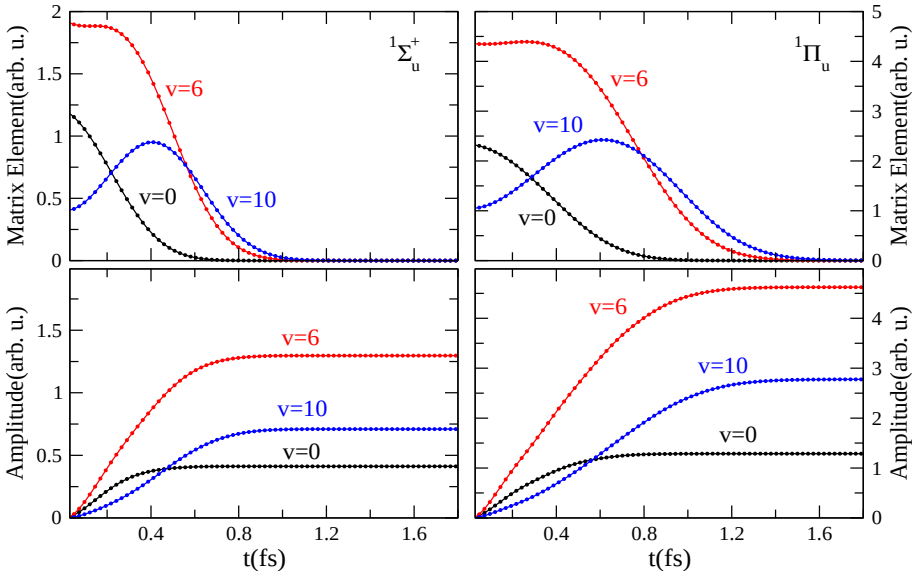

FIGURE 5.6: In the upper panel the matrix elements 5.18 are shown. In the lower panels the amplitude 5.17 integrated over electron energy are shown.

Here R_0 is the equilibrium distance of the system. In the implementation of the model we only include only one channel for photoionization (l=1) and the first resonance of each series. In figure 5.6 the values of $\mathcal{I}_v^{\Gamma}(t)$ and $a_v^{\Gamma}(\varepsilon,t)$ are shown, for different vibrational states, in the upper and lower panels respectively, the values of $\mathcal{I}_v^{\Gamma}(t)$ represent a distribution in time, suggesting that by taking the mean value of the distribution we can assign to each vibrational state a time at which the AI is much likely to occur. Those matrix elements reflects the dynamics on the resonant state during this specific time window. This can be considered as *molecular clock* and could in principle be used to recover the vibrational dynamics of the AI, this idea have been explored in [122] and we will try to go a little bit further. Meanwhile from both magnitudes we can confirm that around t∼2 fs the AI is not playing any role. The selection of which of the resonances include in the model can be discerned from a simple inspection to the autoionization width and the full ab-initio spectrum. Implementation of the model requires the following ingredients:

– Potential energy curve of the doubly excited states.

– Width of the doubly excited states.

– Dipole coupling between the ground state, the doubly excited state and continuum states.

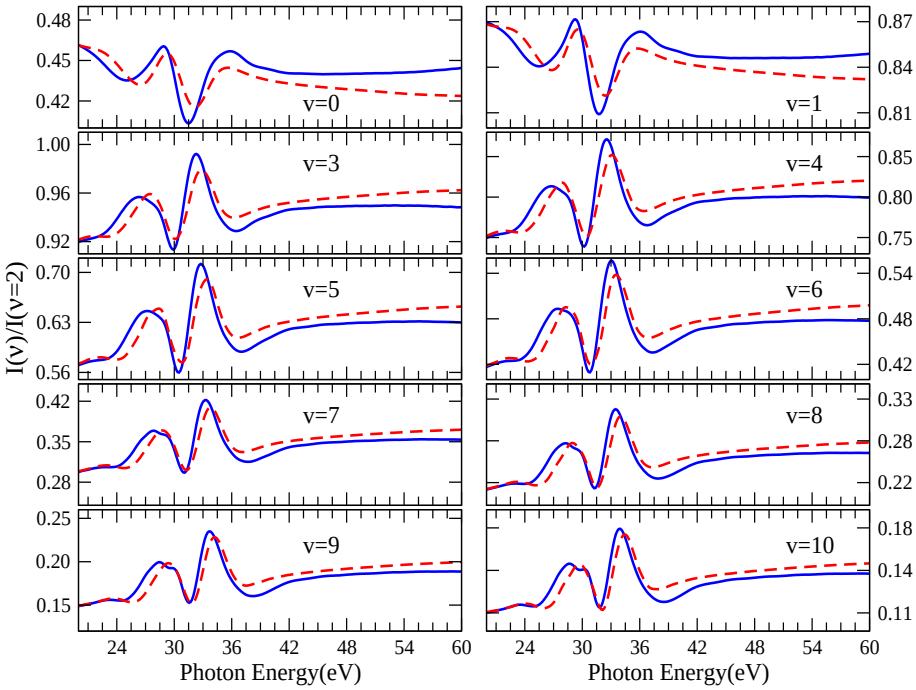

FIGURE 5.7: Same as figure 5.3 but this time we show the results from the model. Dashed red curve: Results from the model. Full blue curve: Full ab-initio calculation.

The validity of this model has been demonstrated by comparing with results obtained with full ab-initio calculation. In figure 5.7 such comparison is presented, as we can see the quality v-ratios obtained with the analytical model is excellent, capturing the main features in the spectrum. The differences are related with the fact we only include a single partial wave in the continuum and more important only the resonance with the highest width, moreover we are neglecting the electronic phase in equation 5.18 by taking the width of the resonance instead of the actual $\boldsymbol{\mathcal{Q}\mathcal{H}}_{el}\boldsymbol{\mathcal{P}}$ coupling. Neglecting all the others resonances has an effect in the

spectrum, like for instance make the peaks more narrower than it should be. Although we used the dipole coupling between the ground state and continuum to reproduce the *direct* component this can be estimated from other procedures like fitting or/and extrapolation. The width can also be fitted knowing a-priori the width in united atom limit (UA) limit alongside the experimental data. Taking into account the simplicity of the model, the agreement with ab-initio calculations is remarkably good. The model, with just a handful of ingredients, properly describes the interference process between the *direct* and *resonant* channels, thus allowing to follow the evolution of the coherent superposition of *resonant* and *direct* channel in time without solving the TDSE.

5.3 Time evolution of the interference patterns

As the autoionization decay takes a few femtoseconds, the nuclei have enough time to move following the corresponding repulsive potential energy curves before the electron is emitted (see the red and blue paths shown in figure 5.1). As a consequence, the populated doubly excited states can efficiently ionize over a wide range of internuclear distances, from the FC region up to well outside this region, thus leading to a broad distribution of $H_2^+(1s\sigma_g)$ vibrational states. In general, the slower the autoionization, the higher the vibrational state in which H_2^+ is left, since the nuclear wave packet evolving on the repulsive $\mathcal{Q}_1$ and $\mathcal{Q}_2$ potential energy curves can reach longer and longer internuclear distances where it can efficiently overlap with higher and higher vibrational states of $H_2^+(1s\sigma_g)$. Therefore, by vibrationally resolving the final state of the remaining H_2^+ ion, one has access to the dynamics of the autoionization decay. In other words, nuclear motion acts as an internal clock that can be used to extract dynamical information about this decay.

By using the analytical model with all the ingredients from the ab-initio calculation, we have thus reconstructed the time evolution of the interference patterns in the vicinity of each resonance. This procedure resembles that followed by Gruson et al [101] in the He atom, except for the fact that the present reconstruction model incorporates the effect of the nuclear dynamics, which is essential to correctly account for the phase evolution of the electronic wave packet. The other important difference is that here the phase information is not retrieved by using an ultrashort light pulse, but from the internal probe provided by the nuclear motion. The results of this reconstruction procedure for the $\mathcal{Q}_1\,^1\Sigma_u^+$ and $\mathcal{Q}_2\,^1\Pi_u$ resonances are shown in figures 5.8 and 5.9. Therefore one can indeed obtain accurate amplitude and phase information about the autoionizing electronic wave packet by vibrationally resolving synchrotron radiation calculations (measurements) performed in a wide range of photon energies and with enough energy resolution to access all the resonance features. It is important to emphasize that, due to the dipole selection rule that operates under the present conditions, the $\mathcal{Q}_1\,^1\Sigma_u^+$

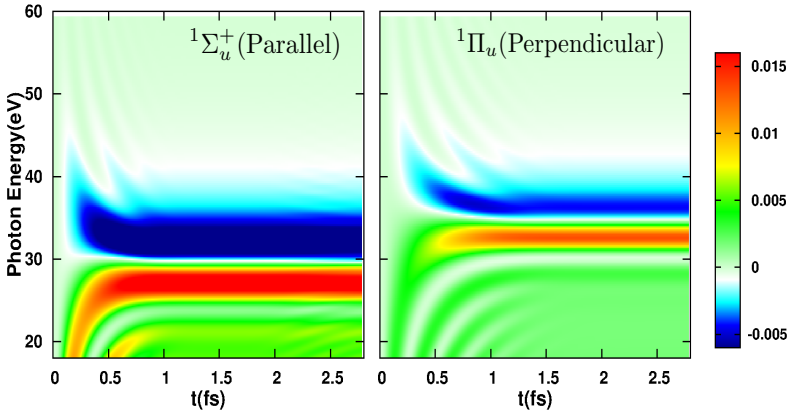

FIGURE 5.8: Build-up in time of the interference resulting from the *direct* and the *resonant* channels for the decay of the lowest $\mathcal{Q}_1\,^1\Sigma_u^+$ (left panel) and the lowest $\mathcal{Q}_2\,^1\Pi_u$ doubly excited state (right panel). Total effective photoionization cross sections, after subtraction of the smooth background associated to the direct channels, i.e. $a(v=5,t)-a(v=5,t=0)$ (see equation 5.15). The effective cross sections are plotted as a function of photon energy (y-axis) and time (x-axis).

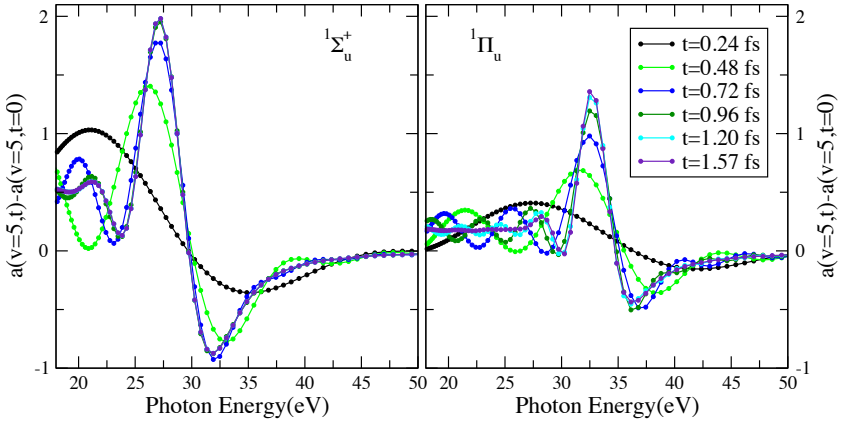

FIGURE 5.9: Slices in time of the figure 5.8, again the decay of the lowest $\mathcal{Q}_1\,^1\Sigma_u^+$ (left panel) and the lowest $\mathcal{Q}_2\,^1\Pi_u$ doubly excited state (right panel) are shown.

and $\mathcal{Q}_2{}^1\Pi_u$ reconstructions correspond to the actual wave packets resulting from molecules oriented parallel and perpendicular to the polarization direction of the synchrotron radiation field, respectively.

Figures 5.8 and 5.9 show that the interference patterns in both symmetries experience dramatic changes during the first femtosecond, with the appearance of more and more nodes as time passes. After this, some of the nodes disappear and at around t=2 fs there are no more significant changes. Therefore, all the interferences resulting from the coupled electron and nuclear dynamics associated with the autoionization decay set up in less than t=2 fs, as we already stated. Although we only show the results corresponding to the v=5 vibrational state all the remaining vibrational states show a similar behavior. One can now compare these results with those recently obtained for the 2s2p^{1}P^0 resonance of He [101], to which the $\mathcal{Q}_1{}^1\Sigma_u^+$ and $\mathcal{Q}_2{}^1\Pi_u$ resonances correlate in the UA limit (R=0). A noticeable difference with the atomic case is that the calculated ionization rate profiles do not follow the standard Fano picture, since they exhibit at least two maxima and two minima (even more at very short times). This is the consequence of the coupling with nuclear motion, which is not present in atomic systems (or molecular systems with heavy atoms). Another interesting result is that the evolution of the $\mathcal{Q}_1{}^1\Sigma_u^+$ and $\mathcal{Q}_2{}^1\Pi_u$ wave packets is different. This is the consequence of the breaking of the spherical symmetry in the molecular case, which leads to different autoionization widths Γ_r for the two resonances. As a consequence, interferences in the $^1\Sigma_u^+$ symmetry evolve faster and the stationary regime is reached earlier when compared with $^1\Pi_u$ symmetry.

In summary, from accurate vibrationally resolved photoelectron spectra, we have been able first to identify the long-awaited signature of H_2 doubly excited states in the non dissociative ionization channel, and then to reconstruct the time evolution of the interference between the *direct* and *resonant* channels in the vicinity of the lowest $\mathcal{Q}_1{}^1\Sigma_u^+$ and $\mathcal{Q}_2{}^1\Pi_u$ doubly excited states by exploiting a very simple semi-classical. Both the time resolution and the phase information necessary for the reconstruction are imprinted in the nuclear motion that follows the excitation by the UV field. Thus, nuclear dynamics acts as an internal probe of the system, in contrast with usual pump-probe schemes in which the probing is performed by using an (external) ultrashort pulse. For the reconstruction to be experimentally feasible, one must have some a priori knowledge of the molecular system under investigation, namely of the potential energy curves (surfaces) of the ground and quasibound states embedded in the continuum, from which the vibrational wave functions can be estimated. In general, this is not difficult for small and medium size molecules, since a plethora of commercial (friendly user) quantum chemistry packages for bound state calculations can provide this information with high accuracy. With this, one can retrieve from experiment the autoionization width as a function of molecular geometry by means of a simple

semi-classical model, and hence reconstruct the time dependent wave packet.

In principle, the method should be applicable to any molecule containing hydrogen atoms, since they move fast and therefore can be used as an internal clock of the system. Measuring vibrationally resolved photoelectron spectra of molecules with high energy resolution is a standard practice in nowadays synchrotrons, so they could be used as complementary tools to attosecond and few-femtosecond pump probe techniques to get dynamical information of the ultrafast autoionizing decay of molecules. Furthermore, by performing isotopic substitution, e.g., by replacing atomic hydrogen by deuterium, one could also exert some control on the timing of the autoionization decay, since the nuclear mass determines the velocity of the nuclear wave packet that is created. Implementation of the present reconstruction method in more complex hydrogen-containing molecules, such as water or ammonia, should be the next step towards understanding autoionization dynamics in molecules of chemical interest.

Part III

UV pump-IR probe techniques

Chapter 6

Mapping highly D_2^+ using ultrashort XUV pulses

In this chapter, we aim to explore the relevance of electron-electron correlations in the dissociative photoionization of D_2 leading to a highly excited D_2^+ molecule. In order to experimentally access these correlation effects, it is necessary to first trigger the dynamics with an XUV ultrashort radiation source and then use a time-delay probe to obtain an image resolved in time. The most widely employed strategy to trace the ultrafast electron (and coupled nuclear) dynamics in atoms (and molecules) is the use of XUV-pump/IR-probe techniques [15–17, 101]. The use of an IR field as a probe is mostly due to the experimental availability, since most experiments use as a probe the same seeding IR field that produce the attosecond pulses (by means of HHG). In this context, we aim to determine the branching ratios for the different dissociative ionization channels associated with this molecular shake-up process as a function of the molecular orientation with respect to the laser polarization. A short, high-harmonic pulse first ionizes the neutral molecule, which is excited into high-lying dissociative electronic states of the parent ion. Although most of the D_2^+ molecules are left in the ground state of the ion, a small fraction of them undergoes excitation-ionization, where a second electron is excited simultaneously during the photoionization process. Such a process is impossible without electron-electron correlation. By using a time-delayed infrared probe pulse we map the energy distributions of the molecular fragments.

This is also a joint experimental and theoretical work, performed together with Prof. P. Ranitovic at ETH in Zurich, who performed the time-resolved measurements and Prof. R. Dörner at Institut für Kernphysik in Frankfurt, who provided the synchrotron radiation data.

We use a 42.6 eV XUV ultrashort pump pulse, synchronized with a probe IR laser (784 nm) to first excite, and then map the dynamics of the highly excited molecular ion. The absorption of the XUV pulse ionizes the neutral D_2 molecule, creating a superposition of highly excited electronic states in the molecular ion, as

shown in figure 6.1. The excited D_2^+ ion can then dissociate along several coherently populated pathways, upon the XUV photoionization, leading to D^++D(n=1) (corresponding to the $1s\sigma_g$ and $2p\sigma_u$ molecular states) and D^++D(n=2) (corresponding to $2p\pi_u$, $2s\sigma_g$, $3p\sigma_u$, $3d\sigma_g$, $3d\pi_g$, $4f\sigma_u$). As the molecular ion dissociates, with the nuclei following the steep potential energy curves of the D_2^+ states, the fragmentation dynamics is mapped by ejecting the second electron using a strong IR laser field. The delayed arrival of the IR pulse interrupts the dissociation process $D_2^+ \Rightarrow D^+$+D(n) at a specific time, by ejecting the second electron and leaving behind two bare deuterons that undergo Coulomb explosion. The latter step is equivalent to projecting the superposition of nuclear wavepackets, created by the XUV pulse, onto the Coulombic $1/R$ potential energy curve associated with the doubly ionized molecule. The kinetic energy release (KER/NKE) and emission direction (parallel or perpendicular to the laser polarization) of the two Coulomb-exploding deuterons is then calculated (measured) as a function of the XUV-IR time delay. From the experimental point of view this can be done by using the COLTRIMS technique [4, 5].

For the theoretical simulations we use our ab-initio method to describe the interaction with the attosecond XUV pulse. The ionization probabilities for the one-photon absorption process from the ground state of the D_2 molecule are obtained from the solution of the TDSE as described in previous sections (D_2 and H_2 share the same electronic structure within the BO approximation). The subsequent action of the delayed IR field to induce the full breakup of the molecule is modeled as a sudden vertical transition in which the D_2^+ nuclear wave packet is projected into the $1/R$ potential energy curve of the doubly ionized molecule, using the FC approximation. The wave function after photoionization by the XUV pulse can be written as:

$$\Psi(\mathbf{r}_1, \mathbf{r}_2, R, t) = \sum_{\alpha} \sum\!\!\!\!\!\!\int_{v_\alpha} \int C^{\epsilon_\alpha}_{\alpha v_\alpha} \varphi^{D_2^+}_{\alpha}(\mathbf{r}_1) \psi_{\varepsilon_\alpha}(\mathbf{r}_2) \chi_{v_\alpha}(R) e^{-iW_{v_\alpha \epsilon_\alpha} t} d\varepsilon_\alpha dE_{v_\alpha} \quad (6.1)$$

Where $\varphi^{D_2^+}_{\alpha}$ represent the state of ion and remaining ingredients correspond to those in the last term of equation 3.23. The probability of breakup (Coulomb explosion) can be found by projecting the wave function after photoionization onto a product of Coulomb functions describing the electrons in the continuum and the vibrational wave function describing the dissociation process, the probability fully differential then reads:

$$\frac{d^3P}{d\varepsilon_{f_1} d\varepsilon_{f_2} dE_{v_f}} = D^2 = \left| \langle \psi_{\varepsilon_{f_1}}(\mathbf{r}_1) \psi_{\varepsilon_{f_2}}(\mathbf{r}_2) \chi_{v_f}(R) | \mathbf{e}_\mu \hat{\boldsymbol{\mathcal{O}}} | \Psi(\mathbf{r}_1, \mathbf{r}_2, R, t) \rangle \right|^2 \quad (6.2)$$

$$\frac{dP}{dE_{v_f}} = \int\int \frac{d^3P}{d\varepsilon_{f_1} d\varepsilon_{f_2} dE_{v_f}} d\varepsilon_{f_1} d\varepsilon_{f_2} \tag{6.3}$$

where $\hat{\boldsymbol{\mathcal{O}}}$ is the dipole operator and $\mathbf{e}_\mu$ is the polarization vector. Inserting equation 6.1 into 6.2 and considering a single active electron in the second step:

$$\begin{aligned} D \propto \sum_\alpha \sum_{v_\alpha} \int C^{\varepsilon_\alpha}_{\alpha v_\alpha} \langle \psi_{\varepsilon_{f_1}}(\mathbf{r}_1) | \mathbf{e}_\mu \hat{\boldsymbol{\mathcal{O}}} | \varphi^{D_2^+}_\alpha(\mathbf{r}_1) \rangle \\ \times \langle \psi_{\varepsilon_{f_2}}(\mathbf{r}_2) | \psi_{\varepsilon_\alpha}(\mathbf{r}_2) \rangle \langle \chi_{v_f}(R) | \chi_{v_\alpha}(R) \rangle e^{-iW_{v_\alpha \epsilon_\alpha} t} d\varepsilon_\alpha dE_{v_\alpha} \end{aligned} \tag{6.4}$$

Within the FC approximation one can neglect the electronic coupling between the D_2^+ ion and the electronic continuum:

$$\langle \psi_{\varepsilon_{f_1}}(\mathbf{r}_1) | \mathbf{e}_\mu \hat{\boldsymbol{\mathcal{O}}} | \varphi^{D_2^+}_\alpha(\mathbf{r}_1) \rangle = 1 \tag{6.5}$$

$$\langle \psi_{\varepsilon_{f_2}}(\mathbf{r}_2) | \psi_{\varepsilon_\alpha}(\mathbf{r}_2) \rangle = \delta(\varepsilon_{f_2} - \varepsilon_\alpha) \tag{6.6}$$

Under those circumstances and using equation 6.6 the breakup probability as a function of the nuclei energy can be written as:

$$\frac{dP}{dE_{v_f}} \propto \int d\varepsilon_\alpha \left| \sum_\alpha \sum_{v_\alpha} C^{\varepsilon_\alpha}_{\alpha v_\alpha} \langle \chi_{v_f}(R) | \chi_{v_\alpha}(R) \rangle e^{-iW_{v_\alpha \epsilon_\alpha} t} dE_{v_\alpha} \right|^2 \tag{6.7}$$

The coefficients $C^{\varepsilon_\alpha}_{\alpha v_\alpha}$ results from the solution TDSE for a T=7 fs duration XUV pulse centered at $\hbar\omega$=42.6 eV and with an intensity of I=10^{12} W/cm^2. The multichannel expansion includes the six lowest ionic states ($1s\sigma_g$, $2p\sigma_u$, $2p\pi_u$, $2s\sigma_g$, $3p\sigma_u$, $3d\sigma_g$) and partial waves for the emitted electron up to a maximum angular momentum l=7 enclosed in a box of r_{max}=60 a.u.. The one-electron orbitals for the bound electron are consistently computed in the same radial box using single-center expansions with corresponding angular momenta up to l=16. Notice that, although for the second step we have made a series of approximations in the first step we include all the necessary ingredients (electron correlation and electronic continuum are properly described). We have found that the excitation probability for populating doubly excited $\mathcal{Q}_3$ and $\mathcal{Q}_4$ series, which lie in the vicinity of the above D_2^+ states, and autoionize on a femtosecond time scale, was significantly smaller than the probability for ionization+excitation into the states dissociating to the n=2 limit, while the $\mathcal{Q}_1$ and $\mathcal{Q}_2$ series are seated energetically far to low to

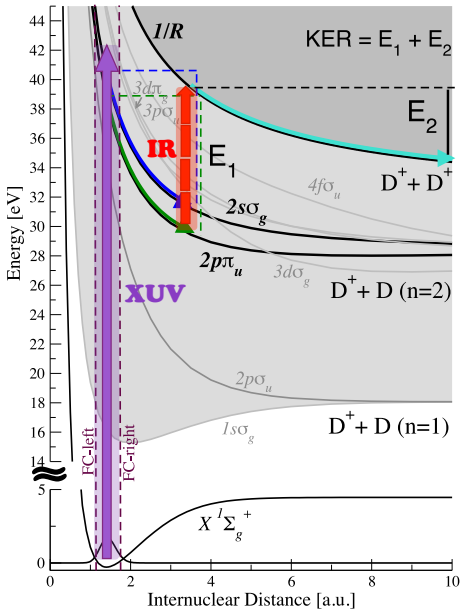

FIGURE 6.1: Correlated electron-electron and nuclear wavepacket dynamics in $D_2+\hbar\omega \Rightarrow D_2^+ + e^-$. An ultrashort and synchrotron XUV pulses with energy centered at $\hbar\omega$=42.6 eV (42 eV) were used to excite a highly correlated manifold of electronic states in D_2^+. The subsequent dissociative process, following the photoionization, was mapped by using time-resolved IR pulses and Coulomb-explosion imaging. Dashed vertical lines indicate the FC boundaries.

have an effect as we will show. Thus, the contribution to the total double ionization yield from these states, in this particular case, is negligible. As explained, the role of the IR probe pulse is to project on the Coulomb explosion curve, $1/R$, the nuclear wave packet generated by the XUV pulse on the manifold of D_2^+ states. The result of this projection depends on the pump-probe delay, which allows one to image the time evolution of the original wave packet.

The double ionization yields are shown in figure 6.2. In the top panel, we show the experimental KER distribution of the two D^+ ions as a function of the delay between the XUV pump and the IR probe pulses, for the molecules dissociating perpendicular and parallel to the XUV polarization, respectively. In the lower panel we present the corresponding calculated KERs. The agreement between experiment and theory is quite reasonable, except for very short time delays. In the theoretical model, the electronic beatings associated to transitions via

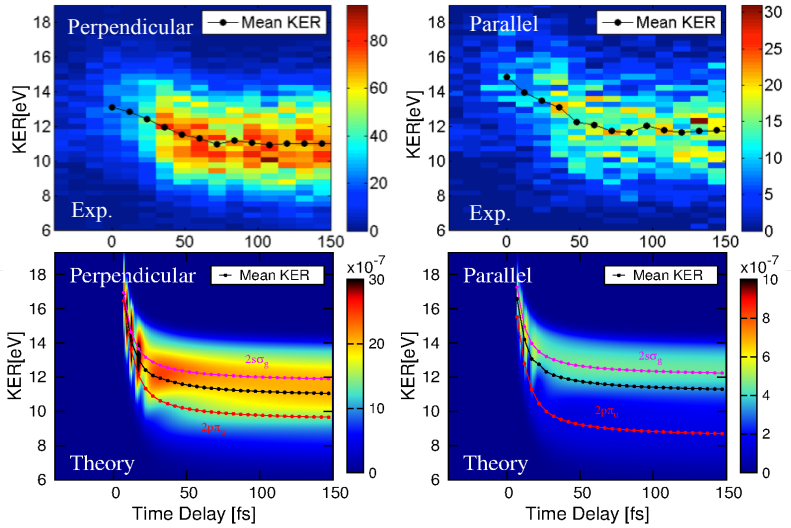

FIGURE 6.2: Measured and calculated dissociative pathways of the highly excited D_2^+ electronic states. Top panel: Measured nuclear kinetic energy release (NKE or KER) versus IR time-delay for the dissociation events perpendicular and parallel to the XUV/IR polarization direction. The dotted line represents the mean KER of the ion yield for each IR delay value. In the perpendicular case, the coherent superposition of the $2s\sigma_g$ and $2p\pi_u$ dissociative pathways gives a slightly lower mean KER curve compared with the parallel case, where the $2s\sigma_g$ is the largest contribution. Lower panel: Theoretical calculations for the NKE vs IR time-delay with two dissociative pathways. In the lower panel we also include the mean KER corresponding to two truncated simulations where only one individual (incoherent) path is included: $2p\pi_u$ in red dotted line or $2s\sigma_g$ in magenta dotted line.

the $2p\pi_u$ and $2s\sigma_g$ ionic states reflect as oscillations in the double ionization yields for delays of 20-30 fs. As all α channels contained in the pumped wave packet dissociate into the same limit, n=2, the amplitude of the oscillations eventually vanishes for long time delays. The oscillations are not seen in the experimental data mostly because ionization by the IR probe pulse requires absorption of many photons, a process that involves several dipole matrix elements, and not a simple projection of the D_2^+ wave packet into the $1/R$ state. Nevertheless, although the time-resolved measurements cannot retrieve the phases and, consequently,

the full wave packet reconstruction cannot be achieved, they still provide a good estimation of the ratio between the corresponding ionization amplitudes $C^{\varepsilon_\alpha}_{\alpha v_\alpha}$.

The molecular orientation with respect to the light polarization determines not only the intensity of the signal, as seen in figure 6.2 by comparing the left and right panels, but also the KER of the fragments obtained after the Coulomb explosion. These polarization-dependent features are solely due to the distinct dynamics initiated by the XUV pump pulse. For each light polarization a different nuclear wave packet is created with components (dictated by the single ionization amplitudes in equation 6.7) that evolve along their corresponding dissociative pathways (see in figure 6.1). Note that, irrespective of the orientation of the molecule with respect to the polarization and the time delay between the two photon pulses, the mean value of the KER distribution does not coincide with those of the individual channels $2p\pi_u$ or $2s\sigma_g$, which in turn appear at different kinetic energies. Thus, the dissociation is mostly governed by the coherent excitation of the dominant channels, the $2s\sigma_g$ and $2p\pi_u$ states, we will confirm this assessment below. Their relevance in the interrupted ultrafast dissociative photoionization of D_2 can be partly disentangled from the measured D^+ yields. The value of the KER for the bare deuterons observed at long time delays already discards the contribution of states correlated to the dissociative channel D^++D(n=1), as schematically depicted in figure 6.1 (KER=E_1+E_2). Here n is the principle quantum number. All the ionic states dissociating into D^++D(n=2) would however lead to similar values of the KER although, as we will further show below, by examining the single ionization step, their relative weight strongly depends on the molecular orientation.

In addition, to analyze in depth the first step of the process (which obviously will condition the outcome of the second step), we also performed calculations at a photon energy of $\hbar\omega$=42 eV. In 6.3 (right panel) we show electron-ion coincidence spectra, averaged over all electron and deuteron angles (randomly oriented molecule), which were used to identify the states excited by the XUV pulse. These data are in excellent agreement with those obtained from fully differential synchrotron COLTRIMS experiments (right panel). The photoelectron energies (electron kinetic energies, EKE) were measured in coincidence with the kinetic energy of the D^+ ions (KER) upon dissociative ionization, D^++D(n). The signals leading to deuterium atoms in a given n state, D(n), follow the energy-conservation lines (see equation 4.3). These energy-conservation values appear along two diagonal lines in figures 6.3 and 6.4 and correspond to total energies of KER+EKE$\sim$24 eV for n=1 and KER+EKE$\sim$14 eV for n=2. The contributions of the $1s\sigma_g$ and $2p\sigma_u$ states are clearly distinguishable along the coincidence line for n=1, because a vertical transition from the ground state to each of them leads to a distinct nuclear KER, 0-2 eV and 14-21 eV respectively. The corresponding signals are weak, which would already explain their minor contribution in the time-resolved spectra (see figure 6.2). Moreover, ejection of the second electron from these channels requires an absorption of a large number of IR photons - much larger than required for

ejecting an electron from highly-excited states (which lie ∼10 eV closer to the double ionization threshold). Thus, the probability of this process occurring is very unlikely. The ionization features of the highly-excited states fully overlap along the n=2 coincidence line due to the repulsive character of all the relevant states in the FC region and their degeneracy in the separated atom limit. All the D_2^+ states corresponding to D(n=2) ($2p\pi_u$, $2s\sigma_g$, $3p\sigma_u$, $3d\sigma_g$) lead to similar electron kinetic energies, ranging from 0 eV to 6 eV, and deuteron energies, from 7 eV to 14 eV, which correspond to the upper and lower limits of the overlap between the ground-state nuclear wave function and the nuclear wave functions associated with the highly excited electronic states in the Franck-Condon region (see figure 6.1).

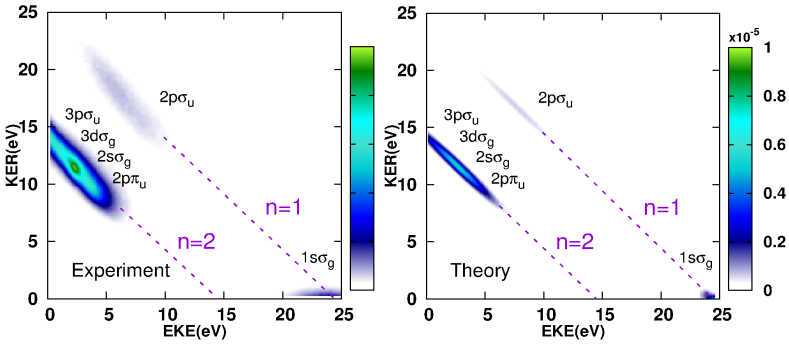

FIGURE 6.3: Experimental (right panel) and calculated (left panel) coincidence pattern using $\hbar\omega$=40 eV XUV pulse. Contributions of all the channels dissociating in the D(n=1) and D(n=2) dissociative limit are shown. Contributions from parallel and perpendicular dissociation against the polarization axis are here averaged. Coincidence dashed lines show maximum available energies of 24 eV and 14 eV for the D(n=1) and D(n=2) dissociation limits, respectively.

In order to understand better what we are actually probing, we split the randomly oriented molecule spectra by contributions of different symmetries ($^1\Sigma_u^+$ parallel and $^1\Pi_u$ perpendicular). In figure 6.4 we show the contributions of each orientation and keep only the $2s\sigma_g$ and $2p\pi_u$ in the n=2 dissociation limit for each symmetry. The main characteristics observed in figure 6.3 remain valid, the only difference is the $2p\sigma_u$ contribution in the parallel orientation is bigger than in the perpendicular. In the perpendicular orientation $\Lambda = \pm 1$ and since $m \leq l$ the minimum value of l in the partial wave expansion for the scattering wave function would start in l=2 instead of l=0 as in the case of the parallel orientation, inducing that dipole matrix elements being bigger in the parallel case. Although it can

be seen that removing the states $3p\sigma_u$ and $3d\sigma_g$ dissociating to n=2 limit does not have any major effect in the coincidence spectrum we can go further and plot the probability differential in the nuclei kinetic energy and see which of the channels dominate.

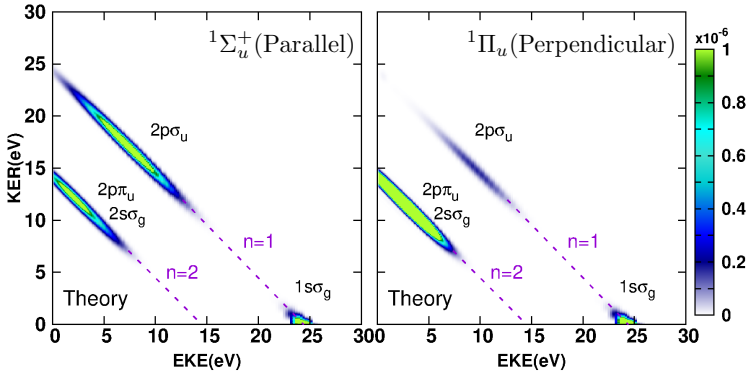

FIGURE 6.4: Parallel (right panel) and perpendicular (left panel) calculated coincidence pattern using $\hbar\omega$=40 eV XUV pulse. Contributions of all the channels dissociating in the D(n=1), the $2s\sigma_g$ and $2p\pi_u$ dissociating to the D(n=2) limit are shown. Coincidence dashed lines show maximum available energies of 24 eV and 14 eV for the D(n=1) and D(n=2) dissociation limits, respectively.

In figure 6.5, we plot the measured and calculated yields of the D^+ ions upon the XUV excitation process in the asymptotic n=2 dissociation limit, integrated over the photoelectron energy. Note that the electron-ion coincidence map, shown in figure 6.3 for randomly oriented molecules, is obtained with the weighted average of both orientations (1/3 parallel + 2/3 perpendicular). We include the calculated individual contributions from the four lowest electronic states within the n=2 ($2p\pi_u$, $2s\sigma_g$, $3p\sigma_u$, $3d\sigma_g$) limit, together with the total yields measured in the synchrotron radiation experiment, confirming that the dominant ionization channels correspond to the $2s\sigma_g$ and $2p\pi_u$ states. Similar to the time-resolved evolution of the dissociative process shown in figure 6.2, the yields of the D^+ ions in the asymptotic dissociative region, shown in figure 6.5, immediately reveal that both parallel and perpendicular excitations involve the $2s\sigma_g$ and $2p\pi_u$ states, with $2s\sigma_g$ being the main excitation channel in both cases. Again, these results cannot be explained by a single-active-electron picture, where only the $2p\pi_u$ state would be populated in a perpendicular transition from the $1s\sigma_g$ state. In contrast, for n=1, i.e. the ionization case where the outgoing electron does not interact with the second electron, a similar one-active-electron picture predicts that the $2p\sigma_u$ state

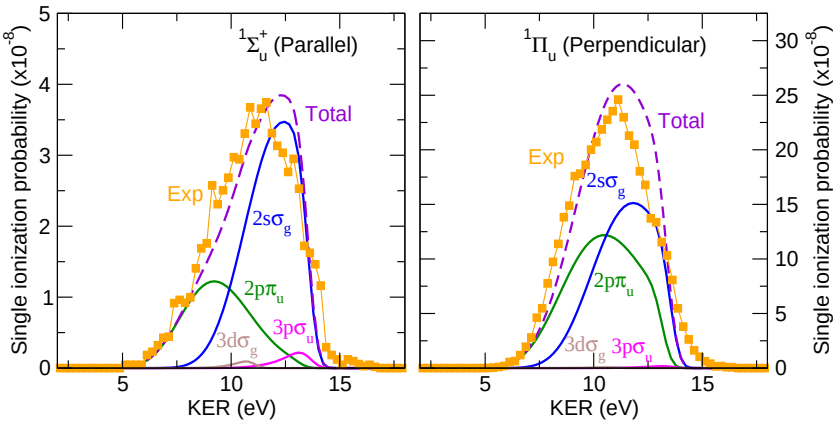

FIGURE 6.5: Calculated (thick dashed line) and renormalized experimental (squares) ion yields for the $D_2^+ \Rightarrow D^+ + D(n=2)$ dissociation limit for the perpendicular and parallel dissociation directions, integrated over all electron energies. The dominant contributions to the total yield mostly come from the D_2^+ $(2s\sigma_g)$ (blue) and D_2^+ $(2p\pi_u)$ states (green), with the $2s\sigma_g$ state being the main excitation channel in both orientations. Higher lying states within the D(n=2) manifold barely contribute and only the D_2^+.

should mainly contribute to the parallel transition, which is in agreement with the results of our ab-initio calculations.

In addition we performed calculations from a simplistic single-channel picture that independently maps each nuclear wave packet associated with each α intermediate state potential ($2p\pi_u$, $2s\sigma_g$) onto the 1/R potential energy curve. This model would assume that the perpendicular and parallel ionization comes solely from one of the states (by removing the sum over α in equation 6.7). Figure 6.6 shows the double ionization yields as a function of the delay using the new model. We observe that, even by using the ab-initio amplitudes for ionization of the neutral molecule, this model does not reproduce the KER obtained in the experiment in any of the possible combinations. The beatings appearing in the figure 6.2 completely vanish here which confirms the source, already explained. From the previous analysis, it is thus clear that while modeling the time-resolved dynamics by assuming that only the $2s\sigma_g$ D_2^+ state is populated for the parallel orientation and the $2p\pi_u$ state is exclusively populated for the perpendicular one would manifestly fail to reproduce the experimental data shown in figure 6.2. Our calculations show that for both orientations the molecule is ionized in a coherent superposition of these two states. Consequently, an accurate evaluation of the ionization amplitudes that includes the effect of electron-electron correlation is required to

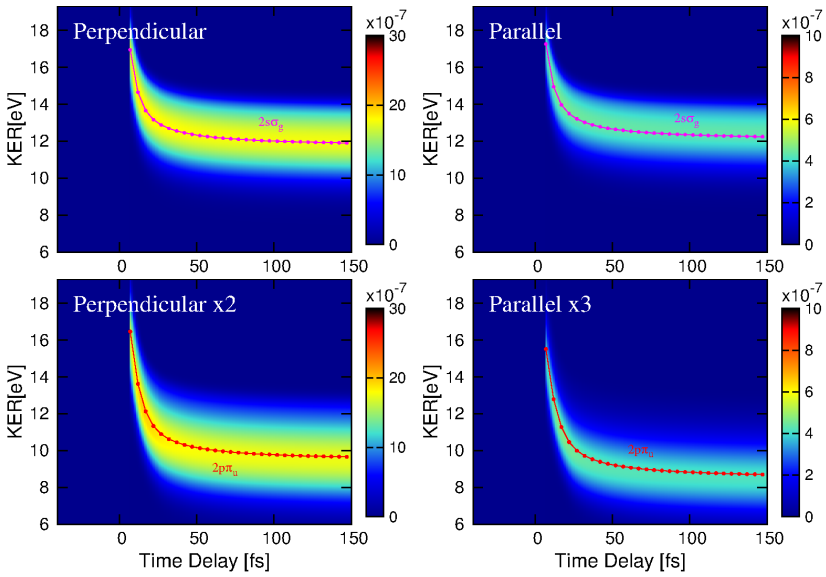

FIGURE 6.6: Calculated dissociative pathways of the highly excited D_2^+ electronic states, assuming the independent contributions from $2s\sigma_g$ (top panel) and $2p\pi_u$ (lower panel) states for each dissociative direction. The mean KER corresponding each individual path is also displayed: $2p\pi_u$ in red dotted line and $2s\sigma_g$ in magenta dotted line.

retrieve dynamics triggered in the excited ion and a single-channel model should be ruled out.

Once the dominant D_2^+ states are properly identified, the time-resolved spectra, shown in figure 6.2, can be fully understood. First, the relative signal intensity for each molecular orientation is a consequence of the different probabilities for single ionization into the D_2^+ $2s\sigma_g$ and $2p\pi_u$ states. Both of them are much larger for the perpendicular than for the parallel case (i.e. see figure 6.5). Second, the higher asymptotic value of the KER for the parallel case is the result of the larger population of the D_2^+ $2s\sigma_g$ state (larger, but not dominant), which lies higher in energy than the D_2^+ $2p\pi_u$ state in the FC region. None of these two features would be observed in the absence of electron-electron correlation either in the D_2 electronic states or during the ionization/excitation process. Ultimately, electron-electron correlation is responsible for changes in the relative population of these states due to changes in the polarization direction of the incoming light, thus leading to a certain degree of control of the D^+ yields under the combined action of the XUV

and the IR pulses.

In conclusion, the presence of correlations between the two electrons in D_2 dictates the photoexcitation and the consecutive dissociation processes. The dissociation process results in a superposition of nuclear wave packets evolving simultaneously on different potential energy curves of the parent ion, mainly those associated with the $2p\pi_u$ and $2s\sigma_g$ electronic states. Since these states dissociate into the same energy limit, Coulomb imaging of the dissociation process always reflects a mixture of both states. This imprints a unique signature on the energy distribution of the molecular fragments. In this way, we unravel effects that help us fully understand how electron interactions drive the nuclear dynamics in the excitation process of the molecular ion. In the future, this work can be extended by demonstrating a high degree of laser-induced control over the dissociation process, and to more complex systems for which ab-initio theoretical calculations are not yet possible.

Chapter 7

IR induced symmetry breaking

As we have seen, pump-probe techniques are nowadays commonly employed to retrieve real-time information of electron dynamics in matter. State-of-the-art experimental set-ups, in particular using XUV-pump/IR-probe approaches as the one described in the previous section, have recently provided images of electron motion upon photoionization of atoms and molecules with unprecedented attosecond resolution, capable of capturing the build-up of Fano profiles in He [101] or a charge migration process in a biomolecule [18]. In this specific framework, electron dynamics can be monitored by recording photoelectron angular and energy distributions as a function of the delay between the pump and probe. Controlling the fragmentation process by changing the relative phase between both pulses remains as one of the main topics of field today, as demonstrated in the problem discussed in the previous section. More interestingly, in experiments capturing the photoelectron ejection angle, asymmetric MFPADs, upon XUV photoionization, have been obtained using the interferences coming from the coherent superposition of ionic states possessing different symmetry i.e. *gerade* and *ungerade* resulting in the localization of the remaining bound electron. Specifically in the H_2/D_2 molecule the asymmetries come from the interference between the *direct* ionization through the $2p\sigma_u$ channel and the ionization through the $1s\sigma_g$ channel by way of delayed $\mathcal{Q}$ autoionization [26, 123]. In the H_2/D_2 molecule, the control of the asymmetry in the ion/electron distributions have been achieved using the combined action of an XUV pulse (SAP or APT) and a relatively weak IR pulse [15, 16, 69]. In these works, the XUV ionize the molecule and the IR creates a coherent superposition of the $1s\sigma_g$ and $2p\sigma_u$ ionic states during the dissociation process. By changing the relative phase between the XUV and the IR the localization of one the electron on one of the nuclei takes place selectively, thus producing the asymmetry in the ion/electron ejection. One of the requirements to observe such asymmetries is the following: one has to be able to detect in coincidence the electrons and ions coming from the same event, in other words one needs a COLTRIMS apparatus.

On the other hand, the breaking of the symmetry in the electron ejection, arising from simultaneous interference photoionization processes have been reported in atomic Rb [124, 125] and more recently in Ne [126]. The mentioned works were focused in atoms, while in molecules very little is known about how the nuclear motion and presence of doubly excited states would affect such mechanism. We aim to explore the possibility of observing electron ejection asymmetry induced and controlled by the IR dressing field. We will employ an XUV pump-IR probe scheme, relaying in the interference between multiple pathways leading to electronic continuum states with the same energy but different symmetry, thus breaking the symmetry of the MFPADs.

In order to investigate the IR-induced asymmetry upon photoionization of H_2, we have considered an XUV (SAP) pump of T=1 fs duration, intensity of I=10^9 Wcm^{-2} and centered at $\hbar\omega$=28 eV in combination with an IR probe pulse of intensity I=3×10^{11} Wcm^{-2}, λ=750 nm ($\hbar\omega$=1.65 eV) and a duration of T=6 fs. Both fields are linearly polarized and parallel to the molecular axis. We have defined the time delay between the pump and probe, as the difference between the times at which the pulses reach the maximum amplitude. In this work, negative time delays imply that the IR pulse arrives before the XUV one. Due to its energy and intensity the IR field cannot ionize the target independently of the XUV pulse. Indeed in order for this to happen for an energy of $\hbar\omega$=1.65 eV the molecule should absorb around ten photons which is unlikely at this intensity. On the other hand the absorption of more than one XUV photon is also unlikely at this intensity and pulse duration, so both situations should be ruled out in the following analysis. Due to the dipole selection rules absorption of one photon leads to a change in the symmetry of the molecule, so one absorbed photon $^1\Sigma_g^+ \Rightarrow {}^1\Sigma_u^+$ leads to *ungerade* symmetry, while two absorbed photons $^1\Sigma_g^+ \Rightarrow {}^1\Sigma_u^+ \Rightarrow {}^1\Sigma_g^+$ leads to *gerade* symmetry. Therefore, the number of absorbed photons will impose the final symmetry of the molecule, which can be independently extracted from our spectral method in a straightforward manner. The short duration of the XUV pulse (large bandwidth $\Delta\omega$=$4\pi/T$) makes possible that the absorption of a single XUV photon and the combined sequence of an XUV-photon absorption with the exchange (absorption or emission) of an IR photon lead to the same final state, consequently populating energy-degenerate states with both *gerade* and *ungerade* symmetry simultaneously. As we have seen the absorption of a photon with energy $\hbar\omega \geq$25 eV effectively populate the doubly excited states, which decay mainly to the dissociative channel leading to more prominent features due to the interference between the *direct* and the *resonant* channels than those observed in the non-dissociative one. Thus, we further expect to see the effect of the IR pulse in such interference.

For the complete theoretical description, the multichannel expansion includes the two lowest ionic states ($1s\sigma_g$, $2p\sigma_u$) and partial waves for the emitted electron up to a maximum angular momentum l=11 enclosed in an electronic box of r_{max}=300 a.u.. The one-electron orbitals for the bound electron are consistently

computed in the same radial box using single-center expansions with corresponding angular momenta up to l=16. The first two series of resonances $\mathcal{Q}_1$ and $\mathcal{Q}_2$ of both symmetries have been included. The use of such "huge" electronic box complies with all the requirements specified in section 3.2. The vibrational (bound and dissociative) wave functions have been expanded in a 240 B-splines in a R_{max}=12 a.u. vibrational box. Note that this basis set is significantly larger than that employed in [16]. This enables the extraction of the fully-energy differential quantities, as well as the angle-resolved photoelectron spectrum. Previous works were limited to integrated yields that are much less affected by unphysical reflections.

In figure 7.1 we show the coincidence pattern for three different time delays between the pump and the probe. We also show the individual contributions of the $^1\Sigma_g^+$ and $^1\Sigma_u^+$ final symmetries. Upon photoionization with an XUV pulse at given photon energy the electron and the ion will share the energy according to conservation line corresponding to a diagonal of slope -1 in the plots. Since the central frequency of the XUV is $\hbar\omega$=28 eV the largest probability are obtained in a diagonal corresponding to a EKE+NKE$\sim$10 eV of total energy absorbed. As widely known from previous works [114, 119] the probability for *direct* ionization is largest at low NKE and decreases rapidly as the NKE increases and practically vanishes around NKE$\sim$3 eV. The probability observed at larger NKE comes from autoionization and the *direct* ionization through the $2p\sigma_u$ channel. As the system evolve in time, the doubly excited states start to decay and both direct ionization and autoionization processes interfere producing the structure at low NKE and EKE$\sim$8 eV. The intensity of the IR field is low enough such that the ionization probability associated to the $^1\Sigma_u^+$ symmetry is very similar to the outcome of using the XUV+IR combination. Nevertheless, the total yield do present contribution of the XUV+IR combination, as demonstrated when looking at the contribution of the $^1\Sigma_g^+$ final symmetry an even number of photons combined one XUV and one IR photon, in particular at low NKE. The $^1\Sigma_g^+$ symmetry population experience significant changes with the delay between the XUV and the IR.

Although the coincidence spectrum contains all the information needed, is more easy to visualize the dependence with the time-delay by integrating over one of the coordinates. In figure 7.2 we show the EKE (upper panel) and NKE (lower panel) distributions as a function of the delay between the XUV and the IR. These distributions can be obtained by integrating the coincidence pattern over EKE/NKE in each case, in the case of the EKE the contribution of the non-dissociative channel have been included (in any experimental set up, the sole detection of the electron does not allow to separate these channels). Again, we show for each spectrum the contribution of the $^1\Sigma_u^+$ and $^1\Sigma_g^+$ final symmetries. As expected for large (t$\leq$-1.5 fs) negative time delays, where both pulses do not overlap, the distributions are identical to those obtained by only using the XUV pulse. As we mentioned before, the IR by itself do not reach the ionization continua from the

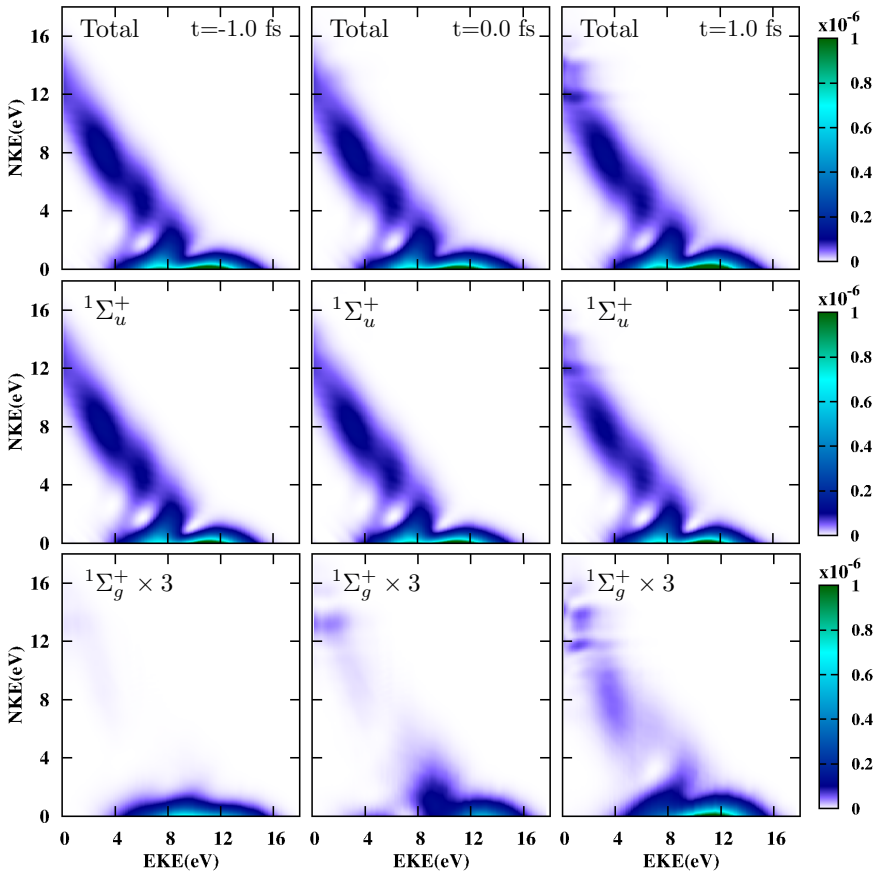

FIGURE 7.1: Calculated coincidence pattern for different time delays between the XUV and the IR. Contributions of all the symmetries *gerade* ($^1\Sigma_g^+$) and *ungerade* ($^1\Sigma_u^+$) to the total spectra are also shown. Top panel: Total spectrum. Middle panel: $^1\Sigma_u^+$ contribution to the total spectrum. Lower panel: $^1\Sigma_g^+$ contribution to the total spectrum, notice that due to the low relative intensity the *gerade* symmetry has been rescaled.

ground state, therefore, as long as it reaches the molecular target earlier and without an effective overlap with the attosecond XUV pulse, the observed spectrum is due to the XUV interaction alone. For time delays at which the fields overlap effectively (t≥-1.5 fs, t≤1.5 fs) the presence of the IR induce a population transfer from the $^1\Sigma_u^+$ to the $^1\Sigma_g^+$ symmetry therefore strongly modifying the ionization

distributions, the probability of populating the $^1\Sigma_g^+$ oscillates with the time delay with maximum value at every half a period of the IR field. For longer time delays (t≥1.5 fs) the pulses hardly overlap, as a consequence the $^1\Sigma_g^+$ contribution becomes negligible again and we recover the spectrum corresponding to the sole interaction of the XUV pulse. While in the EKE distribution is hard to distinguish the role of autoionization, the NKE distribution (dissociative ionization) clearly captures its signature: it manifests as an interference for low NKE between the direct and the autoionization processes. At larger NKE, most of the signal is due to the decay of the doubly excited states and to a lesser extent from *direct* ionization through the $2p\sigma_u$ channel. In the EKE distribution, autoionization implies a much smaller contribution since both dissociative and non-dissociative ionization are added up together, as we have shown in Chapter 4 and Chapter 5. Notice that the distributions are not symmetric with respect to zero time delay, which is consequence of the presence of the doubly excited states. When the XUV arrives first it populates the doubly excited states with its maximum amplitude, these start to decay and after the delay their population are further depleted by the maximum of the IR.

The periodicity of the population transfer $^1\Sigma_u^+ \Rightarrow {}^1\Sigma_g^+$ for a given total energy (diagonal in the coincidence spectrum) can be easily understood within the framework of the perturbation theory. As we stated earlier the *gerade* symmetry is populated through a second order process. Thus, we can reach the same states by the absorption of one XUV photon and one IR photon or the absorption of one XUV photon and the stimulated emission of one IR photon, figure 7.3. The probability of reaching a *gerade* state is then the coherent superposition of both paths:

$$\mathcal{P}_g = |\mathcal{S}^a + \mathcal{S}^e|^2 \tag{7.1}$$

where $\mathcal{S}^a$ and $\mathcal{S}^b$ are the amplitudes corresponding to each one of the paths (see figure 7.3). Each one of these amplitudes can be written in as:

$$\mathcal{S} = -2i\pi \frac{A_\Omega}{2} \frac{A_\omega}{2} \mathcal{M} \tag{7.2}$$

$$\mathcal{M} = \langle \Phi_g | (\mathbf{e}_\mu \hat{\boldsymbol{\mathcal{O}}}) \hat{G}(E_0 + \Omega) (\mathbf{e}_\mu \hat{\boldsymbol{\mathcal{O}}}) | \Psi_0 \rangle \delta(\omega_g - \Omega - \omega) \tag{7.3}$$

Where $\omega_g = E_g - E_0$, A_Ω and A_ω are the complex amplitudes of the XUV and IR pulses, $\hat{G}(E_0+\Omega)$ is the Green function, $\mathcal{M}$ are the two photon matrix elements, Ψ_0 and Φ_g are the ground and final states respectively.

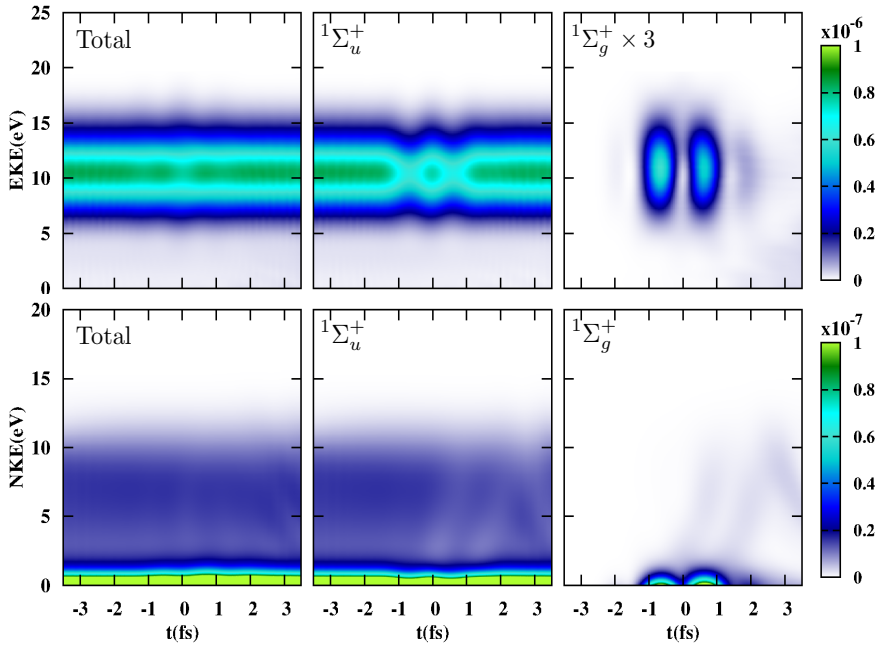

FIGURE 7.2: Top panel: Probability as a function the EKE (integrating over NKE) and the delay between the XUV and the IR. Lower panel: Probability as a function the NKE (integrating over EKE) and the delay. Contributions of each symmetry $^1\Sigma_u^+$ (center panel) and $^1\Sigma_g^+$ (right panel) to the total spectrum (left panel) is also shown in each case.

$$A_\Omega = |A_\Omega| e^{-i\phi_\Omega} \quad A_\omega = |A_\omega| e^{-i(\phi_{IR}+\omega t)} \quad \varphi = \arg(\mathcal{M}) \tag{7.4}$$

where ϕ_Ω and ϕ_{IR} correspond to the phases of the XUV and IR pulses and t the delay between both pulses. Using 7.4, and plugging equations 7.3, 7.2 into 7.1 we get:

$$\begin{aligned}\mathcal{P}_g \propto |A_{\Omega_<} A_\omega \mathcal{M}^a|^2 + |A_{\Omega_>} A_\omega^* \mathcal{M}^e|^2 + 2|A_{\Omega_<} A_\omega \mathcal{M}^a A_{\Omega_>} A_\omega^* \mathcal{M}^e| \\ \times \cos(\phi_{\Omega_>} - \phi_{\Omega_<} - \phi_{IR} + \varphi_- - \varphi_+ - 2\omega t)\end{aligned} \tag{7.5}$$

$$\mathcal{P}_g \propto a + b\cos(2\omega t + \Delta) \tag{7.6}$$

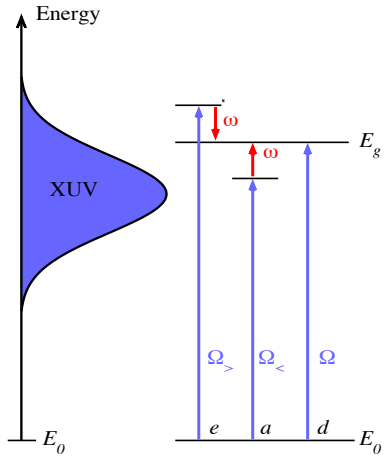

FIGURE 7.3: Schematic of the different quantum paths leading to the same state. Within the bandwidth of the SAP, an state can be reached by the path d where a single XUV photon with frequency Ω is absorbed. Alternatively can be reached by path a where a less energetic photon $\Omega_<$ and an IR photon ω are absorbed, or by path e where a more energetic photon $\Omega_>$ is absorbed and an IR photon ω is emitted.

So the probability of reaching an ${}^1\Sigma_g^+$ state for a given total energy is modulated with the periodicity $2\omega t$ (maximum every half-period of the IR), due to the interferences between the two different quantum paths leading to the same state. The absolute values of the matrix elements $\mathcal{M}^{\pm}$ must have similar values to produce significant interferences. The coherence between the different paths is the basis of different techniques like PROOF [127] or RABBITT [128–130]. The latter being the main topic to be treated in the next chapter.

Much richer information can be extracted from the MFPADs. In the following we are going to consider the MFPADs, neglecting the direction at which the ion was ejected. Avoiding the projection of the wave function in each center (producing an incoherent superposition of the ionization limits, see section 3.2). Figure 7.4 displays the MFPADs at an specific electron and proton energy (which necessarily determines a given total absorbed energy) and for selected values of time delays between the XUV and the IR pulse. The electron and proton energies correspond to ones presented in figure 7.7, indicated in the caption. The MFPADs have been renormalized to the total probability for a better vizualization. These

have been chosen to be in the region where the $^1\Sigma_g^+$ has an non-negligible contribution to the spectrum (see figure 7.1), seating at low NKE (photoionization through $1s\sigma_g$ limit). For all the energies at t=-3.5 fs (solid brown) the MFPADs are completely symmetric, as we already explained at this delay the absorption of a single XUV photon is the only process contributing to photoionization probability. Thus, only $^1\Sigma_u^+$ (odd partial waves, mostly p-like for the bound electron being the $1s\sigma_g$ state) contributes to the MFPADs, and those are completely symmetric as expected. However for bigger time delays the t=-0.5 fs (blue line) and t=1 fs (red line) the IR overlap effectively with the XUV, two photon transitions process takes place. Thus, a coherent superposition of $^1\Sigma_u^+$ (odd partial waves) and $^1\Sigma_g^+$ (even partial waves) will contribute to the MFPADs (p+d)-like, therefore strongly modifying the MFPADs. The most drastic effect is that the MFPADs exhibit signature of right-left asymmetry. For those delays the degree of asymmetry in the MFPADs is significant and close to a uni-direction photo-electron ejection is induced. Besides, it is also striking that in most of the cases the probability of the electron being ejected to the right half-plane or to the left half-plane changes with the time delay. That oscillatory behaviour would suggest a sort of periodicity in the asymmetry with the delay. The asymmetry in the MFPADs can be quantified via the left-right asymmetry parameter as defined in section 3.2.

Figure 7.5 displays the asymmetry parameter as a function of the electron kinetic energy (EKE) and the time delay between the XUV and the IR fields. We have plotted the total ionization probabilities (left panel) along side the $1s\sigma_g$ contribution (right panel). We have integrated over the NKE and sum over the bounds state of the ion. In order to obtain this sort of spectrum from the experimental point of view, one just has to capture all the electrons in either half-plane. That can be achieve, for instance, using a VMI [1–3] apparatus. To strength the analysis, in figure 7.6 we select "cuts" at given values of photoelectron energies (EKE) from the total spectrum in figure 7.5. It is worth mentioning that different signs in the parameter means that the electron has been ejected in semi-plane or the other. As we can see in both figures, most of the previous analysis can be transferred in some degree to the asymmetry parameter. As expected, for long negatives delays the XUV is the only contribution to the spectra, only $^1\Sigma_u^+$ get populated, therefore the asymmetry parameter is zero. As the XUV and the IR start to overlap the population transfer between symmetries begin, so the final state will we a combination of both symmetries producing the asymmetry on the MFPADs. The asymmetry parameter oscillate with the delay between the XUV and the IR with the frequency of the IR. This fact is not surprising at all, asymmetry is only produced when both $^1\Sigma_g^+$ and $^1\Sigma_u^+$ are populated at the same energy. Both symmetries can be populated simultaneously through combinations of the three different paths (see figure 7.3), however *e-d* or *a-d* paths will dominate over the *a-e* path, because the latter involve the exchange of two IR photons ω. Thus, leading to a modulation in the asymmetry with periodicity ωt associated with the exchange of only

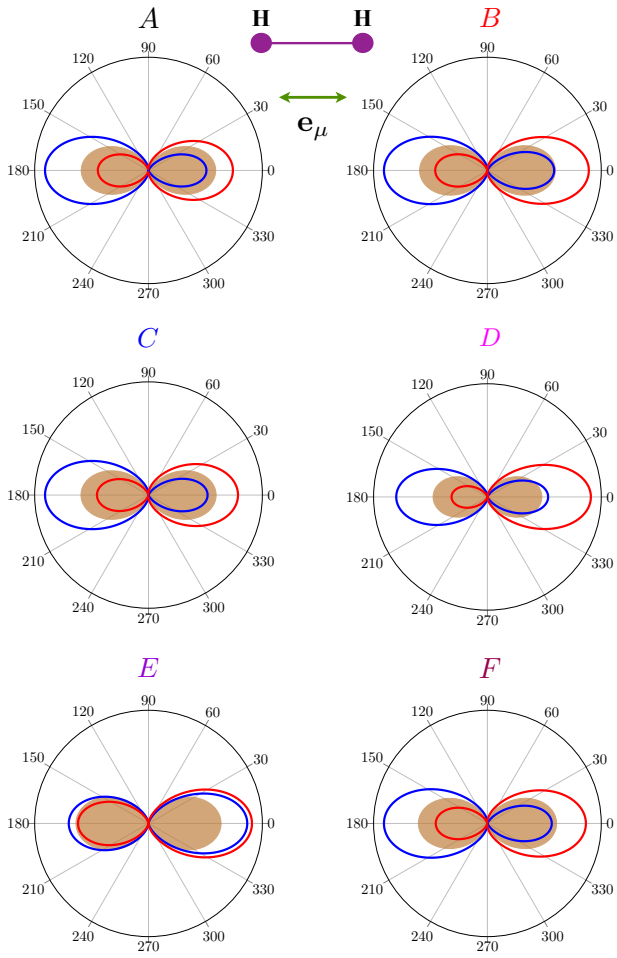

FIGURE 7.4: MFPADs for the XUV pump-IR probe dissociative ionization of H_2. The dependence with the delay between the pump and the probe is presented. Brown solid: t=-3.5 fs, blue line: t=-0.5 fs and red line: t=1.0 fs. Each panel correspond to the energies presented in figure 7.7, that is panels ***A***=(EKE=9.90 eV, NKE=0.10 eV), ***B***=(EKE=11.0 eV, NKE=0.10 eV), ***C***=(EKE=10.4 eV, NKE=0.19 eV), ***D***=(EKE=12.5 eV, NKE=0.19 eV), ***E***=(EKE=8.53 eV, NKE=1.43 eV) and ***F***=(EKE=11.0 eV, NKE=0.29 eV).

one IR photon.

Such modulation is clearly visible in the region EKE=4-16 eV and in the cuts

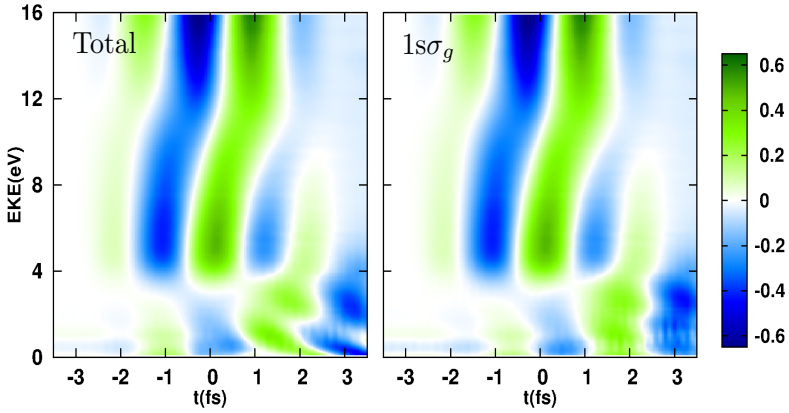

FIGURE 7.5: Asymmetry in the XUV pump-IR probe ionization of H_2. The dependence of the asymmetry parameter on the time delay between the XUV and the IR and the electron kinetic energy is presented. The contribution of the $1s\sigma_g$ channel (right panel) to the total spectrum (left panel) is also shown.

done, the *direct* ionization through the $1s\sigma_g$, autoionization and non-dissociative ionization are the channels contributing in this region (see figure 7.1) being the latter the dominant. While in the region EKE=0-4 eV, population is coming through autoionization and *direct* ionization through $2p\sigma_u$. There we can see a shift in the asymmetry with respect to the EKE=4-16 eV region. The cause behind the shift has two components, the first one is the contribution of the $2p\sigma_u$ which can be seen when compared the Total (left panel) and the $1s\sigma_g$ (right panel) spectra. We observe that the contribution of the $2p\sigma_u$ only play a role at the longest positive delays. For these time delays, the molecular wave packet created in the $1s\sigma_g$ by the XUV pulse has time to evolve and reach larger internuclear distances, outside the FC region, where the energy gap with the second ionization threshold is smaller, thus allowing for further ionization through this limit upon an IR photon absorption. The other source can be attributed to the autoionization, it is well known that the scattering states experience a phase jump in the presence of doubly excited states. This jump will manifest through factor $\varphi = \arg(\mathcal{M})$ where $\mathcal{M}$ is now the single photon transition matrix element. The doubly excited states are also responsible for the tilt in the asymmetry (for an specific delay). Although at every energy it oscillates with the frequency of the IR that would shift the position of the zeros in the asymmetry and how fast it increase/decrease. In figure 7.7 we present the asymmetry parameter as a function of the delay, but this time differential in electron (EKE) and nuclei energies (NKE). The energies correspond

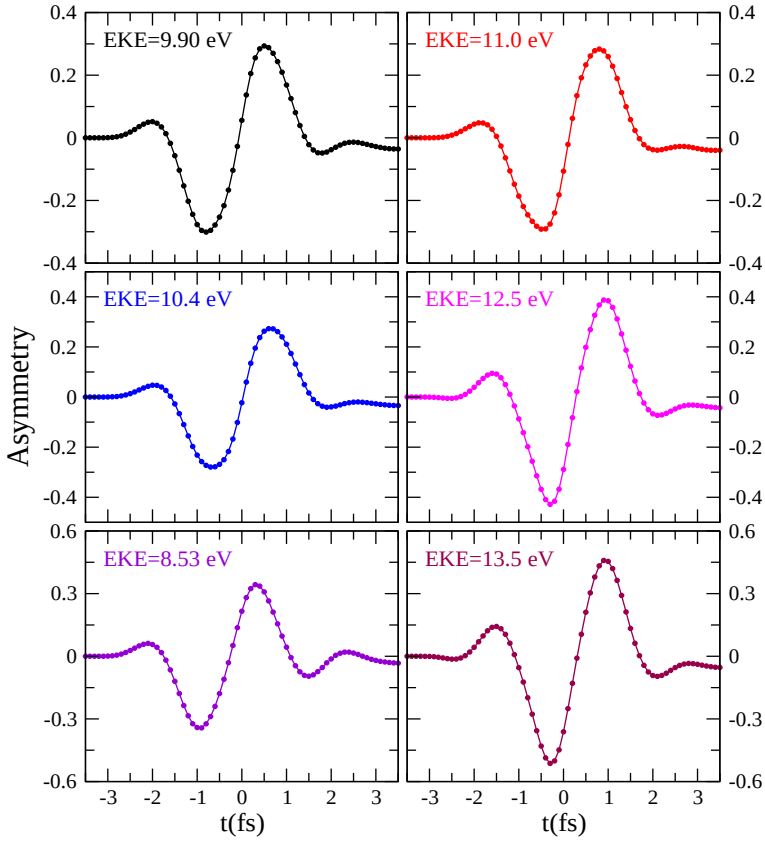

FIGURE 7.6: Cuts in electron kinetic energy of the figure 7.5. The energies at which the cuts have been taken are indicated in the panels.

to the ones at which the MFPADs were presented, all corresponding to the dissociative channel. Here, besides the effects from the doubly excited states and the combination of the two ionization thresholds we are throwing into the pot the nuclear phase (removed in the integration process). We can see that the previous conclusions remain true for the doubly differential asymmetry. The shift in time delay becomes more evident, and now contrary to what should be expected at longer time delays the asymmetry is way off from zero. This is most probably a consequence of the bond-softening-like process [16, 131], the XUV creates a wavepacket this evolve and after the delay emits on IR photon populating the low NKE region and as a consequence creating the asymmetry. Although in some cases the

60% of the electrons are ejected in either direction, due to the weak IR intensity the two photon channel (*a*, *e*) is much weaker than the one-photon one (*d*), therefore the interference between those channel will produce a rather low contrast in the asymmetry oscillation.

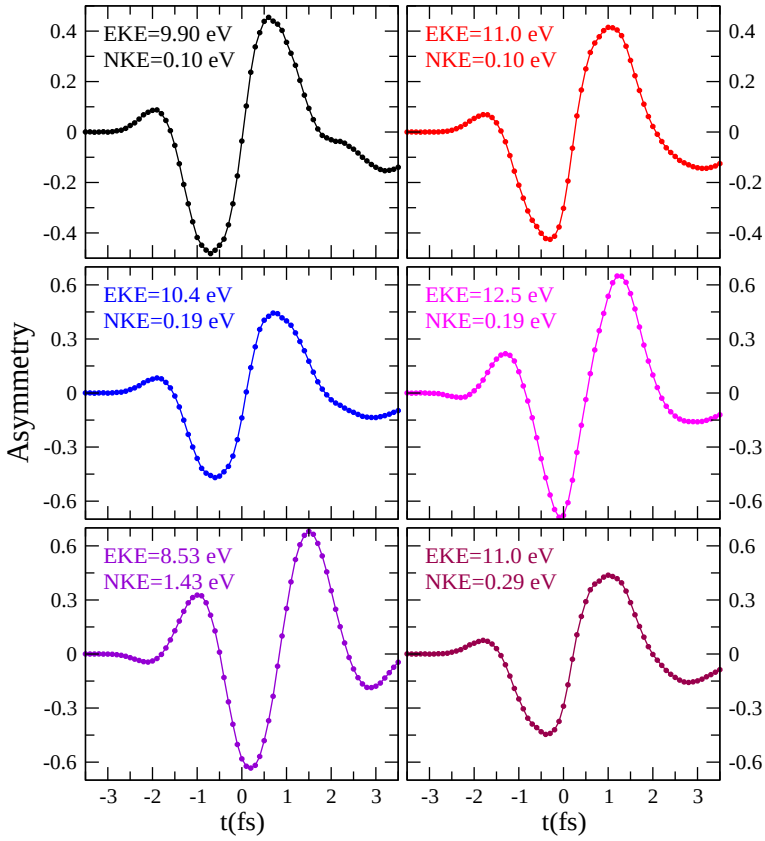

FIGURE 7.7: Asymmetry in the XUV pump-IR probe dissociative ionization of H_2. The dependence of the asymmetry parameter on the time delay between the XUV and the IR is presented for different electron and nuclei energies (total absorbed energies) indicated in the panels.

In order to somehow isolate the photoelectron asymmetry induced by the IR pulse, with respect to those processes involving electron-electron correlation (mainly doubly excited states), we have performed calculations in the H_2^+ molecule

and explore the equivalent process. Through this comparison we expect to still observed the possible effect of nuclear motion and the IR-dependencies in the absence of electron correlation. The H_2^+ molecule is the perfect testing bed, since it has "clean" continuum (free of doubly excited states), only one ionization threshold and the molecule undergoes Coulomb explosion upon photoionization (pure dissociative). Other advantage, it allows one to use a bit longer IR, since the calculations are not as expensive as for the H_2 molecule. In this case the XUV is centered at $\hbar\omega$=40 eV (in order to lead to similar photoelectron energies as in the H_2 study) and the IR has a duration of T=9 fs, all the other pulse parameters remains the same. The procedure for calculating the BO states of H_2^+ is the same we have applied for H_2. Particularly, the multichannel expansion includes the partial waves for the emitted electron up to l=20, the electronic states (scattering and bounds) have been calculated in a r_{max}=600 a.u. box. While for the vibrational wave functions we have the same parameters than for H_2.

In figure 7.8 we present the asymmetry parameter for the H_2^+ molecule, for selected values of NKE and EKE, as a function of the time delay between the XUV and the IR as we did for the H_2 in figure 7.7. Here is more easy to visualize the oscillation of the asymmetry parameter with the frequency of the IR ωt (the longer IR helps in that matter). The asymmetry parameter is nearly symmetric with respect to zero delay for all the total energies shown. Asymmetry parameter perfectly symmetric with respect to zero delay can be obtained by reducing the IR intensity, however yielding a even lower contrast in the asymmetry oscillations.

In summary we have studied the laser assisted photoionization in the H_2 and H_2^+ molecules by using an XUV pump-IR probe scheme. We have found that the MFPADs turn out to be asymmetric when the XUV and the IR effectively overlap. The variation of the asymmetry parameter with the time-delay reflects the scattering phase of the final state, therefore being an indirect measure of how the phase changes with photo-electron energy. As we will see in the next chapter, this is relevant information in similar scenarios where the photoionization time delays are investigated. The photo-electron ejection asymmetry is the result of the interferences between different quantum paths leading to the same states with different symmetry. Thus, it is imperative that both *gerade* ($^1\Sigma_g^+$) and *ungerade* ($^1\Sigma_u^+$) symmetries to be populated at the same total energy simultaneously for the asymmetry to be produced. We can reach states with different symmetry and the same energy through a combination of the *a-d* and *e-d* paths (see figure 7.3) involving the absorption of one XUV photon and the exchange of one IR photon. This is possible only for an XUV pulse such that the absorption of one XUV photon and the exchange of one IR photon will lead to an state seating in energy within the bandwidth of the XUV pulse. We have proven that we can control the asymmetry in the electron ejection by varying the relative phase between the XUV and the IR fields. While in the H_2^+ molecule we have obtained a "clean" asymmetry parameter, in the H_2 molecule there are others striking effects taking place. On the one

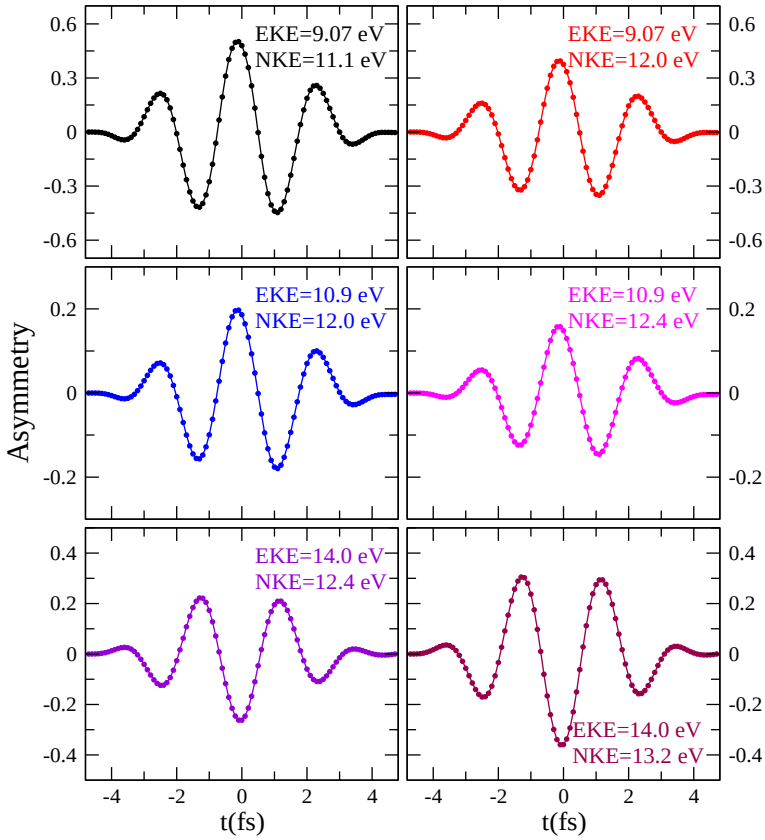

FIGURE 7.8: Asymmetry in the XUV pump-IR probe dissociative ionization of H_2^+. The dependence of the asymmetry parameter on the time delay between the XUV and the IR is presented for different electron and nuclei energies (total absorbed energies) indicated in the panels.

hand we have the autoionization producing a characteristic jump in the scattering phase and tilting-shifting the asymmetry parameter, and on the other hand the $2p\sigma_u$ producing a shift as well.

Chapter 8

Attosecond nuclear-electron dynamics in dissociative ionization

Photoionization dynamics and the timing involved in such processes play a crucial role in many natural phenomena, and consequently has represented a major field of investigation spanning from atomic [132–137], to molecular [16, 18, 138, 139] and condensed matter systems [140, 141]. As an electron is freed from an atom upon absorption of ionizing radiation, rearrangements will take place to compensate the newborn vacancy, triggering multiple relaxation mechanisms depending on the degree of correlation among electrons and nuclei. Thus, the knowledge about the photoemission time delay is indispensable to access such complex and unexplored dynamics in real-time. Extraction of photoemission time delays can be achieved by recording the spectral interference of electron wave packet (EWP) emitted at different energies upon interaction with a two-color field: an infrared (IR) pulse and its high-harmonic order in the energy region of few tens of eV, namely the extreme ultraviolet (XUV). The reconstruction of attosecond beating by interference of two-photon transitions (RABBITT) technique, based on the combination of an XUV attosecond pulse train (APT) with a long and rather weak IR pulse, revealed to be one of the most reliable [137] and established method to investigate not only photoionization time delays in noble gases [132–137], but also in presence of double ionization processes [142], spin-orbit interaction [143] and population of resonances [138, 139]. The first investigation on photoionization time delay in molecular targets was reported by Haessler and coworkers [138] in N_2. They could distinctively observe the influence of complex resonances in the continuum for different vibrational states in N_2^+ comparing the extracted molecular phase to an atomic reference phase assumed to be known form theory (Ar). Recently Huppert et al. [139] measured in the same fashion the photoionization time delay in N_2O and H_2O but comparing the phase of different electronic states within the same molecule. The authors attributed the observation

of large delays in N_2O compared to H_2O because of the presence of molecular shape resonances. It is common knowledge that nuclei, due to their massive nature and thus their high moment of inertia, move in a time scale ranging from tens to hundreds of femtoseconds and even longer. This implies that the interaction between attosecond pulses and molecules enables to follow in real time only the electron dynamics while considering the nuclei as frozen spectators. This is what has been assumed in [138] and [139], allowing them to extract the photoemission time delay information similarly to the atomic case. However, it has already been demonstrated that N_2, N_2O and H_2O, if populating their neutral super-excited states, relax through competing pathway involving electronic and nuclear degrees of freedom, since pre-dissociation and autoionization occur on the same timescale [144–146]. The same holds true for molecules composed by light atomic species, like hydrogen and deuterium, where the nuclear motion emerged to be as fast as the electron dynamics, resulting in a strong coupling between them. As atomic hydrogen is present in most organic and biologically relevant molecules, understanding the coupled electron-nuclear dynamics in these systems is thus highly relevant in chemistry and biology. A complete experimental and theoretical investigation of this nuclear-electronic coupling, at the attosecond time scale, excludes the possibility to study large molecular systems where hydrogen atoms are the main constituents. Therefore we decided to study the photoionization dynamics in molecular hydrogen H_2, the simplest homo-nuclear diatomic neutral molecule composed only by light atoms. For a full access to the coupled nuclear-electronic dynamics, one requires sub-femtosecond time resolution and a coincidence detection of both the ejected electrons and the residual charged molecular fragments. This is very challenging from the experimental point of view since:

- The small angular-resolved count rates associated with the molecular dissociation rate.
- The increased number of degrees of freedom present in molecular targets.

In this work we compare the theoretical results with experimental ones, obtained combining the RABBITT technique with an AttoCOLTRIMS apparatus consisting of a Cold Target Recoil Ion Momentum Spectroscopy (COLTRIMS) allowing for full 3D-coincidence detection [4, 5]. To visualize these dynamics, we ionize H_2 molecules in the energy region where molecular autoionization manifests upon population of doubly excited states (DES) [35, 147, 148]. The calculated relative phases of the EWP resulted not only strongly modified by the existence of resonances embedded in the continua [138, 139], but also influenced by the residual ion. This calls for a new interpretation of the spectral phases extracted from RABBITT spectrum, since nuclei cannot be considered as frozen entities anymore, but as active players during the photoionization process.

8.1 Introduction to the photoionization time delays

Time delay in scattering as an observable was introduced first by Wigner [149, 150]. The time delay correspond to the phase shift experienced by the scattered wave-packet relative to that wave-packet passing through the scattering region in the absence of any interaction potential. This can be calculated as the derivative of the phase shift δ_ε, or more generally (to include different partial waves) by the derivative of the dipole moment between the initial state ψ_0 and the final scattering state $\psi_f(\varepsilon)$ [149–152]:

$$t_w = \frac{\partial \delta_\varepsilon}{\partial \varepsilon} = \frac{\partial}{\partial \varepsilon} \arg\langle \psi_f(\varepsilon) | \hat{\mathbf{e}}_\mu \hat{\boldsymbol{\mathcal{O}}} | \psi_0 \rangle \tag{8.1}$$

On the other hand, from the experimental point of view, the phase of the one photon transition can not be retrieved directly. Instead, it can be accessed by using alternative techniques involving the exchange of multiple photons such as RABBITT or streaking [153–155].

Attosecond streaking relies on the ionization of the system by an XUV pulse (SAP) in the presence of a few-cycle IR pulse, where the interferences of the three different paths *a*, *e* and *d* (see figure 7.3) contributing to the same state is used. One key requirement to accomplish the streaking is that the duration of the XUV pulse needs to be much shorter than one IR cycle (see Chapter 7 where the pulses fulfil this condition). Under this conditions the momentum of the electron upon the XUV ionization would be $\mathbf{p_0}$. Then in the presence of the IR field, the final momentum $\mathbf{p}_f$ of the electron can be approximated as:

$$\mathbf{p}_f(\tau) = \mathbf{p}_0 - \mathbf{A}_{IR}(\tau) \tag{8.2}$$

where τ is the time at which ionization occurs (the moment at which the electron "feels" the IR field). The implicit assumption here is that the photoelectron instantaneously "feels" the IR field neglecting the potential created by the remaining ion. So the photoelectron spectrum is measured as a function of the delay between the XUV pump and IR probe, recording the arrival time in the continuum τ through the modulation of the momentum of the electron. The emission time would be delayed by the t_w time ($\mathbf{A}$ shifted by t_w):

$$\mathbf{p}_f(\tau) = \mathbf{p}_0 - \mathbf{A}_{IR}(\tau + t_w) \tag{8.3}$$

Therefore, t_w can be retrieved by fitting the mean value of the photoelectron momentum to the vector potential to the equation 8.3. Usually the fitted momentum correspond to those electrons emitted parallel to the light polarization

direction (θ_e=0°, 180°). So if the same XUV pulse is used to ionize the system from different states, recording the two streaked images of the momentum one can extract the photoemission time delay between the two states.

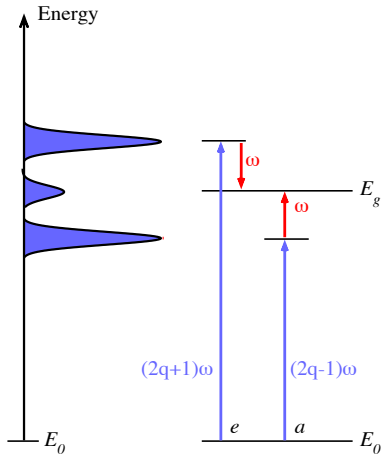

FIGURE 8.1: Schematic of the different quantum paths leading to the same state (SB). The SB can be reached by the path *a* where a lower harmonic (2q-1)ω and an IR photon ω are absorbed, or by path *e* where a higher harmonic (2q+1)ω is absorbed and an IR photon ω is emitted.

On the other hand the RABBITT technique uses a train of XUV attosecond pulses (APT), analogously a burst of coherent odd harmonic frequencies (2q+1)ω in combination with the IR used to generate the harmonics of the APT. The individual action of the APT will produce a photoelectron spectrum consisting on equidistant signals, mainbands (MB), separated by 2ω associated with the single-photon ionization of the system by each harmonic. However due to the presence of the IR field two photon transitions will take place, as results the sidebands (SB) appears. The same SB can be reached by two different quantum paths, either the absorption of a higher harmonic (2q+1)ω and the emission of one ω IR photon (path *e* see figure 8.1) or the absorption of a lower harmonic (2q-1)ω and the absorption of one ω IR photon (path *a*). The interference between this two quantum paths leads to a modulation of the signal intensity of the SB with the delay between the APT and the IR with frequency 2ω:

$$\mathcal{S}_{2q} \propto a + b\cos(2\omega t + \Delta\phi) \tag{8.4}$$

$$\Delta\phi = \phi_{2q-1} - \phi_{2q+1} + \phi_{IR} + \varphi_+ - \varphi_- \tag{8.5}$$

The steps to get these expressions were nicely explained in Chapter 7, note that since the SB are reached by two photon absorption necessarily would have *gerade* symmetry. If both the absolute value of the IR phase ϕ_{IR} and the harmonics phase ϕ_{2q+1}, ϕ_{2q-1} are known what we called "collective nuclear-electron" phase (φ_-, φ_+) can be determined. Is paramount to note that the "collective nuclear-electron" phase explicitly depend on both electron and nuclear degrees of freedom. From the signal of the SB one can extract the "collective nuclear-electron" phase and from it the time delay t_w [154, 155]:

$$t_w = (\varphi_+ - \varphi_-)/2\omega \tag{8.6}$$

There are two principal ways of extracting the phase from the SB signal. First one performs the Fourier transform of the SB signal, and the phase corresponding to the frequency $\omega = 2\omega_{IR}$ is the phase we are looking for (see figure 8.2). Alternatively, one performs the Fourier transform of the SB signal, filter the frequency $\omega = 2\omega_{IR}$, Fourier transform back to the time domain and then fit the remaining signal to equation 8.4 (see figure 8.2).

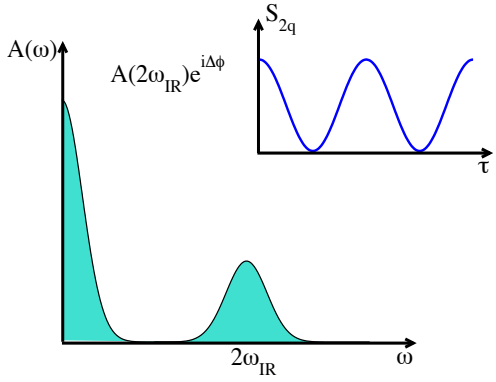

FIGURE 8.2: Schematic illustrating the use of the RABBITT method. Fourier transform of the SB signal ($\mathcal{S}_{2q}$) yielding the phase $\Delta\phi$ as a phase offset at $2\omega_{IR}$ in the Fourier plane.

Few points are worthy of discussion here. In the atomic case, this scattering phase is usually called the atomic phase (φ_-, φ_+) and has been unanimously defined as the sum of two contributions (not in the presence of doubly excited states

[151]): the Wigner scattering phase, and the continuum-continuum term due to the additional IR-induced electronic transitions. How to extend the concept of (φ_-, φ_+) to the molecular case is still an open question. Furthermore, one need to take into account the influence of the nuclear phases and the interferences between different states of the ion, as well as the dependence of the relative molecular orientation compared with the ionization field.

In the RABBITT scheme the intensity of the IR field should be kept low so only the second order transitions (2ω) contribute to the sidebands. In streaking technique, the photoelectron is captured parallel to the light polarization direction. Thus, the possibility of extracting the dependence of the time delay on the photoelectron ejection direction should be ruled out. While, for the RABBITT technique the photoelectrons are collected from all directions allowing to study such dependence [156]. Another disadvantage of the streaking technique is that one can only extract the t_w corresponding to mean value of the momentum. So in order to study the dependence of t_w with the energy of the photoelectron one needs to calculate (measured) the spectrum for several central frequencies of the XUV pulse. While for RABBITT in a single spectrum the information of several SB can be extracted.

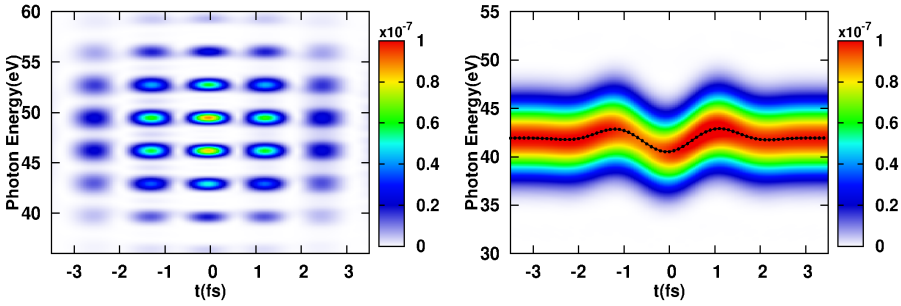

FIGURE 8.3: The typical RABBITT (left panel) and streaking (right panel) spectra are shown. The RABBITT spectrum displays only the population of the SB, while the streaking spectrum displays the mean value of the electron momentum (black points). The spectra correspond to the H_2^+ molecule within the *FNA* framework (R=3.0 a.u.).

We conclude this section by comparing the outputs of the two techniques. Figure 8.3 displays the typical RABBITT spectrum (left panel) and streaking spectrum (right panel) for the H_2^+ molecule within the *FNA* framework (R=3.0). In the RABBITT spectrum only the population of the SB ($^1\Sigma_g^+$ symmetry) is plotted. The population of the SB oscillate with the delay between the pump and probe as expected from equation 8.4. Another effect visible is the tilt in the position of the SB maximum, becoming evident by plotting the phase (time delay t_w) extracted

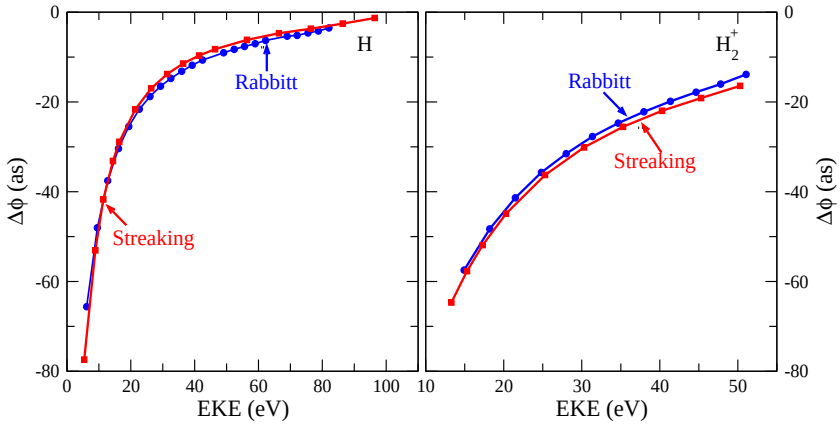

FIGURE 8.4: Comparison between the time shift obtained by using streaking and RABBIT techniques. The comparison is presented for the H atom (left panel) and the H_2^+ molecule (right panel) within the *FNA* framework (R=3.0 a.u.).

from this spectrum. In the streaking spectrum the mean value of the momentum is shown (black points). Notice that the width of the distribution correspond to the width of the SAP used to ionize the molecule. Figure 8.4 displays the comparison between the delays obtained with the two different techniques as a function of the electron kinetic energy (photon energy) for the H atom and H_2^+ molecule (*FNA* R=3.0). The good agreement highlight the possibility of extracting the t_w from completely different methods with attosecond resolution. In the following we are going to use the RABBITT technique to study the H_2 system due to the possibility of comparison with available experimental data.

8.2 Photoemission time delay in H_2

In the present section we aim to elucidate how the coupled nuclear and electronic degrees of freedom in combination with the DES affect the scattering phase, using the RABBITT technique in the H_2 molecule. To accomplish that, we have compared with experimental results obtained in the Ultrafast Laser Physics experimental group at ETH, in Zurich, led by Ursula Keller. The experiment was performed using randomly oriented molecules. Thus, the photoelectron momentum distributions for specific molecular orientations parallel ($^1\Sigma_u^+$ symmetry) and perpendicular ($^1\Pi_u$ symmetry) were recorded. We can only match the experimental outcome for the parallel orientation (perpendicular can not be calculated due

to the size of the problem). However, we are going to use the outcome of the parallel orientation (theory and experiment) in combination with the perpendicular (only experiment) orientation to achieve our goal.

We have considered a APT composed by four attosecond pulses with duration of T=500 as duration and intensity of I=10^9 Wcm^{-2}. The train is combined with an IR probe pulse of intensity I=3×10^{11} Wcm^{-2}, λ=775 nm ($\hbar\omega$=1.60 eV) and a duration of T=7.8 fs. For the APT we used the H_{17} harmonic. Both fields are linearly polarized and parallel to the molecular axis. We have defined the time delay between the XUV (APT) and the IR, as the difference between the times at which the pulses reach the maximum amplitude. In this work, negative time delays imply that the IR pulse arrives before the XUV one. In this case the multichannel expansion includes the two lowest ionic states ($1s\sigma_g$, $2p\sigma_u$) and partial waves for the emitted electron up to a maximum angular momentum l=11 enclosed in an electronic box of r_{max}=300 a.u.. The one-electron orbitals for the bound electron are consistently computed in the same radial box using single-center expansions with corresponding angular momenta up to l=16. The first two series of resonances $\mathcal{Q}_1$ and $\mathcal{Q}_2$ of both symmetries have been included. The use of such "huge" electronic box complies with all the requirements specified in 3.2. The vibrational (bound and dissociative) wave functions have been expanded in a 240 B-splines in a R_{max}=12 a.u. vibrational box.

Figure 8.5 displays the calculated (top panel) and measured (lower panel) coincidence pattern, integrated over the time delay between the APT and the IR. In both cases we can see the MB associated with ionization from each harmonic, panels ***b*** and ***d*** (only the XUV ($^1\Sigma_u^+$ symmetry)). In contrast with the atomic case, where all the energy is taken by the electron, here the energy is shared between electrons and nuclei. Thus, the MB will appear as diagonals in the coincidence spectrum. Each of one correspond to an specific photon energy, namely $\hbar\omega + E_0 = KER + EKE + W_\infty$ (energy conservation line). In the presence of the IR the SB appear between the MB, panels ***a***, ***c***, ***e*** and ***f***. As for the SAP, the probability for *direct* ionization is largest at low KER and decreases rapidly as the KER increases and practically vanishes around 3 eV. The probability observed at larger KER comes from autoionization and the *direct* ionization through the $2p\sigma_u$ channel, as the system evolve in time, the doubly excited states start to decay and both direct ionization and autoionization processes interfere. Notice that although autoionization in the parallel case is produced exclusively by $\mathcal{Q}_1\,^1\Sigma_u^+$ DES, in the perpendicular case (panel ***e***) would be $\mathcal{Q}_2\,^1\Pi_u$ the responsible (due to the low width of the $\mathcal{Q}_1\,^1\Pi_u$, see Chapter 5). The theory nicely reproduce the experiment in the parallel case. However the are some differences between theory and experiment. In fact, panels ***e*** and ***f*** present a double peak profile for ion fragments belonging to the low KER region, which is not visible neither in the total theoretical spectrum panel ***a*** nor in the XUV-only absorption case panels ***b*** and ***d***. Which

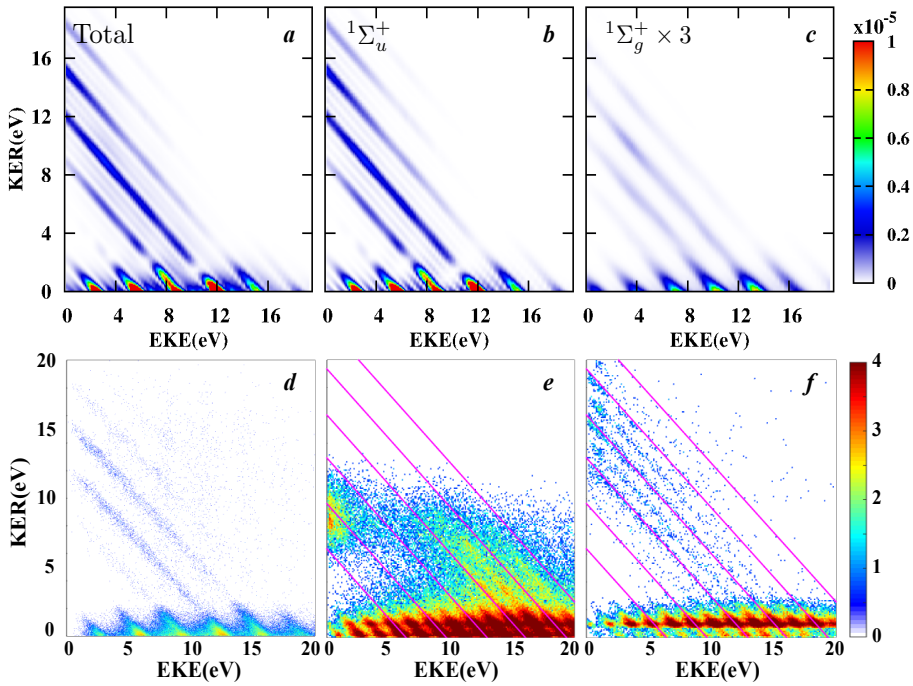

FIGURE 8.5: Calculated (top panel) and measured (lower panel) coincidence pattern integrated over time delays between the XUV and the IR. Panels ***a***: total spectrum, ***b***: $^1\Sigma_u^+$ contribution and ***c***: $^1\Sigma_g^+$ contribution (SB). Panels ***d***: Measured spectrum using only the XUV for parallel orientation of the light ($\beta_\parallel$), ***e***: Using XUV+IR for perpendicular orientation of the light ($\beta_\perp$), and ***f***: Using XUV+IR for parallel orientation of the light.

constitute the major discrepancy between the theory and the experimental measurements. This is a clear indication that the long-IR field is playing an active role during the evolution of the fragmentation process also known as bond-softening effect [16, 131]. For long time delays between the XUV and the IR the wave-packet created in the $1s\sigma_g$ by the XUV, moves and reaches a large internuclear distance. At large internuclear distances the $1s\sigma_g$ and the $2p\sigma_u$ are very close in energy and can be coupled by the IR (even by moderately intense fields). Resulting in ion fragments with slightly higher energy. The shorter pulses employed for the theoretical simulations prevents the appearance of the bond-softening signal at low KER. Note, that we chose such relatively short pulses in order to avoid unphysical reflections.

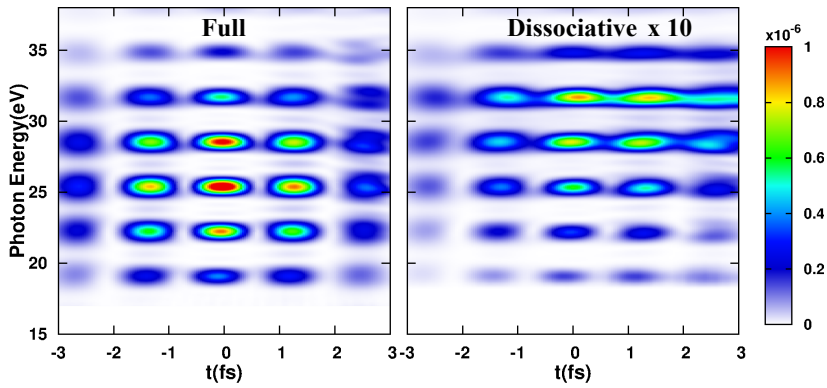

FIGURE 8.6: Theoretical RABBITT spectrum (only SB are displayed). Left panel: Taking into account dissociative and non-dissociative channels. Right panel: Taking into account only dissociative channel.

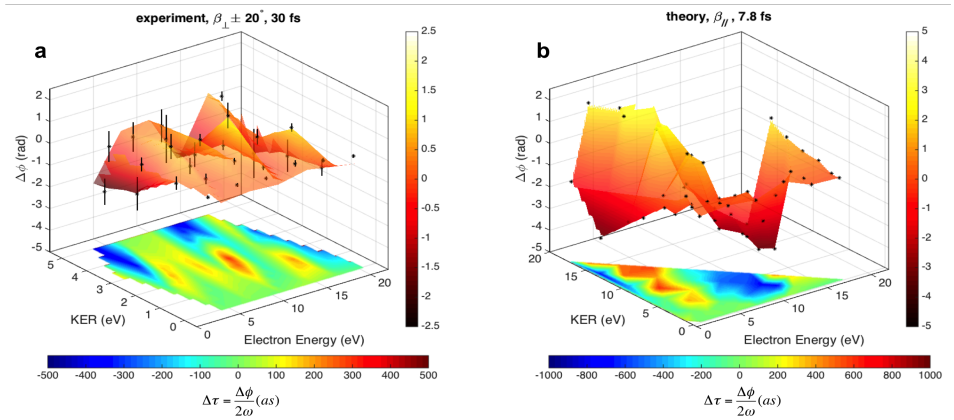

FIGURE 8.7: 3D nuclear-electron phase-time map. Panel ***a*** experimental extracted phases (3D surface) and corresponding time delay (2D projection at the bottom) for the $\beta_\perp$ as a function of both KER and electron energy. Phases and delay are expressed with two different colorbars. Panel ***b*** ab initio calculations. For the experimental data the vertical black lines indicate the errorbars

From figure 8.5 we can construct the typical RABBITT spectrum by integrating over the diagonals corresponding to an specific photon energy. The integration

can be done selecting regions of KER to highlight an specific effect. For instance, figure 8.6 displays the RABBITT spectrum (only SB are displayed) taking into account only the dissociative channel (right panel) and taking into account both dissociative and non-dissociative channels (left panel). While the SB in the "Full" spectrum present a clear modulation with 2ω the one in the dissociative channel are more fuzzy. This is consequence of the DES decaying mostly into the dissociative channel, producing the phase shift in the SB. This effect will remain hidden in the full spectrum due to dominance of the non-dissociative channel over the dissociative one.

To tackle the question on how to extract the scattering phase in the molecular case. We decided to build a 3D map showing the behavior of the extracted spectral phases as a function not only of the electron kinetic energy but also of the KER, similarly to figure 8.5 for the ionization probability. From the experimental point of view, there is no way to access the absolute scattering phase of the photofragments, since it is unknown when the XUV actually initiates the photoemission dynamics. Nevertheless, relative molecular phases can be extracted by computing the difference between two SB phases of the same order 2q but belonging to two different groups of photoemitted electrons, leading to the deletion of the XUV phase term $\Delta\phi_{XUV}$ and to direct comparison between theory and experiment. The choice of the reference to extract such relative molecular phase depends on which aspect of the photoemission process we want to highlight. In this case we calculated the relative phases as follows:

$$\Delta\phi_{2q} = (\Delta\phi_{2q}^{KER} - \Delta\phi_{2q}^{\Delta KER}) \tag{8.7}$$

where $\Delta\phi_{2q}^{KER}$ and $\Delta\phi_{2q}^{\Delta KER}$ are the phases extracted from the fit of the SB of order 2q from RABBITT spectrum integrating over the whole KER and integrating over the specific 1eV-KER interval, respectively. Basically, we subdivided the KER spectrum into intervals of 1 eV (the smallest interval we could choose due to statistical limitation in the experimental data) and construct out the RABBITT spectrum selecting only on those electrons in coincidence with the specific 1eV-KER intervals. Figure 8.8 presents the 3D correlation maps of the resulting relative phases (and times) as a function of the KER and the electron energy for the perpendicular (experiment) and parallel (theory) orientations. Panel ***a*** displays in particular the 3D map of the experimental relative phases for the perpendicular case $\Delta\phi_{2q}^{\beta_\perp}$, while panel ***b*** displays the ab initio calculation for the parallel case $\Delta\phi_{2q}^{\beta_\parallel}$. Both surfaces has been created by linearly interpolating the results reported as black dots. In both cases experiment and theory, the low KER-low electron energy region appears quite flat, while moving towards high energies, especially along the

KER axis, huge modulation of the nuclear-electron phase can be observed as a direct consequence of the population and autoionization from the $\mathcal{Q}_1{}^1\Sigma_u^+$ (theory) and $\mathcal{Q}_2{}^1\Pi_u$ (experiment) DES. Modulations can be observed even up to 20 eV in the KER axis. This behavior is expected when DES play a dominant role in the photoionization process. However, in this case is not only created by the DES but also by the coupled electron-nuclear dynamics as we can see in the figures. These 3D maps allow us to have a general view of the entire photoionization process from both points of views: the electron and the ion. If we can measure the relative scattering phase as a function of the KER, it means that we can define a new "time-delay" relative to the kinetic energy of the ion fragments. This further implies the possibility not only to study but also to control specific electron dynamics occurring only at specific internuclear distances.

To further support this $\Delta\phi_{2q}^{\beta}$ double-dependency, i.e. electron energy and KER, we defined a different relative phase using equation 8.7 by subtracting from the integrated KER phase $\Delta\phi_{2q}^{KER}$ a low-KER interval phase $\Delta\phi_{2q}^{\Delta KER}$ ranging from 0 eV to a variable upper bound. The latter was chosen to span from 0.98 to 1.24 eV, energies where the bond-softening effect is playing a significant role. This definition of the phase difference should highlight the high-KER component where autoionization is the dominant mechanism. Using this relative phase definition we could present the theoretical relative phases in figure 8.8 (panels ***c*** and ***d***) for the parallel orientation and compare with the experimental data for both molecular orientations (panels ***a*** for $\beta_{\parallel}$ and ***b*** for $\beta_{\perp}$). It is quite evident in panel ***a*** that, as the low KER upper bound goes from 0.98 to 1.24 eV, the profile becomes smoother. This indicates a lower limit within which it is possible to neglect bond-softening contributions, because by integrating a wider KER range, the eventual redistributions of fragmentation channels evens out. On the other hand, if we choose an upper KER integration bound that falls in between the energies at which bond softening is present, the redistributing effect will strongly impact on the resulting phase differences (low-KER interval: 0-0.98 and 0-1.0 eV in panel ***a***. Regarding the specific profile of the as a function of photon energy, there is a clear deep at about 29 eV followed by a sudden increase at about 32 eV while the other energy data points are relatively flat within the errorbars. This behavior is nicely reproduced by the theoretical calculations as shown in panel ***c*** and mainly associated to the influence of $\mathcal{Q}_1{}^1\Sigma_u^+$ DES to the molecular DI. The experimental perpendicular configuration shown in panel ***b*** shows two evident features. Below 30 eV, in fact, all curves overlap with each other, unaffected by the low-KER reference choice. Above 30 eV each curve evolves like in the parallel case, i.e. flattening as the low-KER upper bound increases, except for the 40 eV data points. At photon energies above the $\mathcal{Q}_2{}^1\Pi_u$ threshold (above 30 eV) the relative phase presents considerable phase-jumps due to the effective population of $\mathcal{Q}_2{}^1\Pi_u$ DES and subsequent

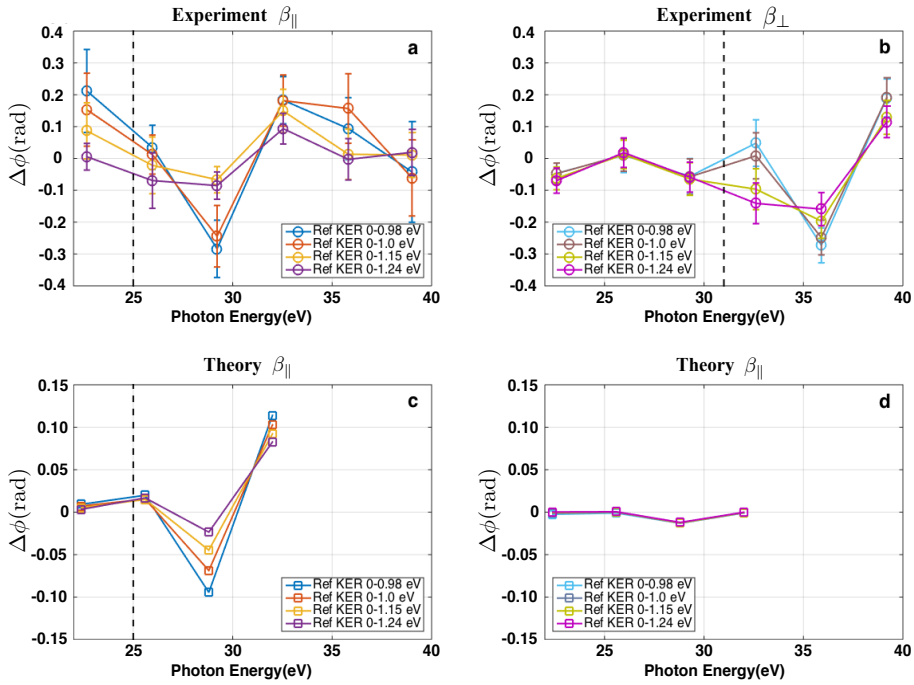

FIGURE 8.8: Relative molecular phases as a function of the photon energy. Experimental data are presented in panels ***a*** and ***b*** corresponding to a $\beta_{\parallel}$ and $\beta_{\perp}$, respectively. The black dashed lines indicate the $\mathcal{Q}_1{}^1\Sigma_u^+$ ***a*** - ***c***, and $\mathcal{Q}_2{}^1\Pi_u$ ***b*** DES thresholds. Panel ***c***: Calculations accounting for all interaction terms reproducing the experimental parallel case. Panel ***d***: truncated calculation removing autoionization.

autoionization. For photon energies below such threshold (below 30 eV), a completely flat profile is expected. Therefore, we conclude that the residual modulation observed in the experimental data is only referable to the nuclear-electronic coupling. This means that the movement of the remaining nuclei after ionization occurs on the ultrafast attosecond timescale and actively modulates the spectral phase of the escaping electron in DI processes. This is a key point that will have to keep into consideration every time a molecular DI process is investigated. Panel ***d*** shows the theoretical data points, although referred to the parallel case, obtained by truncating the calculation, preventing the $\mathcal{Q}_1{}^1\Sigma_u^+$ DES to autoionize, this was done by artificially removing the $\boldsymbol{\mathcal{Q}\mathcal{H}_{el}\mathcal{P}}$ matrix elements from the calculation. This would simulate the long-lived DES as it should be in the perpendicular case,

thus leaving only the electron-nuclear correlation terms. If autoionization of the DES cannot play any role, the expected relative phases should result perfectly flat like in atoms. Contrary to the expectation, the presence of modulations confirms the unavoidable coupling between electron and nuclear degrees of freedom, in line with the experimental observations.

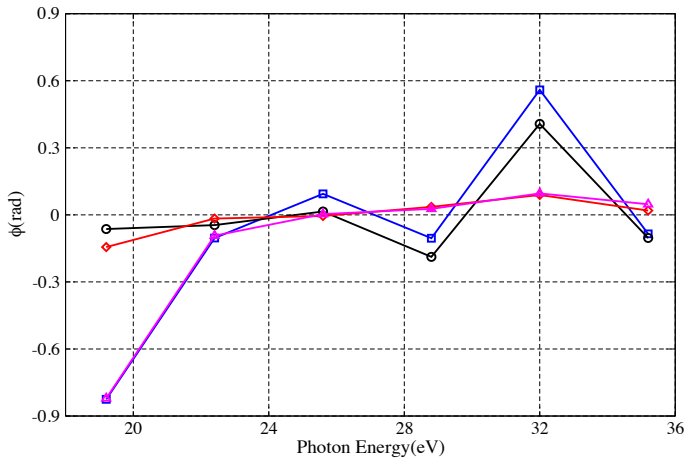

FIGURE 8.9: Calculated absolute phase. Blue squares: Full calculation. Black circles: Truncated calculation including only the $\mathcal{Q}_1{}^1\Sigma_u^+$ serie of DES. Red diamonds: Truncated calculations without including any DES. Magenta triangles: Truncated calculation including all the DES, but removing $\boldsymbol{\mathcal{Q}\mathcal{H}}_{el}\boldsymbol{\mathcal{P}}$ matrix elements (no autoionization).

Finally to strength our conclusions figure 8.9 displays the calculated phase for several truncated calculations, the truncation was done with the purpose of highlight an specific effect. For instance, removing the DES (not allowing the DES to be populated), the remaining structure in the phases can not be assign to any process related with autoionization. Here is clear, when compared the blue (full calculation) and black (including only the $\mathcal{Q}_1{}^1\Sigma_u^+$ DES) curves with magenta (no $\boldsymbol{\mathcal{Q}\mathcal{H}}_{el}\boldsymbol{\mathcal{P}}$) and red (without including any DES) curves, that the modulation observed around 28 eV is product of the autoionization of the $\mathcal{Q}_1{}^1\Sigma_u^+$ DES. On the other hand, comparing magenta and blue curves with the red and black ones we realized that the minimum at 19.2 eV is consequence of the nuclear dynamics. The wave-packet on the DES curves moves reaching large internuclear distances and then instead of decaying emits and IR photon populating the lower SB. Therefore, by comparing several truncated calculation we have been able to assign a source to

almost each structure of the spectrum. In any case, the structures in the extracted phases are consequence not only of the autoionization, but of the electron-nuclear dynamics itself.

To conclude, in the present work we carried out a complete investigation of photoionization dynamics in H_2 to tackle the complex net of correlations building up due to the presence of both nuclear dynamics and electron correlation on the same attosecond time scale. We have validated the theoretical results with state-of-the-art experimental measurements. We used in particular the RABBITT technique to extrapolate the relative phase of the photoemitted EWP belonging to a specific photoionization events selecting on electron kinetic energy, molecular orientation and KER. We observed a clear dependence of these relative phases as a function of all these three parameters confirming that:

- The phase of the escaping EWP is a sensitive probe of the electron and nuclear dynamics in molecular system.
- The double dependency on both electron kinetic energy and KER brought us to reconsider the meaning of these extracted phases.

With the definition of a new "time-delay" parameter depending on the KER, this work pioneers the possibility to extend our degree of knowledge and, more important, control over the entire photoionization process in molecular targets. This is a fundamental and compulsory step towards the possibility to measure and fully comprehend a complete chemical reaction.

Part IV

Two-photon single ionization of H_2 by UV laser pulses

Chapter 9

Control of H_2 dissociative ionization by UV laser pulses

As we have seen in great detail in the previous chapters, there are an extensive number of applications using attosecond XUV pulses in combination with few-femtoseconds IR fields. The experimental capabilities of using attosecond XUV pulses to explore and manipulate electron dynamics in atoms have been largely demonstrated in the last decade, and are expected to shed more light in forthcoming studies in molecules, as the most recent ones just presented in this manuscript. The complexity and richness of photo-induced processes in molecules, introduced through the nuclear degrees of freedom and the coupled electron dynamics, is still to be explored. Nevertheless, an alternative to HHG is the use of XUV pulses generated by free electron lasers (FEL) [19–22], where the intensities are considerably higher but still low enough to achieve a perturbative regime. In contrast with synhrotron radiation (employed in the recent studies described in Chapters 4 and 5), which also presents high tunability, the FELs generate finite pulses (pulse durations of tens of femtoseconds), and the high brilliance, which allows to investigate multi-photon electronic transitions. The continuing development of such intense sources has led to an increased interest in multi-photon processes. Specifically in molecules, where vibration and dissociation occurs in the femtosecond scale and, therefore, may compete efficiently with slow electronic processes. Therefore the use of XUV fs pulses opens up the possibility of study the role of the nuclear degrees of freedom in molecular ionization. In particular, to explore if the nuclear degrees of freedom can be used to induced physical effects not visible in atoms. In this context, recent theoretical studies [23, 24, 157] have shown the possibility of controlling the dissociative channel (DI)/non-dissociative channel (NDI) ratio by varying the pulse duration in a (1+1 REMPI) two-photon ionization scheme by the nuclear degrees of freedom in the intermediate state. These works also shown that, the NDI channel is completely dominant for frequencies $\hbar\omega \simeq 12.5$ eV and durations T$\geq$10 fs. This is a very compelling effect, because for neutral molecules photoionized by a single photon absorption, the NDI channel is always the most

largely populated.

In the present chapter, we aim to explore in detail two-photon single ionization of the H_2 molecule, with special emphasis on the possibility of controlling the DI/NDI ratio and the possibility of obtaining dynamical information (i.e., phases and amplitudes) on the neutral excited molecular target using the relatively long pulses generated in FEL facilities. In fact, this work has been performed in parallel with experiments performed at FERMI FEL by the group of Prof. D. Dowek in Institut des Sciences Moléculaires d'Orsay (France). It is worth to mention that our group have actively contributed to the design and guide the experiment, and to the preparation of experimental proposal for the beam-time at FERMI. This is a rather direct example where our theoretical method has demonstrated its predictive value. The properties of the FEL at FERMI are especially suitable for the problem under study. In the first place, it is the only facility that offers photon energies in the range $\hbar\omega$ $\sim$10-15 eV, which allows for few-photon single ionization of the hydrogen molecule. Moreover, they produce pulses of a few tens of femtoseconds (T$\sim$50-100 fs range), which are of the order of the vibrational motion in the excited molecule, making it a perfect fit to study the role of the coupled nuclear and electron dynamics in the outcome of two-photon NDI and DI. Furthermore, at this energy range, a two photon absorption leads to a population of the H_2 ($\mathcal{Q}_1\,^1\Sigma_g^+$) series of doubly excited states (see figure 9.3). These states can later decay (normally in the fs scale), interfering with *direct* component of ionization, making the problem even more attractive.

Our previous calculations describing multiphoton ionization after the interaction with short pulses (shorter than 10 fs) were performed by directly solving the time-dependent Schrödinger equation (TDSE). However, we need to match the experimental conditions with pulses in the T=50-100 fs range. The use of such long pulses prevent us to solve the TDSE, instead we use the time-dependent second order perturbation theory (TDPT) as explained in section 3.3. The use of the TDPT is adequate since the intensities reached at the UV frequencies are high enough to enable a significant ionization after two-photon absorption, but low enough that ensures a perturbative regime. Moreover, allows one to follow the dynamics in time and still use this long pulses. As a consequence we can not entrust the TDSE to mix the Feshbach sub-spaces, we need to write the total wave function in the continuum taking into account both sub-spaces [119]. For this purpose we have used the *local-approximation*, which allows one to address the problem beyond the *FNA* framework and at the same time to properly mix the Feshbach sub-spaces. The next section is devoted to a short description of the theoretical and technical details. Results are shown in the following sections.

9.1 Local Approximation

In this section we aim to give the main details of the *local-approximation* described in [119–121]. Within this framework the total wave function reads:

$$\Psi_{\alpha v l E}(\mathbf{r},R) = \sum_r \psi_r(\mathbf{r},R)\xi^r_{\alpha v l E}(R) + \psi^{\varepsilon}_{\alpha l}(\mathbf{r},R)\chi_v(R) + \lim_{\eta\to 0}\sum_r \sum_{\alpha' l'} \int d\varepsilon' \times \frac{1}{\varepsilon_r - \varepsilon' + i\eta}\langle\psi_r(\mathbf{r},R)|\hat{\mathcal{Q}}\hat{\mathcal{H}}_{el}\hat{\mathcal{P}}|\psi^{\varepsilon'}_{\alpha' l'}(\mathbf{r},R)\rangle^* \psi^{\varepsilon'}_{\alpha' l'}(\mathbf{r},R)\xi^r_{\alpha v l E}(R) \tag{9.1}$$

here χ_v is the vibrational wave function of the ion (with energy E_v), ψ_r and $\psi^{\varepsilon}_{\alpha l}$ are the electronic wave functions in the resonance r and in the continuum (with energy ε), $E = E_v + \varepsilon = \hbar\omega + E_0$ is the total energy, $\varepsilon_r = E_r(R) - E_0(R)$ is the local electron energy and the functions $\xi^r_{\alpha v l E}$ describe the relative motion of the nuclei when the system is in the r resonant state. This functions can be calculated by solving:

$$\left[E - E_r(R) - \delta E_r(R) + \frac{i}{2}\Gamma_r(R) - \hat{T}(R)\right]\xi^r_{\alpha v l E}(R) = V^r_{\alpha v l E}(R) \tag{9.2}$$

here $\delta E_r(R)$, $\Gamma_r(R)$ are the energy shift and the autoionization width of the resonance r respectively and together with the terms $V^r_{\alpha v l E}(R)$ can be expressed as:

$$V^r_{\alpha v l E}(R) = \langle\psi_r(\mathbf{r},R)|\hat{\mathcal{Q}}\hat{\mathcal{H}}_{el}\hat{\mathcal{P}}|\psi^{\varepsilon}_{\alpha l}(\mathbf{r},R)\rangle\chi_v(R) \tag{9.3}$$

$$\delta E_r(R) = \sum_{\alpha l} \wp \int d\varepsilon \frac{|\langle\psi_r(\mathbf{r},R)|\hat{\mathcal{Q}}\hat{\mathcal{H}}_{el}\hat{\mathcal{P}}|\psi^{\varepsilon}_{\alpha l}(\mathbf{r},R)\rangle|^2}{\varepsilon_r - \varepsilon} \tag{9.4}$$

$$\Gamma_r(R) = 2\pi \sum_{\alpha l} |\langle\psi_r(\mathbf{r},R)|\hat{\mathcal{Q}}\hat{\mathcal{H}}_{el}\hat{\mathcal{P}}|\psi^{\varepsilon=\varepsilon_r}_{\alpha l}(\mathbf{r},R)\rangle|^2 \tag{9.5}$$

Computing the $\xi^r_{\alpha v l E}$ wave functions is the hardest part in the procedure. These function enclose information concerning the interferences between the *resonant* and *direct* dissociation processes, so an accurate solution of equation 9.2 must be obtained in order to properly describe such processes. At photon energies where the doubly excited states are seated both components of these functions oscillate strongly (see figure 9.1). Besides, due to the non-locality (i.e. couple different energies and channels) of equation 9.2 an accurate solution is difficult to

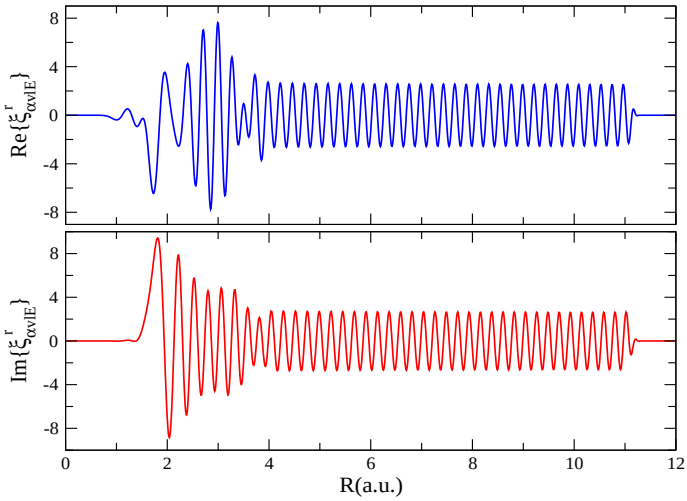

FIGURE 9.1: Nuclear wave function $\xi^r_{\alpha vlE}$ for E=-0.1724 (i.e $\hbar\omega$=27 eV) and E_v=-0.3824 a.u. (i.e 1.6 eV protons) associated with the lowest $^1\Sigma^+_u$ doubly excited state. Upper panel: Real component. Lower panel: Imaginary component.

obtain. Taking this into account, we use as a basis the eigenfunctions resulting from the diagonalization of equation 2.57 using the $E_r(R)$ potential energy curve corresponding to each resonance r.

$$\xi^r_{\alpha vlE}(R) = \sum_i c^{ri}_{\alpha vlE}\chi^r_i(R) \tag{9.6}$$

Inserting equation 9.6 into equation 9.1 and projecting onto χ^r_j will produce a system of linear equations that can be solved with any standard method. In order to avoid any unphysical reflections, we include a short range optical potential (absorber) in the close vicinity of R_{max}.

$$v(R) = \begin{cases} 0 & \text{if } R \leq \mathcal{R} \\ i\mathcal{M}(R-\mathcal{R})^2 & \text{if } R > \mathcal{R} \end{cases} \tag{9.7}$$

where $\mathcal{R} = R_{max} - 1$ and $\mathcal{M}$=30 a.u.. Although the inclusion of the absorber has no consequence in the inner region of the vibrational box, as shown in figure 9.1 it is essential to properly describe the asymptotic behavior of the wave function (see [119] for details). Note that while the second term in equation 9.1 accounts

for the *direct* component of the spectrum the first and the third account for the strong interference between the *direct* and the *resonant* channels. It is worth to mention, that in contrast with the previous implementations of the method where only one resonant state was considered, here we are taking into account the six lowest corresponding to each series. Moreover, since autoionization below the threshold is not allowed, all the electronic matrix elements $\mathcal{QH}_{el}\mathcal{P}$ have been made zero beyond the point where energy the doubly excited states crosses the threshold (see figure 9.3).

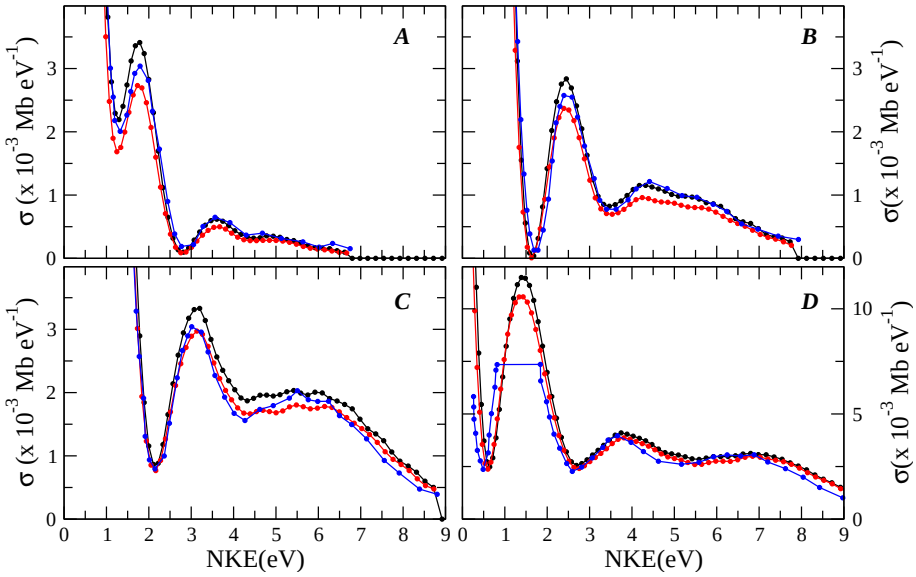

FIGURE 9.2: Single photon ionization cross section as a function of the NKE, for different photon energies (Panels ***A***: $\hbar\omega$=25 eV, ***B***: $\hbar\omega$=26 eV, ***C***: $\hbar\omega$=27 eV and ***D***: $\hbar\omega$=28 eV). The comparison between different approaches is presented. Black points: *local-approximation*, Red points: Results extracted from the exact time-independent calculation [119], Blue points: Results extracted from solving the TDSE [103].

All the ingredients to calculate the total wave function have been calculated the methods previously explained (see Chapter 2). The multichannel expansion includes the two lowest ionic states ($1s\sigma_g$, $2p\sigma_u$) and partial waves for the emitted electron up to a maximum angular momentum l=11 enclosed in an electronic box of r_{max}=300 a.u.. The one-electron orbitals for the bound electron are consistently computed in the same radial box using single-center expansions with corresponding angular momenta up to l=16. The first two series of resonances $\mathcal{Q}_1$

and $\mathcal{Q}_2$ have been included. The vibrational wave functions have been expanded in a 240 B-splines in a R_{max}=12 a.u. vibrational box.

In figure 9.2 we show the single-photon ionization ($^1\Sigma_u^+$ final symmetry) probabilities as a function of the NKE in the photon energy range $\hbar\omega$=25-28 eV. At these energies the $\mathcal{Q}_1\,^1\Sigma_u^+$ series of doubly excited states are reached (see section 5.1). The figure also display the comparison between the results using the *local-approximation* and results obtained from solving the TDSE [103] and from exact time-independent calculation [119]. The *local-approximation* accounts for all the structures coming for the strong interference between the amplitudes associated with the *direct* and the *resonant* channels. Thus, nicely reproducing the exact calculations not only qualitatively but also quantitatively in the whole range of energy as shown in the figure.

9.2 Electron-nuclear dynamics *vs* pulse duration

In the last section we have demostrated that we can reproduce the exact calculations down to slightly details using the *local-approximation*. Therefore, we can use it in combination with the TDPT to study the two-photon single ionization process, so in the following we are considering two-photon processes using the TDPT. In a two-photon transition case, using linearly polarized light parallel to the molecular axis, the optically allowed electronic transitions correspond to the sequence $^1\Sigma_g^+ \Rightarrow {}^1\Sigma_u^+ \Rightarrow {}^1\Sigma_g^+$ due to the dipole selection rules. Thus, states of *gerade* symmetry are the only ones populated by a two-photon process. Given the photon energies employed, the first photon absorption excites the molecule, mostly into the $B^1\Sigma_u^+ / B'^1\Sigma_u^+$ intermediate excited sates of the neutral, and the second photon absorption ionizes the target. Figure 9.3 displays the schematic of the process alongside the relevant potential energy curves. For this purpose we use an XUV pulse linearly polarized and parallel to the molecular axis with a gaussian envelope and intensity of I=10^{12} Wcm^{-2}. We have considered several pulse durations T=2, 10, 20, 30 and 40 fs and photon energies such that the absorption of a single photon will not ionize the molecule. For different pulse durations different mechanisms take place. As the pulse duration increases (bandwidth decreases), up to the order of the vibrational energy spacing of the states involved, the "vibrational selectivity" [23, 24] through specific intermediate states becomes a factor.

Figure 9.4 displays the electron momentum spectrum corresponding to the NDI channel for two different photon energies $\hbar\omega$=12.2 eV and $\hbar\omega$=14.0 eV and a pulse duration of T=2 fs. While in figure 9.5 the EKE spectrum is presented. The EKE spectrum have been obtained integrating the probability over the NKE (sum over bound states of the ion), so taking into account both DI and NDI channels. These energies are in resonance in a vertical one-photon transition from the

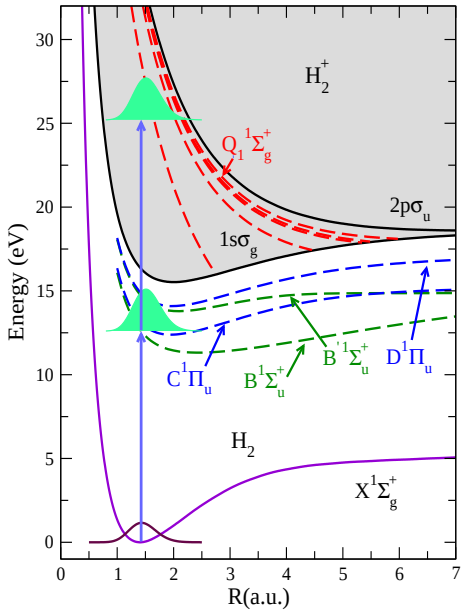

FIGURE 9.3: Potential energy curve of H_2. The figure displays the bound states of *ungerade* symmetry (green and blue dashed lines). The $\mathcal{Q}_1\,^1\Sigma_g^+$ (dashed red line) serie of doubly exited states is also shown. Verticals arrows indicate a (1+1) REMPI two-photon transition leading to ionization.

ground state to the $B^1\Sigma_u^+$ and $B'^1\Sigma_u^+$ states respectively. For this short pulse duration the use of the TDSE still is viable option. Consequently, for both photon energies we have compared the results obtained by solving the TDSE and using the TDPT. The combination of TDPT with the *local-approximation* accurately reproduces the exact solutions obtained by solving the TDSE as shown in both figures. The momentum distributions are symmetric as it should be for this photon energies and pulse durations [157]. The population at p_z=0 is consistent with the dominant d (l=2) partial wave for the electron in the continuum, also expected. On the other hand, the electron kinetic energy distributions present a shoulder in the region EKE$\leq$6 eV (DI channel). This is consequence of the population of the doubly excited states, which later decay and interfere with the *direct* ionization, enhancing the population of the DI channel. As we have discussed in the preceding chapters, the delayed autoionization process preferentially manifests in the dissociative ionization channel. Thus, the properly inclusion of the doubly excited sates is paramount to described two-photon processes and in particular

the NDI/DI channels ratio.

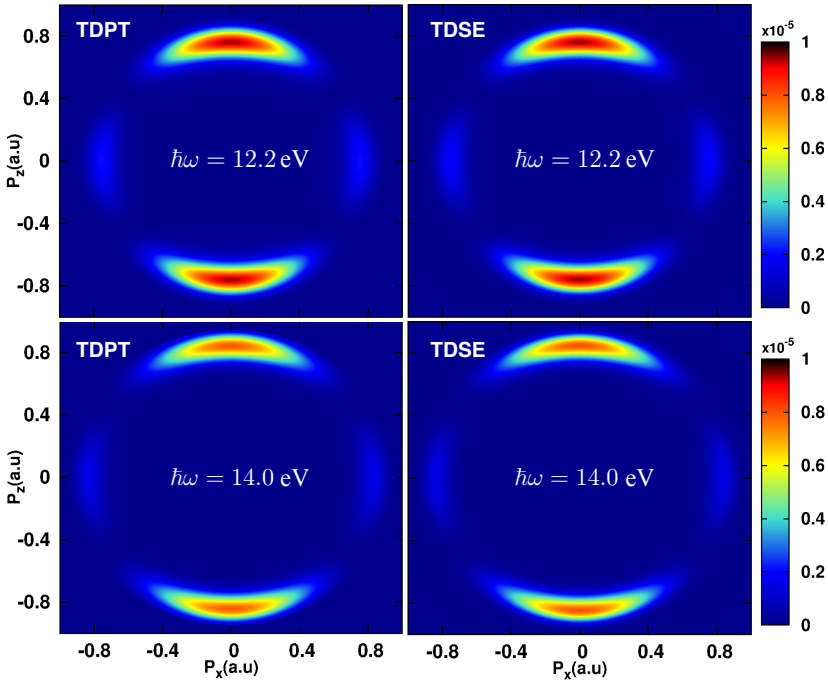

FIGURE 9.4: Calculated electron momentum distributions. The comparison between the TDSE (right panel) and TDPT (left panel) results obtained for T=2 fs pulse duration and different photon energies ($\hbar\omega$=12.2 eV and $\hbar\omega$=14.0 eV) is shown.

Figure 9.6 displays the comparison between the calculated EKE spectrum for $\hbar\omega$=12.51 eV and several pulse durations and the measured spectrum for the same energy. Again we have integrated over the NKE (sum over bound states of the ion) in both, the calculated and the measured spectrum. This energy is in resonance with $B^1\Sigma_u^+(v{=}9)$ intermediate state. The theoretical spectrum have been renormalized with the pulse duration for a better comparison. The theory for T=40 fs duration seems to have reached the infinite-time duration limit. However the comparison with the experiment suggest the opposite, that such limit have not been reached, as the experiment seems to have (the estimated pulse duration in the experiment is T$\sim$50-100 fs). The agreement between theory and experiment is reasonable, as the duration of the pulse increases. We have checked that the NDI region of the spectrum completely correlates with the FC factor between the

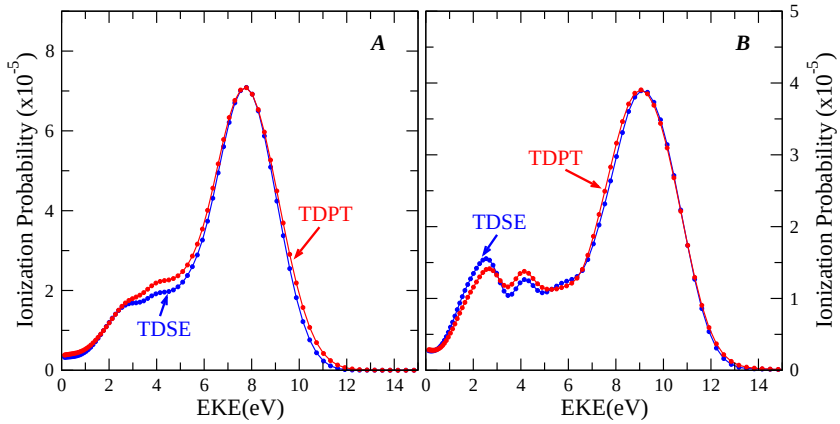

FIGURE 9.5: Electron kinetic energy spectrum. The comparison between the TDSE and TDPT results obtained for T=2 fs pulse duration and different photon energies (Panels ***A***: $\hbar\omega$=12.2 eV and ***B***: $\hbar\omega$=14.0 eV) is shown. The probabilities have been renormalized for a better comparison.

intermediate and the final vibrational states, which may be helpful in the implementation of new models. Figure 9.7 displays the MFPADs for specific values of the electron kinetic energy EKE=3.97 eV and EKE=5.92 eV (DI channel), EKE=7.60 eV and EKE=8.52 eV (NDI channel) corresponding to the spectrum in figure 9.6. The MFPADs have been renormalized by the pulse duration for a better comparison. We have taken into account the direction ejection of the ion, meaning that we have projected the wave function onto an specific center (see Chapter 3) and integrated over NKE energy (sum over bound states of the ion). In the NDI channel (right panel) the shape of these MFPADs are consistent with the dominant production of continuum electrons in the d (l=2) partial wave. In this channel the MFPADs are completely symmetric respect to θ=90° for all the pulse durations as expected. However that is not the case for the NDI channel (left panel). For T=10 fs the MFPADs are symmetric as expected from previous works [157, 158], but as the pulse duration increases the MFPADs become more and more asymmetric. This effect has a very simple explanation, as the pulse duration increases the population in the $2p\sigma_u$ grows, we have checked it by plotting figure 9.6 for each threshold. Thus, a coherent superposition of ionic states possessing different symmetry, namely $1s\sigma_g$ and $2p\sigma_u$, is produced (localizing the remaining bound electron) and as a consequence generating the asymmetry in the MFPADs. Notice that in this situation the MFPADs will be mostly a p+d combination, so aside from the asymmetry it should keep the same shape. In a simplistic picture, for long

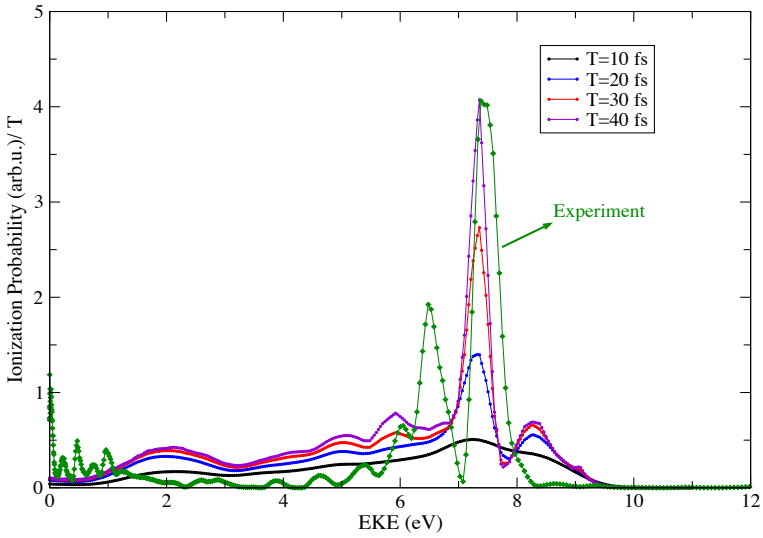

FIGURE 9.6: Calculated and measured electron kinetic energy spectrum. For $\hbar\omega$=12.51 eV and different pulse durations (see legends).

pulse durations the wave-packet created in the $B^1\Sigma_u^+$ (see figure 9.3) propagates to higher internuclear distances where the $1s\sigma_g$ and the $2p\sigma_u$ are close in energy, and both thresholds can be effectively populated by the second photon. Hence, the analysis of the MFPDs integrated over proton kinetic energy for this particular orientation provides aditional information that can be used to understand the physics of the two-photon ionization process.

In the limit of low pulse intensities, where depletion can be neglected (which is the case for I=10^{12} Wcm^{-2}) two photon absorption processes can be classified into two different regimes. The first one is the so called *nonsequential* or *direct* regime where both photons are absorbed almost simultaneously. In this regime the probability of ionization scale linearly with the pulse duration P_{ion} $\propto$T. The second regime is the so called *sequential* where the photons are absorbed in to well separated events. In this regime the probability of ionization scale quadratically with the pulse duration P_{ion} $\propto$T^2. Taking this into account it is interesting to notice that for some angles we find a linearly dependence with T and for other it deviates from it (it is a mixture of T and T^2, which is actually expected in most cases). Interestingly at EKE=8.52 eV for the photoelectron energy, the scaling is quite close to T, thus implying a more *nonsequential* process. The same regime can be observed in the electron kinetic energy distribution figure 9.6 for EKE$\geq$8 eV.

Finally figure 9.8 shows the separate contribution of the NDI and DI channels

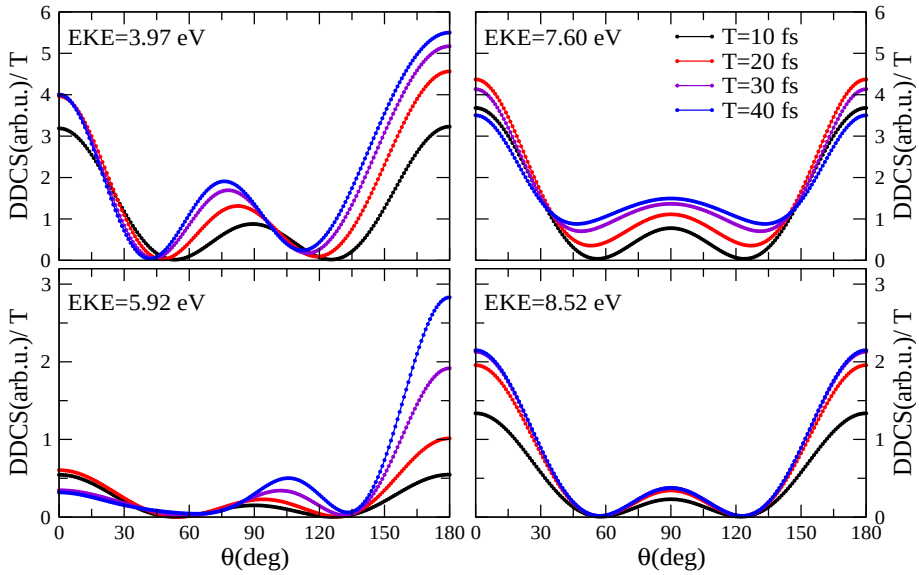

FIGURE 9.7: MFPADs for each pulse duration (see legends) and for different specific values of electron energies: 3.97 eV and 5.92 eV (on the left, DI channel) and 7.60 eV and 8.52 eV (on the right, NDI channel)

to the ionization probability, for the same pulse durations as in figure 9.6. Notice that for $\hbar\omega$=15.4 eV single photon single ionization channel opens up, however this channel has not been included in this figure. As can be seen, the DI and NDI have a similar behaviour for all pulse durations. In the region $\hbar\omega \geq$12.24 eV the DI channel dominates, similar results were reported in [23, 24] for a T=10 fs pulse. This behaviour was attributed to the more favourable FC overlap between the $^1\Sigma_u^+$ vibrational intermediate states and the final dissociative states. However, at $2\hbar\omega$ the doubly excited states are effectively populated, these states decay enhancing the relative weight of the DI channel population. Therefore, the combined action of the "vibrational selectivity" produced by the narrow bandwidth (typically of the order of the vibrational energy spacing of the states involved) of the pulses [24, 157] and the role of the doubly exited states are responsible for this behaviour. For the NDI channel after the raise in the threshold region, a (1+1 REMPI) process through the $B^1\Sigma_u^+$ intermediate state leads to a pronounced peak around $\hbar\omega$=12.0 eV, a similar peak involving the $B'^1\Sigma_u^+$ is also expected but barely visible in the figure. Whereas, for the NDI channel a significant part of the peak in the probability at $\hbar\omega$ =12.24 eV comes from autoionization of the first doubly excited state

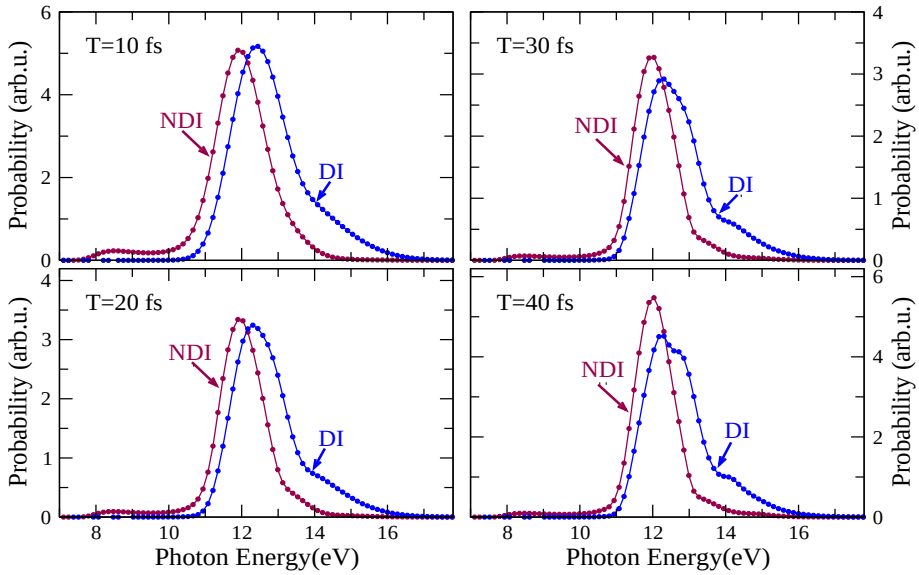

FIGURE 9.8: Ionization probabilities as a function of the photon energy for different pulse durations T=10, 20, 30 and 40 fs. Maroon points: Non-dissociative ionization probability. Blue points: Dissociative ionization probability.

[157]. While the shoulder around $\hbar\omega \sim$14 eV is probably related with the autoionization of the second doubly excited state (which can be reached around $2\hbar\omega$ see figure 9.3).

In summary we have presented a theoretical study of the two-photon single ionization of H_2. We have used the TDPT in combination with *local approximation*, which allows one to use pulses tens of femtosecond long. This combination accounts for all electronic and vibrational degrees of freedom and properly describes autoionization. We have explicitly checked te accuracy of the approximation by comparison with the TDSE solution. We have shown that for T$\geq$10 fs pulse duration and $\hbar\omega \geq$12.24 eV energy the DI channel dominates over NDI one as predicted in [23, 24, 157], due to the narrow bandwidth of the pulses. In this energy region the presence of doubly excited states enhance the dominance of DI over NDI one. So we confirmed that by varying the pulse duration, it is possible to control the DI/NDI ratio. We also have found, for T>10 fs, asymmetric MFPADs in the DI channel, consequence of the growing weight of the $2p\sigma_u$ ionization threshold as the pulse duration increases. Providing a simple way to characterize interferences resulting from the coherent superposition of different

indistinguishable quantum paths. We have reached a very reasonable agreement between theory and experiment, validating the theory. Although, pulses longer than T=10 fs lead to very similar results in the NDI channel for the DI one this is not the case, so for all practical purposes, they can not be considered as pulses of infinite duration which is responsible of the main differences between theory and experiment.

Chapter 10

Conclusions

This thesis has provided a detail theoretical description of the imprint of electron correlation and the coupled electron-nuclear degrees of freedom on processes triggered by different radiation sources in the hydrogenic molecules. In most the process studied, the theoretical results have been supported by experimental measurements, possible to perform only with the recent technicals developments. We have relied on the TDSE and the TDPT, including both electronic and nuclear degrees of freedom within the BO approximation, to describe such processes. Moreover, we have implemented new models, capable of describing the main characteristics of such processes only with a handful of ingredients.

We first studied one-photon single ionization of H_2 using synchrotron radiation in two different regions of the energy spectrum. At high photon energies ($\hbar\omega$=400 eV), we have used for the first time photoionization to examine parts of the H_2 two-electron wave function, in which electron-electron correlation beyond the mean-field level is prominent. We visualized the dependence of the correlated two electron wave function on the internuclear distance. Thanks to the recent technical advances, experiments studying electron correlation at high energies were possible, with detection techniques that allow the distinction of different channels, as the contribution of the Coulomb explosion after double ionization. We have successfully compared with experimental data. We have also studied the Young's slit-like patterns and the confinement effects a this energy, manifesting through the electron angular distributions. In the near future, it would be interesting to extend the imaging technique to larger molecular targets, where there are available tools to describe photoionization [53, 159]. Moreover, in the context of high-photon energies, there are some open questions from the theoretical side, for instance, the possibility of exploring the contribution non-dipole couplings. We have also explored the lower energy region, $\hbar\omega$=20-60 eV, where the doubly excited states are significantly populated. We have reported the vibrationally resolved photoelectron spectra of H_2 exhibiting the signature of autoionizing states. Using the fast nuclear motion as an internal clock in combination with a simple

analytical model we were able to reconstruct the time evolution of the autoionization process. The reconstruction procedure is similar to that followed by Gruson et al [101] in He, with the important difference that here the phase information is not retrieved by using an ultrashort pulse, but from the internal probe provided by the nuclear motion. Our theoretical results are supported by experimental measurements, being the first experiment (to our knowledge) capturing the signature of doubly excited states in the non-dissociative channel.

We have also considered typical attosecond XUV pump-IR probe schemes to retrieve real-time information of the coupled electron-nuclear dynamics in H_2. The RABBITT technique has emerged to be one of the most reliable method to extract photoemission times delays. While most of the studies have been made in atoms, here we have gone further and investigated the effect of autoionization and the nuclear degrees of freedom on the phase of the photoemitted EWP in H_2. We found the phases to be a sensitive probe of the electron and nuclear dynamics in molecular system. At the same time its strong dependence on both EKE and NKE brought us to reconsider the meaning of these extracted phases in the molecular systems. Again we have successfully compared our theoretical calculations with experimental data, obtained with state-of-the-art AttoCOLTRIMS apparatus. Alternatively to the APT using in the RABBITT technique, we have employed a SAP in combination with a weak IR to induce, and ultimately control, asymmetries in the electron ejection direction. In contrast with previous works, where the interference between ionic states was used to induce asymmetry [15, 16, 69], here we used interferences between different quantum paths leading to energy-degenerated states with different symmetry e.g. *gerade* and *ungerade*. The asymmetry can be controlled by varying the relative phase between the pump and probe. Similarly to the photoemission time delays case we have found a distinct influence of autoionization on the asymmetry.

In a more standard approach, we have combined one-photon single ionization with XUV pump-IR probe technique to study the relevance of electron-electron correlations in the dissociative photoionization of D_2 through highly excited states of the D_2^+ molecule. Such a process is impossible without electron-electron correlation. The presence of correlations between the two electrons in D_2 dictates the photoexcitation and the consecutive dissociation processes. The dissociation process results in a superposition of nuclear wave packets evolving simultaneously on different potential energy curves (ionization thresholds) of the parent ion. Again we have successfully compared with experimental data. The experiment has two different steps, each one validated by our theoretical calculations. In the first one synchrotron radiation is used to extract the branching ratios between each dissociation channel. In the second step time resolved XUV pump-IR probe is used to map the energy distributions of the molecular fragments after Coulomb explosion. However, there are still a lot to be done, for instance develop

an exact ab-initio method to describe two-color Coulomb explosion processes in H_2/D_2 molecules. In this context, this work has provided an initial step towards this goal.

Finally, motivated by the recents experiments performed at FERMI FEL, we have implemented a new version of the method to study the role of the coupled electron-nuclei dynamics in two-photon (single color) single ionization of H_2/D_2. The new formalism combine the *local-approximation* with a 2^{nd} order TDPT, allowing to explore longer pulses in consequence with the ones produced at FERMI. We have ensured the accuracy of the approximation by comparing with exact TDSE calculations. We have confirmed that is possible to manipulate the DI/NDI ratio by varying the pulse duration. For durations T$\geq$10 fs, due to the narrow bandwidth of the pulses (vibrational selectivity) energy the DI channel dominates over NDI one as predicted in previous work [23, 24, 157]. In this pulse duration interval, we have found asymmetries in the angular distributions consequence of the electron localization, providing a simple way to characterize interferences resulting from the coherent superposition of different indistinguishable quantum paths. In this context, this work have paved the way for deciphering the role of nuclear degrees of freedom in molecular photoionization.

Chapter 11

Conclusiones

Esta tesis ha proporcionado una pormenorizada descripción teórica de los diferentes procesos que tienen lugar en moléculas de H_2/D_2 bajo la acción de las diferentes tipos de radiación láser. Prestando especial interés al efecto de la correlación electrónica y el acoplamiento entre los grados de libertad electrónicos y nucleares en procesos ultrarrápidos observados en la ionización molecular. Para ello, hemos empleado métodos ab-initio que permiten resolver numéricamente la ecuación de Schrödinger dependiente del tiempo, en combinación con modelos analíticos capaces de describir los procesos estudiados y de extender las predicciones teóricas a sistemas más complejos. La mayor parte de los resultados han sido obtenidos en estrecha colaboración con diferentes grupos experimentales.

En un primer lugar, hemos investigado la ionización inducida por la absorción de un solo fotón en diferentes regiones del espectro. En el caso de fotones de altas energías ($\hbar\omega$=400 eV), hemos usado por primera vez la fotoionización para distinguir los distintos términos responsables de la correlación electrónica en la función de onda del H_2, y al mismo tiempo discernir como varían dichas términos en función de la distancia entre los núcleos. Simultáneamente hemos encontrado efectos de confinamiento y patrones de difracción reflejados a través de las distribuciones angulares electrónicas. A bajas energías ($\hbar\omega$=20-60 eV), donde los estados doblemente excitados de la molécula son accesibles, hemos reportado los espectros foto-electrónicos resueltos vibracionalmente, donde se observa el efecto del proceso de autoionización. La presencia del movimiento nuclear actúa como reloj interno del sistema permitiendo reconstruir la evolución temporal del proceso de autoionización. El proceso de reconstrucción es similar al empleado por Gruson et al [101] en He, no obstante, en nuestro caso hemos usado el movimiento nuclear como *probe* interno en lugar de un pulso ultracorto.

En un segundo bloque, hemos considerado el uso de técnicas de XUV *pump*-IR *probe* para estudiar en tiempo real la correlación entre los grados de libertad electrónicos y nucleares. Usando la técnica RABBITT hemos extraido las fases de los

estados electrónicos del continuo. Hemos demostrado que dichas fases representan una vía directa para el estudio de la dinámica molecular en su escala de tiempo característica. Por otro lado, su fuerte dependencia con las energías del electrón y los núcleos nos llama a reconsiderar su significado físico en sistemas moleculares. Este es el primer estudio en el que se emplea la técnica RABBITT en moléculas ligeras, y por tanto, la primera demostración teórica y experimental del efecto del movimiento nuclear en la definición y extracción de estas fases. Alternativamente hemos usado un pulso aislado XUV junto con un campo IR para inducir y controlar la emisión asimétrica del fotoelectrón. Dicha asimetría proviene de la interferencia resultante entre distintas trayectorias cuánticas que permiten acceder a estados energéticamente degenerados pero con distinta simetría espacial. Hemos demostrado que dicha asimetría puede ser controlada variando la fase relativa entre el XUV y el IR. De manera similar a las fases extraídas con la técnica RABBITT, las asimetría refleja de manera distintiva el efecto de la autoionización.

Por otro lado, usando un esquema *pump-probe* más "estándar", investigamos la disociación ultrarrápida de estados catiónicos excitados tras ionizar la molécula de D_2 usando un pulso XUV. La excitación-ionización a estos estados mediante la absorción de un sólo fotón es exclusivamente debida a los términos de correlación electrónica. En el caso de pulsos ultracortos, la interacción con el láser da lugar a una superposición de estados del ión. La imágen temporal de la dinámica ultrarrápida asociada a este proceso es capturada en la explosión Coulombiana de la molécula, causada por la subsequente absorción de un fotón IR. Dicha imagen temporal en combinación con el estudio de la ionización provocada por la absorción de un fotón permite determinar el peso relativo de cada estado iónico en la disociación.

Por último, hemos investigado la ionización inducida por la absorción de dos fotones a través de estados intermedios resonantes con la energía del fotón. Este estudio está motivado por mediciones recientes llevadas a cabo utilizando laseres de electrones libre FEL. Seleccionando los estados vibracionales (intermedios) que son excitados, lo que es posible gracias a la flexibilidad y resolución de los FEL en la emisión de frequencias, hemos estudiado la influencia del movimiento nuclear en la fotoionización. Para poder llevar a cabo dicha investigación hemos implementado una nueva versión del método combinando TDPT de 2^{do} orden y la *aproximación-local*, lo cual nos permitió explorar pulsos de largas duraciones. La validez y presición de la aproximación fue demostrada comparando con la solución exacta de la TDSE. Hemos demostrado experimental y teóricamente, que es posible controlar el peso relativo entre la ionización disociativa y no disociativa variando los parámetros del FEL. La ionización no disociativa es dominante para duraciones de pulso $T \geq 10$ fs. Para estas duraciones, hemos encontrado asimetrías en las distribuciones angulares electrónica, consecuencias de la localización de electrón en un núcleo u otro.

Appendix A

Parametrization of the MFPADs

We aim to present a brief description of the physical principles involved in the study of the angular distribution of the particles coming from the photoionization process. Specifically we are interested in: the electron and ion angular distributions for fixed-in-space molecules and its dependence with different angles of incidence of the light. For specific details in the formulation see [68]. Within the *dipole approximation* the fully differential cross section for ionization from the ground state $\Psi_0(\mathbf{r}, R)$ to a final state $\Psi_{\alpha v \mathbf{k}_e E}(\mathbf{r}, R)$ is given by:

$$\frac{d\sigma_\alpha^{\mu_0}(\omega)}{d\hat{R}_n d\mathbf{k}_e} = \frac{4\pi^2\omega}{c}\left| \int dR \langle \Psi_{\alpha v \mathbf{k}_e E}(\mathbf{r}, R) | \hat{\mathbf{e}}_{\mu_0} \hat{\boldsymbol{\mathcal{O}}} | \Psi_0(\mathbf{r}, R) \rangle \right|^2 \tag{A.1}$$

where ω is the photon energy, c is the speed of light, $\hat{\mathbf{e}}_{\mu_0}$ is the light polarization vector where μ_0 defines the polarization, for linearly polarized light (μ_0=0) and for circularly polarized light (μ_0 =$\pm$1 for right and left helicity respectively) and $\hat{\boldsymbol{\mathcal{O}}}$ is the dipole operator. $E = E_v + \varepsilon = E_0 + \omega$ is the total energy shared by the electron and the nuclei, $\mathbf{k}_e$ describes the direction of the photoelectron with respect to the molecular reference system and $\hat{R}_n$ provides the orientation of the external electric field with respect to the molecular frame. The final wave function in equation A.1 can be written in a partial wave expansion [68]:

$$\Psi_{\alpha v \mathbf{k}_e E}(\mathbf{r}, R) = \sum_{l,m} i^{-l} e^{i\sigma_l(k)} \Psi_{\alpha v l m E}(\mathbf{r}, R) \mathcal{Y}_l^m(\Omega_e) \tag{A.2}$$

where $\sigma_l(k)$ is the Coulomb phase shift [49]. The procedure to calculate both wave functions, $\Psi_{\alpha v l m E}(\mathbf{r}, R)$ and $\Psi_0(\mathbf{r}, R)$ has been described in Chapter 2. Thus,

the expression for the cross section can be rewritten as:

$$\frac{d\sigma_{\alpha}^{\mu_0}(\omega)}{d\hat{R}_n d\Omega_e dE_v} = \frac{4\pi^2\omega}{c}\left|\sum_{l,m}\int i^l e^{-i\sigma_l(k)}\langle\Psi_{\alpha vlmE}(\mathbf{r},R)|\hat{\mathbf{e}}_{\mu_0}\hat{\boldsymbol{\mathcal{O}}}|\Psi_0(\mathbf{r},R)\rangle\mathcal{Y}_l^{m*}(\Omega_e)dR\right|^2 \tag{A.3}$$

where the sum over l runs over all the electron partial waves (corresponding to each threshold α) included in the calculation and $d\mathbf{k}_e$ has been substituted by $d\Omega_e dE_v$.

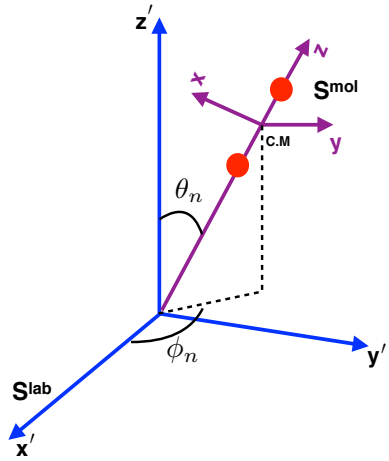

FIGURE A.1: Schematic depicting the laboratory S^{lab} and molecular S^{mol} frames for linear molecules.

The atomic photoelectron angular distributions can be measured only with respect to the laboratory frame axis, however the molecular photoelectron angular distributions can be measured with respect to two different coordinate systems, namely a molecular frame and a laboratory frame [68]. Thus, one can obtain the photoelectron angular distributions in both frames (coordinate system). The first coordinate system is defined with origin in the molecular center of mass (C.M.) and the z axis coinciding with the molecular axis (see figure A.1). For linearly polarized light (μ_0=0) Ω_n is the direction of the polarization of the light, for circularly polarized light ($\mu_0 = \pm 1$) Ω_n define the direction of the propagation of the light. The angles Ω_e define the emission direction of the electron in this coordinate system. The second coordinate system is defined in the laboratory frame, in this frame the emission ejection direction of the photoelectrons is given by Ω_e' and

the orientation of the molecular axis is defined by the angles Ω'_M. The orientation of the laboratory coordinate frame of the light source system with respect to the molecule frame is characterized by the set of Euler angles:

$$\hat{R}_n = \{\alpha, \beta, \gamma\} = \{\phi_n, \theta_n, \pi - \phi_M\} \tag{A.4}$$

Note that the polar coordinates of the laboratory z' axis in the xyz coordinate system are (θ_n, ϕ_n).

While the wave functions in equation A.3 are defined (calculated) in the molecular coordinate system the dipole operator is defined in the laboratory coordinate system. So in order to be consistent one needs to write the dipole operator in the molecular coordinate system, by using the rotations that connect both systems. The polarization direction of the light in the laboratory reference system can be taken along the z' axis. Writing the spherical harmonic in the laboratory coordinate system in terms of the ones in the molecular system:

$$z' = \sqrt{\frac{4\pi}{3}} r \mathcal{Y}_0^1(\theta', \phi') = \sqrt{\frac{4\pi}{3}} r \sum_{\mu=-1}^{\mu=1} \mathcal{Y}_1^{\mu}(\theta, \phi) D^1_{\mu,\mu_0}(\alpha, \beta, \gamma) \tag{A.5}$$

Where $D^1_{\mu,\mu_0}(\alpha, \beta, \gamma)$ is the Wigner rotational matrix [49]. We can the define the dipole matrix elements as:

$$T_{\alpha v l m \mu E} = \sqrt{\frac{4\pi}{3}} \int \langle \Psi_{\alpha v l m E}(\mathbf{r}, R) | r \mathcal{Y}_1^{\mu}(\theta, \phi) | \Psi_0(\mathbf{r}, R) \rangle dR \tag{A.6}$$

In order to reduce the expressions containing the product of the spherical harmonics and Wigner matrices, we can use of the relations:

$$\begin{aligned} \mathcal{Y}_{l_a}^{m_a}(\Omega_e) \mathcal{Y}_{l_b}^{m_b *}(\Omega_e) =& (-1)^{m_b} \sqrt{\frac{(2l_a+1)(2l_b+1)}{4\pi}} \sum_{L_e=|l_a-l_b|}^{l_a+l_b} \frac{1}{\sqrt{2L_e+1}} \\ & \times C(l_a, l_b, L_e, m_a, -m_b) C(l_a, l_b, L_e, 0, 0) \mathcal{Y}_{L_e}^{M_e}(\Omega_e) \end{aligned} \tag{A.7}$$

$$\begin{aligned} D^1_{\mu_b,\mu_0}(\alpha, \beta, \gamma) D^{1*}_{\mu_a,\mu_0}(\alpha, \beta, \gamma) =& (-1)^{\mu_a - \mu_0} \sum_{L_\gamma=0}^{2} C(1, 1, L_\gamma, -\mu_a, \mu_b) \\ & \times C(1, 1, L_\gamma, -\mu_0, \mu_0) D^{L_\gamma}_{M_\gamma,0}(\alpha, \beta, \gamma) \end{aligned} \tag{A.8}$$

$$D^{l}_{m,0}(\alpha,\beta,\gamma)=\sqrt{\frac{4\pi}{(2l+1)}}\mathcal{Y}_{l}^{m*}(\beta,\alpha) \tag{A.9}$$

Where the C functions are are the Clebsh-Gordan coefficients [49], $M_e = m_a - m_b$, $M_\gamma = -\mu_a + \mu_b$. Inserting A.5 into A.3 and using the relations A.6, A.7, A.8, A.9 the fully differential cross section transforms into:

$$\begin{aligned}\frac{d\sigma_{\alpha}^{\mu_0}(\omega)}{d\Omega_n d\Omega_e dE_v} = \frac{4\pi^2\omega}{c}\sum_{\mu_a,\mu_b}\sum_{l_a,m_a}\sum_{l_b,m_b} i^{(l_b-l_a)}e^{i(\sigma_{l_a}-\sigma_{l_b})}(-1)^{m_b+\mu_a-\mu_0}\\ \times\sqrt{(2l_a+1)(2l_b+1)}T^{*}_{\alpha v l_a m_a \mu_a E}T_{\alpha v l_b m_b \mu_b E}\\ \times\sum_{L_e=|l_a-l_b|}^{l_a-l_b} C(l_a,l_b,L_e,-m_a,m_b)C(l_a,l_b,L_e,0,0)\frac{\mathcal{Y}_{L_e}^{M_e}(\Omega_e)}{\sqrt{2L_e+1}}\\ \times\sum_{L_\gamma=0}^{2}(1,1,L_\gamma,-\mu_a,\mu_b)C(1,1,L_\gamma,-\mu_0,\mu_0)\frac{\mathcal{Y}_{L_\gamma}^{M_\gamma *}(\Omega_n)}{\sqrt{2L_\gamma+1}}\end{aligned} \tag{A.10}$$

Although we use the dipole operator in the *length* gauge for simplicity, the results remain valid for the *velocity* gauge. This expression is general in the sense that, by integrating it over one or several differential magnitudes leads to partially differential or total cross sections, each one representing a specific experimental situation. Notice that this cross section is differential in the electron ejection direction, angle of incidence of the light and electron/vibrational energy. In principle one calculates the dipole elements $T_{\alpha v l m \mu E}$ using the directives given in Chapter 3 and the plug it into A.10 and adjust it to the specific situation at hand.

Appendix B

Modeling the pulses

Mathematically, an isolated pulse with a duration T can be defined by its vector potential (within the dipole approximation), using a sine squared envelop:

$$\mathbf{A}(t) = \begin{cases} \hat{\mathbf{e}}_\mu A_0 \sin^2(\pi t/T)\cos[\omega(t-T/2)] & 0 \leq t \leq T \\ 0 & \text{elsewhere} \end{cases} \tag{B.1}$$

where ω is the central frequency of the pulse, $\hat{\mathbf{e}}_\mu$ is the polarization vector. The intensity A_0 is related to the field amplitude through the atomic unit of intensity:

$$\mathcal{E}_0(a.u.) = A_0(a.u.)\omega(a.u.) = \sqrt{\frac{I(\text{Wcm}^{-2})}{I_0}} \tag{B.2}$$

in which $\mathcal{E}_0$ is the electric field amplitude and I_0=3.5095$\times 10^{16}$ Wcm^{-2} is the atomic unit of intensity. Although we have defined the vector potential $\mathbf{A}(t)$, the electric field $\boldsymbol{\mathcal{E}}(t)$ can be unambiguously derived from it (see Chapter 3):

$$\boldsymbol{\mathcal{E}}(t) = -\frac{\partial \mathbf{A}(t)}{\partial t} \tag{B.3}$$

The Fourier transform of equation B.1 gives the amplitude and phase of the frequency components of the pulse. In this case, ω represents the central photon energy in the spectrum that results from the Fourier transform of equation B.1. The corresponding full width at half maximum (FWHM) is given by $\Delta\omega = 4\pi/T$ (bandwidth of the pulse). Therefore, short pulse durations are associated with wide frequency distributions, and the other way around. As an example, figure B.1 displays the vector potential in equation B.1 (left panel) and its Fourier transform (right panel), for T=1 fs and T=2 fs of pulse duration, central frequency of $\hbar\omega$=40 eV (1.47 a.u.) and intensity of I=10^{12} Wcm^{-2}. An important magnitud is

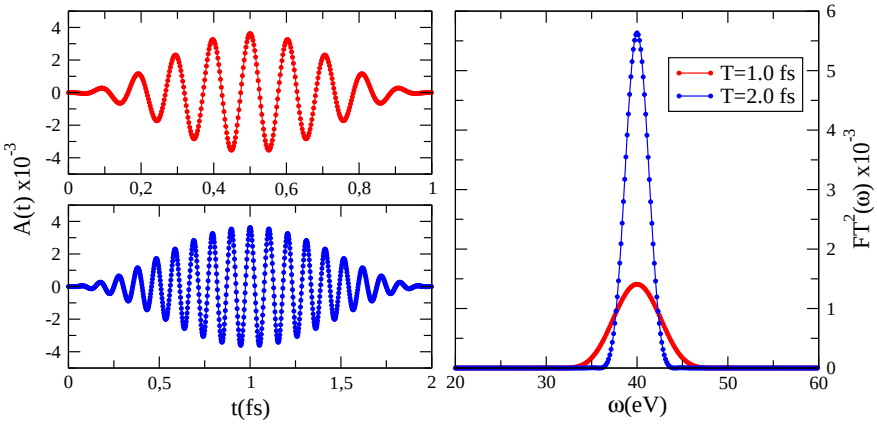

FIGURE B.1: Vector potential $A(t)$ (left panel) and its Fourier transform (right panel), for T=1 fs (red points) and T=2 fs (blue points) pulse durations. The central frequency of the pulses is $\hbar\omega$=40 eV and intensity of I=10^{12} Wcm^{-2}.

number of optical cycles (number of full oscillations of the laser field), n_{cycles}, as the pulses are usually defined by it. The number of optical cycles is related with the frequency and the duration through:

$$n_{cycles} = \frac{\omega T}{2\pi} \tag{B.4}$$

Using the vector potential in equation B.1, the pump-probe scheme can be defined as sequence of pulses, separated by different time delays t_i:

$$\mathbf{A}(t) = \mathbf{A}(t)_{pump} + \sum_i \mathbf{A}_i(t - t_i)_{probe} \tag{B.5}$$

In this work the delay is defined as the difference between the times at which the pulses reach the maximum amplitude. That is, negative time delays imply that the probe pulse arrives before the pump one.

Bibliography

[1] André T. J. B. Eppink and David H. Parker. "Velocity map imaging of ions and electrons using electrostatic lenses: Application in photoelectron and photofragment ion imaging of molecular oxygen". In: *Review of Scientific Instruments* 68.9 (1997), pp. 3477–3484. DOI: 10.1063/1.1148310. eprint: http://dx.doi.org/10.1063/1.1148310. URL: http://dx.doi.org/10.1063/1.1148310.

[2] B. Baguenard et al. "Velocity-map imaging electron spectrometer with time resolution". In: *Review of Scientific Instruments* 75.2 (2004), pp. 324–328. DOI: 10.1063/1.1642749. eprint: http://dx.doi.org/10.1063/1.1642749. URL: http://dx.doi.org/10.1063/1.1642749.

[3] O. Ghafur et al. "A velocity map imaging detector with an integrated gas injection system". In: *Review of Scientific Instruments* 80.3 (2009), p. 033110. DOI: 10.1063/1.3085799. eprint: http://dx.doi.org/10.1063/1.3085799. URL: http://dx.doi.org/10.1063/1.3085799.

[4] R. Dörner et al. "Cold Target Recoil Ion Momentum Spectroscopy: a 'momentum microscope' to view atomic collision dynamics". In: *Physics Reports* 330.2–3 (2000), pp. 95 –192. ISSN: 0370-1573. DOI: https://doi.org/10.1016/S0370-1573(99)00109-X. URL: http://www.sciencedirect.com/science/article/pii/S037015739900109X.

[5] J Ullrich et al. "Recoil-ion and electron momentum spectroscopy: reaction-microscopes". In: *Reports on Progress in Physics* 66.9 (2003), p. 1463. URL: http://stacks.iop.org/0034-4885/66/i=9/a=203.

[6] P. A. Franken et al. "Generation of Optical Harmonics". In: *Phys. Rev. Lett.* 7 (4 1961), pp. 118–119. DOI: 10.1103/PhysRevLett.7.118. URL: https://link.aps.org/doi/10.1103/PhysRevLett.7.118.

[7] P. B. Corkum. "Plasma perspective on strong field multiphoton ionization". In: *Phys. Rev. Lett.* 71 (13 1993), pp. 1994–1997. DOI: 10.1103/PhysRevLett.71.1994. URL: https://link.aps.org/doi/10.1103/PhysRevLett.71.1994.

[8] Kun Zhao et al. "Tailoring a 67 attosecond pulse through advantageous phase-mismatch". In: *Opt. Lett.* 37.18 (2012), pp. 3891–3893. DOI: 10.1364/OL.37.003891. URL: http://ol.osa.org/abstract.cfm?URI=ol-37-18-3891.

[9] E. Goulielmakis et al. "Single-Cycle Nonlinear Optics". In: *Science* 320.5883 (2008), pp. 1614–1617. ISSN: 0036-8075. DOI: 10.1126/science.1157846. eprint: http://science.sciencemag.org/content/320/5883/1614.full.pdf. URL: http://science.sciencemag.org/content/320/5883/1614.

[10] P. M. Paul et al. "Observation of a Train of Attosecond Pulses from High Harmonic Generation". In: *Science* 292.5522 (2001), pp. 1689–1692. ISSN: 0036-8075. DOI: 10.1126/science.1059413. eprint: http://science.sciencemag.org/content/292/5522/1689.full.pdf. URL: http://science.sciencemag.org/content/292/5522/1689.

[11] M. Hentschel et al. "Attosecond metrology". In: *Nature* 414.6863 (Nov. 2001), pp. 509–513. URL: http://dx.doi.org/10.1038/35107000.

[12] Ferenc Krausz and Misha Ivanov. "Attosecond physics". In: *Rev. Mod. Phys.* 81 (1 2009), pp. 163–234. DOI: 10.1103/RevModPhys.81.163. URL: https://link.aps.org/doi/10.1103/RevModPhys.81.163.

[13] Mauro Nisoli et al. "Attosecond Electron Dynamics in Molecules". In: *Chemical Reviews* 117.16 (2017). PMID: 28488433, pp. 10760–10825. DOI: 10.1021/acs.chemrev.6b00453. eprint: http://dx.doi.org/10.1021/acs.chemrev.6b00453. URL: http://dx.doi.org/10.1021/acs.chemrev.6b00453.

[14] J. Itatani et al. "Tomographic imaging of molecular orbitals". In: *Nature* 432.7019 (Dec. 2004), pp. 867–871. URL: http://dx.doi.org/10.1038/nature03183.

[15] K. P. Singh et al. "Control of Electron Localization in Deuterium Molecular Ions using an Attosecond Pulse Train and a Many-Cycle Infrared Pulse". In: *Phys. Rev. Lett.* 104 (2 2010), p. 023001. DOI: 10.1103/PhysRevLett.104.023001. URL: https://link.aps.org/doi/10.1103/PhysRevLett.104.023001.

[16] G. Sansone et al. "Electron localization following attosecond molecular photoionization". In: *Nature* 465.7299 (June 2010), pp. 763–766. URL: http://dx.doi.org/10.1038/nature09084.

[17] F. Kelkensberg et al. "Attosecond Control in Photoionization of Hydrogen Molecules". In: *Phys. Rev. Lett.* 107 (4 2011), p. 043002. DOI: 10.1103/PhysRevLett.107.043002. URL: https://link.aps.org/doi/10.1103/PhysRevLett.107.043002.

[18] F. Calegari et al. "Ultrafast electron dynamics in phenylalanine initiated by attosecond pulses". In: *Science* 346.6207 (2014), pp. 336–339. ISSN: 0036-8075. DOI: 10.1126/science.1254061. eprint: http://science.sciencemag.org/content/346/6207/336.full.pdf. URL: http://science.sciencemag.org/content/346/6207/336.

[19] K. Kondratenko and E. Saldin. "Generating of coherent radiation by a relativistic electron beam in an ondulator". In: *Part. Accel.* 10 (1980), pp. 207–216.

[20] R. Bonifacio, C. Pellegrini, and L. M. Narducci. "Collective instabilities and high-gain regime in a free electron laser". In: *Opt. Commun.* 50 (1984), pp. 373–378. URL: http://dx.doi.org/10.1016/0030-4018(84)90105-6.

[21] S. Milton. "Exponential gain and saturation of a self-amplified spontaneous emission free-electron laser". In: *Science* 292 (2001), pp. 2037–2041. URL: http://dx.doi.org/10.1126/science.1059955.

[22] V. Ayvazyan. "Generation of GW radiation pulses from a VUV free-electron laser operating in the femtosecond regime". In: *Phys. Rev. Lett.* 88 (2002), p. 104802. URL: http://dx.doi.org/10.1103/PhysRevLett.88.104802.

[23] A. Palacios, H. Bachau, and F. Martin. "Enhancement and Control of H_2 Dissociative Ionization by Femtosecond VUV Laser Pulses". In: *Phys. Rev. Lett.* 96 (14 2006), p. 143001. DOI: 10.1103/PhysRevLett.96.143001. URL: https://link.aps.org/doi/10.1103/PhysRevLett.96.143001.

[24] A. Palacios, H. Bachau, and F. Martin. "Excitation and ionization of molecular hydrogen by ultrashort vuv laser pulses". In: *Phys. Rev. A* 75 (1 2007), p. 013408. DOI: 10.1103/PhysRevA.75.013408. URL: https://link.aps.org/doi/10.1103/PhysRevA.75.013408.

[25] A. Palacios, H. Bachau, and F. Martín. "Step-ladder Rabi oscillations in molecules exposed to intense ultrashort vuv pulses". In: *Phys. Rev. A* 74 (3 2006), p. 031402. DOI: 10.1103/PhysRevA.74.031402. URL: https://link.aps.org/doi/10.1103/PhysRevA.74.031402.

[26] F. Martín et al. "Single Photon-Induced Symmetry Breaking of H_2 Dissociation". In: *Science* 315.5812 (2007), pp. 629–633. ISSN: 0036-8075. DOI: 10.1126/science.1136598. eprint: http://science.sciencemag.org/content/315/5812/629.full.pdf. URL: http://science.sciencemag.org/content/315/5812/629.

[27] T. Weber et al. "Complete photo-fragmentation of the deuterium molecule". In: *Nature* 431.7007 (Sept. 2004), pp. 437–440. URL: http://dx.doi.org/10.1038/nature02839.

[28] Thorsten Weber et al. "The hydrogen molecule under the reaction microscope: single photon double ionization at maximum cross section and threshold (doubly differential cross sections)". In: *Journal of Physics B: Atomic, Molecular and Optical Physics* 50.16 (2017), p. 164002. URL: http://stacks.iop.org/0953-4075/50/i=16/a=164002.

[29] D. Akoury et al. "The Simplest Double Slit: Interference and Entanglement in Double Photoionization of H2". In: *Science* 318.5852 (2007), pp. 949–952. ISSN: 0036-8075. DOI: 10.1126/science.1144959. eprint: http://science.sciencemag.org/content/318/5852/949.full.pdf. URL: http://science.sciencemag.org/content/318/5852/949.

[30] Sophie E. Canton et al. "Direct observation of Young's double-slit interferences in vibrationally resolved photoionization of diatomic molecules". In: *Proceedings of the National Academy of Sciences* 108.18 (2011), pp. 7302–7306. DOI: 10.1073/pnas.1018534108. eprint: http://www.pnas.org/content/108/18/7302.full.pdf. URL: http://www.pnas.org/content/108/18/7302.abstract.

[31] L.S. Cederbaum and J. Zobeley. "Ultrafast charge migration by electron correlation". In: *Chemical Physics Letters* 307.3 (1999), pp. 205 –210. ISSN: 0009-2614. DOI: http://dx.doi.org/10.1016/S0009-2614(99)00508-4. URL: http://www.sciencedirect.com/science/article/pii/S0009261499005084.

[32] P. A. Carpeggiani et al. "Disclosing intrinsic molecular dynamics on the 1-fs scale through extreme-ultraviolet pump-probe measurements". In: *Phys. Rev. A* 89 (2 2014), p. 023420. DOI: 10.1103/PhysRevA.89.023420. URL: https://link.aps.org/doi/10.1103/PhysRevA.89.023420.

[33] Alberto González-Castrillo et al. "Clocking Ultrafast Wave Packet Dynamics in Molecules through UV-Induced Symmetry Breaking". In: *Phys. Rev. Lett.* 108 (6 2012), p. 063009. DOI: 10.1103/PhysRevLett.108.063009. URL: https://link.aps.org/doi/10.1103/PhysRevLett.108.063009.

[34] Andreas Fischer et al. "Electron Localization Involving Doubly Excited States in Broadband Extreme Ultraviolet Ionization of $\mathbf{H}_2$". In: *Phys. Rev. Lett.* 110 (21 2013), p. 213002. DOI: 10.1103/PhysRevLett.110.213002. URL: https://link.aps.org/doi/10.1103/PhysRevLett.110.213002.

[35] M. F. Kling et al. "Control of Electron Localization in Molecular Dissociation". In: *Science* 312.5771 (2006), pp. 246–248. ISSN: 0036-8075. DOI: 10.1126/science.1126259. eprint: http://science.sciencemag.org/content/312/5771/246.full.pdf. URL: http://science.sciencemag.org/content/312/5771/246.

[36] A. S. Alnaser et al. "Simultaneous real-time tracking of wave packets evolving on two different potential curves in H_2^+ and D_2^+". In: *Phys. Rev. A* 72 (3 2005), p. 030702. DOI: 10.1103/PhysRevA.72.030702. URL: https://link.aps.org/doi/10.1103/PhysRevA.72.030702.

[37] Th. Ergler et al. "Quantum-Phase Resolved Mapping of Ground-State Vibrational D_2 Wave Packets via Selective Depletion in Intense Laser Pulses". In: *Phys. Rev. Lett.* 97 (10 2006), p. 103004. DOI: 10.1103/PhysRevLett.97.103004. URL: https://link.aps.org/doi/10.1103/PhysRevLett.97.103004.

[38] G. D. Dickenson et al. "Fundamental Vibration of Molecular Hydrogen". In: *Phys. Rev. Lett.* 110 (19 2013), p. 193601. DOI: 10.1103/PhysRevLett.110.193601. URL: https://link.aps.org/doi/10.1103/PhysRevLett.110.193601.

[39] D. Dowek et al. "Circular Dichroism in Photoionization of H_2". In: *Phys. Rev. Lett.* 104 (23 2010), p. 233003. DOI: 10.1103/PhysRevLett.104.233003. URL: https://link.aps.org/doi/10.1103/PhysRevLett.104.233003.

[40] J. F. Pérez-Torres et al. "Circular dichroism in molecular-frame photoelectron angular distributions in the dissociative photoionization of H_2 and D_2 molecules". In: *Phys. Rev. A* 90 (4 2014), p. 043417. DOI: 10.1103/PhysRevA.90.043417. URL: https://link.aps.org/doi/10.1103/PhysRevA.90.043417.

[41] Y. H. Jiang et al. "Investigating two-photon double ionization of D_2 by XUV-pump–XUV-probe experiments". In: *Phys. Rev. A* 81 (5 2010), p. 051402. DOI: 10.1103/PhysRevA.81.051402. URL: https://link.aps.org/doi/10.1103/PhysRevA.81.051402.

[42] Predrag Ranitovic et al. "Attosecond vacuum UV coherent control of molecular dynamics". In: *Proceedings of the National Academy of Sciences* 111.3 (2014), pp. 912–917. DOI: 10.1073/pnas.1321999111. eprint: http://www.pnas.org/content/111/3/912.full.pdf. URL: http://www.pnas.org/content/111/3/912.abstract.

[43] J. D. Power. "Fixed Nuclei Two-Centre Problem in Quantum Mechanics". In: *Philosophical Transactions of the Royal Society of London A: Mathematical, Physical and Engineering Sciences* 274.1246 (1973), pp. 663–697. ISSN: 0080-4614. DOI: 10.1098/rsta.1973.0079. eprint: http://rsta.royalsocietypublishing.org/content/274/1246/663.full.pdf. URL: http://rsta.royalsocietypublishing.org/content/274/1246/663.

[44] A. Salin. "Calculation of wave-functions and collision matrix elements for one-electron diatomic molecules". In: *Computer Physics Communications* 14.1 (1978), pp. 121 –132. ISSN: 0010-4655. DOI: http://dx.doi.org/10.1016/0010-4655(78)90055-3. URL: http://www.sciencedirect.com/science/article/pii/0010465578900553.

[45] G. Hunter and H. O. Pritchard. "Born—Oppenheimer Separation for Three-Particle Systems. II. Two-Center Wavefunctions". In: *The Journal of Chemical Physics* 46.6 (1967), pp. 2146–2152. DOI: 10.1063/1.1841016. eprint: http://dx.doi.org/10.1063/1.1841016. URL: http://dx.doi.org/10.1063/1.1841016.

[46] Liang Tao, C. W. McCurdy, and T. N. Rescigno. "Grid-based methods for diatomic quantum scattering problems. III. Double photoionization of molecular hydrogen in prolate spheroidal coordinates". In: *Phys. Rev. A* 82 (2 2010), p. 023423. DOI: 10.1103/PhysRevA.82.023423. URL: https://link.aps.org/doi/10.1103/PhysRevA.82.023423.

[47] H Bachau et al. "Applications of B -splines in atomic and molecular physics". In: *Reports on Progress in Physics* 64.12 (2001), p. 1815. URL: http://stacks.iop.org/0034-4885/64/i=12/a=205.

[48] Carl de Boor. *A Practical Guide to Splines*. Springer-Verlag New York Inc., United States, 1978. ISBN: 978-0-387-95366-3.

[49] Milton Abramowitz. *Handbook of Mathematical Functions, With Formulas, Graphs, and Mathematical Tables*, Dover Publications, Incorporated, 1974. ISBN: 0486612724.

[50] Alicia Palacios, José Luis Sanz-Vicario, and Fernando Martín. "Theoretical methods for attosecond electron and nuclear dynamics: applications to the H_2 molecule". In: *Journal of Physics B: Atomic, Molecular and Optical Physics* 48.24 (2015), p. 242001. URL: http://stacks.iop.org/0953-4075/48/i=24/a=242001.

[51] Charlotte Froese Fischer. *The Hartree-Fock Method for Atoms: A Numerical Approach*. John Wiley & Sons Inc, 1977. ISBN: 047125990X.

[52] Charlotte Froese Fischer. "A general multi-configuration Hartree-Fock program". In: *Computer Physics Communications* 14.1-2 (1978), pp. 145–153.

[53] Daniele Toffoli and Piero Decleva. "A Multichannel Least-Squares B-Spline Approach to Molecular Photoionization: Theory, Implementation, and Applications within the Configuration–Interaction Singles Approximation". In: *Journal of Chemical Theory and Computation* 12.10 (2016). PMID: 27626466, pp. 4996–5008. DOI: 10.1021/acs.jctc.6b00627. eprint: http://dx.doi.org/10.1021/acs.jctc.6b00627. URL: http://dx.doi.org/10.1021/acs.jctc.6b00627.

[54] M. Brosolo and P. Decleva. "Variational approach to continuum orbitals in a spline basis: An application to H_2^+ photoionization". In: *Chemical Physics* 159.2 (1992), pp. 185–196. ISSN: 03010104. DOI: 10.1016/0301-0104(92)80069-8.

[55] Charlotte Froese Fischer and Muhammad Idrees. "Spline algorithms for continuum functions". In: *Computers in Physics* 3.3 (1989), pp. 53–58.

[56] L A A Nikolopoulos and P Lambropoulos. "Multichannel theory of two-photon single and double ionization of helium". In: *Journal of Physics B: Atomic, Molecular and Optical Physics* 34.4 (2001), p. 545. URL: http://stacks.iop.org/0953-4075/34/i=4/a=304.

[57] M. Brosolo, P. Decleva, and A. Lisini. "Continuum wavefunctions calculations with least-squares schemes in a B-splines basis". In: *Computer Physics Communications* 71.3 (1992), pp. 207 –214. ISSN: 0010-4655. DOI: http://dx.doi.org/10.1016/0010-4655(92)90009-N. URL: http://www.sciencedirect.com/science/article/pii/001046559290009N.

[58] Herman Feshbach. "A unified theory of nuclear reactions. II". In: *Annals of Physics* 19.2 (1962), pp. 287 –313. ISSN: 0003-4916. DOI: http://dx.doi.org/10.1016/0003-4916(62)90221-X. URL: http://www.sciencedirect.com/science/article/pii/000349166290221X.

[59] U. Fano. "Effects of Configuration Interaction on Intensities and Phase Shifts". In: *Phys. Rev.* 124 (6 1961), pp. 1866–1878. DOI: 10.1103/PhysRev.124.1866. URL: https://link.aps.org/doi/10.1103/PhysRev.124.1866.

[60] I. Sánchez and F. Martín. "The doubly excited states of the H_2 molecule". In: *The Journal of Chemical Physics* 106.18 (1997), pp. 7720–7730. DOI: 10.1063/1.473773. eprint: http://dx.doi.org/10.1063/1.473773. URL: http://dx.doi.org/10.1063/1.473773.

[61] I. Sánchez and F. Martín. "Doubly excited autoionizing states of H_2 above the second ionization threshold: the Q_2 resonance series". In: *The Journal of Chemical Physics* 110.14 (1999), pp. 6702–6713. DOI: 10.1063/1.478576. eprint: http://dx.doi.org/10.1063/1.478576. URL: http://dx.doi.org/10.1063/1.478576.

[62] M Cortes and F Martin. "Multichannel close-coupling method with L 2 integrable bases". In: *Journal of Physics B: Atomic, Molecular and Optical Physics* 27.23 (1994), p. 5741. URL: http://stacks.iop.org/0953-4075/27/i=23/a=017.

[63] I. Sánchez and F. Martín. "Photoionization of He above the n=2 threshold". In: *Phys. Rev. A* 44 (11 1991), pp. 7318–7334. DOI: 10.1103/PhysRevA.44.7318. URL: https://link.aps.org/doi/10.1103/PhysRevA.44.7318.

[64] I. Sánchez and F. Martín. "Photoionization of He above the N=2 threshold. II. Angular distribution of photoelectrons and asymmetry parameter". In: *Phys. Rev. A* 45 (7 1992), pp. 4468–4475. DOI: 10.1103/PhysRevA.45.4468. URL: https://link.aps.org/doi/10.1103/PhysRevA.45.4468.

[65] F. Martín. "Completely L^2 integrable method for strong-coupling multichannel photoionization: Photoelectron emission of He between the N=3 and 4 thresholds". In: *Phys. Rev. A* 48 (1 1993), pp. 331–337. DOI: 10.1103/PhysRevA.48.331. URL: https://link.aps.org/doi/10.1103/PhysRevA.48.331.

[66] A. Macias et al. "A practical solution to the unknown normalization problem". In: *International Journal of Quantum Chemistry* 33.4 (1988), pp. 279–300. ISSN: 1097-461X. DOI: 10.1002/qua.560330404. URL: http://dx.doi.org/10.1002/qua.560330404.

[67] K. Wolniewicz, K. Szalewicz, and H. J. Monkhorst. "New Born–Oppenheimer potential energy curve and vibrational energies for the electronic ground state of the hydrogen molecule". In: *The Journal of Chemical Physics* 84.6 (1986), pp. 3278–3283. DOI: 10.1063/1.450258. eprint: http://dx.doi.org/10.1063/1.450258. URL: http://dx.doi.org/10.1063/1.450258.

[68] Dan Dill. "Fixed-molecule photoelectron angular distributions". In: *The Journal of Chemical Physics* 65.3 (1976), pp. 1130–1133. DOI: 10.1063/1.433187. eprint: http://dx.doi.org/10.1063/1.433187. URL: http://dx.doi.org/10.1063/1.433187.

[69] Xiaochun Gong et al. "Two-Dimensional Directional Proton Emission in Dissociative Ionization of H_2". In: *Phys. Rev. Lett.* 113 (20 2014), p. 203001. DOI: 10.1103/PhysRevLett.113.203001. URL: https://link.aps.org/doi/10.1103/PhysRevLett.113.203001.

[70] Carlos Marante, Luca Argenti, and Fernando Martín. "Hybrid Gaussian–B-spline basis for the electronic continuum: Photoionization of atomic hydrogen". In: *Phys. Rev. A* 90 (1 2014), p. 012506. DOI: 10.1103/PhysRevA.90.012506. URL: https://link.aps.org/doi/10.1103/PhysRevA.90.012506.

[71] Amalia Apalategui, Alejandro Saenz, and P Lambropoulos. "Effect of vibration and internuclear axis orientation on multiphoton ionization of H_2^+". In: *Journal of Physics B: Atomic, Molecular and Optical Physics* 33.14 (2000), p. 2791. URL: http://stacks.iop.org/0953-4075/33/i=14/a=316.

[72] E Karule and B Moine. "The general expression for the transition amplitude of two-photon ionization of atomic hydrogen". In: *Journal of Physics B: Atomic, Molecular and Optical Physics* 36.10 (2003), p. 1963. URL: http://stacks.iop.org/0953-4075/36/i=10/a=307.

[73] E Karule. "Analytical continuation of the transition matrix elements and multiphoton above-threshold ionisation of atomic hydrogen". In: *Journal of Physics B: Atomic, Molecular and Optical Physics* 21.11 (1988), p. 1997. URL: http://stacks.iop.org/0953-4075/21/i=11/a=015.

[74] L. A. A. Nikolopoulos. "Electromagnetic transitions between states satisfying free-boundary conditions". In: *Phys. Rev. A* 73 (4 2006), p. 043408. DOI: 10.1103/PhysRevA.73.043408. URL: https://link.aps.org/doi/10.1103/PhysRevA.73.043408.

[75] Andrea Damascelli, Zahid Hussain, and Zhi-Xun Shen. "Angle-resolved photoemission studies of the cuprate superconductors". In: *Rev. Mod. Phys.* 75 (2 2003), pp. 473–541. DOI: 10.1103/RevModPhys.75.473. URL: https://link.aps.org/doi/10.1103/RevModPhys.75.473.

[76] Robin Santra. "Imaging molecular orbitals using photoionization". In: *Chemical Physics* 329.1 (2006). Electron Correlation and Multimode Dynamics in Molecules, pp. 357 –364. ISSN: 0301-0104. DOI: http://dx.doi.org/10.1016/j.chemphys.2006.07.008. URL: http://www.sciencedirect.com/science/article/pii/S0301010406003867.

[77] M. Takahashi et al. "Observation of a Molecular Frame $(e, 2e)$ Cross Section: An $(e, 2e + M)$ Triple Coincidence Study on H_2". In: *Phys. Rev. Lett.* 94 (21 2005), p. 213202. DOI: 10.1103/PhysRevLett.94.213202. URL: https://link.aps.org/doi/10.1103/PhysRevLett.94.213202.

[78] M. Meckel et al. "Laser-Induced Electron Tunneling and Diffraction". In: *Science* 320.5882 (2008), pp. 1478–1482. ISSN: 0036-8075. DOI: 10.1126/science.1157980. eprint: http://science.sciencemag.org/content/320/5882/1478.full.pdf. URL: http://science.sciencemag.org/content/320/5882/1478.

[79] J. Fernández, O. Fojón, and F. Martín. "Double-slit, confinement, and non-Franck-Condon effects in photoionization of H_2 at high photon energy". In: *Phys. Rev. A* 79 (2 2009), p. 023420. DOI: 10.1103/PhysRevA.79.023420. URL: https://link.aps.org/doi/10.1103/PhysRevA.79.023420.

[80] J. Fernández et al. "Two-center effects in one-photon single ionization of H_2^+, H_2, and Li_2^+ with circularly polarized light". In: *Phys. Rev. A* 79 (4 2009), p. 043409. DOI: 10.1103/PhysRevA.79.043409. URL: https://link.aps.org/doi/10.1103/PhysRevA.79.043409.

[81] J. Fernández et al. "Interferences from Fast Electron Emission in Molecular Photoionization". In: *Phys. Rev. Lett.* 98 (4 2007), p. 043005. DOI: 10.1103/PhysRevLett.98.043005. URL: https://link.aps.org/doi/10.1103/PhysRevLett.98.043005.

[82] O. A. Fojón et al. "Interferences in the photoelectron spectrum of H_2^+ molecules at high energy". In: *Physics Letters A* 350.5–6 (2006), pp. 371 –374. ISSN: 0375-9601. URL: http://www.sciencedirect.com/science/article/pii/S0375960105015987.

[83] O. A .Fojón et al. "Interference effects in H_2 photoionization at high energies". In: *Journal of Physics B: Atomic, Molecular and Optical Physics* 37.15 (2004), p. 3035. URL: http://stacks.iop.org/0953-4075/37/i=15/a=003.

[84] L. Ph. H. Schmidt et al. "Spatial Imaging of the $\mathbf{H}_2{}^+$ Vibrational Wave Function at the Quantum Limit". In: *Phys. Rev. Lett.* 108 (7 2012), p. 073202. DOI: 10.1103/PhysRevLett.108.073202. URL: https://link.aps.org/doi/10.1103/PhysRevLett.108.073202.

[85] Michael Walter and John Briggs. "Photo-double ionization of molecular hydrogen". In: *Journal of Physics B: Atomic, Molecular and Optical Physics* 32.11 (1999), p. 2487. URL: http://stacks.iop.org/0953-4075/32/i=11/a=302.

[86] W. Vanroose et al. "Double photoionization of aligned molecular hydrogen". In: *Phys. Rev. A* 74 (5 2006), p. 052702. DOI: 10.1103/PhysRevA.74.052702. URL: https://link.aps.org/doi/10.1103/PhysRevA.74.052702.

[87] Konstantin A. Kouzakov and Jamal Berakdar. "Photoinduced Emission of Cooper Pairs from Superconductors". In: *Phys. Rev. Lett.* 91 (25 2003), p. 257007. DOI: 10.1103/PhysRevLett.91.257007. URL: https://link.aps.org/doi/10.1103/PhysRevLett.91.257007.

[88] R. HANBURY BROWN and R. Q. TWISS. "The Question of Correlation between Photons in Coherent Light Rays". In: *Nature* 178.4548 (Dec. 1956), pp. 1447–1448. URL: http://dx.doi.org/10.1038/1781447a0.

[89] Gregg Jaeger, Abner Shimony, and Lev Vaidman. "Two interferometric complementarities". In: *Phys. Rev. A* 51 (1 1995), pp. 54–67. DOI: 10.1103/PhysRevA.51.54. URL: https://link.aps.org/doi/10.1103/PhysRevA.51.54.

[90] K P Zetie, S F Adams, and R M Tocknell. "How does a Mach-Zehnder interferometer work?" In: *Physics Education* 35.1 (2000), p. 46. URL: http://stacks.iop.org/0031-9120/35/i=1/a=308.

[91] H. Beutler. "Über Absorptionsserien von Argon, Krypton und Xenon zu Termen zwischen den beiden Ionisierungsgrenzen2P 3 2/0 und2P 1 2/0". In: *Zeitschrift für Physik* 93.3 (1935), pp. 177–196. ISSN: 0044-3328. DOI: 10.1007/BF01365116. URL: http://dx.doi.org/10.1007/BF01365116.

[92] Martin Eckstein et al. "Direct Imaging of Transient Fano Resonances in N_2 Using Time-, Energy-, and Angular-Resolved Photoelectron Spectroscopy". In: *Phys. Rev. Lett.* 116 (16 2016), p. 163003. DOI: 10.1103/PhysRevLett.116.163003. URL: https://link.aps.org/doi/10.1103/PhysRevLett.116.163003.

[93] John J. Hopfield. "Absorption and Emission Spectra in the Region $\lambda 600 - 1100$". In: *Phys. Rev.* 35 (9 1930), pp. 1133–1134. DOI: 10.1103/PhysRev.35.1133. URL: https://link.aps.org/doi/10.1103/PhysRev.35.1133.

[94] V. Madhavan et al. "Tunneling into a Single Magnetic Atom: Spectroscopic Evidence of the Kondo Resonance". In: *Science* 280.5363 (1998), pp. 567–569. ISSN: 0036-8075. DOI: 10.1126/science.280.5363.567. eprint: http://science.sciencemag.org/content/280/5363/567.full.pdf. URL: http://science.sciencemag.org/content/280/5363/567.

[95] A. R. Schmidt et al. "Imaging the Fano lattice to 'hidden order'transition in URu2Si2". In: *Nature* 465.7298 (June 2010), pp. 570–576. URL: http://dx.doi.org/10.1038/nature09073.

[96] Jonathan A. Fan et al. "Self-Assembled Plasmonic Nanoparticle Clusters". In: *Science* 328.5982 (2010), pp. 1135–1138. ISSN: 0036-8075. DOI: 10.1126/science.1187949. eprint: http://science.sciencemag.org/content/328/5982/1135.full.pdf. URL: http://science.sciencemag.org/content/328/5982/1135.

[97] V. A. Fedotov et al. "Sharp Trapped-Mode Resonances in Planar Metamaterials with a Broken Structural Symmetry". In: *Phys. Rev. Lett.* 99 (14 2007), p. 147401. DOI: 10.1103/PhysRevLett.99.147401. URL: https://link.aps.org/doi/10.1103/PhysRevLett.99.147401.

[98] Boris Luk'yanchuk et al. "The Fano resonance in plasmonic nanostructures and metamaterials". In: *Nat Mater* 9.9 (Sept. 2010), pp. 707–715. URL: http://dx.doi.org/10.1038/nmat2810.

[99] Dominik M. Bauer et al. "Combination of a magnetic Feshbach resonance and an optical bound-to-bound transition". In: *Phys. Rev. A* 79 (6 2009), p. 062713. DOI: 10.1103/PhysRevA.79.062713. URL: https://link.aps.org/doi/10.1103/PhysRevA.79.062713.

[100] M. Junker et al. "Photoassociation of a Bose-Einstein Condensate near a Feshbach Resonance". In: *Phys. Rev. Lett.* 101 (6 2008), p. 060406. DOI: 10.1103/PhysRevLett.101.060406. URL: https://link.aps.org/doi/10.1103/PhysRevLett.101.060406.

[101] V. Gruson et al. "Attosecond dynamics through a Fano resonance: Monitoring the birth of a photoelectron". In: *Science* 354.6313 (2016), pp. 734–738. ISSN: 0036-8075. DOI: 10.1126/science.aah5188. eprint: http://science.sciencemag.org/content/354/6313/734.full.pdf. URL: http://science.sciencemag.org/content/354/6313/734.

[102] A. Kaldun et al. "Observing the ultrafast buildup of a Fano resonance in the time domain". In: *Science* 354.6313 (2016), pp. 738–741. ISSN: 0036-8075. DOI: 10.1126/science.aah6972. eprint: http://science.sciencemag.org/content/354/6313/738.full.pdf. URL: http://science.sciencemag.org/content/354/6313/738.

[103] Alicia Palacios et al. "Autoionization of Molecular Hydrogen: Where do the Fano Lineshapes Go?" In: *ChemPhysChem* 14.7 (2013), pp. 1456–1463. ISSN: 1439-7641. DOI: 10.1002/cphc.201200974. URL: http://dx.doi.org/10.1002/cphc.201200974.

[104] James A. R. Samson and G. N. Haddad. "Total photoabsorption cross sections of H2 from 18 to 113 eV". In: *J. Opt. Soc. Am. B* 11.2 (1994), pp. 277–279. DOI: 10.1364/JOSAB.11.000277. URL: http://josab.osa.org/abstract.cfm?URI=josab-11-2-277.

[105] S.K. Semenov and N.A. Cherepkov. "Generalization of the atomic RPA method for diatomic molecules: H2 photoionization cross-section calculation". In: *Chemical Physics Letters* 291.3 (1998), pp. 375 –380. ISSN: 0009-2614. DOI: http://dx.doi.org/10.1016/S0009-2614(98)00573-9. URL: http://www.sciencedirect.com/science/article/pii/S0009261498005739.

[106] Kenji Ito, Richard I. Hall, and Masatoshi Ukai. "Dissociative photoionization of H2 and D2 in the energy region of 25–45 eV". In: *The Journal of Chemical Physics* 104.21 (1996), pp. 8449–8457. DOI: 10.1063/1.471594. eprint: http://dx.doi.org/10.1063/1.471594. URL: http://dx.doi.org/10.1063/1.471594.

[107] C J Latimer et al. "The dissociative photoionization of hydrogen via two-electron excitation at 27.5 eV and 30.5 eV". In: *Journal of Physics B: Atomic, Molecular and Optical Physics* 25.8 (1992), p. L211. URL: http://stacks.iop.org/0953-4075/25/i=8/a=003.

[108] I. Sánchez and F. Martín. "Resonant effects in photoionization of H_2 and D_2". In: *The Journal of Chemical Physics* 107.20 (1997), pp. 8391–8396. DOI: 10.1063/1.475039.

[109] L. Medisauskas et al. "Signatures of attosecond electronic-nuclear dynamics in the one-photon ionization of molecular hydrogen: analytical model vs ab-initio calculations". In: *New Journal of Physics* 17 (2015), p. 053011. DOI: 10.1088/1367-2630/17/5/053011.

[110] J.A. López-Domínguez et al. "Mechanisms of Franck–Condon breakdown over a broad energy range in the valence photoionization of N2 and CO". In: *Journal of Electron Spectroscopy and Related Phenomena* 185.8 (2012). Special Issue in honor of Prof. T. Darrah Thomas: High-Resolution Spectroscopy of Isolated Species, pp. 211 –218. ISSN: 0368-2048. DOI: http://dx.doi.org/10.1016/j.elspec.2012.06.016. URL: http://www.sciencedirect.com/science/article/pii/S0368204812000710.

[111] R. R. Lucchese et al. "Vibrationally resolved partial cross sections and asymmetry parameters for nitrogen K-shell photoionization of the N_2O molecule". In: *Phys. Rev. A* 76 (1 2007), p. 012506. DOI: 10.1103/PhysRevA.76.012506. URL: https://link.aps.org/doi/10.1103/PhysRevA.76.012506.

[112] M. Schmidbauer et al. "Shape resonances and multielectron effects in the core-level photoionization of CO_2". In: *Phys. Rev. A* 52 (3 1995), pp. 2095–2108. DOI: 10.1103/PhysRevA.52.2095. URL: https://link.aps.org/doi/10.1103/PhysRevA.52.2095.

[113] Zhe Zhang et al. "Observation of the Interference Effect in Vibrationally Resolved Electron Momentum Spectroscopy of H_2". In: *Phys. Rev. Lett.* 112 (2 2014), p. 023204. DOI: 10.1103/PhysRevLett.112.023204. URL: https://link.aps.org/doi/10.1103/PhysRevLett.112.023204.

[114] A. González-Castrillo et al. "Reproducibility of Observables and Coherent Control in Molecular Photoionization: From Continuous Wave to Ultrashort Pulsed Radiation". In: *The Journal of Physical Chemistry A* 116.11 (2012). PMID: 22103857, pp. 2704–2712. DOI: 10.1021/jp2078049. eprint: http://dx.doi.org/10.1021/jp2078049. URL: http://dx.doi.org/10.1021/jp2078049.

[115] Emmanuel Foumouo et al. "Theory of multiphoton single and double ionization of two-electron atomic systems driven by short-wavelength electric fields: An ab initio treatment". In: *Phys. Rev. A* 74 (6 2006), p. 063409. DOI: 10.1103/PhysRevA.74.063409. URL: https://link.aps.org/doi/10.1103/PhysRevA.74.063409.

[116] A. Palacios, C. W. McCurdy, and T. N. Rescigno. "Extracting amplitudes for single and double ionization from a time-dependent wave packet". In: *Phys. Rev. A* 76 (4 2007), p. 043420. DOI: 10.1103/PhysRevA.76.043420. URL: https://link.aps.org/doi/10.1103/PhysRevA.76.043420.

[117] Fernando Martín. "Ionization and dissociation using B-splines: photoionization of the hydrogen molecule". In: *Journal of Physics B: Atomic, Molecular and Optical Physics* 32.16 (1999), R197. URL: http://stacks.iop.org/0953-4075/32/i=16/a=201.

[118] M W Ruf, T Bregel, and H Hotop. "The electron angular distribution of different rotational branches in the VUV photoelectron spectrum of H_2". In: *Journal of Physics B: Atomic and Molecular Physics* 16.9 (1983), p. 1549. URL: http://stacks.iop.org/0022-3700/16/i=9/a=014.

[119] I. Sánchez and F. Martín. "Resonant dissociative photoionization of H_2 and D_2". In: *Phys. Rev. A* 57 (2 1998), pp. 1006–1017. DOI: 10.1103/PhysRevA.57.1006. URL: https://link.aps.org/doi/10.1103/PhysRevA.57.1006.

[120] J N Bardsley. "Configuration interaction in the continuum states of molecules". In: *Journal of Physics B: Atomic and Molecular Physics* 1.3 (1968), p. 349. URL: http://stacks.iop.org/0022-3700/1/i=3/a=303.

[121] A. U. Hazi, T. N. Rescigno, and M. Kurilla. "Cross sections for resonant vibrational excitation of N_2 by electron impact". In: *Phys. Rev. A* 23 (3 1981), pp. 1089–1099. DOI: 10.1103/PhysRevA.23.1089. URL: https://link.aps.org/doi/10.1103/PhysRevA.23.1089.

[122] Lukas Medišauskas et al. "A molecular clock for autoionization decay". In: *Journal of Physics B: Atomic, Molecular and Optical Physics* 50.14 (2017), p. 144001. URL: http://stacks.iop.org/0953-4075/50/i=14/a=144001.

[123] J. F. Pérez-Torres et al. "Asymmetric electron angular distributions in resonant dissociative photoionization of H_2 with ultrashort xuv pulses". In: *Phys. Rev. A* 80 (1 2009), p. 011402. DOI: 10.1103/PhysRevA.80.011402. URL: https://link.aps.org/doi/10.1103/PhysRevA.80.011402.

[124] Yi-Yian Yin et al. "Asymmetric photoelectron angular distributions from interfering photoionization processes". In: *Phys. Rev. Lett.* 69 (16 1992), pp. 2353–2356. DOI: 10.1103/PhysRevLett.69.2353. URL: https://link.aps.org/doi/10.1103/PhysRevLett.69.2353.

[125] Zheng-Min Wang and D. S. Elliott. "Determination of the Phase Difference between Even and Odd Continuum Wave Functions in Atoms through Quantum Interference Measurements". In: *Phys. Rev. Lett.* 87 (17 2001), p. 173001. DOI: 10.1103/PhysRevLett.87.173001. URL: https://link.aps.org/doi/10.1103/PhysRevLett.87.173001.

[126] PrinceK. C. et al. "Coherent control with a short-wavelength free-electron laser". In: *Nat Photon* 10.3 (Mar. 2016), pp. 176–179. URL: http://dx.doi.org/10.1038/nphoton.2016.13.

[127] Michael Chini et al. "Characterizing ultrabroadband attosecond lasers". In: *Opt. Express* 18.12 (2010), pp. 13006–13016. DOI: 10.1364/OE.18.013006. URL: http://www.opticsexpress.org/abstract.cfm?URI=oe-18-12-13006.

[128] H.G. Muller. "Reconstruction of attosecond harmonic beating by interference of two-photon transitions". In: *Applied Physics B* 74.1 (2002), s17–s21. ISSN: 1432-0649. DOI: 10.1007/s00340-002-0894-8. URL: http://dx.doi.org/10.1007/s00340-002-0894-8.

[129] Valérie Véniard, Richard Taïeb, and Alfred Maquet. "Two-Color Multiphoton Ionization of Atoms Using High-Order Harmonic Radiation". In: *Phys. Rev. Lett.* 74 (21 1995), pp. 4161–4164. DOI: 10.1103/PhysRevLett.74.4161. URL: https://link.aps.org/doi/10.1103/PhysRevLett.74.4161.

[130] Valérie Véniard, Richard Taïeb, and Alfred Maquet. "Phase dependence of (N+1)-color (N>1) ir-uv photoionization of atoms with higher harmonics". In: *Phys. Rev. A* 54 (1 1996), pp. 721–728. DOI: 10.1103/PhysRevA.54.721. URL: https://link.aps.org/doi/10.1103/PhysRevA.54.721.

[131] A. Zavriyev et al. "Ionization and dissociation of H_2 in intense laser fields at 1.064 μm, 532 nm, and 355 nm". In: *Phys. Rev. A* 42 (9 1990), pp. 5500–5513. DOI: 10.1103/PhysRevA.42.5500. URL: https://link.aps.org/doi/10.1103/PhysRevA.42.5500.

[132] P. M. Paul et al. "Observation of a Train of Attosecond Pulses from High Harmonic Generation". In: *Science* 292.5522 (2001), pp. 1689–1692. ISSN: 0036-8075. DOI: 10.1126/science.1059413. eprint: http://science.sciencemag.org/content/292/5522/1689.full.pdf. URL: http://science.sciencemag.org/content/292/5522/1689.

[133] H.G. Muller. "Reconstruction of attosecond harmonic beating by interference of two-photon transitions". In: *Applied Physics B* 74.1 (2002), s17–s21. ISSN: 1432-0649. DOI: 10.1007/s00340-002-0894-8. URL: https://doi.org/10.1007/s00340-002-0894-8.

[134] K. Klünder et al. "Probing Single-Photon Ionization on the Attosecond Time Scale". In: *Phys. Rev. Lett.* 106 (14 2011), p. 143002. DOI: 10.1103/PhysRevLett.106.143002. URL: https://link.aps.org/doi/10.1103/PhysRevLett.106.143002.

[135] D Guénot et al. "Measurements of relative photoemission time delays in noble gas atoms". In: *Journal of Physics B: Atomic, Molecular and Optical Physics* 47.24 (2014), p. 245602. URL: http://stacks.iop.org/0953-4075/47/i=24/a=245602.

[136] Caryn Palatchi et al. "Atomic delay in helium, neon, argon and krypton". In: *Journal of Physics B: Atomic, Molecular and Optical Physics* 47.24 (2014), p. 245003. URL: http://stacks.iop.org/0953-4075/47/i=24/a=245003.

[137] L. Cattaneo et al. "Comparison of attosecond streaking and RABBITT". In: *Opt. Express* 24.25 (2016), pp. 29060–29076. DOI: 10.1364/OE.24.029060. URL: http://www.opticsexpress.org/abstract.cfm?URI=oe-24-25-29060.

[138] S. Haessler et al. "Phase-resolved attosecond near-threshold photoionization of molecular nitrogen". In: *Phys. Rev. A* 80 (1 2009), p. 011404. DOI: 10.1103/PhysRevA.80.011404. URL: https://link.aps.org/doi/10.1103/PhysRevA.80.011404.

[139] Martin Huppert et al. "Attosecond Delays in Molecular Photoionization". In: *Phys. Rev. Lett.* 117 (9 2016), p. 093001. DOI: 10.1103/PhysRevLett.117.093001. URL: https://link.aps.org/doi/10.1103/PhysRevLett.117.093001.

[140] A. L. Cavalieri et al. "Attosecond spectroscopy in condensed matter". In: *Nature* 449.7165 (Oct. 2007), pp. 1029–1032. URL: http://dx.doi.org/10.1038/nature06229.

[141] Reto Locher et al. "Energy-dependent photoemission delays from noble metal surfaces by attosecond interferometry". In: *Optica* 2.5 (2015), pp. 405–410. DOI: 10.1364/OPTICA.2.000405. URL: http://www.osapublishing.org/optica/abstract.cfm?URI=optica-2-5-405.

[142] Erik P. Mansson et al. "Double ionization probed on the attosecond timescale". In: *Nat Phys* 10.3 (Mar. 2014), pp. 207–211. URL: http://dx.doi.org/10.1038/nphys2880.

[143] I. Jordan et al. "Spin-orbit delays in photoemission". In: *Phys. Rev. A* 95 (1 2017), p. 013404. DOI: 10.1103/PhysRevA.95.013404. URL: https://link.aps.org/doi/10.1103/PhysRevA.95.013404.

[144] S. Scheit, L. S. Cederbaum, and H.-D. Meyer. "Time-dependent interplay between electron emission and fragmentation in the interatomic Coulombic decay". In: *The Journal of Chemical Physics* 118.5 (2003), pp. 2092–2107. DOI: 10.1063/1.1531996. eprint: http://dx.doi.org/10.1063/1.1531996. URL: http://dx.doi.org/10.1063/1.1531996.

[145] X. Zhou et al. "Probing and controlling non-Born-Oppenheimer dynamics in highly excited molecular ions". In: *Nat Phys* 8.3 (Mar. 2012), pp. 232–237. URL: http://dx.doi.org/10.1038/nphys2211.

[146] Daniel Strasser et al. "Ultrafast predissociation of superexcited nitrogen molecules". In: *Molecular Physics* 106.2-4 (2008), pp. 275–280. DOI: 10.1080/00268970701790967. eprint: http://dx.doi.org/10.1080/00268970701790967. URL: http://dx.doi.org/10.1080/00268970701790967.

[147] Marlene Wickenhauser et al. "Time Resolved Fano Resonances". In: *Phys. Rev. Lett.* 94 (2 2005), p. 023002. DOI: 10.1103/PhysRevLett.94.023002. URL: https://link.aps.org/doi/10.1103/PhysRevLett.94.023002.

[148] José Luis Sanz-Vicario, Henri Bachau, and Fernando Martín. "Time-dependent theoretical description of molecular autoionization produced by femtosecond xuv laser pulses". In: *Phys. Rev. A* 73 (3 2006), p. 033410. DOI: 10.1103/PhysRevA.73.033410. URL: https://link.aps.org/doi/10.1103/PhysRevA.73.033410.

[149] Eugene P. Wigner. "Lower Limit for the Energy Derivative of the Scattering Phase Shift". In: *Phys. Rev.* 98 (1 1955), pp. 145–147. DOI: 10.1103/PhysRev.98.145. URL: https://link.aps.org/doi/10.1103/PhysRev.98.145.

[150] Felix T. Smith. "Lifetime Matrix in Collision Theory". In: *Phys. Rev.* 118 (1 1960), pp. 349–356. DOI: 10.1103/PhysRev.118.349. URL: https://link.aps.org/doi/10.1103/PhysRev.118.349.

[151] L. Argenti et al. "Control of photoemission delay in resonant two-photon transitions". In: *Phys. Rev. A* 95 (4 2017), p. 043426. DOI: 10.1103/PhysRevA.95.043426. URL: https://link.aps.org/doi/10.1103/PhysRevA.95.043426.

[152] Renate Pazourek, Stefan Nagele, and Joachim Burgdorfer. "Time-resolved photoemission on the attosecond scale: opportunities and challenges". In: *Faraday Discuss.* 163 (0 2013), pp. 353–376. DOI: 10.1039/C3FD00004D. URL: http://dx.doi.org/10.1039/C3FD00004D.

[153] Misha Ivanov and Olga Smirnova. "How Accurate Is the Attosecond Streak Camera?" In: *Phys. Rev. Lett.* 107 (21 2011), p. 213605. DOI: 10.1103/PhysRevLett.107.213605. URL: https://link.aps.org/doi/10.1103/PhysRevLett.107.213605.

[154] J.M. Dahlström et al. "Theory of attosecond delays in laser-assisted photoionization". In: *Chemical Physics* 414 (2013). Attosecond spectroscopy, pp. 53 –64. ISSN: 0301-0104. DOI: http://dx.doi.org/10.1016/j.chemphys.2012.01.017. URL: http://www.sciencedirect.com/science/article/pii/S0301010412000298.

[155] J M Dahlström, A L'Huillier, and A Maquet. "Introduction to attosecond delays in photoionization". In: *Journal of Physics B: Atomic, Molecular and Optical Physics* 45.18 (2012), p. 183001. URL: http://stacks.iop.org/0953-4075/45/i=18/a=183001.

[156] Sebastian Heuser et al. "Angular dependence of photoemission time delay in helium". In: *Phys. Rev. A* 94 (6 2016), p. 063409. DOI: 10.1103/PhysRevA.94.063409. URL: https://link.aps.org/doi/10.1103/PhysRevA.94.063409.

[157] J F Pérez-Torres et al. "The role of autoionizing states in two-photon dissociative ionization of H 2 by xuv ultrashort laser pulses". In: *Journal of Physics B: Atomic, Molecular and Optical Physics* 43.1 (2010), p. 015204. URL: http://stacks.iop.org/0953-4075/43/i=1/a=015204.

[158] S. Selstø et al. "Electron angular distribution in resonance-enhanced two-photon ionization of $H_2{}^+$ by ultrashort laser pulses". In: *Phys. Rev. A* 75 (3 2007), p. 033419. DOI: 10.1103/PhysRevA.75.033419. URL: https://link.aps.org/doi/10.1103/PhysRevA.75.033419.

[159] Carlos Marante et al. "Hybrid-Basis Close-Coupling Interface to Quantum Chemistry Packages for the Treatment of Ionization Problems". In: *Journal of Chemical Theory and Computation* 13.2 (2017). PMID: 28058835, pp. 499–514. DOI: 10.1021/acs.jctc.6b00907. eprint: http://dx.doi.org/10.1021/acs.jctc.6b00907. URL: http://dx.doi.org/10.1021/acs.jctc.6b00907.